

OBSERVING AND SIMULATING GALAXY EVOLUTION

- from X-ray to millimeter wavelengths

Dissertation submitted for the degree of
PHILOSOPHIÆ DOCTOR
to the PhD School of The Faculty of Science, University of Copenhagen

on April 10 2015, by

Karen Pardos Olsen

Supervisors: *Sune Toft* and *Thomas Greve*

Defended on May 18 2015



Dark Cosmology Centre



Cover art:

Nut, goddess of the sky in ancient Egyptian religion. Contrary to most other religions, the sky was feminine and her brother, Geb, personified the Earth. At dusk, Nut would swallow the sun god, Ra, who would pass through her belly during the night and be reborn at dawn. Sometimes she was depicted as a cow, but most of the time as a star-covered nude woman arching over, and protecting, the Earth.

OBSERVING
AND SIMULATING
GALAXY EVOLUTION
- from X-ray to millimeter wavelengths

ABSTRACT

It remains a quest for modern astronomy to answer what main mechanisms set the star formation rate (SFR) of galaxies. Massive galaxies present a good starting point for such a quest due to their relatively easy detection at every redshift. Since stars form out of cold and dense gas, a comprehensive model for galaxy evolution should explain any observed connection between SFR and the amount and properties of the molecular gas of the interstellar medium (ISM). In proposed models of that kind, an active galactic nucleus (AGN) phase is often invoked as the cause for the decrease or cease of star formation. This thesis consists of models and observations of gas and AGNs in massive galaxies at $z \sim 2$, and how they may affect the overall SFR and the subsequent evolutionary trajectory of massive galaxies to $z = 0$.

For an improved understanding of how observed gas emission lines link to the underlying ISM physics, a new code is presented; SImulator of GALaxy Millimeter/submillimeter Emission (**SÍGAME**). By post-processing the outputs of cosmological simulations of galaxy formation with sub-grid physics recipes, **SÍGAME** divides the ISM into different gas phases and derives density and temperature structure, with locally resolved radiation fields. In the **first study**, **SÍGAME** is combined with the radiative transfer code **LIME** to model the spectral line energy distribution (SLED) of CO. A CO SLED close to that of the Milky Way is found for normal star-forming massive galaxies at $z \sim 2$, but with CO-H₂ conversion factors about 3 times smaller and decreasing towards the center of each model galaxy. In a **second study**, **SÍGAME** is adapted to model the fine-structure line of singly ionized carbon, [CII] at $158\text{ }\mu\text{m}$, the most powerful emission line of neutral ISM. Applying **SÍGAME** to the same type of galaxies, most [CII] emission can be traced back to the PDRs (Photodissociation Regions) of their ISM, but at higher SFR the molecular component starts to dominate, while the contribution from HII gas is always negligible. The relation between [CII] luminosity and SFR of the simulated galaxies, displays a steeper slope than that observed for galaxies at $z > 0.5$. A corresponding relation is also established on kpc scales for the first time theoretically.

A **third study** uncovers the presence of AGNs among massive galaxies at $z \sim 2$, and sheds light on the AGN-host co-evolution by connecting the fraction and luminosity of AGNs with galaxy properties. By analyzing a large survey in X-ray, AGNs of high and low X-ray luminosity are extracted among massive galaxies at $z \sim 2$ via AGN classification methods and stacking techniques in X-ray. It is found that about every fifth massive galaxy, quenched or not, contains an X-ray luminous AGN. Interestingly, an even higher fraction of low-luminosity AGNs reside in the X-ray undetected galaxies, and preferentially in the quenched ones, lending support to the importance of AGNs in impeding star formation during galaxy evolution.

CONTENTS

Abstract	iii
Contents	iv
1 Background	1
1.0.1 Setting the scale	1
1.0.2 The cosmic web of galaxies	2
1.1 ‘Normal star-forming galaxies’	2
1.1.1 The turning point at $z \sim 2$	4
1.1.2 The case of ‘massive galaxies’	4
1.2 The Interstellar Medium (ISM)	5
1.2.1 Chemical composition	6
1.2.2 Distribution and density	7
1.2.3 Thermal state	8
1.3 The Active Galactic Nucleus (AGN)	11
1.3.1 Unification models	11
1.4 The ‘spectral fingerprint’ of a galaxy	12
1.5 An exciting time for observations	13
1.5.1 Radio Telescopes	13
1.5.2 X-ray Telescopes	15
1.6 Galaxy simulations	16
1.6.1 ‘Zoom-in’ simulations	17
1.6.2 The calibration to $z = 0$	17
1.7 References	17
2 Introduction to this thesis	20
2.1 Evolution of massive galaxies across cosmic time	20
2.1.1 High-redshift massive galaxy populations	20
2.1.2 Observing galaxies at $z > 4$ via their gas emission lines	22
2.1.3 The red and blue galaxies	22
2.1.4 Quenching star formation	23
2.1.5 Connecting the dots	24
2.2 This thesis	26
2.2.1 All eyes on the gas	27
2.2.2 Quick summary of my projects	29
2.3 References	29

3 CO emission lines from galaxies	35
3.1 Probing the molecular gas	35
3.2 Observations of CO line emission from different types of galaxies at $z \gtrsim 2$	36
3.2.1 The X_{CO} factor	36
3.3 Modeling of CO emission lines	37
4 Simulating CO line emission from massive star-forming galaxies at $z = 2$ (Paper I)	40
4.1 Aim of this project	40
4.2 Cosmological Simulations	41
4.2.1 SPH simulations	41
4.2.2 The model galaxies	41
4.3 Modeling the ISM with SÍGAME	45
4.3.1 Methodology overview	45
4.3.2 The Warm and Cold Neutral Medium	45
4.3.3 HI to H ₂ conversion	47
4.3.4 Structure of the molecular gas	49
4.3.5 Radiative transfer of CO lines	56
4.3.6 Combining the GMC line profiles in a galaxy	57
4.4 Simulating massive $z = 2$ main sequence galaxies	58
4.4.1 Total molecular gas content and H ₂ surface density maps	58
4.4.2 CO line emission maps and resolved excitation conditions	60
4.4.3 The CO-to-H ₂ conversion factor	62
4.4.4 Global CO line luminosities and spectral line energy distributions	63
4.5 Testing different ISM models	65
4.6 Comparison with other models	66
4.7 Conclusions	70
4.8 References	73
5 [CII] line emission from galaxies	76
5.1 Probing the neutral and ionized gas	76
5.2 Observations of [CII] emission in galaxies at high and low redshift	76
5.2.1 The [CII] deficit	77
5.2.2 Contributing gas phases to the [CII] emission	78
5.2.3 [CII] as a star formation rate tracer	78
5.3 Modeling [CII] emission	79
6 Understanding the $L_{[\text{CII}]}$-SFR relation with simulations (Paper II)	80
6.1 Aim of this project	80
6.2 Methodology overview	80
6.3 SPH Simulations	82
6.3.1 SPH simulations of $z = 2$ main sequence galaxies	82
6.4 Modeling the ISM	84
6.4.1 Giant Molecular Clouds	84
6.4.2 The ionized gas	91
6.5 The [CII] line emission	92

6.6	Results and discussion	93
6.6.1	Radial [CII] luminosity profiles	93
6.6.2	The integrated $L_{\text{[CII]}}$ -SFR relation	96
6.6.3	The resolved $\Sigma_{\text{[CII]}} - \Sigma_{\text{SFR}}$ relation	99
6.6.4	Physical underpinnings of the $L_{\text{[CII]}}$ -SFR relation	100
6.7	Comparing with other [CII] simulations	103
6.8	Conclusion	106
7	Outlook	108
7.1	Improvements on SÍGAME	108
7.1.1	Dust temperatures with a radiative transfer code	108
7.1.2	Modeling of asymmetric GMCs	108
7.1.3	Including heating by X-rays and turbulent dissipation	109
7.2	Going to higher redshift	109
7.2.1	The evolution of X_{CO} with redshift	109
7.2.2	The full calibration to normal galaxies at $z \sim 2$	109
7.2.3	Galaxies during the epoch of re-ionization	109
7.3	References	111
II	THE AGN-GALAXY CO-EVOLUTION AT $z \sim 2$	115
8	How to detect an AGN	117
8.1	Dissecting the X-ray emission from an AGN	118
8.1.1	The AGN fraction at $z \gtrsim 2$ from observations in X-ray	120
9	On the prevalence of AGN at $z \sim 2$ (Paper III)	121
9.1	Aim of this project	121
9.2	Our method and galaxy sample	121
9.2.1	X-ray data and stacking analysis	122
9.2.2	Luminous AGN Identification	124
9.2.3	X-ray Inferred SFR	125
9.3	An overwhelmingly large AGN population	127
9.3.1	Luminous AGN Fraction	127
9.3.2	Importance of Low-luminosity AGNs	128
9.3.3	Contribution from Hot Gas Halos	129
9.3.4	Quenching of Star Formation by AGNs?	131
9.4	Conclusions	132
10	Outlook	134
10.1	The AGN-morphology connection	134
10.2	Direct observations of AGN feedback	135
10.3	Future directions: Discerning variability with time	135
10.4	References	137
Summary		140
Sammenfatning		142

Acknowledgments	144
Appendices	145
A Appendix to Chapter 4	147
A.1 Thermal balance of the atomic gas phase	147
A.2 Thermal balance of the molecular gas phase	148
A.3 GMC models	150
B Appendix to Chapter 6	156
B.1 Density of singly ionized carbon	156
B.2 Electron fraction	158
B.3 Heating and cooling rates of molecular and atomic gas inside GMCs	158
B.4 The [CII] cooling rate in gas of different conditions	159
B.5 SPH properties relevant for the [CII] emission	163
B.6 References	164

1

BACKGROUND

Do not feel lonely, the entire Universe is inside you. - Rumi¹

While Europeans were taking their medieval nap, Arabs carried astronomy forward. Not only did they collect and combine the astronomy from e.g. Greece, Egypt and India into one mathematical language, they also made contributions to the Ptolemaic system and created instruments such as celestial globes, astrolabs and large observatories. Their motivation was mostly a practical one of wanting to determine prayer times and the direction to Mecca to high accuracy. But what might the Arabs have thought for themselves while looking up at the stars? While this will remain unknown, we now know that most of that twinkling in the sky comes from our home, the Milky Way. Stars in the Milky Way are organized in a slowly rotating disk of spiral arms, embraced by an additional spheroidal component, the bulge. If you are lucky, you can even see a diffuse and ‘milky’ band, which is the combined light from millions of unresolved stars in this disk. What you can’t see with your naked eye, is all the gas and dust out of which new stars are born. Nor can you see the dark matter, emitting no light at all and believed to inhabit a large sphere embracing the Milky Way entirely. We call such an assembly of baryonic and dark matter a galaxy, and the Universe is full of them. Understanding how these galaxies form and evolve while making room for us², is one of the fundamental aims of modern astronomy. This thesis is about the gas and the black hole component in galaxies. A theoretical model is developed to simulate the amount and state of gas in galaxies as well as its emission. A separate study uncovers the fraction of massive galaxies dominated by the powerful energetics created by their central black hole, during an important cosmic epoch. Together, these projects offer a better view of galaxy evolution and will be useful for predicting and interpreting future observations.

1.0.1 SETTING THE SCALE

The finite speed of light is of great value to astronomers, because it allows us to look back in time. In fact, astronomical distances, both within and between galaxies, are measured in light years (ly; the distance light can travel in 1 year) or parsecs (1 pc = 3.26 ly). On top of that, the expansion of the Universe causes light to ‘stretch’ as it traverses the great expanses between galaxies. The amount of ‘stretching’ serves as a label on every photon, saying how far it has been traveling. We call this ‘the redshift of light’, z , and often use it as a measure of

¹Persian poet and Sufi mystic of the 13th century

²In at least one case

distance from us or age of the Universe. Fig. 1.1 provides a quick calibration between age of the Universe and redshift.

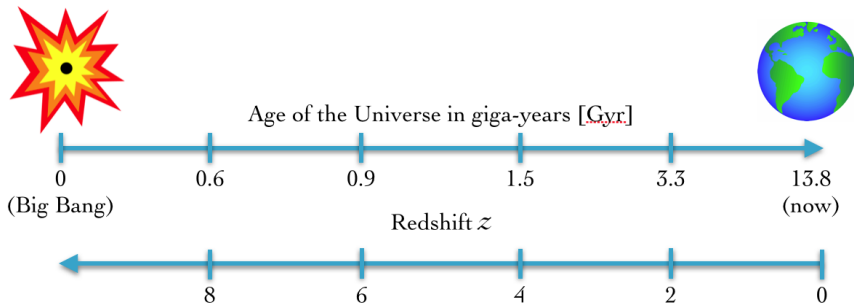


Figure 1.1 A scale comparing age of the Universe with redshift, across its total lifespan of ~ 13.8 Gyr. Note that the redshift drops with age in a exponential-like behaviour, meaning that the Universe reached half its age at quite low redshift, $z \approx 0.7$. Photons decoupled from matter at $z = 1,100$, only $\sim 378,000$ yr after the Big Bang, and that is as far back as we can observe. The ages have been calculated according to the now generally accepted spatially flat Λ CDM cosmology model, that describes the composition of the Universe with just six parameters (fixed here to the most recent results by the Planck Collaboration et al., 2015).

1.0.2 THE COSMIC WEB OF GALAXIES

Galaxies are not evenly distributed in space, but rather follow the underlying cosmic web of dark matter that attracts the gas via gravitation. Fig. 1.2 is a map carried out by Colless et al. (2001) of galaxies close to the MW and out to $z \approx 0.3$ over a total sky area of 2000 deg^2 or almost 5 % of the total sky. Like a Swiss cheese, there are regions with very low density of galaxies (so-called voids) and other regions with many galaxies living close together (clusters) connected by filaments and sheets. It has been confirmed by observations, that in the latter, highly concentrated regions, galaxies are prone to interact and possibly merge into even bigger ones. Galaxies are therefore not isolated systems that go about their own business, but are constantly influenced by their surroundings via e.g. mergers, tidal strippings and gas inflow from the Intra Cluster Medium (ICM). In some of the following sections we will describe their internal components and inner workings, treating them as isolated systems, but one should never forget that galaxies in general interact with their surroundings.

1.1 ‘NORMAL STAR-FORMING GALAXIES’

Galaxies come in a great variety from containing few stars (dwarf galaxies) to containing many stars (massive galaxies), from compact to extended, from star-forming to inactive (quiescent in the following) and with different compositions of stars, gas, dust and dark matter. That said, most of them follow a basic rule: The more stars they have, the more stars they form. In other words, plotted in a star formation rate (SFR) vs. stellar mass (M_*) diagram, most galaxies fall on a power law relation called the ‘main sequence’ (MS). The evolution of this sequence with cosmic time has been investigated recently by Speagle et al. (2014) who compiled 25 studies from the existing literature to find that the MS evolves towards higher SFR as we look back in time. This is shown in Fig. 1.3 with best fits to the observations at different redshifts, without plotting individual galaxies for the sake of simplicity.

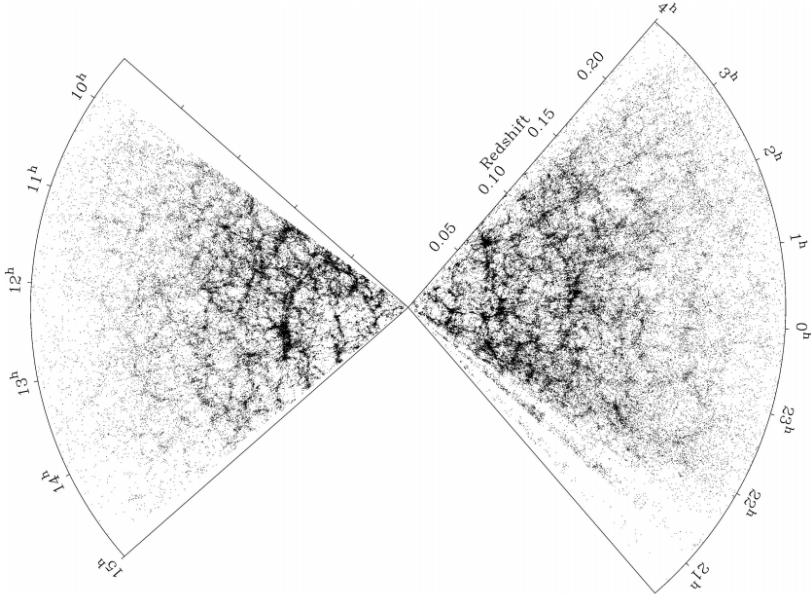


Figure 1.2 Map of galaxies around us and out to $z \approx 0.3$ from the 2dF Galaxy Redshift Survey by (Colless et al., 2001) who studied two strips on the sky, one in the northern (left) and one in the southern (right) hemisphere.

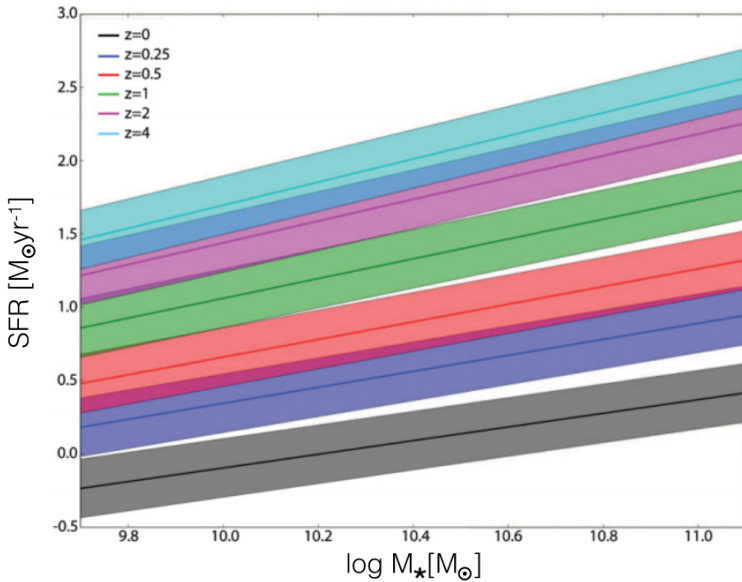


Figure 1.3 Main sequence evolution. Power law fits to star-forming galaxies in different redshift bins from the compilation study of Speagle et al. (2014). Shaded areas show an estimated ‘true’ scatter of 0.2 dex.

Hence, like in crazy adolescent years, back in the day galaxies used to produce stars at much higher rates. The slope of the SFR- M_* relations shown in Fig. 1.3 is also called the specific star formation rate, $\text{SSFR} = \text{SFR}/M_*$, and with very few galaxies at high-redshift, it is still hard to say whether the SSFR continues to rise with redshift or reaches a ‘plateau’ (Behroozi et al.,

2013; Speagle et al., 2014).

1.1.1 THE TURNING POINT AT $z \sim 2$

If one measures SFR per volume, there is a maximum in cosmic SFR density, SFRD, at $z \sim 2$ after which it starts to decline again as shown in Fig. 1.4. The epoch around $z \sim 2$, or about 10 billion years ago, is therefore an interesting one of phase change and one that we are just now beginning to uncover with modern telescopes (see Section 1.5).

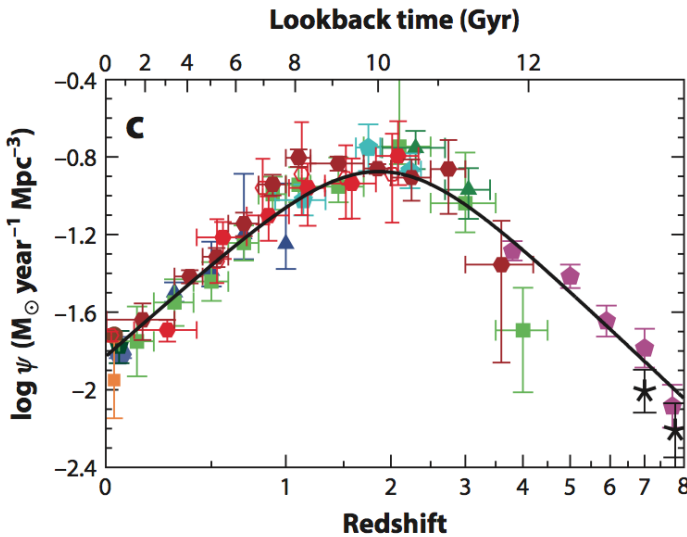


Figure 1.4 The evolution of cosmic SFR density (SFRD) with redshift from the review of Madau & Dickinson (2014).

1.1.2 THE CASE OF ‘MASSIVE GALAXIES’

To understand how galaxies evolved since their formation some million years after the Big Bang, we need observations of all types of galaxies from high redshift until now. This task is impeded by the difficulty of resolving a galaxy very far away, because galaxies start to appear very dim and small. The degree at which a large survey (such as the 2dF Survey in Fig. 1.2) is capturing all galaxies of a certain mass, is referred to as ‘completeness’. The state-of-the-art Cosmic Assembly Near-IR Deep Extragalactic Legacy Survey (CANDELS), carried out with the Hubble Space Telescope (HST), looks all the way back to the high-redshift universe ($z \sim 8$) with observations of different exposure time (depth). But even in the deep fields of GOODS-South/North, a typical lower mass limit of $10^{10} M_\odot$ must be adopted to ensure 100 % completeness for studies going out to $z \sim 2.5$ (see e.g. Wuyts et al., 2012). In the smaller Ultra Deep Fields (UDFs), CANDELS can reach the same mass out to $z \sim 3$ due to longer exposure times³ (Hartley et al., 2013). But galaxies with stellar masses below these limits may exist that these surveys are incapable of detecting with available telescopes and integration time. For this reason, massive (i.e. with high stellar mass) galaxies represent a convenient sample, because

³see http://candels.ucolick.org/survey/files/ferguson_STUC1102_v2.pdf

they are relatively easy to detect at all redshifts. My work concerns mainly massive galaxies, so this denomination will occur frequently in the present dissertation and the exact mass range will always be defined for each particular study.

1.2 THE INTERSTELLAR MEDIUM (ISM)

Let's return for a moment to the sparkling stars that you may observe on a clear night. What you can't see with your naked eye is all the material filling out the vast spaces in between those stars, the Interstellar Medium or ISM. But it is out of this mixture of gas and dust that stars are born, the stars that expel heavier elements during their explosive deaths, thereby providing the universe with the atoms that we are ultimately made of. Carl Sagan once said that '*we are made of starstuff*', yet stars would never have been formed had it not been for the gas that was already there. Fig. 1.5 shows an example of what surprises lie in wait once telescopes are tuned to the frequencies at which the gas lights up in the ISM. The blue image is made of stellar light emission from the Antennae Galaxies – two colliding spiral galaxies about 70 million ly away from us – and the red image is a composite of observations with the interferometric array ALMA (to be described in section 1.5).

Whether a cloud of gas in a galaxy can fragment and collapse to a density that allows fusion, i.e. the ignition of a new star, depends on the properties of that gas. The efficiency by which the gas forms stars is characterised by the gas depletion time, t_{dep} :

$$t_{\text{dep}} = m_{\text{gas}}/\text{SFR} \quad (1.1)$$

that is, the time it would take to use up a cloud of mass m_{gas} if the current SFR stayed constant. Naively, one might expect that t_{dep} would be close to the time it takes a cloud to collapse onto itself under the influence of gravity only, also called the free-fall time, t_{ff} . But observations show that t_{dep} is typically 1-3 orders of magnitude longer than t_{ff} , requiring the existence of processes that slow down the star formation rate resulting from pure gravitation. These processes are broadly gathered under the term 'feedback' from either nearby star formation (see review by Krumholz et al., 2014) or the powerful radiation from an Active Galactic Nucleus (see Section 1.3.1).

Feedback on star formation is a whole topic in itself under fierce exploration with observations and theoretical models. An example of one strong type of feedback, is the ionizing field from young stars. Stars of masses $> 10 M_{\odot}$ emit large quantities of ionizing photons creating large bubbles of expanding hot, ionized gas, that can hit nearby cold clouds and prevent them from collapsing in a type of explosive feedback (Krumholz et al., 2014; Dale et al., 2012).

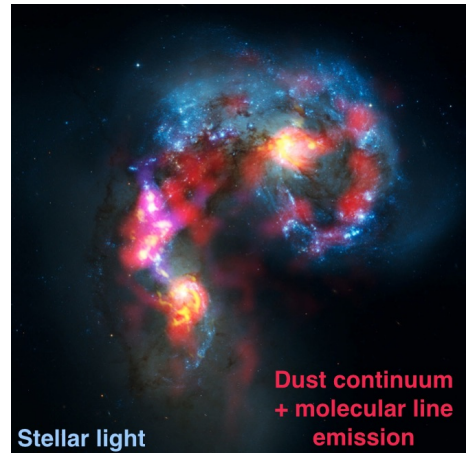


Figure 1.5 The Antennae Galaxies, credit: NASA/ESA HST for the optical image, and ALMA (ESO/NAOJ/NRAO) first science results for the observations of gas and dust at sub-mm wavelengths.

However, recent simulations by Dale et al. (2012) show that the effect of expanding regions of ionized gas in turbulent clouds depends strongly on the escape velocities in the gas. Fig. 1.6 illustrates, with snapshots from their simulations, how photoionization only has a significant impact in clouds of escape velocities, as set by the cloud mass and size, below about 10 km s^{-1} . This example shows that feedback from star formation involves many intercoupled processes. Other types of stellar feedback include those of protostellar outflows, radiation pressure from massive stars, winds from hot stars, supernovae explosions and the mere thermal energy injected into the gas as gravitational potential energy is released during the collapse. In addition, nature most likely combines these mechanisms with the influence of magnetic fields (e.g. Price & Bate, 2009).

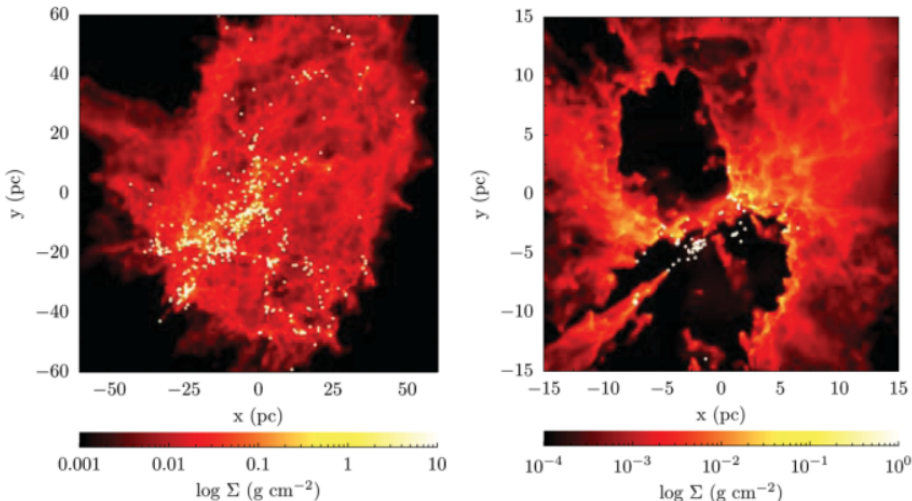


Figure 1.6 *Left:* Column density map of a simulation of star cluster formation in a gas cloud with escape velocity $> 10 \text{ km s}^{-1}$. White dots represent individual stars. *Right:* The same but for an escape velocity of $< 10 \text{ km s}^{-1}$, in which case star formation is suppressed. Adapted from Krumholz et al. (2014).

In principle, being able to observe the composition, turbulence, temperature, density and magnetic fields of the same gas cloud to high angular precision, would provide the building blocks for uniquely defining star formation on small ($< 50 \text{ pc}$) scales. Therefore, *being able to characterise the gas in terms of these properties will help explain why some massive galaxies at $z \sim 2$ are quiescent while others are even more star-forming than their local counterparts.*

1.2.1 CHEMICAL COMPOSITION

Before galaxies formed, the universe was pervaded by a primordial gas of only 4 atomic species; hydrogen (H), helium (He) and a trace of lithium (Li) and beryllium (Be), as well as a few of their isotopes. These were created from about 10 seconds to 20 minutes after the Big Bang⁴, but any elements heavier than Lithium and Beryllium had to wait for the formation of the first stars a few hundreds of million years later, in order to be produced. Today, hydrogen and helium continue to be the dominant species found in the local ISM of the MW, with gas mass fractions

⁴see <http://www.astro.ucla.edu/~wright/BBNS.html>

of $\sim 71.5\%$ and $\sim 27.1\%$ respectively, compared to only 1.4% of heavier elements denoted ‘metals’ (e.g. Przybilla et al., 2008).

All atoms in the ISM can exist in atomic form or be ionized to several degrees or be combined in molecules of increasing complexity (see Tielens 2013 for an overview of just how complicated these molecules can get). For the general life of a galaxy however, only a subset of these species needs to be considered for the structure and thermal state of the ISM relevant for star formation, as we shall see in the next subsections.

1.2.2 DISTRIBUTION AND DENSITY

Stars form generally in clusters as the simulated one depicted in Fig. 1.6 (Krumholz et al., 2014). Such constructions of dense knots and long filaments are collectively called Giant Molecular Clouds (GMCs) and are observed to have radii from about 5 to ~ 100 pc in the MW and local galaxies (Blitz et al., 2007). From measuring the broadening of emission lines from the gas and converting those into velocity dispersions, one can get an estimate of the mass, by assuming the cloud to be in virial equilibrium (Roman-Duval et al., 2010):

$$M_{\text{vir}} = \frac{1.3\sigma_v^2 R}{G} \Rightarrow M_{\text{vir}} [\text{M}_\odot] = 905 \cdot (\sigma_{v,1D} [\text{km s}^{-1}])^2 \cdot R [\text{pc}] \quad (1.2)$$

This was done by for example Blitz et al. (2007), who found the mass spectrum shown to the left in Fig. 1.7, the data of which can be fitted with a power law of slope -1.71 in the outer MW.

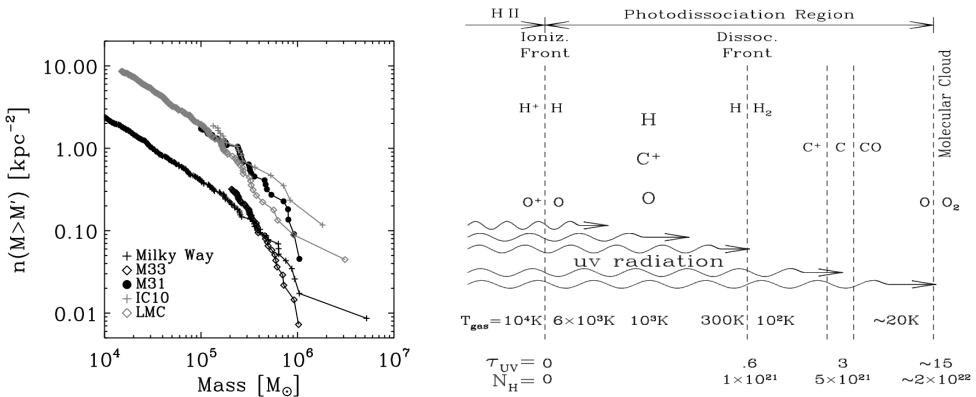


Figure 1.7 *Left:* Mass spectrum of GMCs in the MW and local galaxies (Blitz et al., 2007). *Right:* Schematic overview of the chemical stratification taking place in the PDR of a GMC, from Papadopoulos & Thi (2013).

The reason why all gas in the galaxy is not neutral and forming molecules, is mainly the strong far-ultraviolet (FUV) radiation field from young stars, which ionizes the gas and creates a stratification of the ISM as illustrated on the right-hand side of Fig. 1.7. The region of stratified layers is also referred to as the Photodissociation Region (PDR). In addition to ionizing, the FUV radiation penetrates into the gas and determines its thermal and chemical state. This results in a set of distinct phases of the ISM, that have been observationally identified and are listed in Table 1.1. After the dense, molecular gas, comes the warm and cold neutral medium, often collectively named ‘WCNM’, and finally, the least dense, ionized gas (HII).

If we take a look at the densities listed in Table 1.1, it is clear that the ISM is in general *very*

Chemical state	Gas phase	n [cm $^{-3}$]	T_k [K]
Molecular gas (17% of total mass)	Diffuse H ₂	~ 100	~ 50
	Dense H ₂	$10^3 - 10^6$	10 – 50
Atomic gas (60% of total mass)	Warm HI (WNM)	~ 0.6	~ 5000
	Cold HI (CNM)	30	~ 100
Ionized gas (23% of total mass)	Coronal gas (HIM)	0.004	$10^{5.5}$
	HII gas	$0.3 - 10^4$	10^4

Table 1.1 Gas mass fractions, densities and temperatures of the different phases of interstellar gas, adapted from Draine (2011).

diffuse. You would need a cube of $700 \times 700 \times 700$ meters of the densest H₂ gas phase (with density $n_H \sim 10^6$ cm $^{-3}$) in order to have the same gas mass as present in 1 cm 3 of air at sea level on Earth (with density $\rho \approx 1.2$ kg m $^{-3}$).

Gas mass and SFR are related via the Kennicutt-Schmidt (KS) law, which is an observed tight relation between surface density of SFR, Σ_{SFR} , and gas, Σ_{gas} . As will be explained in further detail in Part I, the line emission from the CO molecule is particularly well suited for estimating the total gas mass. The KS-law for low and high- z star-forming galaxies was estimated by Genzel et al. (2010) using a large data base of CO line observations and SFRs based on several SFR indicators:

$$\log \Sigma_{\text{SFR}} [\text{M}_\odot \text{ yr}^{-1} \text{kpc}^{-2}] = 1.17 \times \log \Sigma_{\text{gas}} [\text{M}_\odot \text{ pc}^{-2}] - 3.48 \quad (1.3)$$

However, recent observations show that this correlation might break down already on scales of ~ 100 pc (Xu et al., 2015).

1.2.3 THERMAL STATE

The thermal state of the ISM is complicated by the fact that the ISM is never in thermodynamic equilibrium, but rather always subject to a flow of energy. It is constantly being heated, primarily by FUV radiation from young stars, while radiating away the heat via dust emission in the infrared and (mostly FIR) gas emission lines (see Section 1.4 for more on the spectrum of a galaxy). To derive the gas kinetic temperature, T_k , one must therefore consider all relevant heating and cooling mechanisms, calculate their energy rates and search for an equilibrium temperature.

Out in the hot, ionized HII regions (see Table 1.1), gas is heated by photo-ionization of HI gas. FUV photons ionize the hydrogen atoms and the free electrons convert their kinetic energy to heat via collisions with other gas particles. Cosmic rays are very energetic protons, most likely produced in supernovae (Ackermann et al., 2013), and they represent a second radiation field that can heat the gas and penetrate even further into it than FUV photons due to their high energies (\sim GeV). Like FUV photons, cosmic rays can ionize the atomic gas and release electrons with kinetic energy, but cosmic rays can also interact with the free electrons, transferring kinetic energy directly via Coulomb interactions.

As for cooling, the gas has several options. First of all, emission lines from hydrogen and heavier elements, in their atomic and ionized states, can remove a great deal of energy, especially at $T_k > 10^4$ K. The cooling rates as function of T_k for the most important elements are shown in Fig. 1.8. The sudden rise in cooling rate at $T_k \sim 10^4$ K makes sure that the temperature

of the HII gas hardly ever exceeds 10^4 K.

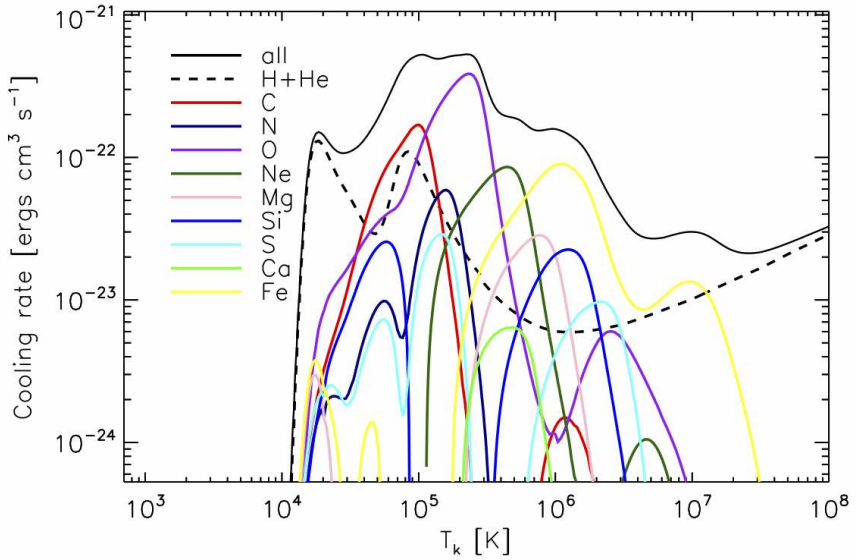


Figure 1.8 Cooling rates of all (black) and individual atoms and ions in the hot ISM as function of temperature. Made with the publicly available code of Wiersma et al. (2009) which includes both collisional- and photo-ionization, though collisional ionization equilibrium (CIE) has been used for this plot. The code takes T_k and n_H as input of which n_H is set to 0.01 cm^{-3} here, and solar abundances are adopted.

In addition to these emission lines, electron recombination with ions can cool the gas, as recombining electrons take away kinetic energy from the plasma, a process which is important at temperatures $> 10^3$ K (Wolfire et al., 2003). At similar high temperatures another important cooling mechanism is the scattering of free electrons off of other free ions, whereby free-free emission removes energy from the gas (Draine, 2011).

Combining all of the above heating and cooling mechanisms, we arrive at one equation that describes the balance between the energy rates of heating and cooling:

$$\Gamma_{\text{PI}} + \Gamma_{\text{CR,HI}} = \Lambda_{\text{ions+atoms}} + \Lambda_{\text{rec}} + \Lambda_{\text{f-f}} \quad (1.4)$$

where Γ_{PI} and $\Gamma_{\text{CR,HI}}$ are the heating rates for photo-ionization and cosmic ray ionization, respectively, whereas $\Lambda_{\text{ions+atoms}}$ is the combined cooling rate from the elements shown in Fig. 1.8. Finally, Λ_{rec} and $\Lambda_{\text{f-f}}$ are the cooling rates due to recombination and free-free interactions as described above.

In the denser and colder ($T_k < 10^4$ K) WCNM, other heating and cooling mechanisms take over. Rather than photo-ionizing the gas, FUV photons now heat the gas more efficiently via the photo-electric effect consisting of a FUV photon knocking loose an electron from the surface of a dust grain, with the same net result: The escaping electron can deposit its kinetic energy as heat in the surrounding gas. The dominating cooling mechanisms in neutral gas are fine-structure line emission from ionised carbon, [CII], to be discussed in more detail in Section 5.1

in Part I, and from neutral atomic oxygen, [OI], leading to the following energy rate equation:

$$\Gamma_{\text{PE}} + \Gamma_{\text{CR,HI}} = \Lambda_{\text{CII}} + \Lambda_{\text{OI}} \quad (1.5)$$

where Γ_{PE} is the heating rate due to the photo-electric effect on dust grains, Λ_{CII} is the cooling rate due to [CII] line emission and Λ_{OI} is the cooling rate due to [OI] line emission. In addition, the Lyman alpha (Ly- α) line of hydrogen at 1216 Å is important in the warm part of the WCNM.

In molecular gas, most of the FUV radiation will be attenuated by dust and self-shielding molecules, leaving in some cases cosmic rays as the dominant source of heating. Indeed, it has been suggested that cosmic rays control the initial conditions for star formation in regions of high SFR density where the sites for star formation might be completely UV-shielded (Papadopoulos et al., 2011; Papadopoulos & Thi, 2013). The prescription for cosmic ray heating per hydrogen atom in molecular gas is in principle different from its form in neutral gas, but the two turn out to be very similar (Stahler & Palla, 2005) (though see Glassgold et al., 2012, who find higher heating rates in molecular gas by a factor 2-3). At increasingly higher temperature, [CII] line cooling gives way for CO line cooling, and at very high densities ($> 10^4 \text{ cm}^{-3}$), cooling by interactions between gas and dust particles can become dominating, as the gas approaches the dust temperature. In molecular gas, line cooling from molecular hydrogen and atomic oxygen also contributes to the cooling rate with typically smaller amounts. Summarized in one equation, the thermal equilibrium in molecular gas can hence be approximated by:

$$\Gamma_{\text{PE}} + \Gamma_{\text{CR,H}_2} = \Lambda_{\text{H}_2} + \Lambda_{\text{CO}} + \Lambda_{\text{OI}} + \Lambda_{\text{CII}} + \Lambda_{\text{gas-dust}} \quad (1.6)$$

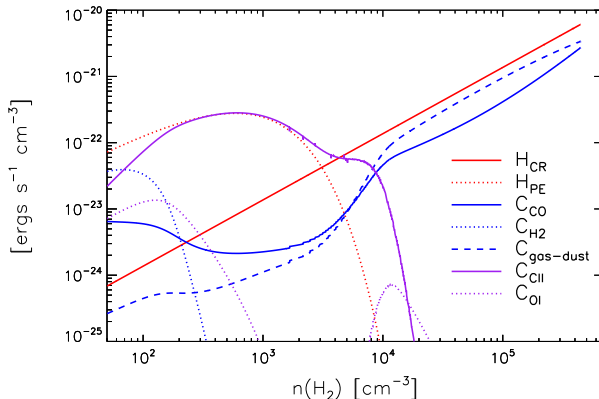


Figure 1.9 Heating and cooling rates in molecular gas. The energy rates shown are calculated at the equilibrium temperature for that density. Calculated for a GMC of mass $m_{\text{GMC}} = 10^4 M_{\odot}$, solar metallicity, an interstellar FUV field of 16 Habing units and a cosmic ray ionization rate of $8 \times 10^{-16} \text{ s}^{-1}$. In the outskirts (low density) of the cloud, [CII] line cooling and photo-electric heating dominate, while in the inner regions (high density), gas-dust cooling and CR heating take over, of which the latter is proportional to the density and hence a straight line of slope 1 (Stahler & Palla, 2005). Made with the SÍGAME code (to be described in Part I).

Fig. 1.9 gives an example of the dominant heating and cooling mechanisms mentioned above as functions of density for the interior of a model GMC of mass $m_{\text{GMC}} = 10^4 M_{\odot}$ and solar metallicity, immersed in an interstellar FUV field of 16 Habing units and a cosmic ray

ionization rate of $8 \times 10^{-16} \text{ s}^{-1}$.

1.3 THE ACTIVE GALACTIC NUCLEUS (AGN)

Apart from the gas, dust, stars and dark matter that I mentioned in the beginning of this introduction, there is a fifth component in the MW: black holes. A particularly big one or ‘supermassive black hole’ (SMBH) is hiding at the very center of the MW, and most likely every galaxy, as it became clear in the 90’s (Magorrian et al., 1998).

The strong gravitational pull from a SMBH creates a rotating accretion disk of matter (yellow part in Fig. 1.10) from its host galaxy. As gravitational energy is converted into mechanical and electromagnetic energy, gas in the accretion disk is heated to very high temperatures and starts to radiate fiercely over a broad range of energies, from radio to X-ray (see Krawczynski & Treister, 2013, for a review of the inner workings of these central engines).

Galaxies in which the spectra are dominated by this type of central energy source, are called Active Galactic Nuclei (AGNs). Observationally, AGNs have been classified into two main groups; (Seyfert) type I and type II based on the width of their optical emission lines. Type I AGNs show strong broad emission lines, while type II AGNs have relatively narrow emission lines and softer X-ray emission. In some cases, relativistic jets are produced perpendicularly to the accretion disk and their strong synchrotron radiation in radio has led to the classification ‘radio-loud’ AGNs. AGNs for which the optical light from the host galaxy is outshined by the central disk itself are dubbed quasars (QSOs).

1.3.1 UNIFICATION MODELS

Over the past two decades, observations have led to the Standard Unified Model suggesting that type I and type II AGNs are intrinsically the same class of objects, but viewed from different angles, as pictured in Fig. 1.10 (Bianchi et al., 2012). In this picture, the accretion disk is surrounded by a clumpy torus of gas and dust, and outflow is mainly allowed within the ionization cone encircling the relativistic jets. A type I AGN is a galaxy inclined so that we see the inner parts of the accretion disk where high orbital speeds result in relatively broad lines. A type II AGN is orientated so that the inner accretion disk is obscured by the clumpy torus and only narrow lines from more distant cold material can be observed.

A tight correlation between optical and X-ray emission of unobscured quasars suggest that all luminous AGNs are intrinsically also X-ray bright (e.g. Steffen et al., 2006; Gibson et al., 2008). But high amounts of obscuring gas and dust in the torus and elsewhere in the host galaxy can decrease the X-ray luminosity or change the spectral slope of the X-ray emission that actually escapes the galaxy, to be discussed further in Section 1.3.1. Alternative sources for strong X-ray emission in a galaxy are High-Mass X-ray Binary systems (HMXBs), which may be significant in case of high SFR (Ranalli et al., 2003), and halos of hot gas (Mulchaey & Jeltema, 2010).

1.4 THE 'SPECTRAL FINGERPRINT' OF A GALAXY

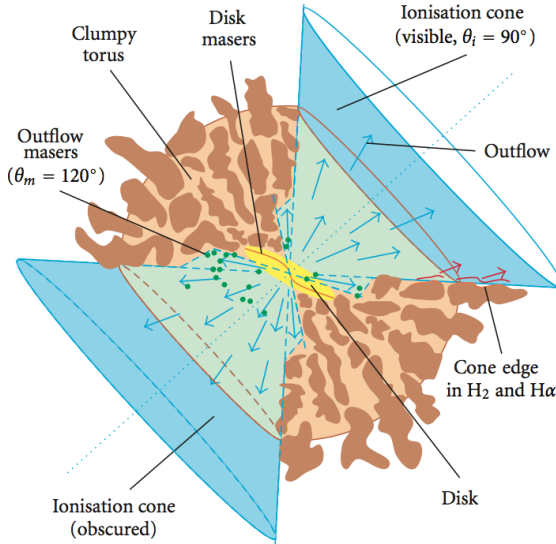


Figure 1.10 Drawing, from the review of (Bianchi et al., 2012), of the inner engine emitting the strong radiation of an AGN, including the disk (yellow) of matter accreting onto the SMBH, the surrounding clumpy torus (brown) and ionization cones (blue), also containing the relativistic jets.

luminosity of $L_{0.5-8 \text{ keV}} = 10^{44} \text{ ergs/s}$.

The best way to measure the conditions of gas in the ISM is by taking a 'spectral fingerprint'. Fig. 1.11 is a cartoon version of the spectral energy distribution (SED) of a galaxy if we were able to measure its emission from the smallest wavelengths (x-ray) to the longest ($\sim 1 \text{ cm}$) of interest for the ISM. Furthermore, the SED is shown in the 'rest frame' of the galaxy rather than in the observers frame, in which the SED would be red-shifted to longer wavelengths if the galaxy happened to be at high redshift. The unit is Jansky ($= \text{Jy} = 10^{-26} \frac{\text{W}}{\text{m}^2 \cdot \text{Hz}}$) which is a typical flux unit in radio astronomy. The SED shown in Fig. 1.11 is that of a typical star-forming spiral galaxy, taken from the publicly available SED templates of Kirkpatrick et al. (2012), with an additional imaginative X-ray flux measurement corresponding to an X-ray luminosity of $L_{0.5-8 \text{ keV}} = 10^{44} \text{ ergs/s}$.

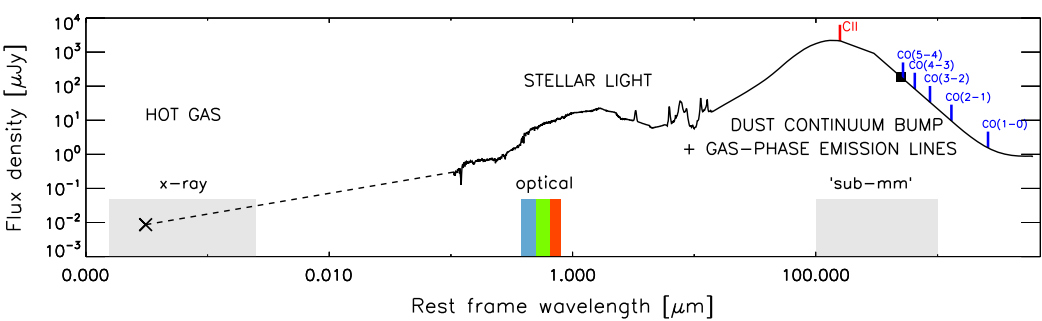


Figure 1.11 The SED of a typical star-forming galaxy at $z = 0$ with indications of the different components contributing to its shape. Also shown are the positions of some important emission lines from the gas, to be described in Part I. The flux has been scaled to the observed $500 \mu\text{m}$ luminosity of local galaxies for a mass of $10^{10} M_\odot$ as marked with a black square (Groves et al., 2015). SED template of Kirkpatrick et al. (2012): <http://www.astro.umass.edu/~pope/Kirkpatrick2012/>.

First noticeable are the two 'bumps' at wavelengths around $1 \mu\text{m}$ and $100 \mu\text{m}$. The first one is dominated by direct stellar light at ultraviolet (UV) to near-infrared (NIR) wavelengths. The UV light is mainly produced by young massive stars recently formed and therefore traces the current SFR well, since massive stars have relatively short lifetimes. On the other hand, the NIR flux is primarily consisting of light from old, less massive stars, making NIR luminosity a good tracer of total stellar mass. Good estimates of SFR and M_* can be made simultaneously

by fitting the entire SED with stellar population synthesis models, typically only requiring assumptions about the initial mass function (IMF) of stars as they are born, the SFR history and the metallicity. For example, the SFRs in Fig. 1.4 were created assuming a Salpeter IMF (Salpeter, 1955).

The second bump is caused by dust that absorbs light at many wavelengths, but it is a particularly powerful absorber of far-ultraviolet (FUV; $\sim 100\text{-}200\text{ nm}$) radiation, which is re-emitted again in the infrared (IR; $\sim 1\text{-}1000\text{ }\mu\text{m}$), thus ‘reprocessing’ the emitted starlight. The shape of the dust ‘bump’ can most of the time be approximated by a combination of a modified blackbody (a ‘greybody’), fixed at the temperature of the dust, and a power law in the mid-infrared (MIR) as described in detail by Casey (2012) and shown with an example in Fig. 1.12. On top of the dust peak a few important gas emission lines are shown, namely the CO (blue) and [CII] (red) lines, that will be described in detail in Part I.

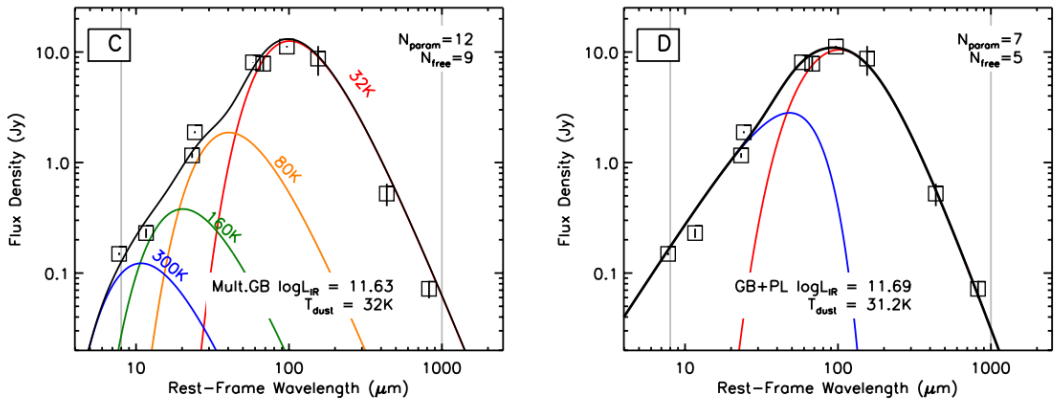


Figure 1.12 Examples of how the spectra in MIR to FIR, caused by dust in a galaxy, can be approximated by either several ‘greybodies’ of different dust temperature (left) or one greybody combined with a power law at high energies (right). Adapted from Casey (2012) who presented the latter, simplified FIR SED fitting technique.

In order to analyze the gas component of a galaxy, there are basically two relevant regimes in wavelength, both of which are indicated with grey areas in the figure:

X-ray regime: Thermal emission from galactic and extra-galactic hot, ionized gas.

Sub-mm regime: Gas emission lines from colder, more neutral gas.

This thesis implements observational and theoretical techniques in both of these regimes, as will be summarized in Section 2.2.

1.5 AN EXCITING TIME FOR OBSERVATIONS

Facilities for observing gas and dust in galaxies across cosmic time are experiencing a true revolution, that is gradually opening our eyes towards normal galaxies at high redshifts. Here, I will briefly go through the most important radio and X-ray telescopes in use or preparation.

1.5.1 RADIO TELESCOPES

Probably the most impressive effort in this regard has been the Atacama Large Millimeter Array (ALMA), even if still under construction. For an idea of its capabilities already in 2011 when the first scientific observations with ALMA began, see the image in Fig. 1.5 made with only 12

antennas. When completed, ALMA will comprise 50 antennas of 12 metres in diameter, acting as a single telescope and with a very high spatial resolution thanks to the art of interferometry. An additional 4 12-m and 12 7-m antennas will create a compact array in the centre. Together, the 66 antennas (each weighing > 100 tons!) can be moved with special designed vehicles into different configurations with maximum antenna distances from 150 m to an astonishing 16 km. A more extended configuration corresponds to a higher spatial resolution, but also a lower sensitivity towards larger (more extended) sources on the sky, a trade-off that must be considered when planning observations. With bands of high spectral resolution from $312\ \mu\text{m}$ to $3.56\ \mu\text{m}$ (and 2 extra bands going down to about $7.4\ \mu\text{m}$ possibly added in the future), ALMA will be able to detect [CII] and CO lines in a normal galaxy at $z = 3$ in a matter of hours. For the next cycle of observations (Cycle 3, starting in October 2015), ALMA is anticipated to encompass a total of 48 antennas with most receiver bands available.

In the Northern Hemisphere, The NOrthern Extended Millimeter Array (NOEMA⁵, former PdBI) will be, upon completion in 2019, the facility in the Northen Hemisphere that comes closest to the capabilities of ALMA, with bands for observing in the $808\ \mu\text{m}$ - $3.7\ \mu\text{m}$ range. At longer wavelengths, the Jansky Very Large Array (JVLA) is currently the superior radio interferometer, covering from 0.6 to 30 cm with 27 antennas of diameter 25 m (Napier, 2006). A number of single-dish radio telescopes can also target gas and dust emission at high redshifts; the LMT, IRAM-30m, GBT, Onsala 20+25m, ARO, NMA and APEX to name a few.

An overview of ALMA, EVLA and NOEMA is intended with Fig. 1.14, comparing the position of their frequency bands with the SED (including [CII] and CO lines) of a typical star-forming galaxy at $z = 2$.

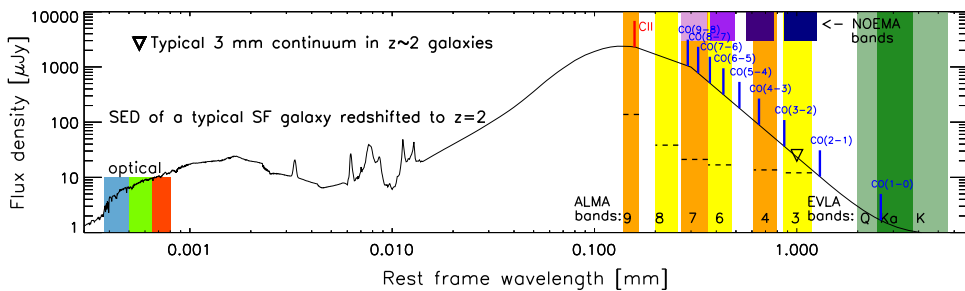


Figure 1.14 The star-forming galaxy SED also used in Fig. 1.11, with the frequency bands of some of the worlds best radio interferometers shown in color. The SED has been scaled to $30\ \mu\text{Jy}$ at $3\ \mu\text{m}$, corresponding to typical massive disk galaxies at $z \sim 2$ (Dannerbauer et al., 2009). The dashed lines in the ALMA bands correspond to 3σ after 5 hrs integration time with the full ALMA.



Figure 1.13 A photo of 19 ALMA antennas as they stood ready for the ALMA Early Science cycle. The array is located on the Chajnantor Plateau at 5000 m above sea level in Atacama desert of northern Chile. Credit: ALMA (ESO/NAOJ/NRAO)/W. Garnier (ALMA).

⁵<http://www.iram.fr/IRAMFR/GILDAS/doc/html/noema-intro-html/noema-intro.html>

The James Webb Space Telescope (JWST), scheduled to launch in 2018, will be an improved version of the famous Hubble Space Telescope (HST, expected to stay in operation until 2020), covering 0.6 to 28 μm with the same resolution in NIR as HST has in the optical.

Between the long wavelength range of EVLA/ALMA and the shorter of JWST, ground-based observations are hampered by atmospheric absorption, but new space missions are awaiting approval for adventuring into the MIR 28–312 μm regime. FIRSPEX is a satellite mission to continue the success of the Herschel Space Observatory (*Herschel*), that ran out of fuel in 2013. The primary goal of FIRSPEX is to carry out a wide survey of the MW in [CII], [NII], [CI] and CO(6 – 5)⁶, possibly detecting nearby galaxies as well that are redshifted into these bands. SPICA is a similar mission, of ~ 2 orders of magnitude higher sensitivity in the FIR than *Herschel* and wavelength coverage from 5 to $\sim 210 \mu\text{m}$ (Goicoechea & Nakagawa, 2011).

1.5.2 X-RAY TELESCOPES

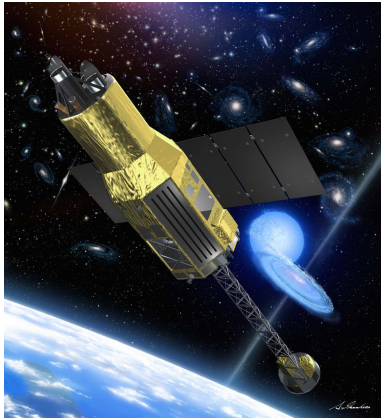


Figure 1.15 An illustration of the upcoming ASTRO-H when in orbit at an altitude of about 5–600 km. From the mission home page: <http://astro-h.isas.jaxa.jp/en/>.

signatures of AGN, with increased sensitivity for the soft X-rays as compared to *Chandra* (Reynolds et al., 2014). Astrosat is India’s first dedicated astronomy satellite and has the advantage of allowing simultaneous multi-wavelength observations at UV and X-ray wavelengths. It will have two bands for detecting X-rays (3–80 keV and 10–150 keV), and a large effective area in the hard X-ray band to facilitate studies of highly variable sources such as AGN (Paul, 2013).

To observe an AGN in X-ray, one has to escape the obscuring atmosphere of the Earth, which has led to many space missions since the beginnings of the 1980’s.

The *Chandra* X-ray (0.1–10 keV) observatory has been in orbit around the Earth since 1999, and has dedicated 2 and 4 Ms to observing the *Chandra* Deep Field North and South respectively (CDF-N and CDF-S). The large covering areas of roughly 450 arcmin² for each have proven ideal for detecting AGNs at redshifts $z \approx 0.1 – 5.2$ (Bauer et al., 2004; Xue et al., 2011). Similar missions, though of lower spatial resolution, include the XMM-Newton, ROSAT and Suzaku. At higher energies, the nuclear spectroscopic telescope array NuStar has been observing from space at 3 – 79 keV since 2012.

The ASTRO-H mission (see Fig. 1.15) is the latest in a long row of Japanese X-ray satellites, though ASTRO-H is being developed in a collaboration between Japanese (ISAS/JAXA) and US (NASA/GSFC) institutions. It will among other things investigate the X-ray reflection

⁶FIRSPEX webpage: <http://astroweb1.physics.ox.ac.uk/~dar/FIR/firspex4.html>

1.6 GALAXY SIMULATIONS

With so many coupled mechanisms in a galaxy on scales from sub-parsecs to kilo-parsecs, the advantage of running numerical simulations of galaxy evolution has proven tremendous. Galaxy simulations can be roughly divided into two kinds: Cosmological simulations that start out with the small density perturbations of dark matter shortly after the Big Bang, and more idealized disk simulations that start out with an analytical density profile for the galaxy and allow gravitational and electromagnetic forces to perturb the galaxy in time. I will focus on the former kind as that is what my theoretical projects build on (see Parts I and II).

The series of images in Fig. 1.16 illustrate how a cosmological simulation works, with snapshots, from high redshift ($z = 4$) and until now ($z = 0$), of the dark matter structures and the resulting gas mass distribution. In the present Λ CDM cosmological model, dark matter formed structures (or ‘minihalos’) before baryonic gas could cool and collapse. Cosmological simulations therefore focus on modeling an underlying dark matter structure (left-hand side of Fig. 1.16) at the same time as the baryonic component of the universe is allowed to condense in these structures via gravity, dissipation and radiation (right-hand side of Fig. 1.16). As the universe ages, filaments and knots in the dark matter density distribution become more pronounced and infalling gas cools enough to form stars and galaxies in regions of high concentration.

The universe is then believed to have proceeded via hierarchical structure formation, in which small gravitationally bound structures, such as stars and galaxies, form first, followed by groups, clusters and superclusters of galaxies, not to mention the cosmic web in between them (c.f. Fig 1.2).

It was soon realized though, that these large-scale simulations with resolutions going down to kpc-scales, could not capture the actual physics inside galaxies, where the most important processes take place on < 1 pc scales. In particular, simulations on smaller scales proved that localized feedback is needed in order to avoid overpredicting the star formation rate and to agree with the observed IMF of star clusters (Tasker, 2011; Krumholz et al., 2011; Hopkins et al., 2011). Made possible by an increasing computing power and technology, cosmological galaxy simulations have seen two big ‘revolutions’ since their beginning in the early 90’s as

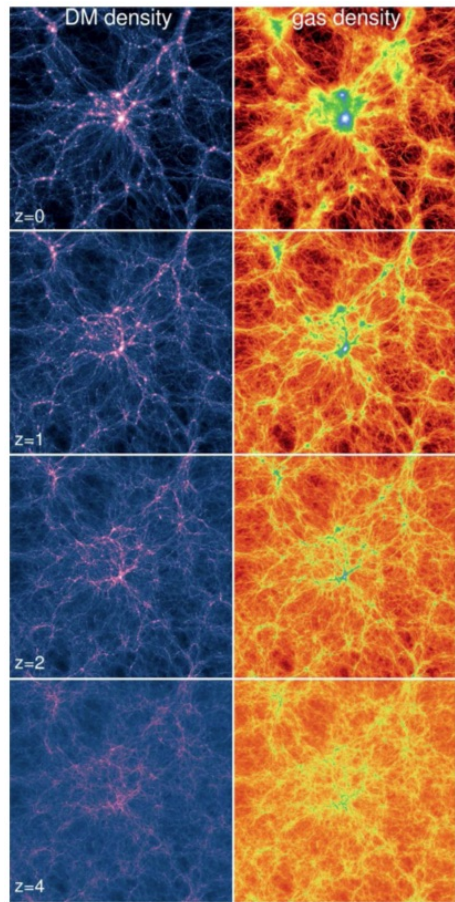


Figure 1.16 106.5 Mpc wide on each side, column density maps are shown of simulated dark matter (left) and gas column densities (right) from $z = 4$ until now (bottom to top). Brightest colors in the column density plot correspond to a density of $\sim 10^4 M_{\odot}/\text{kpc}^3$. The images are from the Illustris Project – one of the most comprehensive cosmological hydrodynamical simulations of galaxy formation to date (Vogelsberger et al., 2014). The recently developed moving-mesh code AREPO (Springel, 2010) was used to follow DM and gas dynamics.

illustrated in Fig. 1.17, of which we are in the middle of the last one, the ‘zoom-in’ simulations.

1.6.1 ‘ZOOM-IN’ SIMULATIONS

The concept behind ‘zoom-in’ simulations is to select a galaxy at low redshift in a cosmological simulation of low resolution ($\gtrsim 1$ kpc), and trace the particles (or cells) comprising it back in time to the beginning of the simulation. A re-simulation is then initiated with much higher resolution, but only following the particles/cells that end up in the galaxy of interest. This re-simulation may take days or months, but provides the opportunity to follow star formation on realistic scales, while staying in agreement with the overall large scale structure. Two computational techniques exist for treating the gas hydrodynamically at the necessary resolution:

Smoothed Particle Hydrodynamic (SPH) simulations: The gas is represented by particles with properties such as mass, density and temperature in addition to a smoothing kernel that roughly speaking smears the particles out across a volume in space. Resolution is increased simply by increasing the number of particles while reducing their mass in order to keep mass conservation.

Adaptive Mesh Refinement (AMR) simulations: The gas is divided into cells that can be subdivided in areas where higher resolution is needed. All interactions between gas cells take place as mass/temperature/pressure exchange through the cell partition walls.

Examples of SPH codes include `GADGET` and `GASOLINE`, whereas `ART`, `ENZO` and `RAMSES` are AMR codes. Kim et al. (2014) presented, with the AGORA project, a comparison of these in terms of resolution, physics of the ISM, feedback and galactic outflows. But see also Springel (2010) for a novel combination of the two methods.

1.6.2 THE CALIBRATION TO $z = 0$

While the initial conditions for galaxy formation and evolution are relatively strict, by e.g. measurements of the Cosmic Microwave Background (CMB), and the final endpoint is anchored with $z = 0$ observations, what goes on in between is less well-defined by observations. Common tests for the evaluation of a cosmological simulation focus on how well it can reproduce the observed main sequence and luminosity functions at low- to high- z . Although simulations on the whole agree with observations, a discrepancy still persists at the time of maximum cosmic star formation ($1 \lesssim z \lesssim 3$), where the simulated main sequence is a factor $\sim 2 - 3$ below the observed one (e.g. Furlong et al., 2014). Possible explanations include an IMF that changes with redshift and galaxy properties (rather than staying fixed to the locally observed one as most simulations assume), or feedback from stellar winds, supernovae and AGN that is not properly accounted for in simulations (e.g. Davé, 2008; Narayanan & Davé, 2012; Sparre et al., 2015). Until more resolved observations of ISM at $z \gtrsim 2$ are obtained, simulations of galaxy evolution are forced to make, and be inhibited by, extrapolations to high- z of local ISM physics and star-formation laws. Some of these restrictions will be discussed in Part I.

1.7 REFERENCES

- Ackermann, M., Ajello, M., Allafort, A., et al. 2013, Science, 339, 807
- Bauer, F. E., Alexander, D. M., Brandt, W. N., et al. 2004, AJ, 128, 2048
- Behroozi, P. S., Wechsler, R. H., & Conroy, C. 2013, ApJ, 770, 57

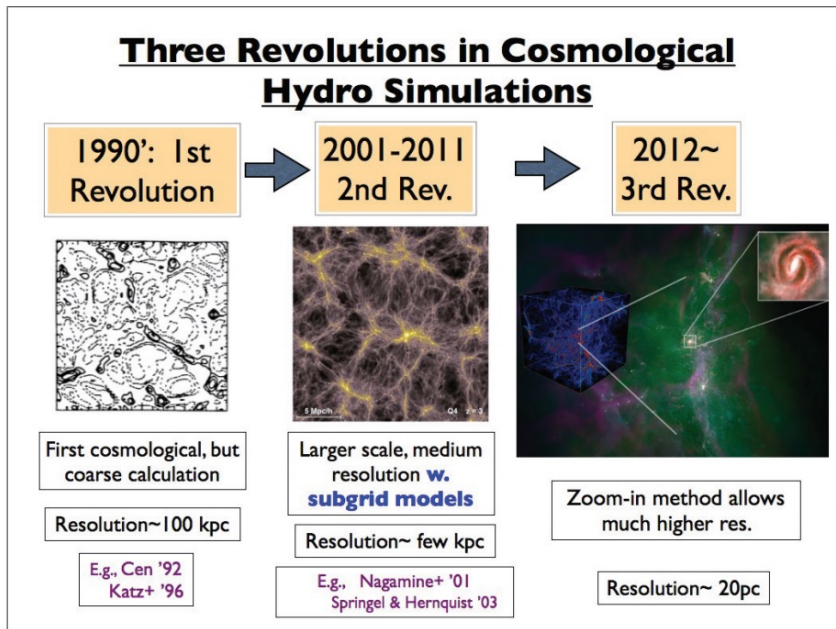


Figure 1.17 Schematic overview of the history of cosmological galaxy simulations and their improvements over the past two decades, with references, as presented in the review by Nagamine (2014).

- Bianchi, S., Maiolino, R., & Risaliti, G. 2012, Advances in Astronomy, 2012, 17
- Blitz, L., Fukui, Y., Kawamura, A., et al. 2007, Protostars and Planets V, 81
- Casey, C. M. 2012, MNRAS, 425, 3094
- Colless, M., Dalton, G., Maddox, S., et al. 2001, MNRAS, 328, 1039
- Dale, J. E., Ercolano, B., & Bonnell, I. A. 2012, MNRAS, 424, 377
- Dannerbauer, H., Daddi, E., Riechers, D. A., et al. 2009, ApJL, 698, L178
- Davé, R. 2008, MNRAS, 385, 147
- Draine, B. T. 2011, Physics of the Interstellar and Intergalactic Medium
- Furlong, M., Bower, R. G., Theuns, T., et al. 2014, ArXiv e-prints
- Genzel, R., Tacconi, L. J., Gracia-Carpio, J., et al. 2010, MNRAS, 407, 2091
- Gibson, R. R., Brandt, W. N., & Schneider, D. P. 2008, ApJ, 685, 773
- Glassgold, A. E., Galli, D., & Padovani, M. 2012, ApJ, 756, 157
- Goicoechea, J. R., & Nakagawa, T. 2011, in EAS Publications Series, Vol. 52, EAS Publications Series, ed. M. Röllig, R. Simon, V. Ossenkopf, & J. Stutzki, 253–258
- Groves, B. A., Schinnerer, E., Leroy, A., et al. 2015, ApJ, 799, 96
- Hartley, W. G., Almaini, O., Mortlock, A., et al. 2013, MNRAS, 431, 3045
- Hopkins, P. F., Quataert, E., & Murray, N. 2011, MNRAS, 417, 950
- Kim, J.-h., Abel, T., Agertz, O., et al. 2014, ApJS, 210, 14
- Kirkpatrick, A., Pope, A., Alexander, D. M., et al. 2012, ApJ, 759, 139
- Krawczynski, H., & Treister, E. 2013, Frontiers of Physics, 8, 609
- Krumholz, M. R., Klein, R. I., & McKee, C. F. 2011, ApJ, 740, 74
- Krumholz, M. R., Bate, M. R., Arce, H. G., et al. 2014, Protostars and Planets VI, 243
- Madau, P., & Dickinson, M. 2014, ARA&A, 52, 415
- Magorrian, J., Tremaine, S., Richstone, D., et al. 1998, AJ, 115, 2285

- Mulchaey, J. S., & Jeltema, T. E. 2010, ApJ, 715, L1
- Nagamine, K. 2014, in American Institute of Physics Conference Series, Vol. 1594, American Institute of Physics Conference Series, ed. S. Jeong, N. Imai, H. Miyatake, & T. Kajino, 41–45
- Napier, P. J. 2006, in Astronomical Society of the Pacific Conference Series, Vol. 356, Revealing the Molecular Universe: One Antenna is Never Enough, ed. D. C. Backer, J. M. Moran, & J. L. Turner, 65
- Narayanan, D., & Davé, R. 2012, MNRAS, 423, 3601
- Papadopoulos, P. P., & Thi, W.-F. 2013, in Advances in Solid State Physics, Vol. 34, Cosmic Rays in Star-Forming Environments, ed. D. F. Torres & O. Reimer, 41
- Papadopoulos, P. P., Thi, W.-F., Miniati, F., & Viti, S. 2011, MNRAS, 414, 1705
- Paul, B. 2013, International Journal of Modern Physics D, 22, 41009
- Planck Collaboration, Ade, P. A. R., Aghanim, N., et al. 2015, ArXiv e-prints
- Price, D. J., & Bate, M. R. 2009, MNRAS, 398, 33
- Przybilla, N., Nieva, M.-F., & Butler, K. 2008, ApJ, 688, L103
- Ranalli, P., Comastri, A., & Setti, G. 2003, A&A, 399, 39
- Reynolds, C., Ueda, Y., Awaki, H., et al. 2014, ArXiv e-prints
- Roman-Duval, J., Jackson, J. M., Heyer, M., Rathborne, J., & Simon, R. 2010, ApJ, 723, 492
- Salpeter, E. E. 1955, ApJ, 121, 161
- Sparre, M., Hayward, C. C., Springel, V., et al. 2015, MNRAS, 447, 3548
- Speagle, J. S., Steinhardt, C. L., Capak, P. L., & Silverman, J. D. 2014, ApJS, 214, 15
- Springel, V. 2010, MNRAS, 401, 791
- Stahler, S. W., & Palla, F. 2005, The Formation of Stars (Wiley)
- Steffen, A. T., Strateva, I., Brandt, W. N., et al. 2006, AJ, 131, 2826
- Tasker, E. J. 2011, ApJ, 730, 11
- Tielens, A. G. G. M. 2013, Reviews of Modern Physics, 85, 1021
- Vogelsberger, M., Genel, S., Springel, V., et al. 2014, MNRAS, 444, 1518
- Wiersma, R. P. C., Schaye, J., & Smith, B. D. 2009, MNRAS, 393, 99
- Wolfire, M. G., McKee, C. F., Hollenbach, D., & Tielens, A. G. G. M. 2003, ApJ, 587, 278
- Wuyts, S., Förster Schreiber, N. M., Genzel, R., et al. 2012, ApJ, 753, 114
- Xu, C. K., Cao, C., Lu, N., et al. 2015, ApJ, 799, 11
- Xue, Y. Q., Luo, B., Brandt, W. N., et al. 2011, ApJS, 195, 10

2

INTRODUCTION TO THIS THESIS

2.1 EVOLUTION OF MASSIVE GALAXIES ACROSS COSMIC TIME

With the previous brief description of the internal composition of galaxies and the observational and theoretical tools used for characterising them, we are now ready to take a look at the populations of massive galaxies so far uncovered and the current status on creating a consistent picture for their evolution with cosmic time.

2.1.1 HIGH-REDSHIFT MASSIVE GALAXY POPULATIONS

An important fact to bear in mind when studying galaxy evolution, is that we are never observing *the same* galaxy at various epochs in the life of the universe. At each redshift, the most we can do is observe galaxies in a snapshot of their lifetime, and often any evolutionary connection between galaxies observed at different redshifts is hampered by different selection techniques and incompleteness (we cannot detect all galaxies at every redshift, cf. Section 1.1.2).

The ideal way of classifying galaxies at all redshifts would be to measure their entire SED (like the one shown in Fig. 1.11) via spectroscopy. But since this would be very time-consuming, clever methods have been developed to first select a candidate group of the galaxies that might be of interest, and then perform high-resolution spectroscopy on these. Such methods typically build on photometry – measuring the total flux through a limited set of photometric bands by applying filters that only allow certain ranges in wavelength. For selecting galaxies of a certain mass, the K -band (centered on $2.2\,\mu\text{m}$ in the NIR) is particularly useful since it captures light from primarily old stellar populations that dominate the mass budget of most galaxies. Therefore, a lower cut in K -band luminosity directly translates into a minimum stellar mass Cimatti (2003). Follow-up spectroscopy can then determine the redshift, stellar mass and SFR to higher precision with SED fitting methods (see Man et al., 2012; Cimatti et al., 2004, for applications of this method). This method works out to $z \sim 4$ where the K -band starts to trace rest-frame UV light, which unlike NIR or optical, is dominated by the strong radiation from young stars, and is therefore a tracer of the amount of current star formation rather than stellar mass.

At $z \gtrsim 3$, another way to classify galaxies is typically via their current amount of star formation. This star formation can be either un-obscured, as revealed in rest-frame UV, or – in galaxies of high dust amount – obscured resulting in high FIR luminosities (dust continuum ‘bump’ in Fig. 1.11), or a combination of the two. Two examples of the first approach are the

Lyman Break Galaxies (LBGs) and BzK-selected galaxies, whereas the second approach has revealed a group of very dusty galaxies, the Sub-mm Galaxies (SMGs) or nowadays, Dusty Star-forming Galaxies (DSFGs; Casey et al., 2014).

LBGs are selected to have a strong break and reduced flux at the wavelength $< \lambda = 912 \text{ \AA}$. This break is caused by neutral hydrogen gas residing inside the galaxy and in the Inter Galactic Medium (IGM), absorbing light at wavelengths below 912 \AA , the threshold for ionizing hydrogen. The LBG technique requires that the galaxy be UV bright (relatively star-forming) and not dust-obscured (Steidel et al., 2003). The advantage of the LBG technique is that it makes a preselection of not only SFR but also redshift, by restricting the location of the break. Carilli et al. (2008) used a method called ‘stacking’ (see application of this in X-ray in Part II), to find that LBGs at $z \sim 3$ have SFRs of $31 \pm 7 M_{\odot} \text{ yr}^{-1}$, that is, not very high on the MS at that redshift (c.f. Fig. 1.3).

The BzK-selection takes advantage of absorption in stellar atmospheres creating a strong break at $\sim 4000 \text{ \AA}$ so that three photometric bands (B , z and K) can effectively be used to select galaxies at $1.4 \lesssim z \lesssim 2.5$ and roughly estimate their SFR (Daddi et al., 2004). Similar groups of color-selected galaxies are those of ‘BX’ and ‘BM’ galaxies, selected via their color in the three UV and optical filters U_n , G and R (Adelberger et al., 2004; Steidel et al., 2004). The color criteria for ‘BX’ galaxies restricts them to lie at $2.0 \leq z \leq 2.5$, while the ‘BM’ galaxies lie at $1.5 \leq z \leq 2.0$. Both techniques give rise to slightly higher SFRs than the BzK-selection would, as shown by Reddy et al. (2005) using X-ray inferred bolometric SFRs.

SMGs on the other hand, are selected for having a strong rest-frame NIR emission, and were first detected with the ground-based instrument SCUBA at $850 \mu\text{m}$ (e.g. Smail et al., 1997; Hughes et al., 1998; Barger et al., 1999), soon followed by surveys including the use of instruments such as MAMBO at 1.2 mm and AzTEC at 1.1 mm (Coppin et al., 2005; Chapman et al., 2005; Greve et al., 2008; Perera et al., 2008). The advantage of looking in the rest-frame $1 - 3 \text{ mm}$ wavelength range at high redshift, is that the flux stays roughly the same owing to the effect of ‘negative K -correction’ as illustrated in Fig. 2.1. Due to this effect, SMGs have been identified mainly at $z \sim 2$ but with a tail extending up to $z \sim 5$ (Chapman et al., 2005; Wardlow et al., 2011; Simpson et al., 2014). Converting the high IR luminosities to dust-obscured SFRs, implies SFRs of $\sim 100 - 1000 M_{\odot} \text{ yr}^{-1}$ (Karim et al., 2013). For the most part, SMGs display disturbed stellar morphologies and/or kinematics as compared to normal non-interacting rotating disks, suggesting recent or ongoing merger events (e.g. Conselice et al., 2003; Chen et al., 2015). The disturbed signatures are backed up by molecular emission line observations of clumps of dense and highly star-forming gas in SMGs (e.g. Tacconi et al., 2008; Riechers et al., 2011; Hodge et al., 2012).

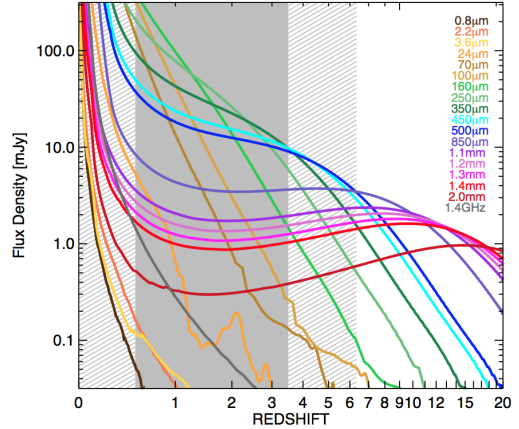


Figure 2.1 Observed flux densities for a typical dusty, star-forming galaxy as presented in the review by Casey et al. (2014). Note the nearly-constant flux density in the $\sim 1 \text{ mm}$ bands accross $1 \lesssim z \lesssim 10$ redshift range.

2.1.2 OBSERVING GALAXIES AT $z > 4$ VIA THEIR GAS EMISSION LINES

In the early ($z > 4$) universe, very few normal star-forming galaxies have so far been detected, typically via the LBG technique (see Behroozi et al., 2013, for a compilation), and even fewer quiescent galaxies have been discovered at $z \gtrsim 2.5$, with the most distant ones at $z \sim 3$ (Gobat et al., 2012; Fan et al., 2013). Only one galaxy at $z > 7$ has so far had its redshift determined from spectroscopy of its stellar continuum. But the galaxy A1689-zD1 at $z = 7.5 \pm 0.2$, has now been detected in dust emission with ALMA resulting in a combined (UV+IR) SFR of $\sim 12 M_{\odot} \text{ yr}^{-1}$ (Watson et al., 2015), i.e. a normal star-forming galaxy. In addition to dust continuum, ALMA can also detect line emission from the gas, thereby determining redshifts and characterizing the ISM at the same time for normal star-forming galaxies (see more on this in the Outlook section of Part I). An example of such an emission line, is [CII] from singly ionized carbon, which is expected to be the most luminous cooling line in neutral gas. We return with a more detailed description of [CII] in Chapter 6, but mention here that at $z \sim 5-7$, the [CII] line falls in bands 6-7 of ALMA, currently the most sensitive millimeter interferometer by an order of magnitude, and therefore a promising tool for detecting [CII] in normal star-forming galaxies at $z \sim 6$. Indeed, it has been detected in and around normal star-forming galaxies at $z \sim 5 - 7$ (Maiolino et al., 2015; Capak et al., 2015). *Our only way of characterizing the ISM of high- z galaxies might very well be to observe emission lines from the gas.*

2.1.3 THE RED AND BLUE GALAXIES

The local galaxy population is bimodal in terms of UV-to-optical color, with a distinct group of blue, star-forming galaxies and another of red, quiescent galaxies (Strateva et al., 2001; Schawinski et al., 2014). This is shown with color-mass diagrams in Fig. 2.2 for low redshift galaxies. The connection between color and star formation activity is a result of younger stars having relatively bluer colors than old stars, which emit their light predominantly at longer (optical and NIR) wavelengths. Historically, the red and blue galaxies are also called ‘early’ and ‘late’-type galaxies from the morphological classification of Hubble (1926). In general, late type galaxies display stellar disks with spiral arms and exponential light profiles whereas the stellar light from early-type galaxies (or sometimes named ellipticals) is more concentrated with even structures and no clear sign of spiral arms. But detailed observations of their stellar populations have later shown that this naming makes sense, since the nearby red galaxies most likely formed much earlier than the blue ones (e.g. Kartaltepe et al., 2014). As always, dust plays an important role and can make star-forming galaxies appear red by absorbing the blue light and re-emitting it in the FIR. Indeed Sodré et al. (2013) showed that some local galaxies with extremely red colors, are reddened by dust more than by older (redder) stellar populations. But the diagrams in Fig. 2.2 have been corrected for reddening by dust, by measuring the dust extinction in optical light.

In between the red and the blue group, lies the ‘green valley’ with very few galaxies. There is a discussion about how many of these green galaxies are actually late-type galaxies being quenched (Pan et al., 2013; Schawinski et al., 2007) and how many are early-type galaxies with star formation initiated recently in a sort of ‘rejuvenation’ (Fang et al., 2012). In Section 1.1 the main sequence (MS) of star formation was introduced, and Fig. 1.3 showed how the MS grows towards higher SFR with redshift. Blue galaxies lie on the MS relation, whereas red galaxies lie below and typically at high stellar mass. One of the biggest quest in astronomy for understanding galaxy evolution is; *Why did blue galaxies form more stars at higher redshift?*

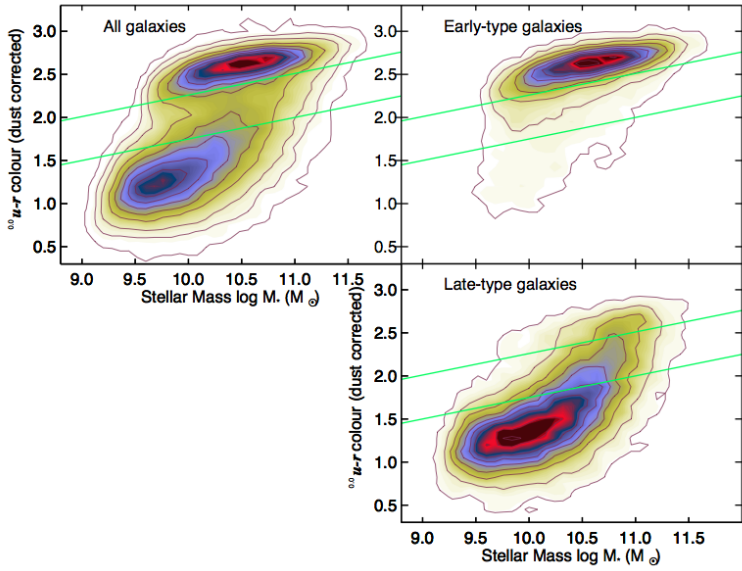


Figure 2.2 The UV-optical color bimodality of $0.02 < z < 0.05$ galaxies, as measured by Schawinski et al. (2014) using the SDSS+GALEX+Galaxy Zoo data. The ‘0.0’ in 0.0_u refers to the K -correction of the observed color to $z = 0$ (see Section 2.1.1). Green lines indicate the ‘green valley’ in between the two galaxy populations.

By now, the division into quiescent or star-forming has been observationally confirmed out to $z \sim 3$, (Kriek et al., 2008; Williams et al., 2009; Viero et al., 2013; Man et al., 2014), leading to a second, equally important, question: *When did the onset of the red sequence take place and what caused it?*

2.1.4 QUENCHING STAR FORMATION

AGNs are one of the preferred hypothesized mechanisms for quenching star formation, as radiation, winds and jets from the central accreting black hole can remove the gas or heat it so that contraction of molecular clouds cannot take place (see Fabian 2012 and McNamara & Nulsen 2007 for a reviews on models and observational evidence). A distinction is made between ‘quasar mode’, by which feedback from an AGN ejects all gas from the galaxies (Granato et al., 2004), and ‘radio mode’, during which powerful jets heat the circumgalactic medium to such high temperatures that further accretion of cold gas onto the galaxy is prevented (Croton et al., 2006). Semi-analytical simulations, by e.g. Di Matteo et al. (2005), show how reasonable descriptions of the AGN feedback on star formation in elliptical galaxies can reproduce the observed local mass function.

In addition to quenching by AGNs (possibly ignited by a major merger), the environment in which the galaxy lives is believed to raise further quenching mechanisms. This suspicion came from observations showing that galaxies in clusters are in general more quenched and passive than field galaxies (Verdugo et al., 2008). Similar to AGNs, most of these proposed internal/external mechanisms have to do with the removal, distribution or heating of gas, i.e. the fuel for further star formation. This can happen via galaxy-galaxy interactions or influence by the Intra Cluster Medium (ICM) itself. The following are some of the more popular environmental quenching mechanisms, but see reviews by e.g. Boselli & Gavazzi (2006) and Blanton &

Moustakas (2009) for a much more complete overview: i) Harassment, when during close encounters or direct mergers, galaxies alter each others' morphology (Moore et al., 1998); ii) Ram pressure stripping, where galaxies traveling through the ICM at high speed have their ISM shock-heated and eventually stripped off, ending up in the cluster as seen in observations of individual cases and proposed by several simulations (e.g. Steinhauser et al., 2012; Bösch et al., 2013; Ebeling et al., 2014); iii) Tidal stripping, by which galaxies passing through the ICM feel the global tidal field of their host, significantly altering their morphologies (Villalobos et al., 2014); iv) Cosmological 'starvation' or 'strangulation', when the hot gas halo around a galaxy is removed due to hydrodynamical interactions with the ICM, and further infall of gas is prevented causing the galaxy to slowly run out of fuel on time scales of a few Gyr (Balogh et al., 2000; Bekki et al., 2002; Feldmann & Mayer, 2015); v) Compactness quenching, as suggested by observations of satellites in the outskirts of haloes, that show a strong correlation between quenching and compactness of the galaxy (Woo et al., 2015).

These last types of quenching mechanisms are also referred to collectively as 'satellite quenching', because they primarily happen to satellite galaxies in a cluster. However, it has been hypothesized that satellite quenching and that of AGN (also called 'mass-quenching'), are actually manifestations of the same underlying process (Carollo et al., 2014; Knobel et al., 2015).

2.1.5 CONNECTING THE DOTS

The fact that the red sequence is already in place at $z \sim 2$, means that we have to push even further out in redshift in order to find the onset of this 'dead' population, and with that, hopefully also the 'murder weapon'. In addition, half of the most massive galaxies ($M_* > 10^{11} M_\odot$) at $z \approx 2$ are already compact and quiescent galaxies (CQGs) with old stellar populations (e.g. Toft et al., 2007; van Dokkum et al., 2008; Szomoru et al., 2012). The stellar spectra suggest that major starburst events took place in CQGs some 1-2 Gyr prior to the time of observation, but were quenched by mechanisms either internal or external (or both) to the galaxy (e.g. Gobat et al., 2012; Whitaker et al., 2013; van de Sande et al., 2013). So far, very few have CQGs have been found in the present-day universe (e.g. Trujillo et al., 2009; Taylor et al., 2010), though see also Graham et al. (2015) who suggest that CQGs could be hiding in the local universe as the bulges of spheroidal galaxies having grown an additional (2D) disk over the past 9-11 Gyr.

It is still an open question what kind of galaxy evolution leads to the CQGs observed at $z \sim 2$, and how they increased in size, without increasing their SFR significantly, down to $z \sim 0$, for which a size increase by a factor of $\sim 3 - 6$ is required (e.g. Trujillo et al., 2006; Toft et al., 2007; Szomoru et al., 2012). Basically, three formation scenarios have been put forth:

- i) Massive CQGs formed in a monolithic way, assembling most of their mass at $z > 2 - 3$ and then 'puffed up' (by adiabatic expansion) into the big, red ellipticals we see today (e.g. Bezanson et al., 2009; Damjanov et al., 2009).
- ii) A similar scenario to i), but CQGs enhanced their size from $z \sim 2$ to 0 by inside-out growth, most likely due to merging with other small galaxies (minor merging), following a type of hierarchical structure formation like the dark matter (Naab et al., 2009; Oser et al., 2012). The minor merging scenario is in good agreement with the observed metallicity gradients (Kim & Im, 2013) and stellar kinematics (e.g. van de Sande et al., 2013; Arnold et al., 2014) in $z = 0$ quiescent galaxies.
- iii) The third possibility, requires a bit more thought. Compared to star-forming galaxies, local quiescent galaxies are more massive at the same SFR but also slightly smaller at the same mass,

for redshifts out to $z \sim 2$. This can be seen in Fig. 2.3 which shows the main sequence of galaxies, including the quiescent ones below it, from $z \sim 0$ to $z \sim 2$. The average size of the quiescent population could grow with time simply if recently quenched (larger) star-forming galaxies are constantly being added to the sample as time moves forward (Trujillo et al., 2012; Poggianti et al., 2013; Krogager et al., 2014, e.g.). This hypothesis also goes under the name ‘progenitor bias’. However, Belli et al. (2015) argued that, for at least half of all CQGs at $z = 2$, the increase in size until $z = 1.5$ must have taken place via growth rather than additions of increasingly larger galaxies to the sample.

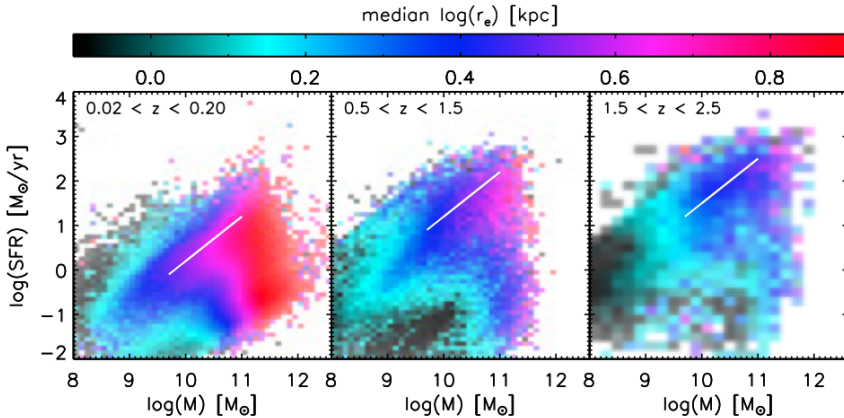


Figure 2.3 Galaxy SFR-mass diagrams in three redshift bins, colorcoded by size which is expressed as a circularized effective radius from fitting a Sérsic profile to the rest frame visible or NIR depending on redshift. From Wuyts et al. (2011), who study galaxies from various large samples, including CANDELS (see Section 1.1.2).

The potential quenching by AGNs has led to the idea of a fast evolutionary path from compact starbursting galaxy at $z \sim 3$ to a galaxy quenched by AGN feedback some 1–2 Gyr later and, via size-growth, to a larger, however still quiescent galaxy at $z = 0$. This is illustrated in Fig. 2.4 as an ‘early-track’ route (Barro et al., 2013). In addition, Barro et al. (2013) suggest a late-track evolutionary path, by which larger $z \sim 2$ star-forming galaxies slowly turn off star formation between $z = 2$ and $z = 0$, without passing through a compact phase. This idea was expanded upon by Williams et al. (2014), who suggest that massive, compact galaxies take the fast route and quench sooner than the normally-sized LBGs at $z \sim 2–3$.

Galaxy mergers present the kind of violent events that are required for the ‘early-track’ route. In particular, simulations have shown that gas-rich (wet) mergers can lead to bursts of star formation, but that gas is driven towards the center via dissipation and may ignite an AGN. Wet mergers can increase the stellar mass but leave a more compact remnant, whereas gas-poor (dry) mergers can build up a galaxy in mass and size without altering star formation too much (see Lin et al., 2008,

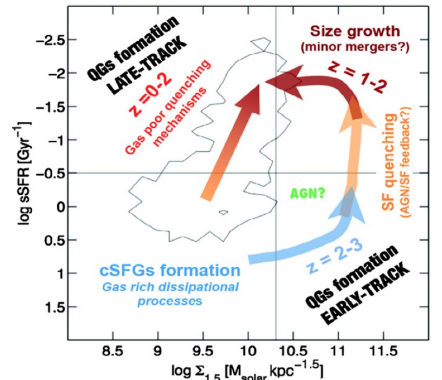


Figure 2.4 Two suggested evolutionary paths from star-forming galaxies at $z = 2–3$ to quiescent galaxies at $z = 0$ (Barro et al., 2013).

and references therein). In addition, major mergers are those between galaxies of similar mass whereas minor mergers are those in which the stellar masses differ by a factor of at least ~ 4 (Man et al., 2014).

In order to find the actual progenitors (and descendants for that matter) of the CQGs, we have to look outside the MS, consisting of normal galaxies. Fig. 2.5 illustrates an evolutionary sequence connecting $z \gtrsim 3$ SMGs through compact quiescent $z \sim 2$ galaxies to local elliptical ones (Hopkins et al., 2006; Ricciardelli et al., 2010; Toft et al., 2014; Marchesini et al., 2014). Here, gas-rich major mergers in the early universe trigger a short time period (42_{-29}^{+40} Myr) of high SFR in the form of a nuclear dust-enshrouded starbursts, that we observe as an SMG. That star formation is subsequently quenched either due to gas exhaustion, feedback from the starburst itself or the ignition of an AGN. What is left behind, is a compact stellar remnant that is observed as a CQG about a Gyr after, at $z \sim 2$. Finally, the CQGs grow gradually, and primarily through minor merging, into the elliptical galaxies that we observe today.

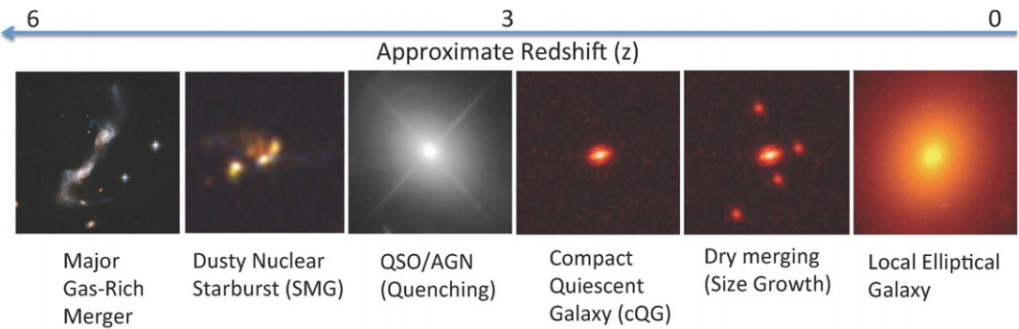


Figure 2.5 The proposed evolutionary sequence by Toft et al. (2014) going from major gas-rich mergers at high redshift (left) to local elliptical quiescent galaxies (right).

But observations of merger rates in massive galaxies at $z \sim 3 - 0$ show that major and minor merging is not enough to bring the CQGs to the sizes of locally observed early-type galaxies, suggesting that other mechanisms are needed for the size growth (Man et al., 2014). And, as summarized in Section 2.1.4, there are many alternative ways to quench star formation in addition to the powerful feedback of an AGN. In order to understand evolution of massive galaxies at high redshifts, it is fundamental to find out which of these mechanisms dominate and when.

2.2 THIS THESIS

The two fundamental questions about galaxy evolution, that were posed in the beginning of this chapter, in Section 2.1.3, could both be related to the observed main sequence of star formation (MS; see Section 1.1):

- 1) *Why does the MS evolve towards higher SFR with redshift?*
- 2) *What causes some galaxies to be outliers to the MS, or ‘quiescent’ galaxies?*

These issues are illustrated in Fig. 2.6, and compose the focus of this thesis. Stars form out of gas, and it would therefore seem natural that these questions translate into: *At what rate did galaxies acquire and use up their gas mass?* The larger part of my thesis focuses on the gas content of galaxies, on which the following subsection expands upon.

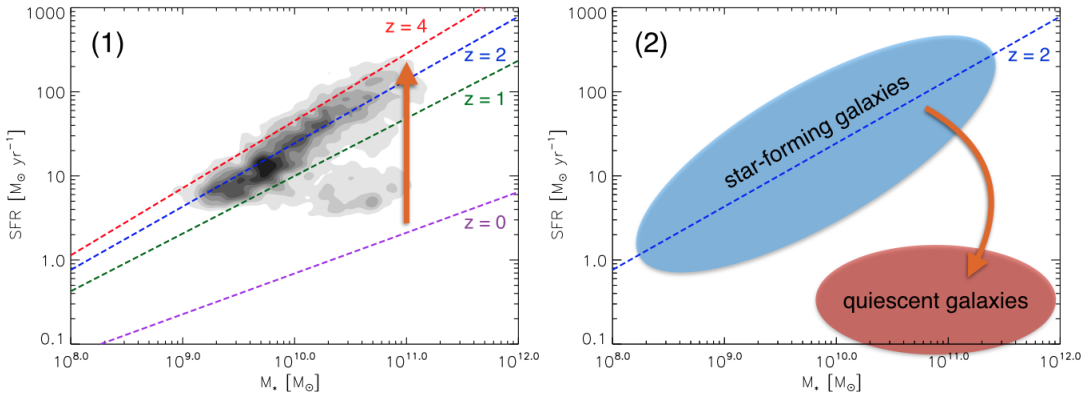


Figure 2.6 Plots showing the MS at various redshifts from Speagle et al. (2014), illustrating the two open questions that need to be answered in order to understand galaxy evolution across cosmic time: 1) Why the MS evolves towards higher SFR with redshift and, 2) Why some galaxies are hardly forming stars, creating a group of red, quiescent galaxies observed all the way out to redshift 3. Contours in the left-hand plot show the position of star-forming galaxies at $1.4 < z < 2.5$ from the NEWFIRM Medium-Band Survey (Whitaker et al., 2011).

2.2.1 ALL EYES ON THE GAS

Most of the above-mentioned mechanisms depend in one way or another on gas amount, as summarized below:

- The gas content together with the amount of in/outflow of gas sets the fuel available for star formation and thereby a 1st order estimate of how long the galaxy can continue producing stars at the current SFR.
- Removal or heating of this gas is what quenches star formation, and is an important milestone in the life of massive galaxies.
- Mergers and the resulting triggering of an AGN, are often invoked as a quenching mechanism, but the outcome of a merger depends critically on how gas-rich the merging galaxies are.

As mentioned in section 1.1, typical galaxies spend 95 % of their lifetime since $z = 1$ within a factor 4 of their average SFR at a given M_* (Noeske et al., 2007). In light of this, most of the evolution in the MS, where galaxies spend most of their lives, might be due to a rising gas mass fraction with redshift. The general consensus is that galaxies at higher redshift were definitely more gas-rich, but the very few observations at $z > 3$ make this statement hard to quantify, as Fig. 2.7 illustrates. This figure shows the gas mass fraction defined as $f_{\text{gas}} = M_{\text{gas}} / (M_{\text{gas}} + M_*)$ as a function of redshift and reveals the uncertainty in its evolution at $z \gtrsim 2$.

Another topic related to the gas and under current debate, is whether the KS law (introduced in Section 1.2.2) might be different in normal galaxies compared to starburst galaxies or mergers, as shown in Fig. 2.8 (though such conclusions depend critically on how the gas mass is determined, a topic we return to in Part I).

A huge missing piece to the puzzle is therefore knowledge of the gas (and dust) in massive galaxies, especially at $z \gtrsim 2$. The premonition, shared by several research groups, is that future observations of the gas and dust content, morphology and dynamics in high- z MS and quiescent galaxies, will solve the puzzle (Carilli & Walter, 2013; Blain, 2015). As put by Glazebrook (2013): ‘...we need to consider the fuel as well as the fire’. As mentioned in 1.5, it is now possible with radio telescopes such as ALMA, JVLA and NOEMA to access the high-redshift domain

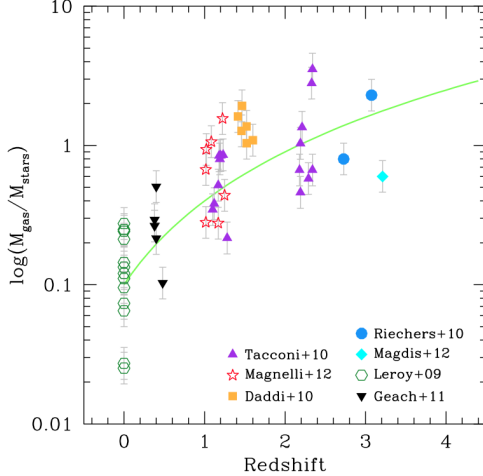


Figure 2.7 Evolution of the gas to stellar mass ratio, M_{gas}/M_{\star} , with redshift for star-forming disk galaxies with $M_{\star} > 10^{10} M_{\odot}$ (Carilli & Walter, 2013).

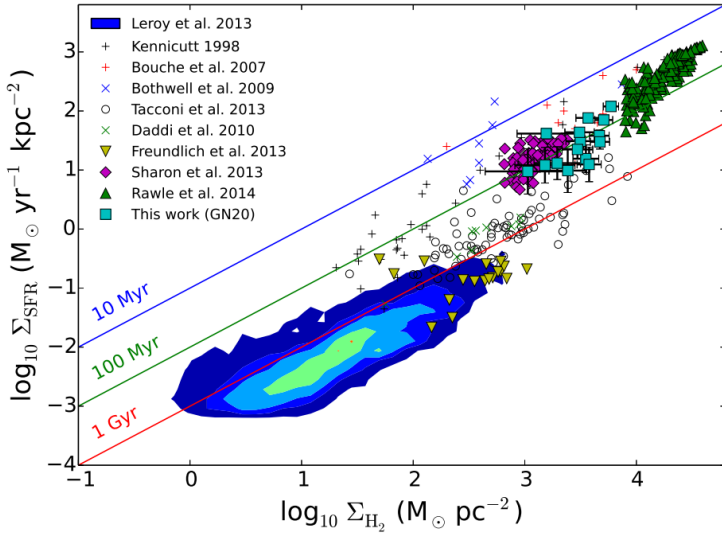


Figure 2.8 The KS law for different galaxy types at high and low redshift from the work of Hodge et al. (2015) who carried out resolved CO(2-1) observations of the $z = 4.05$ SMG GN20, shown with cyan squares. GN20 lies significantly above the relation for local MS galaxies (contours), together with two other strongly lensed, resolved SMGs (magenta diamonds and green triangles), unresolved SMGs (blue crosses and red plus-signs) and local ultraluminous infrared galaxies (ULIRGs; black plus-signs). Close to the local MS galaxies are $z \sim 1.2$ massive star-forming galaxies (yellow upside-down triangles), $z \sim 1 - 3$ color-selected galaxies (black open circles) and $z \sim 1.5$ BzK galaxies (green crosses). See references for these observations in Hodge et al. (2015).

where the red sequence must have formed.

To answer the above questions, we not only need to observe the gas at high redshift in more detail, we also need to know how to interpret those observations better.

2.2.2 QUICK SUMMARY OF MY PROJECTS

I have worked on improving our knowledge of the evolutionary state of massive galaxies at $z = 2$, with regard to 3 aspects:

- Amount and distribution of molecular gas in the ISM

A key species for studying the gas in the ISM was already introduced in Chapter 1 (Section 1.2.2) and will be described in detail in Part I: carbonmonoxide (CO). I used galaxy simulations and developed sub-grid procedures that could be combined with radiative transfer calculations in order to improve predictions for the use of CO lines to estimate the amount and distribution of molecular gas in the ISM of normal star-forming galaxies at $z \sim 2$ (SÍGAME, see Part I Chapter 3).

- Tracing SFR on local and global scales

The line emission of C⁺ has been used to trace SFR and various phases of the ISM, including neutral and ionized gas, but it holds many mysteries with its exact origin still unknown. Combining galaxy simulations with sub-grid procedures, I developed a method for modeling [CII] line emission in order to study its origin in the ISM, and make predictions for its use as a star formation tracer at $z \sim 2$ (SÍGAME, see Part I Chapter 5).

- Importance of AGNs in massive galaxies at $z \sim 2$

By analyzing *Chandra* X-ray data from a sample of galaxies at $1.5 \lesssim z \lesssim 2.5$, including the stacked signal from low-luminosity sources, I derive the fraction of luminous and low-luminosity AGNs in star-forming as well as in quiescent massive galaxies (see Part II).

At the beginning of the following chapters some additional background is provided on the specific techniques used in the above listed project, and each chapter will be followed by a list of references.

2.3 REFERENCES

- Adelberger, K. L., Steidel, C. C., Shapley, A. E., et al. 2004, ApJ, 607, 226
Arnold, J. A., Romanowsky, A. J., Brodie, J. P., et al. 2014, ApJ, 791, 80
Balogh, M. L., Navarro, J. F., & Morris, S. L. 2000, ApJ, 540, 113
Barger, A. J., Cowie, L. L., Smail, I., et al. 1999, AJ, 117, 2656
Barro, G., Faber, S. M., Pérez-González, P. G., et al. 2013, ApJ, 765, 104
Behroozi, P. S., Wechsler, R. H., & Conroy, C. 2013, ApJ, 770, 57
Bekki, K., Couch, W. J., & Shioya, Y. 2002, ApJ, 577, 651
Belli, S., Newman, A. B., & Ellis, R. S. 2015, ApJ, 799, 206
Bezanson, R., van Dokkum, P. G., Tal, T., et al. 2009, ApJ, 697, 1290
Blain, A. W. 2015, ArXiv e-prints
Blanton, M. R., & Moustakas, J. 2009, ARA&A, 47, 159
Bösch, B., Böhm, A., Wolf, C., et al. 2013, A&A, 549, A142
Boselli, A., & Gavazzi, G. 2006, PASP, 118, 517
Capak, P. L., Carilli, C., Jones, G., et al. 2015, ArXiv e-prints
Carilli, C. L., & Walter, F. 2013, ARA&A, 51, 105
Carilli, C. L., Lee, N., Capak, P., et al. 2008, ApJ, 689, 883
Carollo, C. M., Cibinel, A., Lilly, S. J., et al. 2014, ArXiv e-prints

- Casey, C. M., Narayanan, D., & Cooray, A. 2014, Phys. Rep., 541, 45
- Chapman, S. C., Blain, A. W., Smail, I., & Ivison, R. J. 2005, ApJ, 622, 772
- Chen, C.-C., Smail, I., Swinbank, A. M., et al. 2015, ApJ, 799, 194
- Cimatti, A. 2003, in The Mass of Galaxies at Low and High Redshift, ed. R. Bender & A. Renzini, 124
- Cimatti, A., Daddi, E., Renzini, A., et al. 2004, Nature, 430, 184
- Conselice, C. J., Chapman, S. C., & Windhorst, R. A. 2003, ApJ, 596, L5
- Coppin, K., Halpern, M., Scott, D., Borys, C., & Chapman, S. 2005, MNRAS, 357, 1022
- Croton, D. J., Springel, V., White, S. D. M., et al. 2006, MNRAS, 365, 11
- Daddi, E., Cimatti, A., Renzini, A., et al. 2004, ApJ, 617, 746
- Damjanov, I., McCarthy, P. J., Abraham, R. G., et al. 2009, ApJ, 695, 101
- Di Matteo, T., Springel, V., & Hernquist, L. 2005, Nature, 433, 604
- Ebeling, H., Stephenson, L. N., & Edge, A. C. 2014, ApJ, 781, L40
- Fabian, A. C. 2012, ARA&A, 50, 455
- Fan, L., Fang, G., Chen, Y., et al. 2013, ApJ, 771, L40
- Fang, J. J., Faber, S. M., Salim, S., Graves, G. J., & Rich, R. M. 2012, ApJ, 761, 23
- Feldmann, R., & Mayer, L. 2015, MNRAS, 446, 1939
- Glazebrook, K. 2013, in IAU Symposium, Vol. 295, IAU Symposium, ed. D. Thomas, A. Pasquali, & I. Ferreras, 368–375
- Gobat, R., Strazzullo, V., Daddi, E., et al. 2012, ApJ, 759, L44
- Graham, A. W., Dullo, B. T., & Savorgnan, G. A. D. 2015, ArXiv e-prints
- Granato, G. L., De Zotti, G., Silva, L., Bressan, A., & Danese, L. 2004, ApJ, 600, 580
- Greve, T. R., Pope, A., Scott, D., et al. 2008, MNRAS, 389, 1489
- Hodge, J. A., Carilli, C. L., Walter, F., et al. 2012, ApJ, 760, 11
- Hodge, J. A., Riechers, D., Decarli, R., et al. 2015, ApJ, 798, L18
- Hopkins, P. F., Hernquist, L., Cox, T. J., et al. 2006, ApJS, 163, 1
- Hubble, E. P. 1926, ApJ, 64, 321
- Hughes, D. H., Serjeant, S., Dunlop, J., et al. 1998, Nature, 394, 241
- Karim, A., Swinbank, A. M., Hodge, J. A., et al. 2013, MNRAS, 432, 2
- Kartaltepe, J. S., Mozena, M., Kocevski, D., et al. 2014, ArXiv e-prints
- Kim, D., & Im, M. 2013, ApJ, 766, 109
- Knobel, C., Lilly, S. J., Woo, J., & Kovač, K. 2015, ApJ, 800, 24
- Kriek, M., van der Wel, A., van Dokkum, P. G., Franx, M., & Illingworth, G. D. 2008, ApJ, 682, 896
- Krogager, J.-K., Zirm, A. W., Toft, S., Man, A., & Brammer, G. 2014, ApJ, 797, 17
- Lin, L., Patton, D. R., Koo, D. C., et al. 2008, ApJ, 681, 232
- Maiolino, R., Carniani, S., Fontana, A., et al. 2015, ArXiv e-prints
- Man, A. W. S., Toft, S., Zirm, A. W., Wuyts, S., & van der Wel, A. 2012, ApJ, 744, 85
- Man, A. W. S., Zirm, A. W., & Toft, S. 2014, ArXiv e-prints
- Marchesini, D., Muzzin, A., Stefanon, M., et al. 2014, ApJ, 794, 65
- McNamara, B. R., & Nulsen, P. E. J. 2007, ARA&A, 45, 117
- Moore, B., Lake, G., & Katz, N. 1998, ApJ, 495, 139
- Naab, T., Johansson, P. H., & Ostriker, J. P. 2009, ApJ, 699, L178
- Noeske, K. G., Weiner, B. J., Faber, S. M., et al. 2007, ApJ, 660, L43
- Oser, L., Naab, T., Ostriker, J. P., & Johansson, P. H. 2012, ApJ, 744, 63
- Pan, Z., Kong, X., & Fan, L. 2013, ApJ, 776, 14
- Perera, T. A., Chapin, E. L., Austermann, J. E., et al. 2008, MNRAS, 391, 1227

- Poggianti, B. M., Moretti, A., Calvi, R., et al. 2013, *ApJ*, 777, 125
 Reddy, N. A., Erb, D. K., Steidel, C. C., et al. 2005, *ApJ*, 633, 748
 Ricciardelli, E., Trujillo, I., Buitrago, F., & Conselice, C. J. 2010, *MNRAS*, 406, 230
 Riechers, D. A., Carilli, L. C., Walter, F., et al. 2011, *ApJ*, 733, L11
 Schawinski, K., Thomas, D., Sarzi, M., et al. 2007, *MNRAS*, 382, 1415
 Schawinski, K., Urry, C. M., Simmons, B. D., et al. 2014, *MNRAS*, 440, 889
 Simpson, J. M., Swinbank, A. M., Smail, I., et al. 2014, *ApJ*, 788, 125
 Smail, I., Ivison, R. J., & Blain, A. W. 1997, *ApJ*, 490, L5
 Sodré, L., Ribeiro da Silva, A., & Santos, W. A. 2013, *MNRAS*, 434, 2503
 Speagle, J. S., Steinhardt, C. L., Capak, P. L., & Silverman, J. D. 2014, *ApJS*, 214, 15
 Steidel, C. C., Adelberger, K. L., Shapley, A. E., et al. 2003, *ApJ*, 592, 728
 Steidel, C. C., Shapley, A. E., Pettini, M., et al. 2004, *ApJ*, 604, 534
 Steinhauser, D., Haider, M., Kapferer, W., & Schindler, S. 2012, *A&A*, 544, A54
 Strateva, I., Ivezić, Ž., Knapp, G. R., et al. 2001, *AJ*, 122, 1861
 Szomoru, D., Franx, M., & van Dokkum, P. G. 2012, *ApJ*, 749, 121
 Tacconi, L. J., Genzel, R., Smail, I., et al. 2008, *ApJ*, 680, 246
 Taylor, E. N., Franx, M., Glazebrook, K., et al. 2010, *ApJ*, 720, 723
 Toft, S., van Dokkum, P., Franx, M., et al. 2007, *ApJ*, 671, 285
 Toft, S., Smolčić, V., Magnelli, B., et al. 2014, *ApJ*, 782, 68
 Trujillo, I., Carrasco, E. R., & Ferré-Mateu, A. 2012, *ApJ*, 751, 45
 Trujillo, I., Cenarro, A. J., de Lorenzo-Cáceres, A., et al. 2009, *ApJ*, 692, L118
 Trujillo, I., Förster Schreiber, N. M., Rudnick, G., et al. 2006, *ApJ*, 650, 18
 van de Sande, J., Kriek, M., Franx, M., et al. 2013, *ApJ*, 771, 85
 van Dokkum, P. G., Franx, M., Kriek, M., et al. 2008, *ApJ*, 677, L5
 Verdugo, M., Ziegler, B. L., & Gerken, B. 2008, *A&A*, 486, 9
 Viero, M. P., Moncelsi, L., Quadri, R. F., et al. 2013, *ApJ*, 779, 32
 Villalobos, Á., De Lucia, G., & Murante, G. 2014, *MNRAS*, 444, 313
 Wardlow, J. L., Smail, I., Coppin, K. E. K., et al. 2011, *MNRAS*, 415, 1479
 Watson, D., Christensen, L., Knudsen, K. K., et al. 2015, *Nature*, 519, 327
 Whitaker, K. E., Labb  , I., van Dokkum, P. G., et al. 2011, *ApJ*, 735, 86
 Whitaker, K. E., van Dokkum, P. G., Brammer, G., et al. 2013, *ApJ*, 770, L39
 Williams, C. C., Giavalisco, M., Cassata, P., et al. 2014, *ApJ*, 780, 1
 Williams, R. J., Quadri, R. F., Franx, M., van Dokkum, P., & Labb  , I. 2009, *ApJ*, 691, 1879
 Woo, J., Dekel, A., Faber, S. M., & Koo, D. C. 2015, *MNRAS*, 448, 237
 Wuyts, S., Förster Schreiber, N. M., van der Wel, A., et al. 2011, *ApJ*, 742, 96

Part I

Modeling the ISM of $z \sim 2$ galaxies with SÍGAME

3

CO EMISSION LINES FROM GALAXIES

3.1 PROBING THE MOLECULAR GAS

Due to the high abundance of hydrogen, the most common molecule to find in the ISM, is by far H₂. But in terms of observing cold molecular gas, H₂ is practically invisible, because the lack of an electric dipole moment means that the lowest possible rotational transitions of H₂ are electric quadrupole moments with very high energy. The first rotational transition, S(0), is at 510 K, meaning that even the lowest rotational transitions can only be excited in shock waves, FUV-rich PDRs or regions affected by turbulent dissipation (Ingalls et al., 2011).

The second most abundant molecule is carbonmonoxide, CO, consisting of one carbon and one oxygen atom. The abundance relative to H₂, [CO/H₂], is roughly 10⁻⁴ in MW ISM as has been determined via observations of early cold cores in the MW (Glover & Mac Low, 2011; Liu et al., 2013) and simulations of molecular clouds with $n_{\text{H}} \gtrsim 1000 \text{ cm}^{-3}$ (Glover & Mac Low, 2011).

CO is the most used molecule for observing molecular gas, since its rotational transitions conveniently sample the typical densities and temperatures inside GMCs. To probe the very densest parts of GMCs, other molecular tracers exist with higher critical densities (again see Tielens 2013 for an overview of most detected molecules, and Aalto 2013 for a subset of the denser gas tracers), but the low CO lines have proven excellent for capturing the majority of the molecular gas.

Fig. 3.1 provides an illustration of the rotating CO molecule, together with the frequencies and critical densities of the first 5 transitions. Also, the positions of the first 5 transitions on a typical SED can be seen in Fig. 1.11. In GMCs, the excitation of CO molecules to higher rotational levels is believed to come mainly from collisions with H₂ molecules. The population of the various rotational levels are therefore deter-

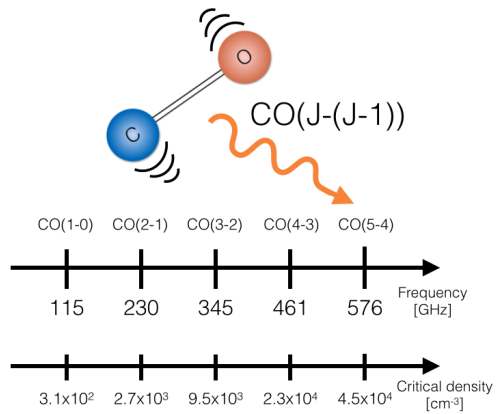


Figure 3.1 Illustration of the rotating CO molecules together with the frequencies of the first 5 rotational lines of the CO molecular are shown. Below are the corresponding critical densities ($n_{\text{crit}} = A_{ul} \Sigma_{i \neq u} C_{ui}$) as calculated by Greve et al. (2014) for a kinetic temperature of $T_k = 40 \text{ K}$ and assuming H₂ to be the main collision partner.

mined by density and temperature (how fast the molecules are moving) of the gas. The amount of flux in each rotational transition creates a CO Spectral Line Energy Distribution (SLED) or ‘CO ladder’ which can take on different shapes depending on the gas properties.

3.2 OBSERVATIONS OF CO LINE EMISSION FROM DIFFERENT TYPES OF GALAXIES AT $z \gtrsim 2$

At $z \sim 2$, the vast majority of CO observations have been of extreme galaxies, such as submillimeter galaxies (SMGs) with very high SFRs or quasi-stellar objects (QSOs) containing powerful AGNs. Only a few galaxies on the “main sequence of star formation” (MS, e.g. Wuyts et al., 2011), have been observed in CO. These are typically massive ($10^{10} - 10^{11} M_{\odot}$) galaxies selected by the BzK technique to be moderately star-forming with $\text{SFR} \simeq 10 - 500 M_{\odot} \text{ yr}^{-1}$, i.e. specific SFR (SSFR) of around 0.5 Gyr^{-1} . The molecular gas of SMGs and QSOs is highly excited with peak fluxes at the CO(5-4) and CO(6-5) transitions, which is evidence of dense and possibly warm gas (Papadopoulos et al., 2012), but little is known for the normal star-forming galaxies observed in CO to date. The only such galaxies, with 4 observed CO transitions, are the BzK-selected galaxies BzK-4171, BzK-16000 and BzK-21000 (Daddi et al., 2014). These galaxies were previously believed to contain mainly gas reminiscent to that of the Milky Way (MW) (Dannerbauer et al., 2009; Aravena et al., 2014), but new CO(5-4) observations by Daddi et al. (2014) require a second component of higher density and possibly higher temperature.

With instruments of high spatial resolution, it has recently become possible to resolve galaxies at $z \gtrsim 2$ on kiloparsec scales, as shown with the VLA by e.g. Walter et al. (2007) when observing low- J CO transitions. Scales of 1 kpc require a resolution of $\sim 0.1''$ at $z = 2$, achievable with ALMA for higher CO lines that are not redshifted below its bands.

When measuring the CO ladder of galaxies with different compositions, SFR and AGN activity, a huge variety emerges. Fig. 3.2 compares the rather low-excitation ladder of the MW to the CO ladders of SMGs and QSOs which peak at increasingly higher J -values. An upper limit as to how steep the ladder can be, is reached if the gas is in Local Thermal Equilibrium (LTE), in which case the level populations just follow a Boltzmann distribution set by the gas kinetic temperature and no radiative transitions are considered. For gas in LTE and of kinetic temperature above that of the upper level transition level, the CO ladder would grow as J^2 as indicated in Fig. 3.2 in blue. But in general, this upper limit is not reached by the local kinetic temperature and the high J -levels are less populated.

3.2.1 THE X_{CO} FACTOR

Probably the widest use of CO emission lines, is the estimation of total molecular gas mass. The low critical density ($\sim 300 \text{ cm}^{-3}$) of the first CO(1-0) transition makes it a tracer of most gas in a GMC. In order to convert from CO(1-0) line intensity and column density of H₂, the CO-H₂ conversion factor (X_{CO} or ‘X-factor’) gives the H₂ column density per CO(1-0) intensity unit:

$$X_{\text{CO}} [\text{cm}^{-2}/(\text{K km s}^{-1})^{-1}] = N(\text{H}_2)/W_{(\text{CO}(1-0))} \quad (3.1)$$

A similar conversion factor exists between total H₂ gas mass amount and CO line luminosity:

$$\alpha_{\text{CO}} [M_{\odot}/(\text{K km pc}^{-2})^{-1}] = M(\text{H}_2)/L_{\text{CO}(1-0)} \quad (3.2)$$

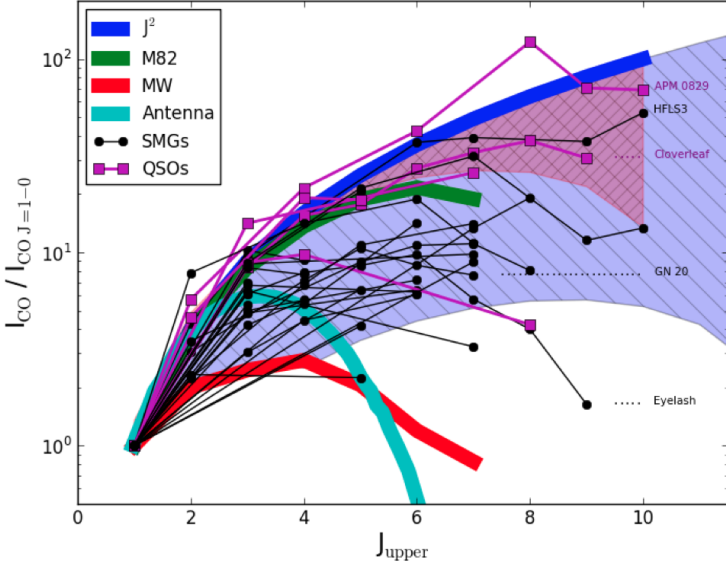


Figure 3.2 Observed CO ladders for different galaxies, normalized to the CO(1-0) transition. From the review of Casey et al. (2014).

The most common way of inferring their values, is to estimate the gas mass from either (i) the CO line width assuming the GMCs are in virial equilibrium (cf. eq. 1.2), (ii) the dust mass assuming a dust-to-gas mass ratio, or (iii) γ -ray emission from cosmic ray interactions with H₂ (see references in Narayanan et al., 2012). In the inner disk of the MW, they are relatively constant at $X_{\text{CO}} \approx 2 \times 10^{20} \text{ cm}^{-2}/(\text{K km s}^{-1})^{-1}$ and $\alpha_{\text{CO}} \approx 4.3 \text{ M}_\odot/(\text{K km pc}^{-2})^{-1}$ (from the comprehensive review on the X -factor by Bolatto et al., 2013).

But recent observations, at low and high redshift, show that X_{CO} must be lower in galaxies of high-surface density environments, and larger in low-metallicity environments. This has led to the belief that maybe there exists two versions of the KS star formation relation, one for gas-rich mergers and another for star-forming normal disk galaxies (Genzel et al., 2010). Based on detailed modeling, Narayanan et al. (2012) came up with a function for X_{CO} that depends on CO line luminosity and metallicity. With this prescription for X_{CO} a single continuous KS star formation relation can be drawn for starbursts and normal disk galaxies at low and high redshift as shown in Fig. 3.3. However, see the work of Hodge et al. (2015), implying that SMGs really can have more efficient star formation on small scales, regardless of the choice of conversion factor.

3.3 MODELING OF CO EMISSION LINES

The CO ladder of a galaxy can be modeled by combining galaxy simulations (either zoom-in versions of cosmological simulations or isolated galaxy models, cf. Section 1.6) with sub-grid prescriptions for the GMC structure and radiative transfer codes or LVG models for the transport of CO line emission through the ISM. Over the past decade in particular, detailed modeling of CO emission has been developed, the basic s.pdf of which can be summarised as follows: (1) Simulate a galaxy with dark matter, stars and atomic gas (if possible, with a multiphase molec-

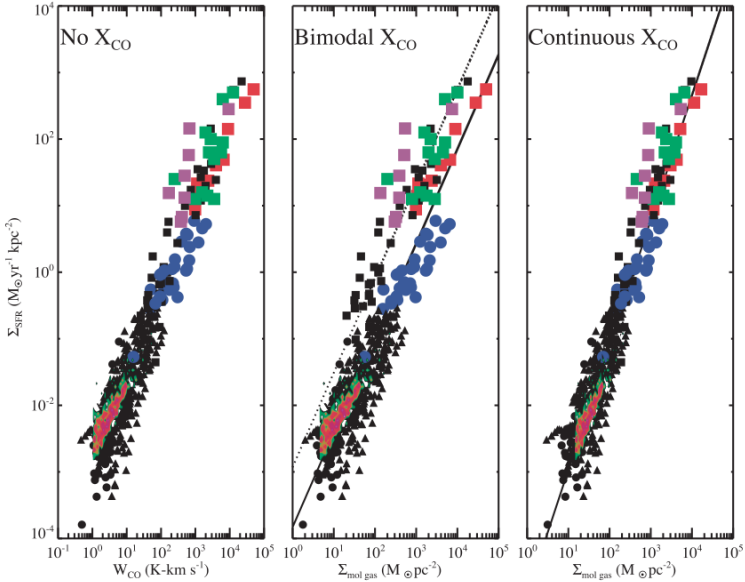


Figure 3.3 The effect of using an effectively bimodal X_{CO} factor (mid panel; $\alpha_{\text{CO}} = 4.5$ for local disks, 3.6 for high- z disks and $0.8 M_{\odot}/(\text{K km pc}^{-2})^{-1}$ for mergers) or a continuous one (right panel) on the KS law (Narayanan et al., 2012).

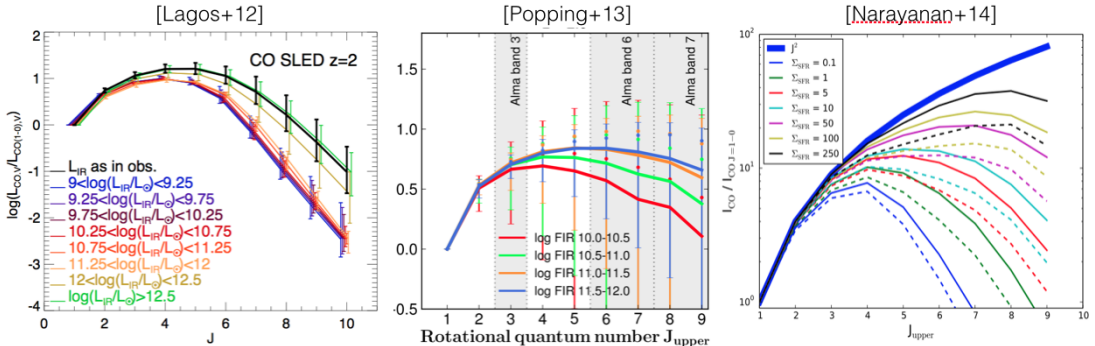


Figure 3.4 Examples of simulated CO ladders for different galaxy types. *Left:* The shape of CO ladders for $z = 2$ galaxies, binned according to infrared ($8 - 1000 \mu\text{m}$) luminosity, L_{IR} , as predicted by Lagos et al. (2012). *Middle:* The same as in the left panel according to the method of Popping et al. (2014). *Right:* CO ladders parameterized by Σ_{SFR} for simulations of resolved (solid) and unresolved (dashed) cases, as derived by Narayanan & Krumholz (2014).

ular gas), (2) Apply semi-analytical physical recipes to estimate the amount and state of dust and molecular gas, (3) Calculate the radiative transfer of selected CO lines. A full description of such a process can be found in Narayanan et al. (2008b), who investigated the signatures in CO morphology and line profile of outflows created by active galactic nuclei (AGNs) and starbursts. The same method has been used to study other aspects of the ISM, such as the Kennicutt-Schmidt relation and the X_{CO} factor which relates velocity-integrated CO line intensity to H₂ column density, in low- and high-redshift galaxies (e.g., Narayanan et al., 2011; Narayanan & Hopkins, 2013). By running smoothed particle hydrodynamical (SPH) simulations with the GADGET-3 code, Narayanan et al. (2011) were able to follow the evolution with

time of a multiphase ISM in isolated disk galaxies undergoing a merger, allowing the gas to cool down to temperatures of ~ 10 K. Lagos et al. (2012) simulated the CO emission of quiescently star-forming as well as starburst galaxies at redshifts ranging from $z = 0$ to $z = 6$ by coupling cosmological galaxy formation simulations with the tabulated output of a code describing photon dominated regions (PDRs). Lagos et al. (2012) found that the global velocity-integrated CO line intensity peaks at higher rotational transitions with increasing infrared (IR) luminosity (J -level 4 to 5 when median L_{IR} of the sample goes from about $1.3 \sim 10^9$ to $8 \times 10^{12} L_{\odot}$). In a similar study, Popping et al. (2014) found that models of normal star-forming galaxies at high redshift have much higher rotational transitions than their local counterparts. Finally, the modeling of CO lines from a large set of simulated disk galaxies, recently carried out by Narayanan & Krumholz (2014) showed that the CO line energy distribution can be parameterised better with respect to SFR surface density compared to total SFR. Simulated CO SLEDs in Fig. 3.4 provide examples of these previous works. However simulations of resolved CO line emission have been lacking.

4

SIMULATING CO LINE EMISSION FROM MASSIVE STAR-FORMING GALAXIES AT $z = 2$ (PAPER I)

4.1 AIM OF THIS PROJECT

We¹ wanted to expand on previous modeling done by other groups of CO emission lines from galaxies at high redshift by developing a method that focuses on radial gradients of the X_{CO} factor and CO line ratios. This would provide a preview for what instruments might one day observe in ‘normal’ star-forming galaxies at $z = 2$.

With this project, we present a new numerical framework for simulating the line emission of normal star-forming galaxies. The code – SImulator of GALaxy Millimeter/submillimeter Emission (SÍGAME²) – combines (non-)cosmological (SPH or grid-based) simulations of galaxy formation with subgrid prescriptions for the H₂/HI fraction and thermal balance throughout the ISM, down to parsec scales. SÍGAME accounts for a FUV and cosmic ray intensity field that vary with local SFR density within the galaxy. SÍGAME can be applied to any galaxy simulated in the SPH formalism, though currently restricted to galaxies dominated by star formation processes rather than AGN and with mean metallicities above about $0.01Z_{\odot}$. Here, we adapt the code to cosmological SPH simulations of three massive, normal star-forming galaxies at $z = 2$ (i.e., so-called main-sequence galaxies), and model their CO rotational line spectrum using a publically available 3D radiative transfer code. We show that SÍGAME reproduces observed low- J CO line luminosities and provides new estimates of the X_{CO} factor for main-sequence galaxies at $z \sim 2$, while at the same time predicting their CO line luminosities at high- J ($J_{\text{up}} > 6$) transitions where observations are yet to be made.

The structure of this chapter is as follows. Section 4.2 describes the cosmological SPH simulations used, along with the basic properties of the three star-forming galaxies extracted from the simulations. A detailed description of SÍGAME is presented in Section 4.3. The CO emission maps and spectra obtained after applying SÍGAME to the three simulated galaxies are presented in Section 4.4, where we also compare to actual CO observations of similar galaxies at $z \sim 2$.

¹Collaborators: Thomas R. Greve, Christian Brinch, Jesper Sommer-Larsen, Jesper Rasmussen, Sune Toft and Andrew Zirm

²SÍGAME in Spanish translates as ‘follow me’ - which in this context refers to the pursue of line emission through a galaxy.

Section 4.6 discusses the strengths and weaknesses of SÍGAME in the context of other molecular line (CO) simulations and recent observations. Finally, in Section 4.7 I summarise the main s.pdf of SÍGAME, and list its main findings and predictions regarding the CO line emission from massive, star-forming galaxies at $z \simeq 2$. We adopt a flat cold dark matter (Λ CDM) scenario with $\Omega_m = 0.3$, $\Omega_\Lambda = 0.7$ and $h = 0.65$.

4.2 COSMOLOGICAL SIMULATIONS

4.2.1 SPH SIMULATIONS

We employ a cosmological TreeSPH code for simulating galaxy formation and evolution, though in principle, grid-based hydrodynamic simulations could be incorporated equally well. The TreeSPH code used for the simulations is in most respects similar to the one described in Sommer-Larsen et al. (2005) and Romeo et al. (2006). A cosmic baryon fraction of $f_b = 0.15$ is assumed, and simulations are initiated at a redshift of $z = 39$. The implementation of star formation and stellar feedback, however, has been manifestly changed.

Star formation is assumed to take place in cold gas ($T_k \lesssim 10^4$ K) at densities $n_H > 1 \text{ cm}^{-3}$. The star formation efficiency (or probability that a gas particle will form stars) is formally set to 0.1, but is, due to effects of self-regulation, considerably lower. Star formation takes place in a stochastic way, and in a star formation event, 1 SPH gas particle is converted completely into 1 stellar SPH particle, representing the instantaneous birth of a population of stars according to a Chabrier (2003) stellar initial mass function (IMF; Chabrier (2003)) – see further below.

The implementation of stellar feedback is based on a subgrid super-wind model, somewhat similar to the ‘high-feedback’ models by Stinson et al. (2006). These models, though, build on a supernova blast-wave approach rather than super-wind models. Both types of models invoke a Chabrier (2003) IMF, which is somewhat more top-heavy in terms of energy and heavy-element feedback than, e.g., the standard Salpeter IMF. The present models result in galaxies characterized by reasonable $z = 0$ cold gas fractions, abundances and circum-galactic medium abundance properties. They also improve considerably on the “angular momentum problem” relative to the models presented in, e.g., Sommer-Larsen et al. (2003). The models will be described in detail in a forthcoming paper (Sommer-Larsen et al. 2015, in prep.).

4.2.2 THE MODEL GALAXIES

Three model galaxies, hereafter referred to as G1, G2 and G3 in order of increasing SFR, were extracted from the above SPH simulation and re-simulated using the ‘zoom-in’ technique described in (e.g., Sommer-Larsen et al., 2003). The emphasis in this study is on massive ($M_* \gtrsim 5 \times 10^{10} M_\odot$) galaxies, and the three galaxies analyzed are therefore larger, rescaled versions of galaxies formed in the $10/h$ Mpc cosmological simulation described in Sommer-Larsen et al. (2003). The linear scale-factor is of the order 1.5, and since the CDM power spectrum is fairly constant over this limited mass range the rescaling is a reasonable approximation.

Galaxy G1 was simulated at fairly high resolution, using a total of 1.2×10^6 SPH and dark matter particles, while about 9×10^5 and 1.1×10^6 particles were used in the simulations of G2 and G3, respectively. For the G1 simulation, the masses of individual SPH gas, stellar and dark matter particles are $m_{\text{SPH}} = m_* \approx 6.3 \times 10^5 h^{-1} M_\odot$ and $m_{\text{DM}} = 3.5 \times 10^6 h^{-1} M_\odot$, respectively. Gravitational (cubic spline) softening lengths of 310, 310 and $560 h^{-1} \text{ pc}$, respectively, were employed. Minimum gas smoothing lengths were about $50 h^{-1} \text{ pc}$. For the lower resolution

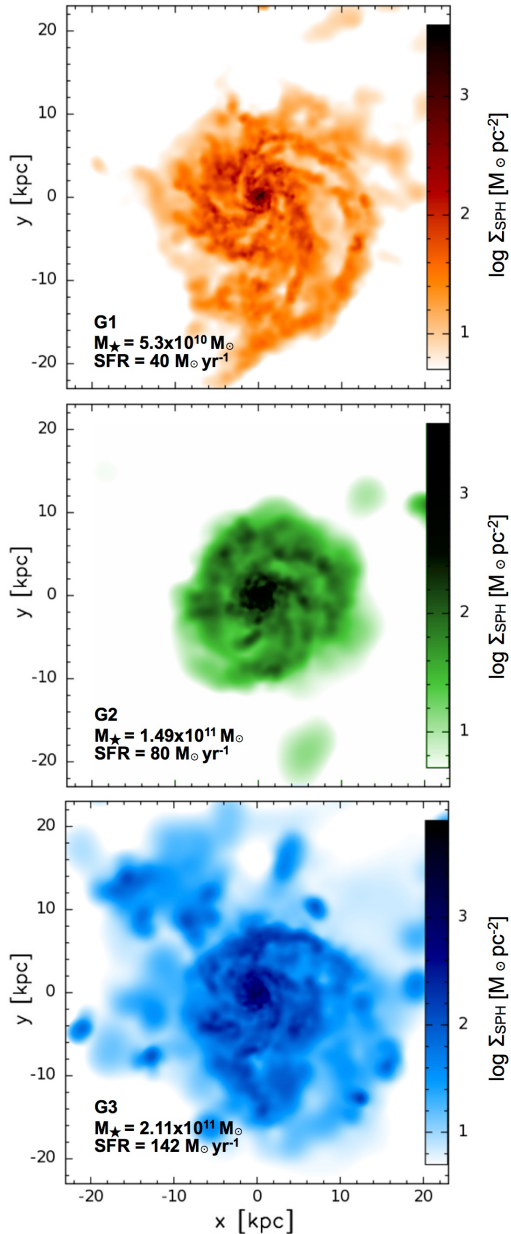


Figure 4.1 SPH gas surface density maps of the three model galaxies G1 (top), G2 (middle), and G3 (bottom) viewed face-on. The stellar masses and SFRs of each galaxy are indicated (see also Table 4.1). The maps have been rendered with the visualization tool SPLASH version 2.4.0 (Price, 2007) using the gas smoothing lengths provided by the simulations.

simulations of galaxies G2 and G3, the corresponding particle masses are $m_{\text{SPH}} = m_* \approx 4.7 \times 10^6 h^{-1} M_\odot$ and $m_{\text{DM}} = 2.6 \times 10^7 h^{-1} M_\odot$, respectively, and the gravitational softening lengths were 610, 610 and 1090 $h^{-1} \text{pc}$. Minimum gas smoothing lengths were about $100 h^{-1} \text{pc}$.

Due to effects of gravitational softening, typical velocities in the innermost parts of the galaxies (typically at radii less than about $2.pdflon_{\text{SPH}}$, where $.pdflon_{\text{SPH}}$ is the SPH and

Table 4.1 Physical properties of the three simulated galaxies G1, G2, and G3

	SFR [M_{\odot} yr $^{-1}$]	M_* [$10^{11} M_{\odot}$]	M_{SPH} [$10^{10} M_{\odot}$]	f_{SPH}	Z'	R_{cut} [kpc]
G1	40	0.53	2.07	29%	1.16	20
G2	80	1.49	2.63	14%	1.97	15
G3	142	2.11	4.66	11%	1.36	20

Notes. All quantities are determined within a radius R_{cut} , which is the radius where the cumulative radial stellar mass function of each galaxy becomes flat. The gas mass (M_{SPH}) is the total SPH gas mass within R_{cut} . The metallicity ($Z' = Z/Z_{\odot}$) is the mean of all SPH gas particles within R_{cut} .

star particle gravitational softening length) are somewhat below dynamical values (see, e.g. Sommer-Larsen et al., 1998). The dynamical velocities will be of the order $v_{\text{dyn}} = \sqrt{GM(R)/R}$, where G is the gravitational constant, R is the radial distance from the centre of the galaxy and $M(R)$ is the total mass located inside of R . Indeed, it turns out that for the simulated galaxies considered here, SPH particle velocities inside of $2.\text{pdfilon}_{\text{SPH}}$ are only about 60-70% of what should be expected from dynamics. To coarsely correct for this adverse numerical effect, for SPH particles inside of $2.\text{pdfilon}_{\text{SPH}}$ the velocities are corrected as follows: For SPH particles of total velocity less than v_{dyn} , the tangential component of the velocity is increased such that the total velocity becomes equal to v_{dyn} . Only the tangential component is increased in order not to create spurious signatures of merging. With this correction implemented, the average ratio of total space velocity to dynamical velocity of all SPH particles inside of $2.\text{pdfilon}_{\text{SPH}}$ equals unity.

Figure 4.1 shows surface density maps of the SPH gas in G1, G2, and G3, i.e., prior to any post-processing by SÍGAME. The gas is seen to be strongly concentrated towards the centre of each galaxy and structured in spiral arms containing clumps of denser gas. The spiral arms reach out to a radius of about 20 kpc in G1 and G3, with G2 showing a more compact structure that does not exceed $R \sim 15$ kpc. Table 4.1 lists key properties of these galaxies, namely SFR, stellar mass (M_*), SPH gas mass (M_{SPH}), SPH gas mass fraction ($f_{\text{SPH}} = M_{\text{SPH}}/(M_* + M_{\text{SPH}})$), and metallicity Z' . These quantities were measured within a radius (R_{cut} , also given in Table 4.1) corresponding to where the radial cumulative stellar mass function has flattened out. The metallicity is in units of solar metallicity and is calculated from the abundances of C, N, O, Mg, Si, S, Ca and Fe in the SPH simulations, and adjusted for the fact that not all heavy metals have been included according to the solar element abundances measured by Asplund et al. (2009).

The location of our three model galaxies in the SFR- M_* diagram is shown in Figure 4.2 along with a sample of 3754 $1.4 < z < 2.5$ main-sequence galaxies selected in near-IR from the NEWFIRM Medium-Band Survey (Whitaker et al., 2011). The latter used a Kroupa IMF but given its similarity with a Chabrier IMF no conversion in the stellar mass and SFR was made (cf., Papovich et al. (2011) and Zahid et al. (2012) who use conversion factors of 1.06 and 1.13, respectively). Also shown are recent determinations of the main-sequence relation at $z > 1$ (Daddi et al., 2007; Elbaz et al., 2007; Rodighiero et al., 2010). When comparing to the relation at $z = 2$ of Daddi et al. (2007), G1, G2, and G3 are seen to lie at the massive end of the sequence, albeit somewhat on its lower (i.e., ‘passive’) side. This latter tendency is also found among

a subset of CO-detected BX/BM galaxies at $z \sim 2 - 2.5$ (Tacconi et al., 2013), highlighted in Figure 4.2 along with a handful of $z \sim 1.5$ BzK galaxies also detected in CO (Daddi et al., 2010). The BX/BM galaxies are selected by a UGR colour criteria (Adelberger et al., 2004), while the BzK galaxies are selected by the BzK colour criteria (Daddi et al., 2004). Based on the above we conclude that, in terms of stellar mass and SFR, our three model galaxies are representative of the star-forming galaxy population detected in CO at $z \sim 2$.

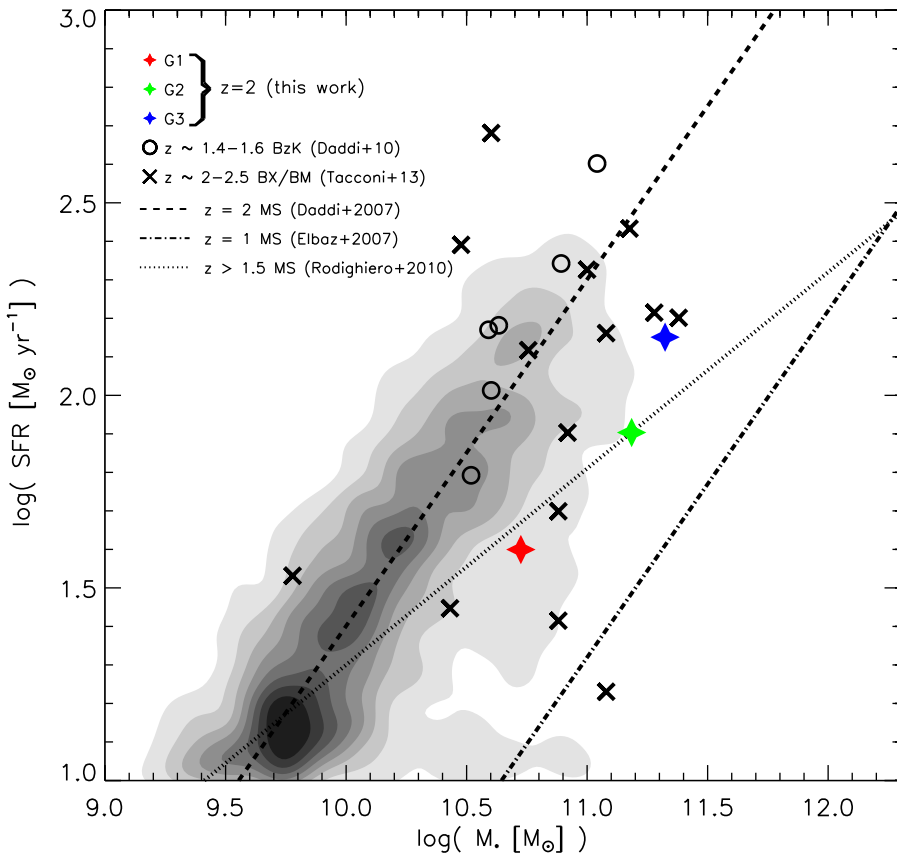


Figure 4.2 Position of the three model galaxies studied here (G1, G2 and G3 with red, green and blue stars respectively), on a SFR- M_* diagram. The grey filled contours show the $z \sim 2$ number density of 3754 $1.4 < z < 2.5$ galaxies from the NEWFIRM Medium-Band Survey (Whitaker et al., 2011). The dashed, dash-dotted and dotted lines indicate the SFR- M_* relation at $z = 2$ (Daddi et al., 2007), $z = 1$ (Elbaz et al., 2007) and $z > 1.5$ (Rodighiero et al., 2010), respectively. Also shown are six $z \sim 1.4 - 1.6$ BzK galaxies (black circles; Daddi et al. 2010) and 14 $z \sim 2 - 2.5$ BX/BM galaxies (black crosses; Tacconi et al. 2013). The BzK galaxies are from top to bottom: BzK–12591, BzK–21000, BzK–16000, BzK–17999, BzK–4171 and BzK–2553 (following the naming convention of Daddi et al. 2010).

4.3 MODELING THE ISM WITH SÍGAME

4.3.1 METHODOLOGY OVERVIEW

What follows in this section is an overview of the major s.pdf that go into SÍGAME, along with a brief description of each. The full details of each step are given in subsequent sections and in appendices A.1 through A.3. We stress, that SÍGAME operates entirely in the post-processing stage of an SPH simulation, and can in principle easily be adapted to any given SPH galaxy simulation as long as certain basic quantities are known for each SPH particle in the simulation, namely: position (\vec{r}), velocity (\vec{v}), atomic hydrogen density (n_{H}), metallicity (Z'), kinetic temperature (T_k), smoothing length (h), and star formation rate (SFR). The key s.pdf involved in SÍGAME are:

1. Cooling of the SPH gas. The initially hot ($T_k \sim 10^{3-7}$ K) SPH gas particles are cooled to temperatures typical of the warm neutral medium ($\lesssim 10^4$ K) by atomic and ionic cooling lines primarily.
2. Inference of the molecular gas mass fraction ($f'_{\text{mol}} = m_{\text{H}_2}/m_{\text{SPH}}$) of each SPH particle after the initial cooling in step 1. f'_{mol} for a given SPH particle is calculated by taking into account its temperature, metallicity, and the local cosmic ray and FUV radiation field impinging on it.
3. Distribution of the molecular gas into GMCs. Cloud masses and sizes are obtained from random sampling of the observed GMC mass-spectrum in nearby quiescent galaxies and applying the local GMC mass-size relation.
4. GMC thermal structure. A radial density profile is adopted for each GMC and used to calculate the temperature structure throughout individual clouds, taking into account heating and cooling mechanisms relevant for neutral and molecular gas, when exposed to the local cosmic ray and attenuated FUV fields.
5. Radiative transport of CO lines. Finally, the CO line spectra are calculated separately for each GMC with a radiative transfer code and accumulated on a common velocity axis for the entire galaxy.

Determining the temperature (step *i*) and the molecular gas mass fraction (step *ii*) of a warm neutral gas SPH particle cannot be done independently of each other, but must be solved for simultaneously in an iterative fashion (see Sections 4.3.2 and 4.3.3). As already mentioned, we shall apply SÍGAME to the SPH simulations of galaxies G1, G2, and G3 described in Section 4.2, and in doing so we will use them to illustrate the workings of the code.

4.3.2 THE WARM AND COLD NEUTRAL MEDIUM

In SPH simulations of galaxies the gas is typically not cooled to temperatures below a few thousand Kelvin (Springel & Hernquist, 2003). This is illustrated in Figure 4.3, which shows the SPH gas temperature distribution (dashed histogram) in G1 (for clarity we have not shown the corresponding temperature distributions for G2 and G3, both of which are similar to that of G1). Minimum SPH gas temperatures in G1, G2 and G3 are about 1200 K, 3100 K and 3200 K, respectively, and while temperatures span the range $\sim 10^{3-7}$ K, the bulk ($\sim 80 - 90\%$) of the gas mass in all three galaxies is at $T_k \lesssim 10^5$ K.

At such temperatures all gas will be in atomic or ionised form and H atoms that attach to grain surfaces via chemical bonds (chemisorbed) will evaporate from dust grains before H₂ can be formed. H₂ can effectively only exist at temperatures below $\sim 10^3$ K, assuming a realistic desorption energy of 3×10^4 K for chemisorbed H atoms (see Cazaux & Spaans, 2004). The first step of SÍGAME is therefore to cool some portion of the hot SPH gas down to $T_k \lesssim 10^3$ K, i.e., a temperature range characteristic of a warm and cold neutral medium for which we can meaningfully employ a prescription for the formation of H₂.

SÍGAME employs the standard cooling and heating mechanisms pertaining to a hot, partially ionised gas. Cooling occurs primarily via emission lines from H, He, C, O, N, Ne, Mg, Si, S, Ca, and Fe in their atomic and ionised states, with the relative importance of these radiative cooling lines depending on the temperature (Wiersma et al., 2009). In addition to these emission lines, electron recombination with ions can cool the gas, as recombining electrons take away kinetic energy from the plasma, a process which is important at temperatures $> 10^3$ K (Wolfire et al., 2003). At similar high temperatures another important cooling mechanism is the scattering of free electrons off other free ions, whereby free-free emission removes energy from the gas (Draine, 2011). Working against the cooling is heating caused by cosmic rays via the expulsion of bound electrons from atoms or the direct kinetic transfer to free electrons via Coulomb interactions (Simnett & McDonald, 1969). Since this cooling step is targeted towards the hot, ionised gas, we shall ignore photo-ionization as a heating process, but include it in the subsequent temperature calculations (see Section 4.3.4).

We arrive at a first estimate of the temperature of the neutral medium by requiring energy rate equilibrium between the above mentioned heating and cooling mechanisms:

$$\Gamma_{\text{CR,HI}} = \Lambda_{\text{ions+atoms}} + \Lambda_{\text{rec}} + \Lambda_{\text{f-f}}, \quad (4.1)$$

where $\Lambda_{\text{ions+atoms}}$ is the cooling rate due to atomic and ionic emission lines, Λ_{rec} and $\Lambda_{\text{f-f}}$ are the cooling rates from recombination processes and free-free emission as described above, and $\Gamma_{\text{CR,HI}}$ is the cosmic ray heating rate in atomic, partly ionised, gas. The detailed analytical expressions employed by SÍGAME for these heating and cooling rates are given in appendix A.1.

The abundances of the atoms and ions, listed above, entering the $\Lambda_{\text{ions+atoms}}$ cooling term either have to be calculated in a self-consistent manner as part of the SPH simulation or set by hand. For our set of galaxies, the SPH simulations follow the abundances of H, C, N, O, Mg, Si, S, Ca and Fe, while for the abundances of He and Ne, we adopt solar mass fractions of 0.2806 and 10^{-4} , respectively, as used in Wiersma et al. (2009).

$\Gamma_{\text{CR,HI}}$ depends on the *primary* cosmic ray ionization rate (ζ_{CR}), a quantity that is set by the number density of supernovae since they are thought to be the main source of CRs (Ackermann et al., 2013). In SÍGAME, this is accounted for by parameterizing ζ_{CR} as a function of the *local* star formation rate density (SFRD) as it varies across the simulated galaxy. The details of this parameterization are deferred to Section 4.3.4.

It is important to emphasize that the ionization fraction of the gas depends on the *total* cosmic ray ionization rate (i.e., ζ_{CR} corrected for secondary ionizations of H and He), the gas temperature (T_k), and H I density (n_{HI}) with a procedure kindly provided by I. Pelupessy (see also Pelupessy 2005) and these quantities are interdependent. The major drawback of this method is that it does not depend on the free electrons from ionization of carbon, which renders the method less suitable for the CNM compared to the WNM. In the following application of

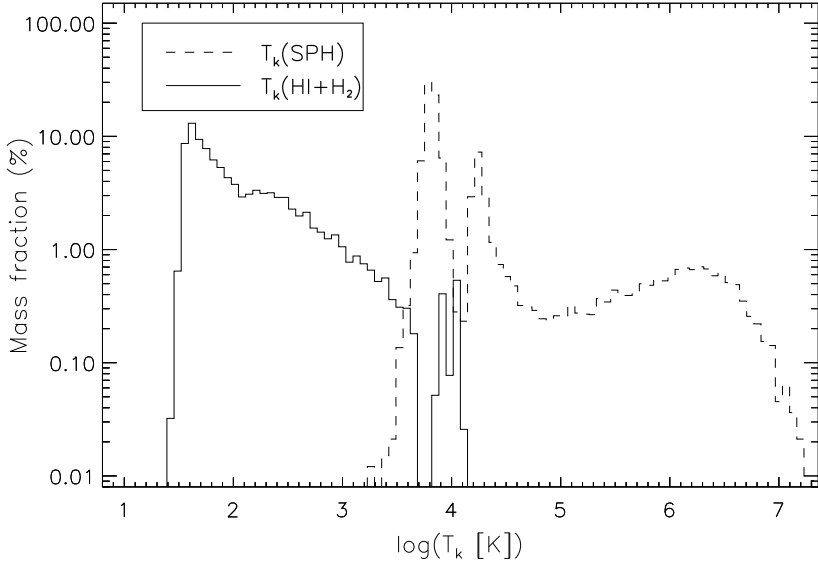


Figure 4.3 The distributions of gas kinetic temperature before (dashed histogram) and after (solid histogram) applying the heating and cooling mechanisms of eq. 4.1 to galaxy G1. The original hot SPH gas is seen to span a temperature range from about 10^3 K up to $\sim 10^7$ K, while once the gas has been cooled the temperature distribution only barely exceeds $\sim 10^4$ K.

SÍGAME, we changed this method to rely on results with the chemical evolution code CLOUDY (see Chapter 5). Returning to eq. 4.1, all terms depend on T_k , n_{HI} , and the electron density (n_e) for a fixed ζ_{CR} , see appendix A.1. The latter is calculated taking into account the ionization of H and He, and is a function of both T_k and ζ_{CR} . Since, n_{HI} is set by the molecular gas mass fraction (f'_{mol}), which in turn also depends on T_k (see Section 4.3.3 on how f'_{mol} is calculated), eq. 4.1 has to be solved in an iterative fashion until consistent values for T_k , n_e , and f'_{mol} are reached. Example solutions are given in Figure A.1 in Appendix A.1.

The temperature distribution that results from solving eq. 4.1 for every SPH particle in the G1 simulation is shown in Figure 4.3 (very similar distributions are obtained for G2 and G3). The gas has been cooled to $T_k \lesssim 10^4$ K, with temperatures extending down to 25, 30 and 27 K respectively for G1, G2 and G3. We identify this gas as the warm neutral medium (WNM) and the cold neutral medium (CNM), and it is from this gas phase that we shall construct our molecular gas phase in the subsequent sections.

4.3.3 HI TO H₂ CONVERSION

For the determination of the molecular gas mass fraction associated with each SPH gas particle we use the prescription of Pelupessy et al. (2006), inferred by equating the formation rate of H₂ on dust grains with the photodissociation rate of H₂ by Lyman-Werner band photons, and taking into account the self-shielding capacity of H₂ and dust extinction. We ignore H₂ production in the gas phase (cf., Christensen et al., 2012) since only in diffuse low metallicity ($\lesssim 0.1 Z_\odot$) gas is this thought to be the dominant formation route (Norman & Spaans, 1997),

and so should not be relevant in our model galaxies that have mean metallicities $Z' > 1$ (see Table 4.1) and very little gas exists at $Z' < 0.1$ (see Figure A.3 in Appendix A.3). We adopt a steady-state for the H_I→H₂ transition, meaning that we ignore any time dependence owing to temporal changes in the UV field strength and/or disruptions of GMCs, both of which can occur on similar time scales as the H₂ formation. This has been shown to be a reasonable assumption for environments with metallicities $\gtrsim 0.01 Z_{\odot}$ (Narayanan et al., 2011; Krumholz & Gnedin, 2011).

The first step is to derive the FUV field strength, G_0 , which sets the H_I→H₂ equilibrium. In SÍGAME, G_0 consists of a spatially varying component that scales with the local SFRD (SFRD_{local}) in different parts of the galaxy on top of a constant component set by the total stellar mass of the galaxy. This is motivated by Seon et al. (2011) who measured the average FUV field strength in the MW ($G_{0,\text{MW}}$) and found that about half comes from star light directly with the remainder coming from diffuse background light. We shall assume that in the MW the direct stellar contribution to $G_{0,\text{MW}}$ is determined by the average SFRD (SFRD_{MW}), while the diffuse component is fixed by the stellar mass ($M_{*,\text{MW}}$). From this assumption, i.e., by calibrating to MW values, we derive the desired scaling relation for G_0 in our simulations:

$$G_0 = G'_{0,\text{MW}} \left(0.5 \frac{\text{SFRD}_{\text{local}}}{\text{SFRD}_{\text{MW}}} + 0.5 \frac{M_*}{M_{*,\text{MW}}} \right), \quad (4.2)$$

where $G_{0,\text{MW}} = 0.6$ Habing (Seon et al., 2011), and $M_{*,\text{MW}} = 6 \times 10^{10} M_{\odot}$ (McMillan, 2011). For SFRD_{MW} we adopt $0.0024 M_{\odot} \text{ yr}^{-1} \text{ kpc}^{-3}$, inferred from the average SFR within the central 10 kpc of the MW ($0.3 M_{\odot} \text{ yr}^{-1}$; Heiderman et al., 2010) and within a column of height equal to the scale height of the young stellar disk (0.2 kpc; Bovy et al., 2012) of the MW disk. SFRD_{local} is the SFRD ascribed to a given SPH particle, and is calculated as the volume-averaged SFR of all SPH particles within a 5 kpc radius, the latter chosen in order to resolve the galaxies and at the same time not going to scales where different stellar populations must be considered. Note, that the stellar mass sets a lower limit on G_0 , which for G1, G2, and G3 are 0.22, 0.62, and 0.88 Habing, respectively.

Next, the gas upon which the FUV field impinges is assumed to reside in logotropic clouds, i.e., clouds with radial density profiles given by $n(r) = n_{\text{H,ext}} (r/R)^{-1}$, where $n_{\text{H,ext}}$ is the density at the cloud radius R . From Pelupessy et al. (2006) we then have that the molecular gas mass fraction, including heavier elements than hydrogen, of each cloud is given by³:

$$f'_{\text{mol}} \equiv \frac{m_{\text{mol}}}{m_{\text{SPH}}} = \exp \left[-4 \frac{A_{\text{v}}^{(\text{tr})}}{\langle A_{\text{v}} \rangle} \right]. \quad (4.3)$$

Here $\langle A_{\text{v}} \rangle$ is the area-averaged visual extinction of the cloud and $A_{\text{v}}^{(\text{tr})}$ is the extinction through the outer layer of neutral hydrogen. The mean extinction $\langle A_{\text{v}} \rangle$ is calculated from metallicity and average cloud density, $\langle n_{\text{H}} \rangle$:

$$\langle A_{\text{v}} \rangle = 7.21 \times 10^{-22} Z' \langle n_{\text{H}} \rangle R, \quad (4.4)$$

where $\langle n_{\text{H}} \rangle R$ is set by a density-size relation normalized by the external boundary pressure,

³We will use lower case m when dealing with individual SPH particles. Furthermore, f'_{mol} is not to be confused with f_{mol} describing the total molecular gas mass fraction of a galaxy and to be introduced in Section 4.4.

P_{ext} , of virialized cloud:

$$\langle n_{\text{H}} \rangle R/\text{pc} = n_{\text{ds}} \left(\frac{P_{\text{ext}}/\text{k}_B}{10^4 \text{ cm}^{-3} \text{ K}} \right)^{1/2}, \quad (4.5)$$

where the normalization constant is set to $n_{\text{ds}} = 10^3 \text{ cm}^{-3}$, motivated by studies of molecular clouds in the MW (Larson, 1981; Wolfire et al., 2003; Heyer & Brunt, 2004) (note that Pelupessy et al. (2006) uses 1520 cm^{-2}). The external hydrostatic pressure for a rotating disk of gas and stars is calculated at mid-plane following Swinbank et al. (2011):

$$P_{\text{tot}} \approx \frac{\pi}{2} G \Sigma_{\text{gas}} \left[\Sigma_{\text{gas}} + \left(\frac{\sigma_{\text{gas}\perp}}{\sigma_{*\perp}} \right) \Sigma_* \right], \quad (4.6)$$

where $\sigma_{\text{gas}\perp}$ and $\sigma_{*\perp}$ are the local vertical velocity dispersions of gas and stars respectively, and Σ denotes surface densities of the same. These quantities are all calculated directly from the simulation output, using the neighbouring SPH particles within 1 kpc. neighbouring particles within two smoothing lengths, weighted by mass, density and the cubic spline kernel (see also Monaghan, 2005) For a logotropic density profile, the external density is given by $n_{\text{H,ext}} = 2/3 \langle n_{\text{H}} \rangle$, where we approximate $\langle n_{\text{H}} \rangle$ with the original SPH gas density. The external cloud pressure that enters in eq. 4.5, is assumed to be equal to $P_{\text{tot}}/(1 + \alpha_0 + \beta_0)$ for relative cosmic and magnetic pressure contributions of $\alpha_0 = 0.4$ and $\beta_0 = 0.25$ (Elmegreen, 1989; Swinbank et al., 2011). For the MW, $P_{\text{ext}}/\text{k}_B \sim 10^4 \text{ cm}^{-3} \text{ K}$ (Elmegreen, 1989), but as shown in Fig. A.3 in Appendix A.3, our model galaxies span a wide range in $P_{\text{ext}}/\text{k}_B$ of $\sim 10^2 - 10^7 \text{ cm}^{-3} \text{ K}$. In order to best account for their $z \sim 2$ nature, we will scale the density-size relation in eq. 4.5 and the σ_{v} -size relation with P_{ext} (see Section 4.3.5).

For $A_{\text{v}}^{(\text{tr})}$, the following expression is provided by Pelupessy et al. (2006):

$$A_{\text{v}}^{(\text{tr})} = 1.086 \nu \xi_{\text{FUV}}^{-1} \times \ln \left[1 + \frac{\frac{G'_0}{\nu \mu S_{\text{H}}(T_k)} \sqrt{\frac{\xi_{\text{FUV}}}{Z' T_k}}}{n_{\text{H,ext}}/135 \text{ cm}^{-3}} \right], \quad (4.7)$$

where ξ_{FUV} is the ratio between dust FUV absorption cross section (σ) and the effective grain surface area (σ_d), and is set to $\xi_{\text{FUV}} = \sigma/\sigma_d = 3$. $S_{\text{H}} = (1 + 0.01 T_k)^{-2}$ is the probability that HI atoms stick to grain surfaces, where T_k is the kinetic gas temperature (determined in an iterative way as explained in Section 4.3.2). Furthermore, $\nu = n_{\text{H,ext}} R \sigma (1 + n_{\text{H,ext}} R \sigma)^{-1}$, and μ (set to 3.5 as suggested by Pelupessy et al., 2006) is a parameter which incorporates the uncertainties associated with primarily S_{H} and σ_d .

Following the above prescription SÍGAME determines the molecular gas mass fraction and thus the molecular gas mass ($m_{\text{mol}} = f'_{\text{mol}} m_{\text{SPH}}$) associated with each SPH particle. Depending on the environment (e.g., G_0 , Z' , T_k , P_{ext} , ...), the fraction of the SPH gas converted into H₂ can take on any value between 0 and 1, as seen from the f'_{mol} distribution of G1 in Figure 4.4. Overall, the total mass fraction of the SPH gas in G1, G2, and G3 (i.e., within R_{cut}) that is converted to molecular gas is 29 %, 52 % and 34 %, respectively.

4.3.4 STRUCTURE OF THE MOLECULAR GAS

Molecular gas is known to clump on scales $\lesssim 100 \text{ pc}$, significantly below the typical resolution in simulations of galaxy evolution, thus posing a general problem when modelling molecular emission lines (Narayanan et al., 2011; Popping et al., 2014; Narayanan & Krumholz, 2014).

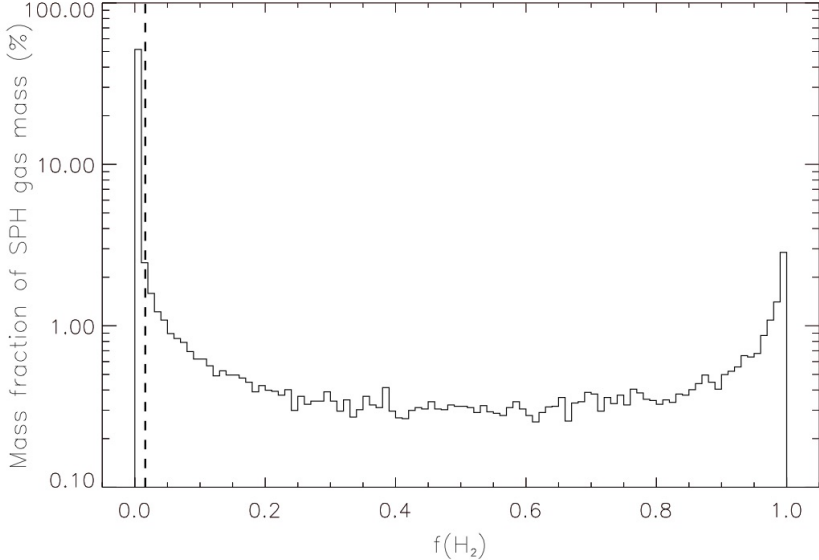


Figure 4.4 The distribution of the H_2 gas mass fraction of the SPH particles in G1 calculated according to eq. 4.3 (solid line histogram). Similar distributions are found for G2 and G3. The lower limit on f'_{mol} , defined as described in Section 4.3.4, is indicated by the dashed vertical line.

In relatively undisturbed, moderately star-forming galaxies, molecular gas is believed to be distributed in giant molecular clouds (GMCs) of sizes $\sim 6 - 60$ pc with internal substructures similar to those observed in the MW (Kauffmann et al., 2010), and as suggested by simulations (e.g. Vázquez-Semadeni et al., 2010). Having determined the molecular gas mass fractions, SÍGAME proceeds by distributing the molecular gas into GMCs, and calculates the masses and sizes, along with the internal density and temperature structure, for each GMC as described in the following.

GMC masses and sizes

The molecular gas associated with a given SPH particle is divided into a number of GMCs, the masses of which are assumed to follow a power-law spectrum of the form:

$$\frac{dN}{dm_{\text{GMC}}} \propto m_{\text{GMC}}^{-\beta}. \quad (4.8)$$

For the MW disk and Local Group galaxies $\beta \simeq 1.8$ (Blitz et al., 2007), and this will be our default choice unless otherwise stated. Lower and upper mass cut-offs at $10^4 M_\odot$ and $10^6 M_\odot$, respectively, are enforced in order to span the mass range observed by Blitz et al. (2007). A similar approach was adopted by Narayanan et al. (2008b,a). Note, in the case of G1 the upper cut-off on the GMC masses is in fact set by the mass resolution of the SPH simulation ($6.3 \times 10^5 h^{-1} M_\odot$). For G1, typically $\lesssim 30$ GMCs are created in this way per SPH particle, while for G2 and G3, which were run with SPH gas particles masses almost an order of magnitude higher, as much as ~ 100 GMCs can be extracted from a given SPH particle for $\beta = 1.8$. Figure

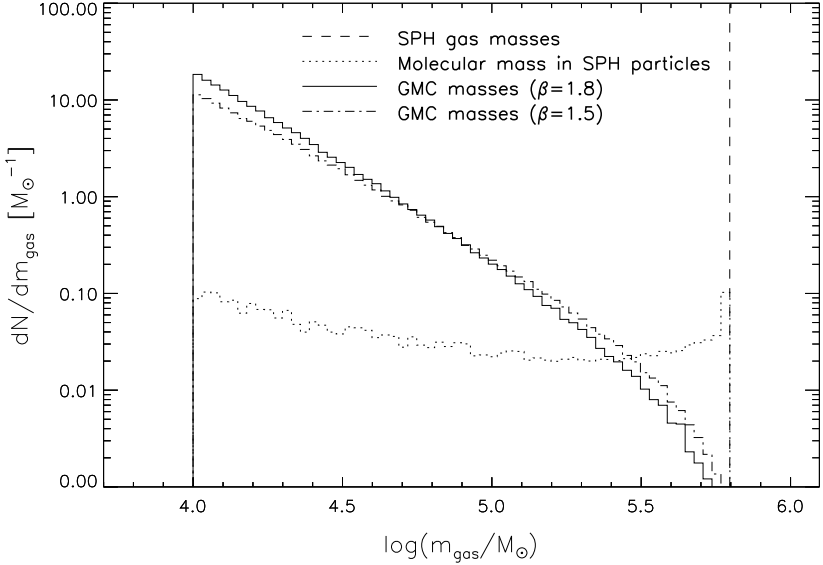


Figure 4.5 The distribution of GMC masses in G1 obtained by applying eq. 4.8, with $\beta = 1.8$ (solid histogram) and $\beta = 1.5$ (dash-dotted histogram), to the total molecular gas masses associated with SPH particles (distribution shown as dotted histogram). The dashed vertical line indicates the SPH gas mass resolution of the simulation ($= 6.3 \times 10^5 h^{-1} M_\odot$ in the case of G1).

4.5 shows the resulting mass distribution of all the GMCs in G1, along with the distribution of molecular mass associated with the SPH gas particles prior to it being divided into GMCs. The net effect of re-distributing the H₂ mass into GMCs is a mass distribution dominated by relatively low cloud masses, which is in contrast to the relatively flat SPH H₂ mass distribution. Note, the lower cut-off at $m_{\text{GMC}} = 10^4 M_\odot$ implies that if the molecular gas mass associated with an SPH particle (i.e., $m_{\text{mol}} = f'_{\text{mol}} m_{\text{SPH}}$) is less than this lower limit it will not be redistributed into GMCs. Since m_{SPH} is constant in our simulations ($6.3 \times 10^5 h^{-1} M_\odot$ for G1 and $4.7 \times 10^6 h^{-1} M_\odot$ for G2 and G3) the lower limit imposed on m_{GMC} translates directly into a lower limit on f'_{mol} (0.016 for G1 and 0.002 for G2 and G3, shown as a dashed vertical line for G1 in Figure 4.4). As a consequence, 0.2, 0.005 and 0.01 % of the molecular gas in G1, G2, and G3, respectively, does not end up in GMCs. These are negligible fractions and the molecular gas they represent can therefore be safely ignored.

The sizes, R_{eff} , of the GMCs are derived via application of the virial theorem, by which R_{eff} depends on the GMC mass and the external pressure, P_{ext} :

$$\frac{R_{\text{eff}}}{\text{pc}} = \left(\frac{P_{\text{ext}}/k_B}{10^4 \text{ cm}^{-3} \text{ K}} \right)^{-1/4} \left(\frac{m_{\text{GMC}}}{290 M_\odot} \right)^{1/2}, \quad (4.9)$$

and σ_v depends on R_{eff} and P_{ext} via:

$$\frac{\sigma_v}{\text{km s}^{-1}} = 1.2 \left(\frac{P_{\text{ext}}/k_B}{10^4 \text{ cm}^{-3} \text{ K}} \right)^{1/4} \left(\frac{R_{\text{eff}}}{\text{pc}} \right)^{1/2}, \quad (4.10)$$

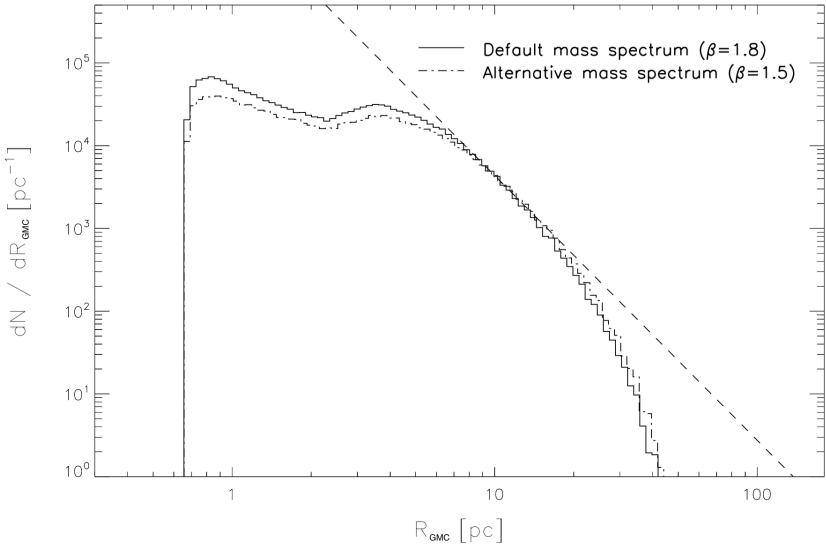


Figure 4.6 The distribution of GMC radii in G1 for the adopted cloud mass spectrum with $\beta = 1.8$ (solid histogram) and for a slightly modified spectrum with $\beta = 1.5$ (dash-dotted histogram). Similar distributions are found for G2 and G3. The dashed line shows the best-fit power-law to the distribution: $\frac{dN}{dR_{\text{GMC}}} \propto R_{\text{GMC}}^{-3.2}$. Observations of clouds in the outer Galactic disk found a size distribution with a power-law slope of -3.2 ± 0.1 over a similar size range (Heyer et al., 2001).

see, e.g., Elmegreen (1989); Swinbank et al. (2011). Figure 4.6 shows the resulting distribution of GMC sizes (R_{eff}) for G1, for the two GMC mass spectra investigated here (see beginning of this Section). Upper and lower limits on cloud sizes of ~ 0.07 pc and ~ 60 pc, respectively, are set by the maximum and minimum GMC masses and pressure in G1.

Since observations have indicated that the shape of the GMC mass spectrum might be different at high redshift, in particular in gas-rich systems harbouring a high-pressure ISM and massive star-forming clumps of molecular gas (e.g. Swinbank et al., 2011; Leroy et al., 2015), we examined the effects of adopting a different index, namely $\beta = 1.5$, corresponding to virialized ($\sigma_v \propto \sqrt{R}$) clouds (Padoan & Nordlund, 2002). The mass distribution resulting from this lower value of β is more top-heavy than our adopted spectrum (see Figure 4.5), and as a result there are more clouds with sizes $R_{\text{GMC}} \gtrsim 10$ pc and fewer clouds at smaller radii (Figure 4.6). Yet, the total amount of molecular gas in our galaxies does not change significantly between $\beta = 1.8$ and $\beta = 1.5$, and we therefore conclude that our simulation results are robust against (reasonable) changes in the mass-spectrum.

As the final step, the GMCs are placed randomly around the position of their ‘parent’ SPH particle, albeit with an inverse proportionality between radial displacement and mass of the GMC. The latter is done in order to retain the mass distribution of the original galaxy simulation as best as possible. The GMCs are assigned the same bulk velocity, \bar{v} , Z' , G_0 and ζ_{CR} as their ‘parent’ SPH particle.

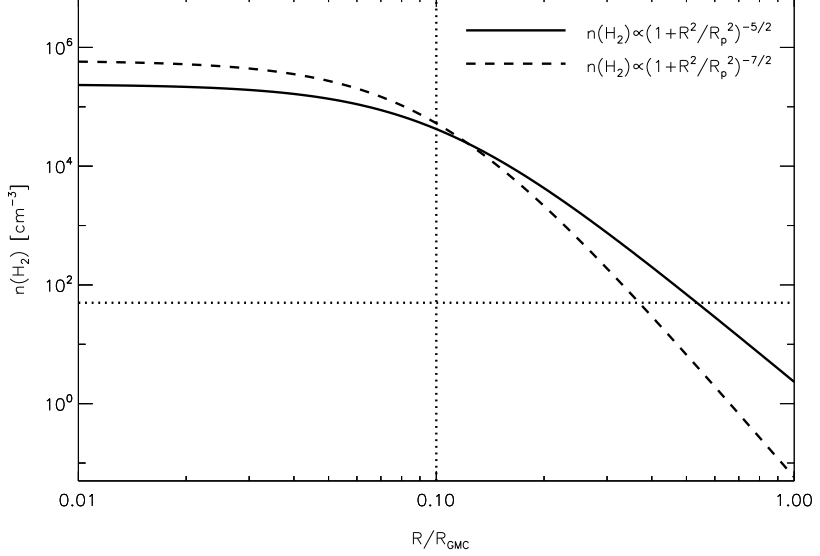


Figure 4.7 Plummer density profiles (eq. 4.11) with power-law exponents of $-5/2$ (solid line) and $-7/2$ (dashed line) for a GMC mass of $10^4 M_\odot$ and an external pressure of $P_{\text{ext}}/k_B = 10^4 \text{ K cm}^{-3}$. The corresponding cloud radius is $R_{\text{cloud}} = 5.9 \text{ pc}$ (eq. 4.9). The vertical dotted line marks the Plummer radius ($= 0.1 R_{\text{GMC}}$), and the horizontal dotted line the n_{H_2} value (50 cm^{-3}) below which CO is assumed to photo-dissociate in our simulations.

GMC density structure

In order to ensure a finite central density in our GMCs, SÍGAME adopts a Plummer radial density profile (e.g., Gieles et al., 2006; Miettinen et al., 2009):

$$n_{\text{H}_2}(R)[\text{cm}^{-3}] = 20.23 \frac{3m_{\text{GMC}}[\text{M}_\odot]}{4\pi 1.36(R_p [\text{pc}])^3} \left(1 + \frac{R^2}{R_p^2}\right)^{-5/2}, \quad (4.11)$$

where R_p is the so-called Plummer radius, which we set to $R_p = 0.1 R_{\text{eff}}$. The latter allows for a broad range in gas densities throughout the clouds, from $\sim 10^6 \text{ cm}^{-3}$ in the central parts to a few 10 cm^{-3} further out. The factor 1.36 in the denominator accounts for the presence of helium in the GMC. We test the effects of a steeper GMC density profile on our final results by adopting an exponent of $-7/2$ in eq. 4.11 and re-running our simulations. Plummer profiles with exponents $-5/2$ and $-7/2$ are shown in Figure 4.7 for a GMC with mass of $10^4 M_\odot$ and external pressure 10^4 K cm^{-3} .

GMC thermal structure

Having established the masses, sizes, and density structure of the GMCs, SÍGAME next solves for the kinetic temperature throughout the clouds. This means balancing the relevant heating and cooling mechanisms as a function of cloud radius.

GMCs are predominantly heated by FUV photons (via the photo-electric effect) and cosmic rays. For the strength of the FUV field impinging on the GMCs, we take the previously cal-

culated values at the SPH gas particle position (eq. 4.2). We shall assume that the cosmic ray ionization rate scales in a similar manner, having its origin in supernovae and therefore also being closely related to nearby star formation and the total stellar mass of the galaxy:

$$\zeta_{\text{CR}} = \zeta_{\text{CR,MW}} \left(0.5 \frac{\text{SFRD}_{\text{local}}}{\text{SFRD}_{\text{MW}}} + 0.5 \frac{M_*}{M_{*,\text{MW}}} \right) \quad (4.12)$$

where $\text{SFRD}_{\text{local}}$, SFRD_{MW} and $M_{*,\text{MW}}$ are as described in Section 4.3.3, and ζ_{CR} is scaled to the ‘canonical’ MW value of $\zeta_{\text{CR,MW}} = 3 \times 10^{-17} \text{ s}^{-1}$ (e.g. Webber, 1998). While the FUV radiation is attenuated by dust and therefore does not heat the GMC centres significantly, cosmic rays can penetrate these dense regions and heat the gas there (Papadopoulos et al., 2011). For this reason we will attenuate the FUV field, but not the cosmic ray field, assuming that the latter k.pdf the same intensity throughout the GMCs. The extinction of the FUV field at a certain point within a GMC is derived by integrating the Plummer density profile from that point and out to the cloud surface, which is taken to be R_{eff} . This H column density is converted into a visual extinction ($A_V = N_{\text{H}} / 2.2 \times 10^{21} \text{ cm}^{-2}$) so that attenuated FUV field becomes:

$$G_{0,\text{att}} = G_0 e^{-1.8 A_V}, \quad (4.13)$$

where the factor of 1.8 is the adopted conversion from visual to FUV extinction (Black & Dalgarno, 1977). We calculate the temperature throughout each GMC via the following heating and cooling rate balance:

$$\Gamma_{\text{PE}} + \Gamma_{\text{CR,H}_2} = \Lambda_{\text{H}_2} + \Lambda_{\text{CO}} + \Lambda_{\text{OI}} + \Lambda_{\text{CII}} + \Lambda_{\text{gas-dust}}. \quad (4.14)$$

Γ_{PE} is the photo-electric heating by FUV photons, and $\Gamma_{\text{CR,H}_2}$ is the cosmic ray heating in molecular gas. Λ_{H_2} is the cooling rate of the two lowest H_2 rotational lines (S(0) and S(1)), and Λ_{CO} is the cooling rate of the combined CO rotational ladder. $\Lambda_{\text{gas-dust}}$ is the cooling rate due to interactions between gas molecules and dust particles, which only becomes important at densities above 10^4 cm^{-3} (e.g., Goldsmith, 2001; Glover & Clark, 2012). Λ_{CII} and Λ_{OI} are the cooling rates due to $[\text{CII}]$ and $[\text{OI}]$ line emission, respectively, the strongest cooling lines in neutral ISM. The abundances of carbon and oxygen used in the prescriptions for their cooling rates, scale with the cloud metallicity, while the CO cooling scales with the relative CO to neutral carbon abundance ratio, set by the molecular density (see Appendix A.2).

The dust temperature, T_{dust} , used for $\Lambda_{\text{gas-dust}}$ in eq. 4.14 is set by the equilibrium between absorption of FUV and the emission of IR radiation by the dust grains. We adopt the approximation given by Tielens (2005):

$$\frac{T_{\text{dust}}}{\text{K}} \simeq 33.5 \left(\frac{a}{1 \mu\text{m}} \right)^{-0.2} \left(\frac{G_{0,\text{att}}}{10^4 \text{ Habing}} \right)^{0.2}, \quad (4.15)$$

where $G_{0,\text{att}}$ is the dust-attenuated FUV field (eq. 4.13) and a is the grain size, which we set to $1 \mu\text{m}$ for simplicity. Values for T_{dust} using eq. 4.15 range from 0 to 8.9 K , but we enforce a lower limit on T_{dust} equal to the $z = 2$ CMB temperature of 8.175 K . T_{dust} is therefore essentially constant ($\sim 8 - 9 \text{ K}$) throughout the inner region of the GMC models, similar to the value of $T_{\text{dust}} = 8 \text{ K}$ adopted by Papadopoulos & Thi (2013) for CR-dominated cores. However, due to a re-radiated IR component, T_{dust} can easily be $> 50 \text{ K}$ even when the FUV field is extinguished due to high optical depth (see Krumholz, 2014). Analytical expressions for all of the above

heating and cooling rates are given in Appendix A.2, which also shows their relative strengths as a function of density for two example GMCs (Figure A.2).

Figure A.4 in Appendix A.3 shows the resulting T_k versus n_{H_2} behaviour for 80 GMCs spanning a broad range of GMC masses, metallicities, and star formation rate densities. As seen in the displayed GMC models, some general trends can be inferred from the $T_k - n_{H_2}$ diagrams. At fixed metallicity and mass, an increase in FUV radiation field, G_0 (and therefore also CR ionization rate, ζ_{CR}), leads to higher temperatures throughout the models. In the outer regions this is due primarily to the increased photoelectric heating, while in the inner regions, heating by the unattenuated cosmic rays takes over as the dominating heating mechanism (Figure A.2). Keeping G_0 (and ζ_{CR}) fixed, lower T_k -levels and shallower $T_k - n_{H_2}$ gradients are found in GMCs with higher metallicities, Z' . Both these trends are explained by the fact that the [[CII]] and [OI] cooling rates scale linearly with Z' (see Appendix A.2).

Moving from the outskirts and inward towards the GMC centres (i.e., towards higher densities), T_k drops as the attenuation of G_0 reduces the photoelectric heating. However, the transition from the cooling by [[CII]] to the less efficient cooling mechanism by CO lines, causes a local increase in T_k at $n_{H_2} \sim 10^3 - 10^{4.5} \text{ cm}^{-3}$, as also seen in the detailed GMC simulations by Glover & Clark (2012). The exact density at which this ‘bump’ in T_k depends strongly on the mass of the GMC, which is an effect of the chosen mass distribution within the GMCs. Our choice of the Plummer model for the radial density profile means that the extinction, A_V , at a certain density increases with GMC mass. This in turn decreases the FUV heating, and as a result the $T_k - n_{H_2}$ curve moves to lower densities with increasing GMC mass.

As the density increases towards the cloud centres (i.e., $n_{H_2} \gtrsim 10^{4-5} \text{ cm}^{-3}$) molecular line cooling and also gas-dust interactions become increasingly efficient and start to dominate the cooling budget. The $T_k - n_{H_2}$ curves are seen to be insensitive to changes in Z' , which is expected since the dominant heating and cooling mechanisms in these regions do not depend on Z' . Eventually, in the very central regions of the clouds, the gas reaches temperatures close to that of the ambient CMB radiation field, irrespective of the overall GMC properties and the conditions at the surface (Figure A.2).

GMC grid models

The $T_k - n_{H_2}$ curve for a given GMC is determined by the following basic quantities:

- The FUV radiation (G_0), and with that the cosmic ray field strength, ζ_{CR} (proportional to G_0), together governing the heating of the gas.
- The GMC mass (m_{GMC}), which (together with P_{ext}) determines the effective radius of a cloud (eq. 4.9) and thus its density profile (eq. 4.11).
- The local metallicity (Z'), which influences the fraction of H_2 gas and plays an important role in cooling the gas.
- The external pressure (P_{ext}), which determines the $m_{GMC}-R_{eff}$ and σ_v-R_{eff} relations.

Of these, G_0 and ζ_{CR} are set by the local star formation rate density ($SFRD_{local}$) and the total stellar mass (M_*) according to eqs. 4.2 and 4.12, Z' is taken directly from the simulations while m_{GMC} is extracted randomly from a probability distribution as explained in Section 4.3.4. The distributions of m_{GMC} , Z' , G_0 , ζ_{CR} and P_{ext}/k_B for each of the galaxies G1, G2 and G3 are shown in Figure A.3.

Table 4.2 Grid parameter values

G_0 [Habing]	0.5, 1, 4, 7, 10, 13, 16, 19, 23, 27
$\log(m_{\text{GMC}} [\text{M}_\odot])$	4.0, 4.25, 4.5, 4.75, 5.0, 5.25, 5.5, 5.75, 6.0
$\log(Z/Z_\odot)$	-1, -0.5, 0, 0.5, 1, 1.4, 1.8
$\log(P_{\text{ext}}/k_B [\text{K cm}^{-3}])$	4.0, 5.5, 6.5

There are more than 100,000 GMCs in a single model galaxy and, as Figure A.3 shows, they span a wide range in G_0 , m_{GMC} , Z' and P_{ext}/k_B . Thus, in order to shorten the computing time, we calculated n_{H_2} and T_k profiles for a set of 630 GMCs, chosen to appropriately sample the distributions in G_0 , m_{GMC} and Z' at certain grid values (listed in Table 4.2, and marked by vertical black lines in Figure A.3). Our default for P_{ext}/k_B will be a MW-like value of 10^4 K cm^{-3} , but we also constructed the above grid for $P_{\text{ext}}/k_B = 10^{5.5} \text{ K cm}^{-3}$ and $10^{6.5} \text{ K cm}^{-3}$. In addition we test the two radial GMC density profiles defined in Section 4.3.4. $T_k - n_{\text{H}_2}$ curves were calculated for each possible combination of the parameter grid values listed in Table 4.2 giving us a total of $3 \times 2 \times 630 = 3780$ GMC grid models. Every GMC in our simulations was subsequently assigned the $T_k - n_{\text{H}_2}$ curve of the GMC grid model closest to it in our $(G_0, m_{\text{GMC}}, Z')$ parameter space.

4.3.5 RADIATIVE TRANSFER OF CO LINES

SÍGAME assumes the density of CO follows that of the H₂ gas with a fixed CO abundance equal to the Galactic value of $[\text{CO}/\text{H}_2] = 2 \times 10^{-4}$ (Lee et al., 1996; Sofia et al., 2004, and see Section 4.6 for a justification of this value) everywhere in the GMCs except for $n_{\text{H}_2} < 50 \text{ cm}^{-3}$, where CO is no expected to survive photo-dissociation processes (e.g. Narayanan et al., 2008a). This was chosen for simplicity as a cut in A_v would be more physical, but we have left this exercise for a future study. Now we are ready to solve the radiative transfer for each GMC individually and derive the emerging CO line emission from the entire galaxy.

Individual GMCs

For the CO radiative transfer calculations we use a slightly modified version of the Line Modeling Engine (LIME ver. 1.4; Brinch & Hogerheijde (2010)) - a 3D molecular excitation and radiative transfer code. LIME has been modified in order to take into account the redshift dependence of the CMB temperature, which is used as boundary condition for the radiation field during photon transport, and we have also introduced a redshift correction in the calculation of physical sizes as a function of distance. We use collision rates for CO (assuming H₂ as the main collision partner) from Yang et al. (2010). In LIME, photons are propagated along grid lines defined by Delaunay triangulation around a set of appropriately chosen sample points in the gas, each of which contain information on n_{H_2} , T_k , σ_v , $[\text{CO}/\text{H}_2]$ and \bar{v} . SÍGAME constructs such a set of sample points throughout each GMC: about 5000 points distributed randomly out to a radius of 40 pc, i.e., beyond the effective radius of all GMCs in G1, G2, and G3 (Figure 4.6) and in a density regime below the threshold density of 50 cm^{-3} adopted for CO survival (see previous paragraph). The concentration of sample points is set to increase towards the centre of each GMC where the density and temperature vary more drastically.

For each GMC, `LIME` generates a CO line data cube, i.e., a series of CO intensity maps as a function of velocity. The velocity-axis consists of 50 channels, each with a spectral resolution of 1.0 km s^{-1} , thus covering the velocity range $v = [-25, +25] \text{ km s}^{-1}$. The maps are 100 pc on a side and split into 200 pixels, corresponding to a linear resolution of 0.5 pc/pixel (or an angular resolution of $5.9 \times 10^{-5}''/\text{pixel}$ at $z = 2$). Intensities are corrected for arrival time delay and redshifting of photons.

Figure A.5 shows the area- and velocity-integrated CO Spectral Line Energy Distributions (SLEDs) for the same 80 GMCs used in Section 4.3.4 to highlight the $T_{\text{k}} - n_{\text{H}_2}$ profiles (Figure A.4). The first thing to note is that the CO line fluxes increase with m_{GMC} , which is due to the increase in size, i.e., surface area of the emitting gas, with cloud mass (Section 4.3.4). Turning to the shape of the CO SLEDs, a stronger G_0 (and ζ_{CR}) increases the gas temperature and thus drives the SLEDs to peak at higher J -transitions. Only the higher, $J_{\text{up}} > 4$, transitions are also affected by metallicity, displaying increased flux with increased Z' for $Z' \gtrsim 1$ and $G_0 \gtrsim 1$. For GMCs with high G_0 , the high metallicity levels thus cause the CO SLED to peak at $J_{\text{up}} > 8$.

The effects of dust

Dust absorbs the UV light from young O and B stars and re-emits in the far-IR, leading to possible ‘IR pumping’ of molecular infrared sources. However, due to the large vibrational level spacing of CO, the molecular gas has to be at a temperature of at least 159 K, for significant IR pumping of the CO rotational lines to take place, when assuming a maximum filling factor of 1, as shown by Carroll & Goldsmith (1981). Most of the gas in our GMC models is at temperatures below 100 K, with only a small fraction of the gas, in the very outskirts, of the GMCs reach $T_{\text{k}} > 159$ K, as seen in Figure A.4 in Appendix A.3. This happens only if the metallicity is low ($Z' \leq 0.1$) or in case of a combination between high FUV field ($G_0 \geq 4$) and moderate metallicity. On the other hand, the CO emission lines could be subject to dust extinction, which is however only important in extremely dust-enshrouded sources such as Arp 220 (Papadopoulos et al., 2010), and therefore not significant for our set of normal galaxies.

Upon these reflections, we have chosen not to include dust in the radiative transfer calculations of each GMC, although we mention that `LIME` is fully capable of including a dust component, provided that a table of dust opacities as function of wavelength be supplied together with the input model.

4.3.6 COMBINING THE GMC LINE PROFILES IN A GALAXY

The CO emission line profile is derived for each galaxy GMC by assigning to it the GMC model that corresponds to the nearest grid point (in log space for m_{GMC} and Z'). The total line profiles of the galaxies are derived by adding the line profiles of individual GMCs to a common velocity axis at their respective projected velocities within each galaxy. This assumes that the molecular line emission from each GMC is radiatively decoupled from all other GMCs, which is a reasonable assumption due to the large velocity gradients through the galaxies (σ_v of $\sim 200 - 500 \text{ km s}^{-1}$ in our model galaxies) and the relatively small internal turbulent line widths expected for the GMC (typically $\sim 1 - 3 \text{ km s}^{-1}$ for Galactic GMCs; Heyer et al., 2009).

CO moment 0 maps are constructed by overlaying a grid of 500×500 pixels on each galaxy and adding the area-integrated CO line profiles from all GMCs within each pixel to a common velocity axis and integrating this line profile in velocity. This way, we create maps with a fixed width of 20 kpc and a resolution of ~ 80 pc. By integrating in area instead of velocity, we create

total line profiles, and by further integrating these line profiles in velocity space, the CO SLED for the entire galaxy can be derived. All this will be examined in the following section and the results discussed further in Section 4.6.

4.4 SIMULATING MASSIVE $z = 2$ MAIN SEQUENCE GALAXIES

In this section we examine the H₂ surface density and CO emission maps resulting from applying SÍGAME to the three SPH galaxy simulations G1, G2, and G3 (Section 4.2), and we compare with existing CO observations of main sequence galaxies at $z \sim 1 - 2.5$. As mentioned in previous sections, our default grid will be that corresponding to a Plummer density profile and a pressure of $P_{\text{ext}}/k_{\text{B}} = 10^4 \text{ cm}^{-3} \text{ K}$, combined with a GMC mass spectrum of slope $\beta = 1.8$, unless otherwise stated.

4.4.1 TOTAL MOLECULAR GAS CONTENT AND H₂ SURFACE DENSITY MAPS

The total molecular gas masses of G1, G2 and G3 – obtained by summing up the GMC masses associated with all SPH particles within each galaxy (i.e., $M_{\text{mol}} = \sum m_{\text{GMC}} = \sum f'_{\text{mol}} m_{\text{SPH}}$) – are 7.1×10^9 , 1.7×10^{10} , and $2.1 \times 10^{10} M_{\odot}$, respectively, corresponding to about 34, 59 and 45 % of the original total SPH gas masses of the galaxies within $R_{\text{cut}} = 20 \text{ kpc}$.⁴ The global molecular gas mass fractions (i.e., $f_{\text{mol}} = M_{\text{mol}}/(M_{*} + M_{\text{mol}})$) are 11.8, 9.8 and 9.1 % for G1, G2, and G3, respectively.

For the high-redshift samples we use for comparison in Figure 4.10, f_{mol} assumes mean values of; $59 \pm 23\%$ for the $z \sim 1 - 1.3$ SFGs of Magnelli et al. (2012), $57 \pm 6\%$ for the $z \sim 1.5$ BzKs of Daddi et al. (2010), $48 \pm 14\%$ for the $z \sim 1 - 2.2$ SFGs of Tacconi et al. (2013) and $52 \pm 20\%$ for the $z \sim 2 - 2.5$ BX/BM galaxies of Tacconi et al. (2013). The mean for all these galaxies is $\sim 47\%$ or $\sim 4 - 5$ times above that of our galaxies. In comparison, local star-forming galaxies are relatively gas-poor as shown by Saintonge et al. (2011), who estimated molecular masses for a sample of nearby star-forming galaxies by applying a MW-like α_{CO} factor to 119 detections in CO(1–0) and to a stack of 103 non-detections. Correcting their molecular masses for the contribution from helium (1.36), the mean f_{mol} is only $\sim 6.7 \pm 4.5\%$. While our model galaxies have molecular gas mass fractions about a factor 4–5 below $z \sim 1 - 2.5$ star-forming galaxies, they are within the observed range for the local counterparts. The main cause for this discrepancy between our model galaxies and observations made at $z \sim 2$, is most likely the relatively low SPH gas mass fractions to begin with, i.e. $f_{\text{SPH}} = M_{\text{SPH}}/(M_{*} + M_{\text{SPH}}) = 9 - 26\%$, restricting f_{mol} to be below these values.

The molecular surface density (Σ_{mol}) maps of G1, G2, and G3, depicting the average Σ_{mol} within pixels $80 \text{ pc} \times 80 \text{ pc}$ in size, are shown in Figure 4.8 (top panels). The pixel size was chosen in order to avoid resolving the GMCs, which have typical sizes of $R_{\text{eff}} \approx 0.7 - 30 \text{ pc}$ (see Section 4.3.4).

Some molecular gas is seen to extend out to radii of $\sim 10 \text{ kpc}$ and beyond, but generally the molecular gas concentrates within the inner regions of each galaxy. Thus, the distribution of molecular gas broadly follows the central disk and spiral arms where the SPH surface density (Σ_{SPH}) is also the highest (Figure 4.1). The correspondence is far from one-to-one, however, as

⁴These global molecular-to-SPH gas mass fractions are calculated as $M_{\text{mol}}/M_{\text{SPH}} = \sum m_{\text{GMC}} / \sum m_{\text{SPH}}$, where the sums are over all SPH particles.

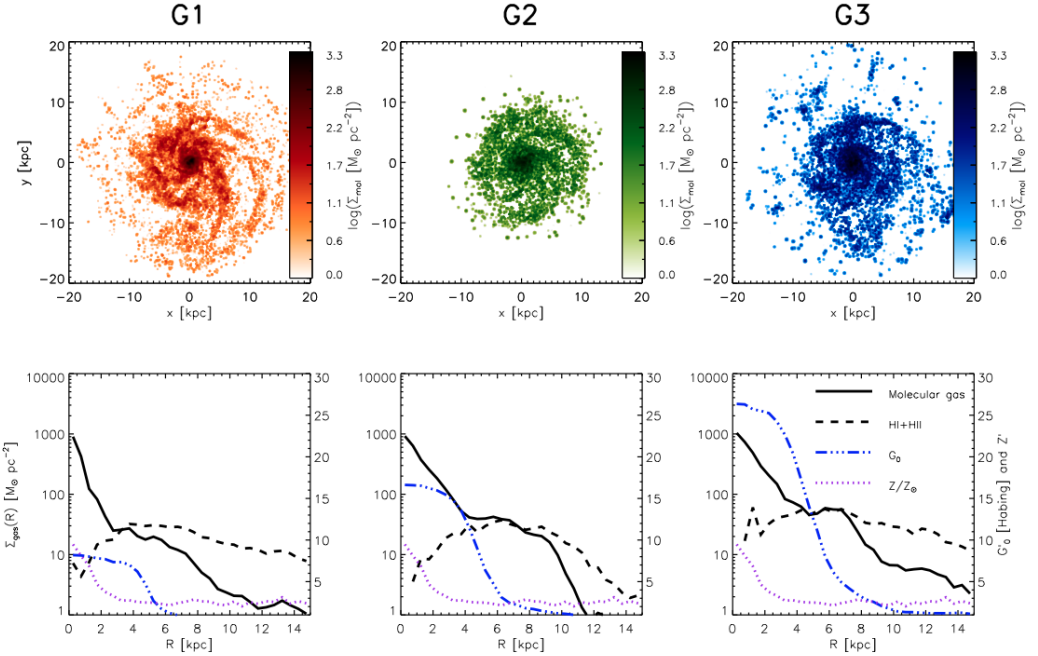


Figure 4.8 Top row: Molecular surface density maps of our model galaxies seen face-on. The maps have been smoothed using a circular Gaussian with full width at half maximum (FWHM) of 3 pixels corresponding to 0.24 kpc. Comparing to the SPH gas density maps in Figure 4.1 the molecular gas surface density maps are seen to trace the same spiral arms and inner disk as well as a few dense clumps further out. Bottom row: azimuthally averaged radial profiles of the HI +HII (dashed curve) and molecular (solid curve) gas surface densities, of the mean metallicity (dotted curve) and of G_0 (dot-dashed curve) – determined from 50 radial bins stretching from 0 to 15 kpc from the centre of each galaxy. The molecular gas is the result of applying the recipes in Section 4.3.3 to the SPH simulations presented in Section 4.2.2, while the HI +HII gas is the initial SPH gas mass minus the derived molecular gas mass, including a contribution from heavier elements. We estimate G_0 by averaging over the FUV fields impinging on all GMCs in each radial bin.

seen by the much larger extent of the SPH gas, i.e., regions where H_2 has not formed despite the presence of atomic and ionized gas. This point is further corroborated in the bottom panels of Figure 4.8, which show azimuthally-averaged radial surface density profiles of the molecular gas and of the HI +HII gas, both including a contribution from heavier elements. In order to compare values of Σ_{HI+HII} and Σ_{mol} with observations, we set the radial bin width to 0.5 kpc – the typical radial bin size used for nearby spirals in the work of Leroy et al. (2008)⁵. The radially binned Σ_{mol} reaches $\sim 800 - 1000 M_\odot pc^{-2}$ in the central regions of our simulated galaxies, which is comparable to observational estimates of Σ_{mol} (of several $100 M_\odot pc^{-2}$) towards the centres of nearby spirals (Leroy et al., 2008). In all three galaxies, the HI +HII surface density dips within the central $\sim 1 - 2$ kpc, coinciding with a strong peak in Σ_{mol} . Thus, despite the marked increase in the FUV radiation field towards the centre (the radial profile of G_0 is shown as dash-dotted line in Figure 4.8), the formation of H_2 driven by the increase in gas pressure is able to overcome photo-dissociative destruction of H_2 by FUV photons. The central H_2 surface densities are similar for all galaxies and is a direct consequence of very similar SPH gas surface densities in the centre combined with molecular gas mass fractions approaching

⁵The H_2 surface density maps in Fig. 4.8 are averaged over areas 80×80 pc in size, and therefore give higher peak surface densities than the radial profiles which are averaged over ~ 0.5 kpc wide annuli.

1. From $R \sim 2$ kpc and out to ~ 10 kpc, the HI +HII surface density remains roughly constant with values of ~ 40 , ~ 70 and ~ 100 M_{\odot} pc $^{-2}$ for G1, G2 and G3, respectively.

Radial profiles of the HI and molecular gas surface density that are qualitatively very similar to our simulations have been observed in several nearby star-forming disk galaxies (e.g., Leroy et al., 2008; Bigiel et al., 2008). In local galaxies, however, the HI surface density, including helium, rarely exceeds ~ 10 M_{\odot} pc $^{-2}$, while in our simulations we find HI +HII surface densities that are $4 - 10 \times$ higher, indicating that there is a substantial fraction of ionised gas in our model galaxies.

4.4.2 CO LINE EMISSION MAPS AND RESOLVED EXCITATION CONDITIONS

Moment zero maps of the CO(1–0), CO(3–2) and CO(7–6) emission from G1, G2 and G3 are shown in Figure 4.9. Comparing with the H₂ surface density maps in Figure 4.8, both the CO(1–0) and CO(3–2) emission are seen to trace the H₂ gas distribution well, while the CO(7–6) emission is restricted to the central ~ 7 kpc of the galaxies.

Also shown in Figure 4.9 (bottom row) are the azimuthally averaged CO 3–2/1–0 and 7–6/1–0 brightness temperature line ratios (denoted r_{32} and r_{76} , respectively) as a function of radius for G1, G2 and G3. The profiles show that the gas is clearly more excited in the central ~ 5 kpc, where typical values of r_{32} and r_{76} are $\sim 0.55 - 0.65$ and $\sim 0.02 - 0.08$, respectively, compared to $r_{32} \sim 0.5$ and $r_{76} < 0.01$ further out in the disk. This radial behaviour of the line ratios does not reflect the H₂ gas surface density, which peaks towards the centre rather than flattens, and gradually trails off out to $R \sim 12$ kpc instead of dropping sharply at $R \sim 4 - 6$ kpc (Figure 4.9). Rather, r_{32} and r_{76} seem to follow closely the behaviour of G_0 (and thus ζ_{CR}), which makes sense since G_0 and ζ_{CR} are the most important factors for the internal GMC temperature distribution (Figure A.4). The central values for r_{32} and r_{76} increase when going from G1 to G3, as expected from the elevated levels of star formation density (and of G_0 and ζ_{CR} , accordingly) towards the centre. Beyond ~ 6 kpc the line ratios are constant (~ 0.5 and < 0.01) and the same for all three galaxies, due to relatively similar FUV fields here.

At high- z , resolved observations of single CO lines are starting to appear (e.g. Genzel et al., 2013; Hodge et al., 2014), but since resolved excitation studies using multiple lines have so far not been obtained, we instead compare our results to local quiescent and extreme galaxies. The increase in r_{32} towards the centres, are in agreement with observations of nearby galaxies as those carried out by Dumke (2000). Geach & Papadopoulos (2012) modeled two extreme cases of gas conditions, and found that while r_{32} might only be ~ 0.13 in quiescent environments, it is typically ~ 0.88 in denser gas. Mao et al. (2010) observed 125 nearby galaxies of different types and found r_{32} to be 0.61 ± 0.16 in normal galaxies, but > 0.89 in starbursts and (U)LIRGs. Iono et al. (2009) and Papadopoulos et al. (2012) finds slightly lower r_{32} in their samples of (U)LIRGs, with mean values of 0.48 ± 0.26 and 0.67 ± 0.62 respectively. In light of these observations, the r_{32} radial profiles of our model galaxies, suggest a denser, ULIRG-like environment in the central ($R < 5$ kpc) region together with a more quiescent and diffuse gas phase further out in the disk of $z = 2$ normal star-forming galaxies.

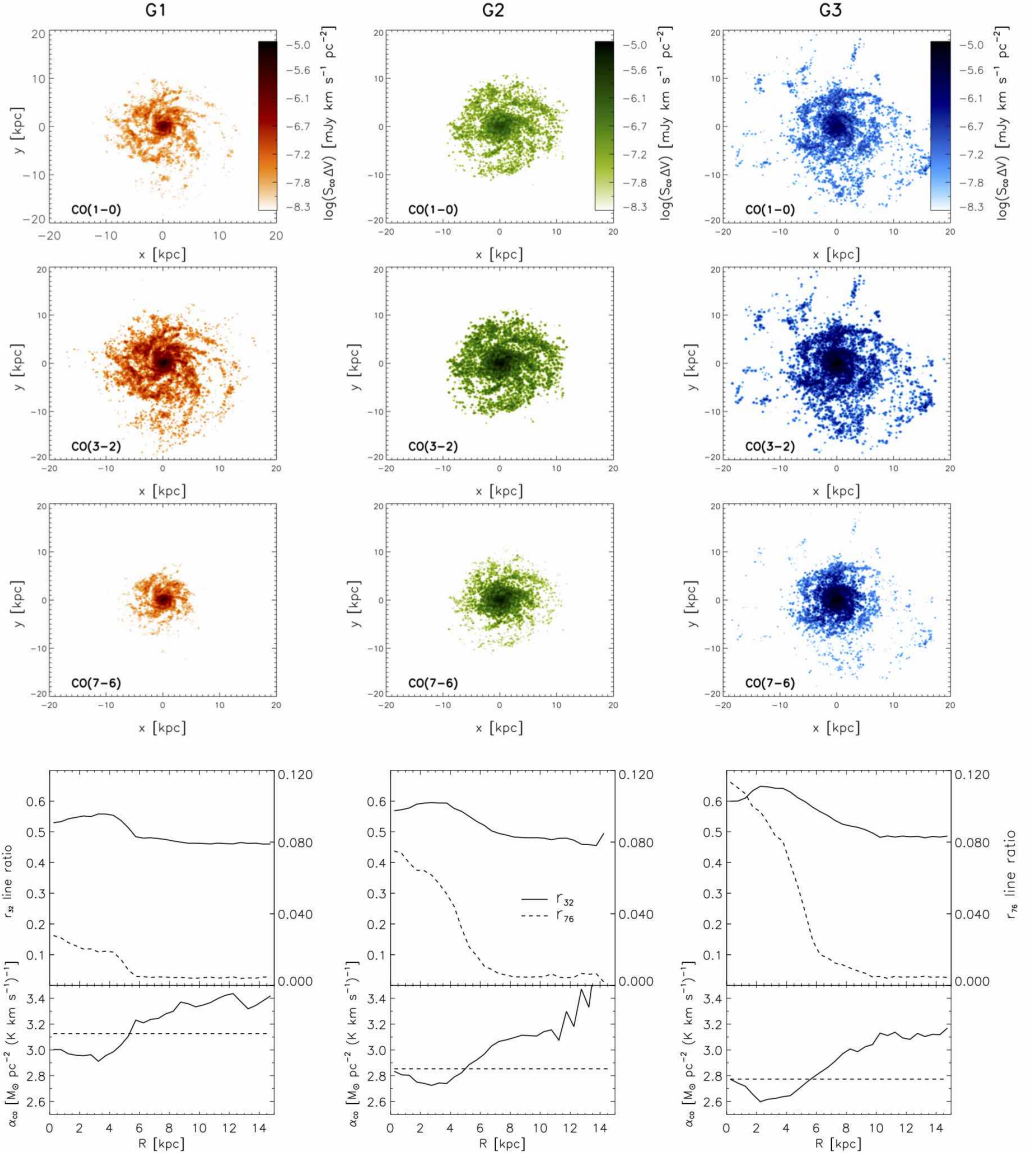


Figure 4.9 The top three rows show the moment zero maps of the CO(1–0), CO(3–2) and CO(7–6) emission from G1, G2 and G3. The CO maps have been smoothed using a circular Gaussian with full width at half maximum (FWHM) of 3 pixels corresponding to 0.24 kpc, and as with the SPH and molecular gas surface density maps, a logarithmic scale has been applied in order to better display extended emission. The bottom row shows the azimuthally averaged CO 3–2/1–0 and 7–6/1–0 brightness temperature line ratios (denoted r_{32} and r_{76} , respectively) as functions of projected radius for each of the three galaxies. A radial bin-size of 0.5 kpc was used. Also shown are the azimuthally averaged radial profiles of CO-to-H₂ conversion factor $\alpha_{\text{CO}}(R) = \Sigma_{\text{H}_2}/I_{\text{CO}(1-0)}$ in units of $M_{\odot} \text{ pc}^{-2} (\text{K km s}^{-1})^{-1}$ with a dashed line indicating the global α_{CO} factor.

4.4.3 THE CO-TO-H₂ CONVERSION FACTOR

The CO-to-H₂ conversion factor (α_{CO}) connects CO(1–0) line luminosity (in surface brightness temperature units) with the molecular gas mass (M_{mol}) as follows:

$$\alpha_{\text{CO}} = \frac{M_{\text{mol}}}{L'_{\text{CO}(1-0)}}, \quad (4.16)$$

From the CO(1 – 0) surface brightness and H₂ surface density maps of our model galaxies, we calculate α_{CO} in radial bins surrounding the galaxy centres (Figure 4.9). The resulting radial α_{CO} factors for our model galaxies lie in the range of $\sim 3 - 4 M_{\odot} \text{ pc}^{-2} (\text{K km s}^{-1})^{-1}$, and show a clear transition from lower α_{CO} -values inside the central $R \sim 5 \text{ kpc}$ to higher values at $R \gtrsim 6 \text{ kpc}$. The drop in α_{CO} from the disk average to the central value is about a factor $\sim 1.6 - 1.7$, similar to the drop in observed α_{CO} profiles. Recently, Blanc et al. (2013) measured a drop in α_{CO} by a factor of two when going from $R \sim 7 \text{ kpc}$ to the centre of the Sc galaxy NGC 628, by using a constant gas depletion timescale in order to convert SFR surface densities into gas masses. Similarly, Sandstrom et al. (2013) found a drop by a factor of on average ~ 2 from α_{CO} averaged across the galaxy disks to α_{CO} of the central $R \leq 1 \text{ kpc}$ in 26 nearby spiral galaxies, by converting inferred dust masses into gas masses.

One could expect α_{CO} to be correlated with Z' , as higher metallicity means higher C and O abundances as well as more dust that help shielding H₂ formation sites from FUV radiation, and thereby increase the amount of CO, possibly lowering α_{CO} . On the other hand, although a higher FUV field leads to more ionization and photo-dissociation, it also increases the gas temperatures, which translates into more excited CO molecules and again a lower α_{CO} factor. Comparison of the α_{CO} radial profiles with those of G_0 and Z' in the bottom panel of Figure 4.8, suggests that the transition in α_{CO} is caused by a change in G_0 rather than a change in Z' , since α_{CO} and G_0 generally start to drop at around $R \sim 6 \text{ kpc}$ while Z' already drops drastically at 1 kpc from the centre. Our modeling therefore implies that α_{CO} is controlled by G_0 rather than Z' in normal star-forming galaxies at $z \sim 2$, in agreement with the observations by Sandstrom et al. (2013) who do not find a strong correlation with Z' .

From the total molecular gas masses and CO(1 – 0) luminosities of our galaxies, we derive their global α_{CO} factors. This gives global values of $\alpha_{\text{CO}} = 1.6, 1.5$ and $1.4 M_{\odot} \text{ pc}^{-2} (\text{K km s}^{-1})^{-1}$ for G1, G2 and G3, respectively (In Section 4.5 we investigate the effect on α_{CO} of different prescriptions for the GMC modeling, but for now stick to the default choices as specified above). These values are lower (by a factor ~ 3) than the global MW value of $\alpha_{\text{CO,MW}} \simeq 4.4 \pm 0.9 M_{\odot} \text{ pc}^{-2} (\text{K km s}^{-1})^{-1}$, calibrated from dynamical, dust, and γ -ray studies (e.g., Strong & Mattox, 1996; Dame et al., 2001; Pineda et al., 2008), but closer to the typical mergers/starburst α_{CO} -values ($\sim 0.2 \times \alpha_{\text{CO,MW}}$) inferred from CO dynamical studies of local ULIRGs (e.g., Solomon et al., 1997; Downes & Solomon, 1998; Bryant & Scoville, 1999) and $z \sim 2$ SMGs (e.g., Tacconi et al., 2008). Our α_{CO} -values are also below those inferred from dynamical modeling of $z \sim 1.5$ BzKs ($\alpha_{\text{CO}} = 3.6 \pm 0.8 M_{\odot} \text{ pc}^{-2} (\text{K km s}^{-1})^{-1}$; Daddi et al., 2010).

On the other hand, the α_{CO} factors of the $z \sim 1 - 1.3$ star-forming galaxies studied by Magnelli et al. (2012) occupy the same region of the M_{*} –SFR plane as our model galaxies, but have α_{CO} factors at least a factor ~ 6 higher. Their α_{CO} are $\sim 5 - 20 M_{\odot} \text{ pc}^{-2} (\text{K km s}^{-1})^{-1}$ when converting dust masses to gas masses using a metallicity-dependent gas-to-dust ratio, and Magnelli et al. (2012) further find that the same galaxies have relatively low dust temperatures of $\lesssim 28 \text{ K}$ compared to the galaxies further above the main sequence of Rodighiero et al.

(2010). The fact that the main-sequence galaxies of Magnelli et al. (2012) are all of near-solar metallicity as ours, cf. Table 4.1, suggests that other factors, such as dust temperature caused by strong FUV radiation, can be more important than metallicity in regulating α_{CO} , in line with our study of the α_{CO} radial profiles.

4.4.4 GLOBAL CO LINE LUMINOSITIES AND SPECTRAL LINE ENERGY DISTRIBUTIONS

The global CO SLEDs of G1, G2 and G3 are shown in Figure 4.10 in three different incarnations: 1) total CO line luminosities ($L'_{\text{CO}_{J,J-1}}$), 2) brightness temperature ratios ($T_{\text{B},\text{CO}_{J,J-1}}/T_{\text{B},\text{CO}_{1,0}} = L'_{\text{CO}_{J,J-1}}/L'_{\text{CO}_{1,0}}$) and 3) line intensity ratios⁶. In Figure 4.10 we have also compiled all relevant CO observations of normal star-forming galaxies at $z \sim 1 - 3$ to date in order to facilitate a comparison with our simulated CO SLEDs of such galaxies. Samples are the same as in Figure 4.2, but including an additional 7 star-forming galaxies (SFGs) at $z \sim 1.2$ (Magnelli et al., 2012) and another 39 SFGs at $z \sim 1 - 1.5$ (Tacconi et al., 2013). The first sample of galaxies are all detected in CO(2–1) as well as in *Herschel*/PACS bands, and have $\log M_* = 10.36 - 11.31$ and $\text{SFR} \sim 29 - 74 \text{ M}_\odot \text{ yr}^{-1}$. The sample from Tacconi et al. (2013) comes from the Extended Growth Strip International Survey (EGS), is covered by the CANDELS and 3D-HST programs ($J - H$ bands and $\text{H}\alpha$ respectively), and has $\log M_* = 10.40 - 11.23$ and $\text{SFR} \sim 28 - 630 \text{ M}_\odot \text{ yr}^{-1}$.

First, we compare the total CO(3–2) luminosities of our model galaxies with those of the $z \sim 2 - 2.5$ BX/BM galaxies of Tacconi et al. (2013), which are not only closest in redshift to our model galaxies but also occupy the same region of the $\text{SFR}-M_*$ plane (see Figure 4.2). We find that G2 and G3, the two most massive ($M_* > 10^{11} \text{ M}_\odot$) and star-forming ($\text{SFR} \gtrsim 80 \text{ M}_\odot \text{ yr}^{-1}$) galaxies of our simulations, have CO(3–2) luminosities of $\sim 0.7 - 1 \times 10^{10} \text{ K km s}^{-1} \text{ pc}^2$, which is in the range of CO(3–2) luminosities of the BX/BM galaxies at an average of $\sim 1.2 \pm 0.9 \times 10^{10} \text{ K km s}^{-1} \text{ pc}^2$. The more quiescent G1 is about a factor 4 below the average $L'_{\text{CO}(3-2)}$ of BX/BM galaxies, and the offset from the BzK galaxies is even bigger. Our G2 and G3 simulations, however, are able to reproduce the CO luminosities of the $z \simeq 1 - 1.5$ SFGs observed by Magnelli et al. (2012) and Tacconi et al. (2013), which span a range in CO(2–1) and CO(3–2) luminosities of $(3.6 - 12.5) \times 10^9$ and $(1.4 - 41.3) \times 10^9 \text{ K km s}^{-1} \text{ pc}^2$, respectively. In general, the BzK galaxies are more luminous than our model galaxies, with the exception of BzK-16000 at a $\text{SFR} = 152 \text{ M}_\odot \text{ yr}^{-1}$ only slightly above our G2 model galaxy ($142 \text{ M}_\odot \text{ yr}^{-1}$). As mentioned in Section 4.4.1, the molecular gas mass fractions of our galaxies is about a factor 6 below the mean of the observed galaxies at $z \sim 1 - 2.5$ with which we compare, and we propose this as the main reason for the comparatively low CO luminosities.

Differences in the global CO excitation conditions between G1, G2 and G3 are best seen in the CO(1–0) normalized luminosity (and intensity) ratios, i.e., middle (and bottom) panel in Figure 4.10). The CO SLEDs of all three galaxies follow each other quite closely up to the $J = 3 - 2$ transition where the SLEDs all peak; at $3 < J_{\text{up}} < 7$ the SLEDs gradually diverge. While the metallicity distributions in G1, G2 and G3 are similar (see Figure A.3), the rise in G_0 presents a likely cause to the increasing high- J flux when going from G1 to G3, as higher G_0 leads to more flux primarily in the $J > 4$ transitions (see Figure A.5).

Our simulated galaxies are seen to have CO 2–1/1–0, 3–2/1–0, and 5–4/1–0 brightness temperature ratios of $r_{21} \simeq 1$, $r_{32} \simeq 0.55$, and $r_{54} \simeq 0.15$, respectively. The first two ratios

⁶ $I_{\text{CO}_{J,J-1}}/I_{\text{CO}_{1,0}} = L'_{\text{CO}_{J,J-1}}/L'_{\text{CO}_{1,0}} \times \left(\nu_{\text{CO}_{J,J-1}}/\nu_{\text{CO}_{1,0}}\right)^2$

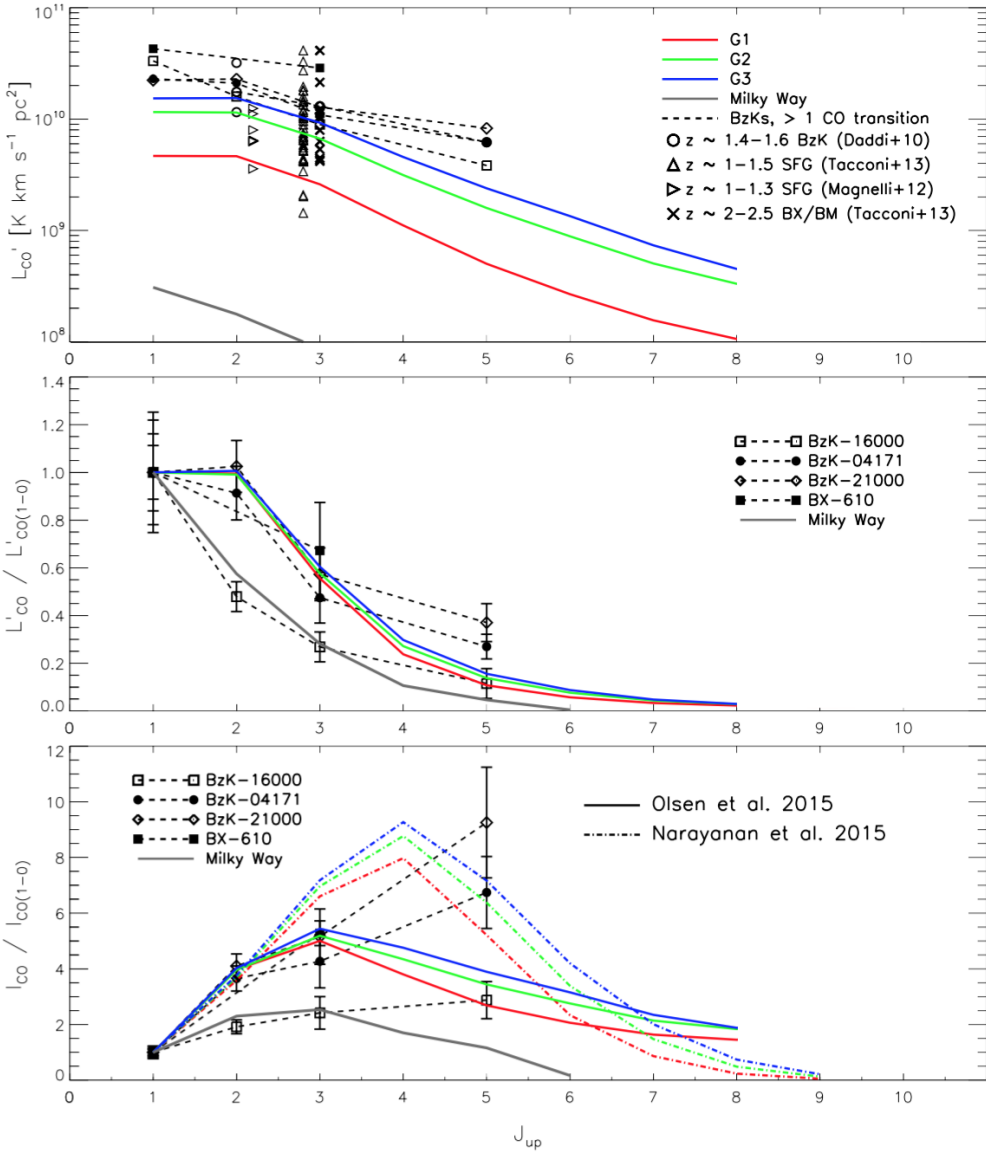


Figure 4.10 Global CO SLEDs of our three model galaxies G1, G2 and G3 shown as red, green and blue solid curves, respectively. The SLEDs are given as absolute line luminosities in units of $\text{K km s}^{-1} \text{ pc}^{-2}$ (top panel), as brightness temperature ratios normalized to the $\text{CO}(1-0)$ transition (middle panel), and as velocity-integrated intensity ratios normalized to $\text{CO}(1-0)$ (bottom panel). The model CO SLEDs are compared with observations of $z \sim 1.4 - 1.6$ BzK galaxies ($\text{CO}(1-0)$ and $\text{CO}(2-1)$; Dannerbauer et al., 2009; Daddi et al., 2010, 2014; Aravena et al., 2010, 2014), $z \sim 1 - 1.5$ star-forming galaxies ($\text{CO}(3-2)$; empty triangles; Tacconi et al., 2013), $z \sim 1 - 1.3$ star-forming galaxies ($\text{CO}(1-0)$ and $\text{CO}(2-1)$; rightfacing triangles; Magnelli et al., 2012), and $z \sim 2 - 2.5$ BX/BM galaxies ($\text{CO}(3-2)$; crosses; Tacconi et al., 2013). Also shown is the global CO SLED of the MW (grey line; Fixsen et al., 1999). Three BzK galaxies (BzK-16000, BzK-4171, and BzK-21000) have been observed in $\text{CO}(1 - 0)$ and at least one additional transition to date, and are highlighted by connecting dashed lines. Also shown in the bottom panel, with dash-dotted lines, are the line ratio predictions of Narayanan & Krumholz (2014) (D14), calculated for the Σ_{SFR} of our galaxies (see text).

compare extremely well with the line ratios measured for BzK-4171 and BzK-21000, i.e., $r_{21} \simeq 0.9 - 1$, and $r_{32} \simeq 0.5 - 0.6$ (Dannerbauer et al., 2009; Aravena et al., 2010; Daddi et al., 2010, 2014), and suggest that our simulations are able to emulate the typical gas excitation conditions

responsible for the excitation of the low- J lines in normal $z \sim 1 - 3$ SFGs. In contrast, $r_{54} = 0.3 - 0.4$ observed in BzK–4171 and BzK–21000 (Daddi et al., 2014), is nearly $2\times$ higher than our model predictions. Daddi et al. (2014) argue that this is evidence for a component of denser and possibly warmer molecular gas, not probed by the low- J lines. In this picture, we would expect CO(4–3) to probe both the cold, low-excitation gas as well as the dense and possibly warm star-forming gas traced by the CO(5–4) line; and we would expect CO(6–5) to be arising purely from this more highly excited phase and thus departing even further from our models.

However, significant scatter in the CO line ratios of main-sequence galaxies is to be expected, as demonstrated by the significantly lower line ratios observed towards BzK–16000: $r_{21} \simeq 0.4$, $r_{32} \simeq 0.3$, and $r_{54} \simeq 0.1$ (Aravena et al., 2010; Daddi et al., 2010, 2014) and, in fact, the average r_{54} for all three BzK galaxies above ($\simeq 0.2$; Daddi et al. (2014)) is consistent with our models. It may be that G2 and G3, and perhaps even G1, are more consistent with the CO SLEDs of the bulk $z \sim 1 - 3$ main-sequence galaxies. We stress, that to date, no $z \sim 1 - 3$ main sequence galaxies have been observed in the $J = 4 - 3$ nor the $6 - 5$ transitions, and observations of these lines, along with low- and high- J lines in many more BzK and main-sequence $z \sim 1 - 3$ galaxies are needed in order to fully delineate the global CO SLEDs in a statistically robust way.

4.5 TESTING DIFFERENT ISM MODELS

In this section we investigate the effects on our simulation results when adopting i) a shallower GMC mass spectrum slope of $\beta = 1.5$, ii) a steeper GMC density profile, i.e., a Plummer profile exponent of $-7/2$, and iii) GMC model grid that includes a the external cloud pressure, P_{ext} , as a fourth parameter. In order to carry out option iii), the GMC model grid was produced for pressures of $P_{\text{ext}}/k_{\text{B}} = 10^4 \text{ cm}^{-3} \text{ K}$ (default), $10^{5.5} \text{ cm}^{-3} \text{ K}$ and $10^{6.5} \text{ cm}^{-3} \text{ K}$, allowing for a look-up table of CO SLEDs in $(G_0, m_{\text{GMC}}, Z', P_{\text{ext}})$ parameter space. We examine the effects that options i)-iii) have on the global CO SLED of galaxy G2 (Figure 4.11) and how combinations of option i) and ii) change the values of the global CO-to-H₂ conversion factor (Table 4.3). Also, we show the impact changes ii) and iii) have on the CO SLEDs of the individual GMC grid models in Figures A.6 and A.7.

Changing the GMC mass spectrum from $\beta = 1.8$ to 1.5 leaves the CO SLED virtually unchanged (dotted and dot-dashed curves in the top panel of Figure 4.11) with only a marginal increase in the line ratio for $J_{\text{up}} \geq 4$.

Adopting the modified Plummer density profile with a power-law exponent of $-7/2$ instead of $-5/2$ leads to significantly higher line intensity ratios (i.e., $I_{\text{CO}}/I_{\text{CO}(1-0)}$) for $J_{\text{up}} \geq 3$ (see dotted vs. dashed curve and dot-dashed vs. solid curves in top panel of Figure 4.11.) This increase in line intensity comes from an increase in central densities, as shown in Fig. 4.7, leading to the excitation of higher J lines.

Including external pressures of $P_{\text{ext}}/k_{\text{B}} = 10^{5.5} \text{ cm}^{-3} \text{ K}$ and $10^{6.5} \text{ cm}^{-3} \text{ K}$ to the GMC model grid, leads to more compact GMCs with decreased velocity dispersions (see eqs. 4.9 and 4.10), both of which act to suppress the CO luminosity at high transitions via increased optical depths. The effect of employing these high pressure grids on the global CO SLED, is depicted in the bottom panel of Figure 4.11. The most noticeable change in the global CO SLEDs is a steeper decline at high ($J_{\text{up}} \geq 4$) transitions.

In Table 4.3 we compare the global α_{CO} factors pertaining to different choices for the GMC mass spectrum and density profile. As evident from Fig. A.5, higher GMC mass leads to an

Table 4.3 The average of the global H₂-to-CO conversion factors (in units of M_⊙/(K km s⁻¹ pc²)) for G1, G2, and G3, for different ISM models. The pressure has been kept fixed at $P_{\text{ext}}/k_{\text{B}} = 10^4 \text{ cm}^{-3} \text{ K}$.

	$\beta = 1.8 \text{ (MW)}$	$\beta = 1.5 \text{ (vir)}$
Plummer profile	1.51 ± 0.10	1.47 ± 0.10
Modified Plummer profile	3.62 ± 0.44	3.45 ± 0.46

increase in CO(1 – 0) luminosity for individual GMC models. Using the shallower slope of $\beta = 1.5$ for the GMC mass spectrum results in an increase in the fraction of massive GMCs at the expense of low-mass GMCs. This fractional increase in massive GMCs produces a smaller CO(1 – 0) luminosity contribution than the low-mass GMCs removed, and the net effect of adopting $\beta = 1.5$ is therefore a reduction in the global CO(1 – 0) luminosity. In terms of α_{CO} , changing β from 1.8 to 1.5 therefore leads to the slightly larger α_{CO} factors provided in Table 4.3. Similarly, despite the increasing line ratios at $J_{\text{up}} \geq 3$, a steeper GMC density profile decreases the CO(1 – 0) luminosity of our GMC models as evident in Fig. A.6, thereby increasing α_{CO} . In both cases though, α_{CO} is still kept below the standard MW-value. From the numbers in Table 4.3, α_{CO} for normal star-forming $z \sim 2$ galaxies is predicted to lie in the range $\sim 1.4 - 4.0 \text{ M}_{\odot} \text{ pc}^{-2} (\text{K km s}^{-1})^{-1}$ or $\sim 0.3 - 0.9$ times the MW value.

4.6 COMPARISON WITH OTHER MODELS

SÍGAME relies on subgrid physics to describe the molecular gas in high- z galaxies, e.g., cloud masses, their density and temperature structure etc. It is assumed that the scaling and thermal balance equations that have been established and calibrated to GMC complexes in our own Galaxy can be extrapolated to the ISM conditions in high- z galaxies. Similarly, all other numerical simulations made to date of the molecular gas in galaxies and their CO line emission rely to smaller or larger degree on subgrid physics (e.g., Narayanan et al., 2006; Pelupessy et al., 2006; Greve & Sommer-Larsen, 2008; Christensen et al., 2012; Lagos et al., 2012; Muñoz & Furlanetto, 2013; Narayanan & Krumholz, 2014; Lagos et al., 2012; Popping et al., 2014). In this section we will highlight and discuss some of the differences in the subgrid physics between SÍGAME and other simulations.

First, however, we compare the SÍGAME CO SLEDs of G1, G2, and G3 with those predicted by other CO emission simulations of similar main-sequence galaxies. A direct comparison with SÍGAME can be made in the case of the models presented by Narayanan & Krumholz (2014), where the global CO SLED is parametrised as a function of the SFR surface density (Σ_{SFR}). Using the SFR surface densities (averaged over the inner 5 kpc) of our model galaxies, the corresponding CO SLEDs inferred from the Narayanan & Krumholz (2014) parametrisation are shown as dash-dotted lines in Figure 4.10 (bottom panel). The SLEDs of Narayanan & Krumholz (2014) all peak at $J = 4 - 3$ and not $3 - 2$ as our SLEDs, and the line flux ratios are significantly higher at transitions between $J = 3 - 2$ and $6 - 5$. While a direct comparison is not possible, we note that (Lagos et al., 2012) provide CO SLED predictions for $z = 2$ main-sequence galaxies are in agreement with those of Narayanan & Krumholz (2014), when comparing galaxies of similar infrared luminosities as ours. Converting SFRs to

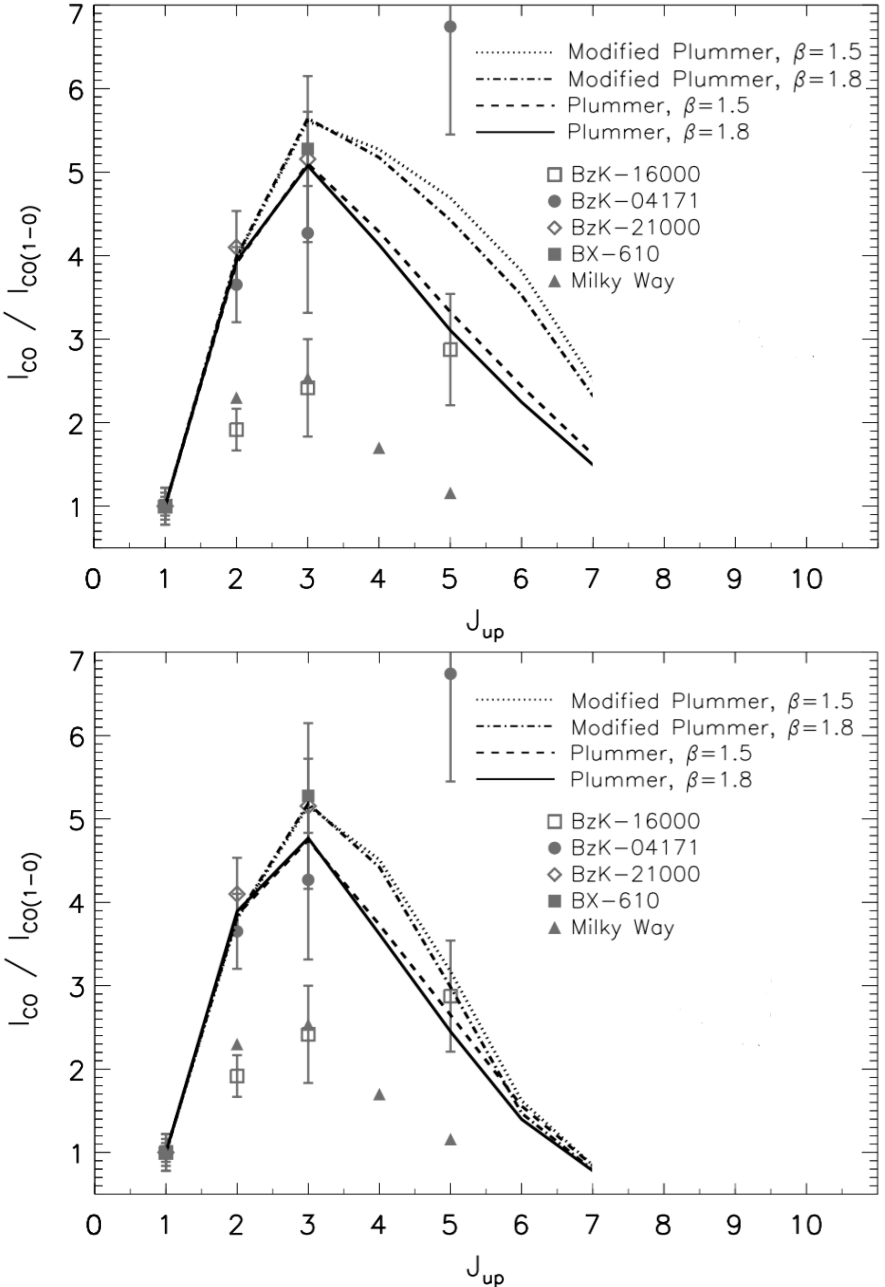


Figure 4.11 Global CO SLEDs of our model galaxy G2 for different choices of ISM prescriptions. *Top:* For a pressure fixed of $10^4 \text{ cm}^{-3} \text{ K}$. *Bottom:* Using the P_{ext} as a fourth parameter in the GMC model grid (see Section 4.3.4).

infrared luminosities with the Kennicutt (1998) conversion factor adapted to a Chabrier IMF, $L_{\text{IR}}/L_{\odot} = \text{SFR}/[\text{M}_{\odot} \text{ yr}^{-1}] \times 10^{10}$ (see Daddi et al., 2010), our simulated galaxies G1, G2 and G3 have L_{IR} of 0.40, 0.80 and $1.4 \times 10^{12} L_{\odot}$, respectively, which is in the bottom of the range typically observed for BzK galaxies (L_{IR} from 0.6 to $4.0 \times 10^{12} L_{\odot}$; Daddi et al., 2010). For galaxies with infrared luminosities $L_{\text{IR}} \sim 10^{11.25} - 10^{12} L_{\odot}$, corresponding to the range of L_{IR} in our

simulated galaxies, Lagos et al. (2012) predict CO SLEDs that peak in the CO(4 – 3) transition, that is, again implying slightly more excited gas than SÍGAME does. Popping et al. (2014) find an interesting trend with redshift in their semi-analytical study of MS galaxies at $z = 0, 1.2$ and 2 ; Galaxies with far-infrared (FIR) luminosities of $\log(L_{\text{FIR}}/L_{\odot}) = 11 - 12$ peak at CO(3 – 2) or CO(4 – 3) at $z = 0$, but at CO(6 – 5) at $z = 2$. Our galaxies lie in the same FIR luminosity range ($\log(L_{\text{FIR}}/L_{\odot}) = 11.4 - 11.9$ when converting L_{IR} to L_{FIR} by dividing by 1.7; Chapman et al., 2000), but again SÍGAME predicts less excited gas when comparing to the $z \sim 2$ MS galaxies of Popping et al. (2014).

- *Implementation of G_0 and ζ_{CR}*

SÍGAME stands out from most other simulations to date in the way the FUV radiation field and the CR flux that impinge on the molecular clouds are modelled and implemented. Most simulations adopt a fixed, galaxy-wide value of G_0 and ζ_{CR} , scaled by the total SFR or average gas surface density across the galaxy (e.g., Lagos et al., 2012; Narayanan & Krumholz, 2014). SÍGAME refines this scheme by determining a spatially varying G_0 (and ζ_{CR}) set by the local SFRD, as described in Section 4.3.3. By doing so, we ensure that the molecular gas in our simulations is calorimetrically coupled to the star formation in their vicinity. If we adopt the method of Narayanan & Krumholz (2014) and calculate a global value for G_0 by calibrating to the MW value, using $\text{SFR}_{\text{MW}} = 2 \text{ M}_{\odot} \text{ yr}^{-1}$ and $G_{0,\text{MW}} = 0.6$ Habing, our galaxies would have G_0 ranging from about 12 to 42, whereas, with the SFR surface density scaling of Lagos et al. (2012), global G_0 values would lie between about 6 and 9. For comparison, the locally determined G_0 in our model galaxies spans a larger range from 0.3 to 27 (see Figure A.3). Narayanan & Krumholz (2014) determines the global value of ζ_{CR} as $2 \times 10^{-17} \text{ Z}' \text{s}^{-1}$, corresponding to values of $3.7 - 6.2 \times 10^{-17} \text{ s}^{-1}$ in our model galaxies, when using the mass-weighted mean of Z' in each galaxy. Typical values adopted in studies of ISM conditions are around $(1 - 2) \times 10^{-17} \text{ s}^{-1}$ (Wolfire et al., 2010; Glover & Clark, 2012), but again, the local values of ζ_{CR} in our galaxies span a larger range, from 1.3×10^{-17} to $1.3 \times 10^{-15} \text{ s}^{-1}$.

- *The molecular gas mass fraction*

In SÍGAME the molecular gas mass fraction (f'_{mol}) is calculated following the work by Pelupessy et al. (2006), in which f'_{mol} depends on temperature, metallicity, local FUV field, and boundary pressure on the gas cloud in question. Other methods exist, such as those of Blitz & Rosolowsky (2006) and Krumholz et al. (2009) (K09). Most recently, Narayanan & Krumholz (2014) applied the K09 model in order to derive the H₂ gas mass, and we compare this method to that of Pelupessy et al. (2006) (P06), used by SÍGAME, in Figure 4.12. The gas surface density that enters in the K09 method was estimated within 1 kpc of each SPH particle, as used in our calculation of P_{ext} (see Section 4.3.3). Both methods produce higher f'_{mol} for increasingly more metal-rich gas, as expected since higher metallicity leads to more dust onto which the H₂ molecules can form. As shown in Fig. 4.12, the two methods agree overall albeit with increasing scatter towards lower metallicity. For high metallicity, the P06 method tends to give larger values of f'_{mol} than the K09 method. This leads to systematically lower total molecular gas masses when using the method of K09 instead of P06. In particular, the molecular gas mass fractions, $f_{\text{mol}} = M_{\text{mol}}/(M_* + M_{\text{mol}})$, of G1, G2 and G3 decrease from 8.5, 7.8 and 6.8 % to 9.8, 10.3 and 9.5 % respectively.

A common feature of the above H_I → H₂ prescriptions is that they assume an instantaneous H_I to H₂ conversion, once the conditions for H₂ formation are met. By actually incorporating their H_I → H₂ subgrid model in an N-body/SPH dwarf galaxy simulation, Pelupessy

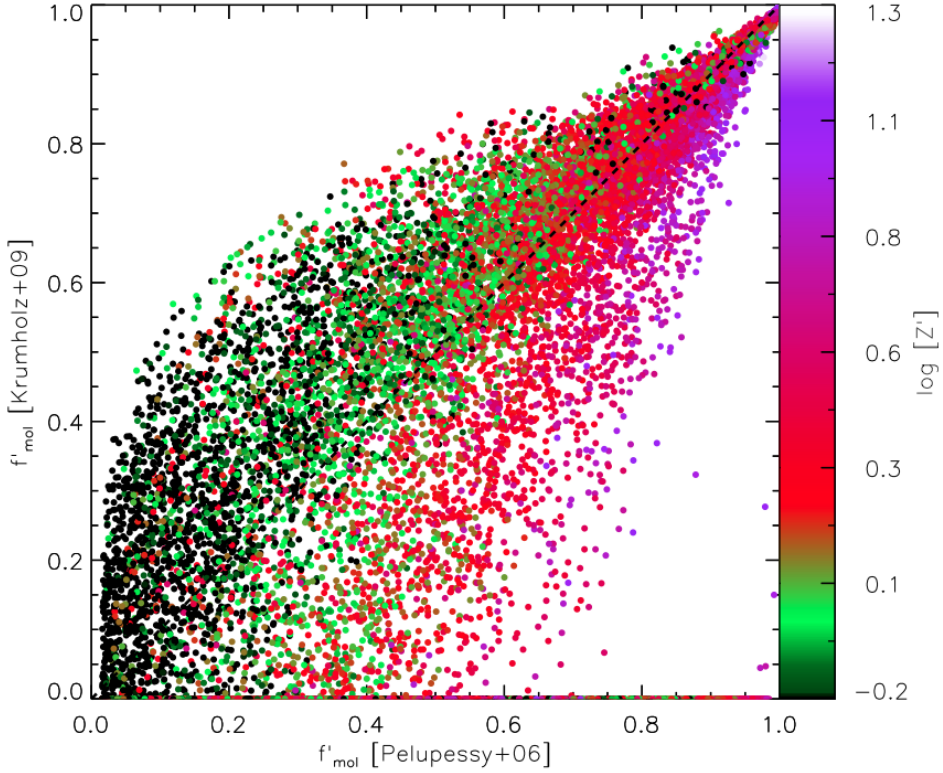


Figure 4.12 Comparison of two methods for calculating the molecular gas mass fraction, f'_{mol} , of SPH particles in G1: That of Pelupessy et al. (2006) with external cloud pressure derived from hydrostatic mid-plane equilibrium as done in this work (abscissa) and that of Krumholz et al. (2009) (ordinate) used by e.g., Narayanan & Krumholz (2014), color-coded by metallicity.

et al. (2006) find that typical timescales for H_2 cloud formation are of order $\sim 10^7$ yr. Such timescales are comparable to a wide variety of processes that can potentially alter or even fully disrupt typical molecular clouds, leading to the conclusion that modeling of the $\text{HI} \rightarrow \text{H}_2$ transition should be time-dependent, in order to embrace such phenomena as clump-clump collisions and star formation, which can drive H_2 formation in both directions. Relying on the findings of Narayanan et al. (2011) and Krumholz & Gnedin (2011), the static solution for H_2 formation is a valid approximation for $Z' > 0.01$, which is the case for the three model galaxies studied here, but restricts SÍGAME to the domain of galaxies with at least $Z' \sim 0.01$.

• CO abundance

For the density of CO, we assumed that CO follows the structure of H_2 gas, and adopted a constant Galactic abundance of $[\text{CO}/\text{H}_2] = 2 \times 10^{-4}$. In reality, H_2 gas can self-shield better than the CO gas, creating an outer region or envelope of ‘CO-dark’ gas (Bolatto et al., 2008). Observations in the MW by Pineda et al. (2013) indicate that the amount of dark gas grows with decreasing metallicity and the resulting absence of CO molecules. By modeling a dynamically evolving ISM with cooling physics and chemistry incorporated on small scales, Smith et al. (2014) showed that in a typical MW-like disk of gas, the dark gas mass fraction, f_{DG} , defined as having $W_{\text{CO}} < 0.1 \text{ K km s}^{-1}$, is about 42 %, but up to 62 % in a radiation field ten times that

of the solar neighbourhood. While Smith et al. (2014) kept metallicity constant throughout the disk, Wolfire et al. (2010) found f_{DG} values of about $0.5 - 0.7$ for the low metallicity cases with $Z' = 0.5$, however using a 1D PDR model only. Recently, Bisbas et al. (2015) showed how relatively modest CR ionization rates of $10 - 50 \times \zeta_{\text{CR,MW}}$ can effectively destroy most CO in GMCs. Such studies show, that $[\text{CO}/\text{H}_2]$ is lower in regions of low metallicity and/or intense FUV fields, effectively leading to underestimates of the α_{CO} conversion factor when not accounted for in models. Since in this paper we have restricted our simulations to main-sequence galaxies with solar or higher than solar metallicities, adopting a constant Galactic $[\text{CO}/\text{H}_2]$ seems a reasonable choice, but see Lagos et al. (2012), Narayanan et al. (2012) and Narayanan & Krumholz (2014) for alternative approaches.

- *GMC density and thermal structure*

When solving for the temperature structure of each GMC, SÍGAME includes only the most dominant atomic and molecular species in terms of heating and cooling efficiencies. In this approximation, we also neglect X-ray irradiation and turbulence, leaving these for a future study. We have, however, checked our $T_{\text{k}} - n_{\text{H}_2}$ curves in Figure A.4 against those of Glover & Clark (2012), who performed time-resolved, high-resolution ($\delta m \simeq 0.05 - 0.5 \text{ M}_{\odot}$) SPH simulations of individual FUV irradiated molecular clouds using a chemical network of 32 species (see their Figure 2). Overall, there is great similarity in the T_{k} vs. n_{H_2} behaviour of the two sets of simulations. This includes the same main trend of decreasing temperature with increasing hydrogen density, as well as the local increase in T_{k} at $\sim 10^3 - 10^4 \text{ cm}^{-3}$ and the subsequent decrease to $T_{\text{k}} < 10 \text{ K}$ at $n_{\text{H}_2} > 10^{5.5} \text{ cm}^{-3}$. Thus, our GMCs models, despite their simplified density profiles and chemistry, seem to agree well with much more detailed simulations and we take this as an indication that they also mimic the conditions in real molecular clouds well.

4.7 CONCLUSIONS

In this chapter SÍGAME has been presented, a code that simulates the molecular line emission of galaxies via a detailed post-processing of the outputs from cosmological SPH simulations. A sequence of subgrid prescriptions are applied to a simulation snapshot in order to derive the molecular gas density and temperature from the SPH particle information such as SFR, gas density, temperature and metallicity. SÍGAME stands out from other methods of its kind by combining cosmological galaxy simulations with the following aspects:

1. *Local FUV field and cosmic ray ionization rate*

In SÍGAME, the energetics of the ISM are driven by the local star formation rate density, which is what sets the local FUV and cosmic ray field, i.e. G_0 and ζ_{CR} respectively, and thus the heating and ionization of the gas. Unlike other simulations, SÍGAME can therefore be used to study resolved properties within a galaxy, as for example line ratios and α_{CO} factors.

2. *Multiphase ISM*

The partly ionised gas in the SPH simulation is first cooled down to a cold neutral phase by including only heating by cosmic rays, counter-balanced by cooling via metal line emission, recombination processes and free-free emission. In a second cooling step, SÍGAME determines the internal radial temperature profile of each GMC by considering cosmic

ray heating and photo-electric heating by FUV photons as well as cooling by H₂, CO, OI, [CII] lines in addition to gas-dust interactions.

3. Radiative transfer on sub-parsec scales

We constructed a grid of GMC models that probe a large range in m_{GMC} , Z' and G_0 . On each model, the novel radiative transfer code `LIME` was employed for determining the CO line emission, so that `SÍGAME` can interpolate in $[m_{\text{GMC}}, Z', G_0]$ -space and sum up the emission in several CO lines for an entire galaxy in a few minutes.

We have used `SÍGAME` to create line emission velocity-cubes of the full CO rotational ladder for three cosmological N-body/SPH simulations of massive ($M_* \gtrsim 10^{10.5} M_\odot$) main-sequence galaxies at $z = 2$.

Molecular gas is produced more efficiently towards the centre of each galaxy, and while H_i surface gas densities (including helium) do not exceed $\sim 100 M_\odot \text{ pc}^{-2}$ anywhere in the disk, central molecular gas surface densities reach $\sim 1000 M_\odot \text{ pc}^{-2}$ on spatial scales of $80 \text{ pc} \times 80 \text{ pc}$, in good agreement with observations made at similar spatial resolution. This strong increase in molecular surface density is brought on by a similar increase in total gas surface density, overcoming the increase in photo-dissociating FUV field towards the centre of each galaxy.

Turning to the CO emission, the velocity-integrated moment 0 maps reveal distinct differences in the various transitions as molecular gas tracers. The morphology of molecular gas in our model galaxies is well reproduced in CO(1-0), but going to higher transitions, the region of CO emitting gas shrinks towards the galaxy centres. The global CO SLEDs of our simulated galaxies all peak at $J = 3 - 2$, indicating a dominating low-excitation gas. Recent CO(5 – 4) observations of $z \sim 1.5$ BzK galaxies seem to suggest that these galaxies actually peak at higher J , presenting an important test case that we will be following closely in the future in order to benchmark `SÍGAME` fully at $z \sim 2$ before moving to e.g. higher redshifts. The CO(3 – 2) line luminosities of our model galaxies are within the range of corresponding observed samples at redshifts $z \sim 1 - 2.5$, however on the low side. In particular, the model galaxies are below or at the CO luminosities of BzK-selected galaxies of comparable mass and SFR but at $z \sim 1.5$. The low luminosities are most likely a consequence of molecular gas mass fractions in our galaxies about 6 times below the observed values in the star-forming galaxies at $z = 1 - 2.5$ used to compare with.

Combining the derived H₂ gas masses with the CO(1 – 0) line emission found, we investigate local variations in the CO-H₂ conversion factor α_{CO} . The radial α_{CO} profiles all show a decrease towards the galaxy centres, dropping by a factor of $\sim 1.6 - 1.7$ in the central $R \leq 1 \text{ kpc}$ region compared to the disk average, and the main driver being the FUV field rather than a gradient in density or metallicity. Global α_{CO} factors range from 1.4 to $1.6 M_\odot \text{ pc}^{-2} (\text{K km s}^{-1})^{-1}$ or about 0.3 times the MW value, but closer to values for $z \sim 1.5$ normal star-forming galaxies identified with the BzK colour criteria.

The CO luminosity ratios of CO 3–2/1–0 and 7–6/1–0 (r_{32} and r_{76} respectively) drop off in radius about where the FUV radiation drops in intensity, and thus likely controlled by FUV field as α_{CO} . The global ratios of $r_{21} \simeq 1.4$ and $r_{32} \simeq 0.7$ agree very well with observations of BzK galaxies, while the r_{54} of about 0.8 is low compared to recent observations in BzK–4171 and BzK–21000. However, more observations of $J_{\text{up}} > 3$ lines towards high- z main-sequence galaxies, such as the BzKs, are still needed in order to determine the turn-over in their CO SLEDs and better constrain the gas excitation.

Finally, it is noted that SÍGAME in principle is able to simulate the emission from a broad range of molecular and atomic lines in the far-IR/mm wavelength regime provided measured collision rates exist, such as those found in the LAMDA database⁷, are available. For more on future applications of SÍGAME, see the Outlook chapter after the following chapter.

⁷<http://www.strw.leidenuniv.nl/~moldata/>, Schöier et al. (2005)

4.8 REFERENCES

- Aalto, S. 2013, in IAU Symposium, Vol. 292, IAU Symposium, ed. T. Wong & J. Ott, 199–208
- Ackermann, M., Ajello, M., Allafort, A., et al. 2013, Science, 339, 807
- Adelberger, K. L., Steidel, C. C., Shapley, A. E., et al. 2004, ApJ, 607, 226
- Aravena, M., Carilli, C., Daddi, E., et al. 2010, ApJ, 718, 177
- Aravena, M., Hodge, J. A., Wagg, J., et al. 2014, MNRAS, 442, 558
- Asplund, M., Grevesse, N., Sauval, A. J., & Scott, P. 2009, ARA&A, 47, 481
- Bigiel, F., Leroy, A., Walter, F., et al. 2008, AJ, 136, 2846
- Black, J. H., & Dalgarno, A. 1977, ApJs, 34, 405
- Blanc, G. A., Schruba, A., Evans, II, N. J., et al. 2013, ApJ, 764, 117
- Blitz, L., Fukui, Y., Kawamura, A., et al. 2007, Protostars and Planets V, 81
- Blitz, L., & Rosolowsky, E. 2006, ApJ, 650, 933
- Bolatto, A. D., Leroy, A. K., Rosolowsky, E., Walter, F., & Blitz, L. 2008, ApJ, 686, 948
- Bolatto, A. D., Wolfire, M., & Leroy, A. K. 2013, ARA&A, 51, 207
- Bovy, J., Rix, H.-W., & Hogg, D. W. 2012, ApJ, 751, 131
- Brinch, C., & Hogerheijde, M. R. 2010, A&A, 523, A25
- Bryant, P. M., & Scoville, N. Z. 1999, AJ, 117, 2632
- Carroll, T. J., & Goldsmith, P. F. 1981, ApJ, 245, 891
- Casey, C. M., Narayanan, D., & Cooray, A. 2014, Phys. Rep., 541, 45
- Cazaux, S., & Spaans, M. 2004, ApJ, 611, 40
- Chabrier, G. 2003, PASP, 115, 763
- Chapman, S. C., Scott, D., Steidel, C. C., et al. 2000, MNRAS, 319, 318
- Christensen, C., Quinn, T., Governato, F., et al. 2012, MNRAS, 425, 3058
- Daddi, E., Cimatti, A., Renzini, A., et al. 2004, ApJ, 617, 746
- Daddi, E., Dickinson, M., Morrison, G., et al. 2007, ApJ, 670, 156
- Daddi, E., Bournaud, F., Walter, F., et al. 2010, ApJ, 713, 686
- Daddi, E., Dannerbauer, H., Liu, D., et al. 2014, ArXiv e-prints
- Dame, T. M., Hartmann, D., & Thaddeus, P. 2001, ApJ, 547, 792
- Dannerbauer, H., Daddi, E., Riechers, D. A., et al. 2009, ApJL, 698, L178
- Downes, D., & Solomon, P. M. 1998, ApJ, 507, 615
- Draine, B. T. 2011, Physics of the Interstellar and Intergalactic Medium (Princeton University Press)
- Dumke, M. 2000, in Astronomical Society of the Pacific Conference Series, Vol. 221, Stars, Gas and Dust in Galaxies: Exploring the Links, ed. D. Alloin, K. Olsen, & G. Galaz, 15
- Elbaz, D., Daddi, E., Le Borgne, D., et al. 2007, A&A, 468, 33
- Elmegreen, B. G. 1989, ApJ, 344, 306
- Fixsen, D. J., Bennett, C. L., & Mather, J. C. 1999, ApJ, 526, 207
- Geach, J. E., & Papadopoulos, P. P. 2012, ApJ, 757, 156
- Genzel, R., Tacconi, L. J., Gracia-Carpio, J., et al. 2010, MNRAS, 407, 2091
- Genzel, R., Tacconi, L. J., Kurk, J., et al. 2013, ApJ, 773, 68
- Gieles, M., Portegies Zwart, S. F., Baumgardt, H., et al. 2006, MNRAS, 371, 793
- Glover, S. C. O., & Clark, P. C. 2012, MNRAS, 421, 9
- Glover, S. C. O., & Mac Low, M.-M. 2011, MNRAS, 412, 337
- Goldsmith, P. F. 2001, ApJ, 557, 736
- Greve, T. R., & Sommer-Larsen, J. 2008, A&A, 480, 335
- Greve, T. R., Leonidaki, I., Xilouris, E. M., et al. 2014, ApJ, 794, 142
- Heiderman, A., Evans, II, N. J., Allen, L. E., Huard, T., & Heyer, M. 2010, ApJ, 723, 1019

- Heyer, M., Krawczyk, C., Duval, J., & Jackson, J. M. 2009, *ApJ*, 699, 1092
- Heyer, M. H., & Brunt, C. M. 2004, *ApJL*, 615, L45
- Heyer, M. H., Carpenter, J. M., & Snell, R. L. 2001, *ApJ*, 551, 852
- Hodge, J. A., Riechers, D., Decarli, R., et al. 2014, ArXiv e-prints
—. 2015, *ApJ*, 798, L18
- Ingalls, J. G., Bania, T. M., Boulanger, F., et al. 2011, *ApJ*, 743, 174
- Iono, D., Wilson, C. D., Yun, M. S., et al. 2009, *ApJ*, 695, 1537
- Kauffmann, J., Pillai, T., Shetty, R., Myers, P. C., & Goodman, A. A. 2010, *ApJ*, 712, 1137
- Kennicutt, Jr., R. C. 1998, *ARA&A*, 36, 189
- Krumholz, M. R. 2014, *MNRAS*, 437, 1662
- Krumholz, M. R., & Gnedin, N. Y. 2011, *ApJ*, 729, 36
- Krumholz, M. R., McKee, C. F., & Tumlinson, J. 2009, *ApJ*, 699, 850
- Lagos, C. d. P., Bayet, E., Baugh, C. M., et al. 2012, *MNRAS*, 426, 2142
- Larson, R. B. 1981, *MNRAS*, 194, 809
- Lee, H.-H., Bettens, R. P. A., & Herbst, E. 1996, *A&As*, 119, 111
- Leroy, A. K., Walter, F., Brinks, E., et al. 2008, *AJ*, 136, 2782
- Leroy, A. K., Bolatto, A. D., Ostriker, E. C., et al. 2015, *ApJ*, 801, 25
- Liu, T., Wu, Y., & Zhang, H. 2013, *ApJ*, 775, L2
- Magnelli, B., Saintonge, A., Lutz, D., et al. 2012, *A&A*, 548, A22
- Mao, R.-Q., Schulz, A., Henkel, C., et al. 2010, *ApJ*, 724, 1336
- McMillan, P. J. 2011, *MNRAS*, 414, 2446
- Miettinen, O., Harju, J., Haikala, L. K., Kainulainen, J., & Johansson, L. E. B. 2009, *A&A*, 500, 845
- Monaghan, J. J. 2005, *Reports on Progress in Physics*, 68, 1703
- Muñoz, J. A., & Furlanetto, S. R. 2013, *MNRAS*, 435, 2676
- Narayanan, D., Cox, T. J., Shirley, Y., et al. 2008a, *ApJ*, 684, 996
- Narayanan, D., & Hopkins, P. F. 2013, *MNRAS*, 433, 1223
- Narayanan, D., Krumholz, M., Ostriker, E. C., & Hernquist, L. 2011, *MNRAS*, 418, 664
- Narayanan, D., & Krumholz, M. R. 2014, *MNRAS*, 442, 1411
- Narayanan, D., Krumholz, M. R., Ostriker, E. C., & Hernquist, L. 2012, *MNRAS*, 421, 3127
- Narayanan, D., Cox, T. J., Robertson, B., et al. 2006, *ApJL*, 642, L107
- Narayanan, D., Cox, T. J., Kelly, B., et al. 2008b, *ApJs*, 176, 331
- Norman, C. A., & Spaans, M. 1997, *ApJ*, 480, 145
- Padoan, P., & Nordlund, Å. 2002, *ApJ*, 576, 870
- Papadopoulos, P. P., Isaak, K., & van der Werf, P. 2010, *ApJ*, 711, 757
- Papadopoulos, P. P., & Thi, W.-F. 2013, in *Advances in Solid State Physics*, Vol. 34, *Cosmic Rays in Star-Forming Environments*, ed. D. F. Torres & O. Reimer, 41
- Papadopoulos, P. P., Thi, W.-F., Miniati, F., & Viti, S. 2011, *MNRAS*, 414, 1705
- Papadopoulos, P. P., van der Werf, P. P., Xilouris, E. M., et al. 2012, *MNRAS*, 426, 2601
- Papovich, C., Finkelstein, S. L., Ferguson, H. C., Lotz, J. M., & Giavalisco, M. 2011, *MNRAS*, 412, 1123
- Pelupessy, F. I. 2005, PhD thesis, Leiden Observatory, Leiden University, P.O. Box 9513, 2300 RA Leiden, The Netherlands
- Pelupessy, F. I., Papadopoulos, P. P., & van der Werf, P. 2006, *ApJ*, 645, 1024
- Pineda, J. E., Caselli, P., & Goodman, A. A. 2008, *ApJ*, 679, 481
- Pineda, J. L., Langer, W. D., Velusamy, T., & Goldsmith, P. F. 2013, *A&A*, 554, A103
- Popping, G., Somerville, R. S., & Trager, S. C. 2014, *MNRAS*, 442, 2398

- Price, D. J. 2007, Publications of the Astronomical Society of Australia, 24, 159
- Rodighiero, G., Cimatti, A., Gruppioni, C., et al. 2010, A&A, 518, L25
- Romeo, A. D., Sommer-Larsen, J., Portinari, L., & Antonuccio-Delogu, V. 2006, MNRAS, 371, 548
- Saintonge, A., Kauffmann, G., Kramer, C., et al. 2011, MNRAS, 415, 32
- Sandstrom, K. M., Leroy, A. K., Walter, F., et al. 2013, ApJ, 777, 5
- Schöier, F. L., van der Tak, F. F. S., van Dishoeck, E. F., & Black, J. H. 2005, A&A, 432, 369
- Seon, K.-I., Edelstein, J., Korpela, E., et al. 2011, ApJs, 196, 15
- Simnett, G. M., & McDonald, F. B. 1969, ApJ, 157, 1435
- Smith, R. J., Glover, S. C. O., Clark, P. C., Klessen, R. S., & Springel, V. 2014, MNRAS, 441, 1628
- Sofia, U. J., Lauroesch, J. T., Meyer, D. M., & Cartledge, S. I. B. 2004, ApJ, 605, 272
- Solomon, P. M., Downes, D., Radford, S. J. E., & Barrett, J. W. 1997, ApJ, 478, 144
- Sommer-Larsen, J., Götz, M., & Portinari, L. 2003, ApJ, 596, 47
- Sommer-Larsen, J., Romeo, A. D., & Portinari, L. 2005, MNRAS, 357, 478
- Sommer-Larsen, J., Vedel, H., & Hellsten, U. 1998, MNRAS, 294, 485
- Springel, V., & Hernquist, L. 2003, MNRAS, 339, 289
- Stinson, G., Seth, A., Katz, N., et al. 2006, MNRAS, 373, 1074
- Strong, A. W., & Mattox, J. R. 1996, A&A, 308, L21
- Swinbank, A. M., Papadopoulos, P. P., Cox, P., et al. 2011, ApJ, 742, 11
- Tacconi, L. J., Genzel, R., Smail, I., et al. 2008, ApJ, 680, 246
- Tacconi, L. J., Neri, R., Genzel, R., et al. 2013, ApJ, 768, 74
- Tielens, A. G. G. M. 2005, The Physics and Chemistry of the Interstellar Medium (Cambridge University Press)
- . 2013, Reviews of Modern Physics, 85, 1021
- Vázquez-Semadeni, E., Colín, P., Gómez, G. C., Ballesteros-Paredes, J., & Watson, A. W. 2010, ApJ, 715, 1302
- Walter, F., Riechers, D. A., Carilli, C. L., et al. 2007, in Astronomical Society of the Pacific Conference Series, Vol. 375, From Z-Machines to ALMA: (Sub)Millimeter Spectroscopy of Galaxies, ed. A. J. Baker, J. Glenn, A. I. Harris, J. G. Mangum, & M. S. Yun, 182
- Webber, W. R. 1998, ApJ, 506, 329
- Whitaker, K. E., Labb  , I., van Dokkum, P. G., et al. 2011, ApJ, 735, 86
- Wiersma, R. P. C., Schaye, J., & Smith, B. D. 2009, MNRAS, 393, 99
- Wolfire, M. G., Hollenbach, D., & McKee, C. F. 2010, ApJ, 716, 1191
- Wolfire, M. G., McKee, C. F., Hollenbach, D., & Tielens, A. G. G. M. 2003, ApJ, 587, 278
- Wuyts, S., F  rster Schreiber, N. M., van der Wel, A., et al. 2011, ApJ, 742, 96
- Yang, B., Stancil, P. C., Balakrishnan, N., & Forrey, R. C. 2010, ApJ, 718, 1062
- Zahid, H. J., Dima, G. I., Kewley, L. J., Erb, D. K., & Dav  , R. 2012, ApJ, 757, 54

5

[CII] LINE EMISSION FROM GALAXIES

5.1 PROBING THE NEUTRAL AND IONIZED GAS

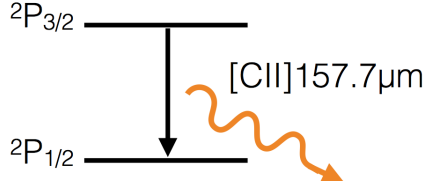


Figure 5.1 The two level system of ionized carbon leading to the line emission at $\sim 158 \mu\text{m}$. The excitation happens via collisions with either electrons, atoms or molecules.

Being the fourth most common element after hydrogen in the Milky Way (MW), it comes as no surprise that carbon is nearly ubiquitous throughout the various phases of the ISM in star-forming galaxies (e.g. Dartois & Muñoz-Caro, 2007; Esteban et al., 2014; James et al., 2014). Much of that carbon is ionized by the ultraviolet (UV) radiation permeating the ISM, due to the low ionization potential of carbon (11.3 eV cf. 13.6 eV for hydrogen). As a result, singly ionized carbon (CII) is found in regions of ionized as well as neutral gas. In both regions, the $^2\text{P}_{3/2}$ - $^2\text{P}_{1/2}$ fine structure transition of CII can be collisionally excited by electrons (e^-), atoms (H I) or molecules (H₂), depending on the gas phase, resulting in an emission line at $157.714 \mu\text{m}$ or 1900.5369 GHz (hereafter [CII]).

The critical densities of [CII] are only 16 cm^{-3} , 2400 cm^{-3} and 4800 cm^{-3} for collisions with e^- , H I and H₂ respectively at a temperature of 500 K (Goldsmith et al., 2012). Together, these facts are what makes [CII] one of the strongest cooling lines of the ISM, with a line luminosity equivalent to $\sim 0.1 - 1\%$ of the far-infrared (FIR) luminosity of galaxies (e.g. Stacey et al., 1991; Brauher et al., 2008).

5.2 OBSERVATIONS OF [CII] EMISSION IN GALAXIES AT HIGH AND LOW REDSHIFT

Due to high atmospheric opacity at these frequencies, observations of [CII] in the local Universe must be done at high altitudes or in space. Indeed, the very first detections of [CII] towards Galactic objects (Russell et al., 1980; Stacey et al., 1983; Kurtz et al., 1983) and other galaxies (Crawford et al., 1985; Stacey et al., 1991; Madden et al., 1992) were done with airborne observatories such as the NASA Lear Jet and the Kuiper Airborne Observatory. The advent of the Infrared Space Observatory (ISO) allowed for the first systematic [CII] surveys of local galaxies (e.g. Malhotra et al., 1997; Luhman et al., 1998, 2003). Detections of [CII] at high- z have also

become feasible over recent years with ground-based facilities (Hailey-Dunsheath et al., 2010; Stacey et al., 2010), as well as the *Herschel* Space Observatory (see the recent review by Casey et al., 2014).

5.2.1 THE [CII] DEFICIT

Early observations and modeling suggested that [CII] is predominantly associated with Photodissociation Regions (PDRs) in the outskirts of molecular clouds exposed to intense far-ultraviolet (FUV) radiation, hence predicting a strong correlation between [CII] luminosity, $L_{\text{[CII]}}$, and that of reprocessed FUV light as measured in far-infrared (FIR), L_{FIR} (Tielens & Hollenbach, 1985; Crawford et al., 1985). However, a deficit in $L_{\text{[CII]}}$ relative to L_{FIR} was soon observed towards local ultraluminous infrared galaxies (ULIRGs) and high- z galaxies dominated by an AGN (e.g. Malhotra et al., 1997; Luhman et al., 1998; Malhotra et al., 2001; Luhman et al., 2003; Díaz-Santos et al., 2013; Farrah et al., 2013). Some indications suggest that this ‘[CII] deficit’ persists at high- z , with the ratio extending to other FIR lines (e.g. Graciá-Carpio et al., 2011), though the existence of a high- z deficit is debated (Hailey-Dunsheath et al., 2010; Wagg et al., 2010; De Breuck et al., 2011; Ferkinhoff et al., 2011; Swinbank et al., 2012). Magdis et al. (2014) find that intermediate $z \sim 0.3$ ULIRGs actually fall on the relation for local normal galaxies measured by Malhotra et al. (2001), suggesting that high- z ULIRGs are in fact scaled-up versions of local star-forming galaxies, rather than the disturbed systems resulting from mergers that are typically associated with local $z < 0.2$ ULIRGs. The [CII] deficit increases with higher dust temperatures on both global and resolved scales in local galaxies (e.g Croxall et al., 2012; Díaz-Santos et al., 2013; Herrera-Camus et al., 2015), shown with an example in Fig. 5.2, suggesting that dust plays a crucial role in controlling the $L_{\text{[CII]}}/L_{\text{FIR}}$ ratio.

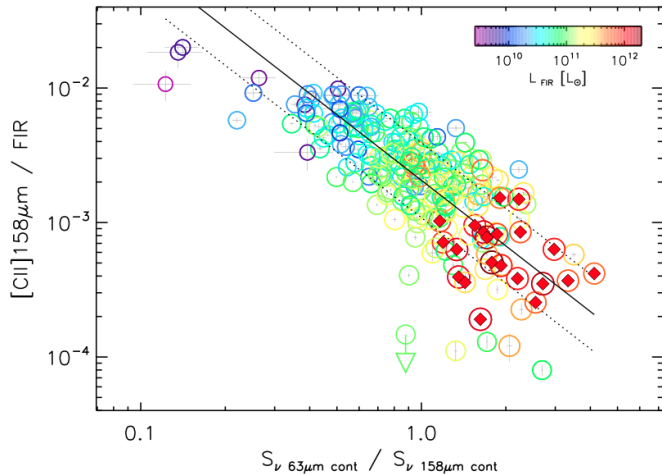


Figure 5.2 The [CII] deficit as investigated and plotted by Díaz-Santos et al. (2013) for local luminous infrared galaxies (LIRGs). Deviation from the global [CII]-FIR relation increases with dust temperature corresponding to increasing 60/100 μm color.

Various scenarios have been put forward as causing the [CII] deficit (see a summary of these in e.g. Malhotra et al., 2001; Herrera-Camus et al., 2015), but a consensus has not been achieved with observations and models so far. Favoured scenarios causing the [CII] deficit are ones in which the efficiency of the FUV light to heat the gas is decreased or obscuring dust absorbs the

FUV radiation before it reaches the potential sources of [CII] emission. Such scenarios include i) large HII regions created by high ionization parameters where most of the FUV radiation is absorbed by dust rather than goes to heating the gas via photo-ionization (e.g. Tielens & Hollenbach, 1985; Abel et al., 2009; Graciá-Carpio et al., 2011; Croxall et al., 2012), ii) high levels of grain charging, primarily in PDRs, which decrease the efficiency of photoelectric heating of the gas by FUV radiation (e.g. Malhotra et al., 2001; Croxall et al., 2012; Ibar et al., 2015), and iii) dust-bounded clouds or PDRs in ULIRGs, where high dust masses in the HII regions absorb most FUV light before it reaches regions with more ionized carbon (Luhman et al., 2003; Farrah et al., 2013; Abel et al., 2009).

5.2.2 CONTRIBUTING GAS PHASES TO THE [CII] EMISSION

Knowing the relative contributions to $L_{\text{[CII]}}$ from different gas phases in the ISM would help sorting out in the possible causes for the [CII] deficit. But observations of [CII] emission alone, will not readily give away information on the different ISM phases contributing, unless combined with some other gas tracer such as [NII] (122 μm) (Malhotra et al., 2001) or HI (21 cm) as well as CO line emission as done by Pineda et al. (2013) for the MW, in order to separate contributions from ionized, neutral and molecular gas. Updated in Pineda et al. (2014), the ISM phases considered are found to contribute with roughly amounts to the total $L_{\text{[CII]}}$ with 30 % from dense PDRs, 25 % from cold HI, 25 % from CO-dark H₂ gas and 20 % from ionized gas. Observing 60 normal, star-forming galaxies in [CII] and [NII], Malhotra et al. (2001) estimated that a rough mean of 50 % of $L_{\text{[CII]}}$ comes from ionized gas and the rest from PDRs. Even larger PDR contributions were found in the giant HII region N11 in the Large Magellanic Cloud (LMC), by Lebouteiller et al. (2012) who conclude, from comparison of [CII] with [NII], that 95 % of $L_{\text{[CII]}}$ arises in diffuse PDRs, whereas dense PDRs are better traced by [OI], also considered the second most important cooling line in neutral gas.

5.2.3 [CII] AS A STAR FORMATION RATE TRACER

Since [CII] is sensitive to the local FUV field which itself probes OB star formation activity, it was early on suggested that $L_{\text{[CII]}}$ correlates with SFR of a galaxy, and observations soon revealed a $L_{\text{[CII]}}$ -SFR correlation for nearby galaxies (Stacey et al., 1991; Leech et al., 1999; Boselli et al., 2002). More comprehensive studies were performed by de Looze et al. (2011); De Looze et al. (2014) and Farrah et al. (2013) for modest star-forming galaxies and ULIRGs in the local Universe. The scatter in the $L_{\text{[CII]}}$ -SFR relation is substantial though, apparently regardless of the overall galaxy classification (Sargsyan et al., 2012), and increasing towards low metallicity, warm dust temperatures and large filling factors of ionized, diffuse gas (De Looze et al., 2014).

With the Photodetector Array Camera & Spectrometer (PACS) on board *Herschel*, resolved observations of [CII] in local galaxies became possible (e.g. De Looze et al., 2014; Herrera-Camus et al., 2015; Kapala et al., 2015), and the advent of the Atacama Large Millimeter Array (ALMA) promises to make such detections and observations relatively routine, even at high- z (e.g. Wang et al., 2013). The $L_{\text{[CII]}}$ -SFR relation has now also observed on kpc-scales in local galaxies as a kind ‘[CII] KS relation’ between surface density of SFR, Σ_{SFR} , and that of [CII] luminosity, $\Sigma_{\text{[CII]}}$ (e.g. De Looze et al., 2014; Herrera-Camus et al., 2015; Kapala et al., 2015). Kapala et al. (2015) concluded that [CII] traces SFR in the spiral arms of the Andromeda Galaxy (M31) similarly to what is seen in larger samples of more distant galaxies, although with a significant contribution to [CII] from outside star-forming regions, and a shallower slope of the

$\Sigma_{\text{[CII]}}\text{-}\Sigma_{\text{SFR}}$ relation on ~ 50 pc scales than on kpc scales. For the MW, Pineda et al. (2014) find that only the combined emission of all gas phases, leads to a slope of the $\Sigma_{\text{[CII]}}\text{-}\Sigma_{\text{SFR}}$ relation in agreement with extragalactic observations. But the $\Sigma_{\text{[CII]}}\text{-}\Sigma_{\text{SFR}}$ relation for local galaxies also suffers from a great deal of scatter. De Looze et al. (2014) find, when observing 32 local dwarf galaxies on kpc-scales, that this scatter is most likely due to internal ISM conditions, rather than large variations within individual galaxies. Analyzing 46 nearby (mostly spiral) galaxies from the *Herschel* KINGFISH sample, Herrera-Camus et al. (2015) succeeded in reducing the scatter on the $\Sigma_{\text{[CII]}}\text{-}\Sigma_{\text{SFR}}$ relation at warm IR colors, by deriving a set of IR color adjustments that can be applied to normal, star-forming galaxies in the absence of strong AGNs. But a firm physical reason for the scatter is still missing.

Metallicity is a potentially important factor for the $L_{\text{[CII]}}\text{-SFR}$, as an increase in metallicity translates into a higher mass fraction of carbon and dust, both of which affect the $L_{\text{[CII]}}\text{-SFR}$ relation. Similar to De Looze et al. (2014), Herrera-Camus et al. (2015) found an increased scatter around the $L_{\text{[CII]}}\text{-SFR}$ relation at low metallicities, implying that at low metallicities, a non-negligible fraction of the neutral gas cooling takes place via the [OI] $63\,\mu\text{m}$ cooling line instead the [CII] line. In M31, Kapala et al. (2015) see an increasing trend in $L_{\text{[CII]}}/L_{\text{TIR}}$ with radius as expected if $L_{\text{[CII]}}$ itself dependeded strongly on metallicity, since M31 excibits a clearly decreasing metallicity with radius (Sanders et al., 2012). However, Kapala et al. (2015) cannot rule out other factors such as stellar density and radiation field strength. Kramer et al. (2013) found a sharp increase in $L_{\text{[CII]}}/L_{\text{FIR}}$ at $R \sim 4.5$ kpc in M33, but dismiss metallicity as the sole cause, due to the rather shallow metallicity gradient in M33 (Magrini et al., 2010). The effect of low metallicity together with the disruption of molecular clouds is also becoming an important subject for studies of the Epoch of Reionization (EoR) at $z \sim 6$, as a possible explanation for several non-detections of normal star-forming galaxies. Examples include the lensed Ly α emitter at $z = 6.56$ and the Himiko galaxy at $z \sim 6.5$ forming stars at a rate of ≈ 10 and $\sim 100\,\text{M}_\odot\,\text{yr}^{-1}$, respectively (Kanekar et al., 2013; Ouchi et al., 2013), and more recently 3 Lyman Break Galaxies at $z \sim 7$ of SFR $\sim 10\,\text{M}_\odot\,\text{yr}^{-1}$ (Maiolino et al., 2015).

5.3 MODELING [CII] EMISSION

With the [CII] line increasingly being used as a tracer of gas and star formation at high redshifts, efforts have also recently been made to simulate the [CII] emission from galaxies. Various sub-grid ‘gas physics’ approaches have been applied to both semi-analytical (Popping et al., 2014a; Muñoz & Furlanetto, 2013) and hydrodynamical (Nagamine et al., 2006; Vallini et al., 2013, 2015) simulations of galaxies. The simulations by Nagamine et al. (2006) focus on the [CII] detectability of lyman break galaxies at $z = 3$, while Vallini et al. (2013) apply their simulations to observed upper limits on the [CII] emission from the $z = 6.6$ Ly α emitter (LAE) Himiko (Ouchi et al., 2013) finding that its metallicity must be subsolar. Both set of simulations consider a two-phase ISM consisting of a cold and a warm neutral in pressure equilibrium, and both find that the the [CII] emission is dominated by the cold gas. Most recently, Vallini et al. (2015) combined a $z \approx 7$ galaxy simulated with GADGET-2 with different SFRs to show that most [CII] emission originates in the PDRs, irregardless of the SFR due a strong coupling between the neutral gas and the CMB at $z \sim 7$. For SFRs ranging from 0.1 to $100\,\text{M}_\odot\,\text{yr}^{-1}$, the authors predict a $L_{\text{[CII]}}\text{-SFR}$ relation slightly below the locally observed ones for dwarfs and starburst galaxies, however differing the inclusion of stellar feedback in the model for a future work.

6

UNDERSTANDING THE $L_{\text{[CII]}}$ -SFR RELATION WITH SIMULATIONS (PAPER II)

6.1 AIM OF THIS PROJECT

As described in the previous chapter, simulations hold promise in aiding interpretation of the [CII] emission. In this chapter, an expansion and improvement of SÍGAME is presented, enabling the simulation of [CII] emission from galaxies, with the principle goal of understanding the dominant sites of origin of [CII] emission in modestly star-forming galaxies, and how the $L_{\text{[CII]}}$ -SFR relation is created on global and resolved scales. Much of the formalism and methodology of SÍGAME stay unchanged and the reader is referred to the previous Chapter I for those details. However, instead of making use of a radiative transfer code, the [CII] emission is calculated analytically for each ISM phase separately. SÍGAME in its new form is then applied to a cosmological SPH simulation of 7 massive star-forming galaxies on the main sequence at $z \sim 2$ in order to simulate their [CII] emission. By modeling the internal structure of the molecular gas on scales down to about ~ 0.5 pc as well as the ionized gas, we¹ investigate the origin of the $L_{\text{[CII]}}$ -SFR relation on global and resolved scales and how metallicity affects the $L_{\text{[CII]}}/\text{SFR}$ radial gradient for normal galaxies of different SFR at $z = 2$. Throughout, a flat cosmology is adopted with $\Omega_M = 0.27$, $\Omega_\Lambda = 0.73$, and $h = 0.71$ (Spergel et al., 2003).

6.2 METHODOLOGY OVERVIEW

SÍGAME is the method that I created for post-processing of an SPH simulation with the aim of predicting line emission from the ISM using subgrid physics prescriptions (see also Chapter I). For the application towards predicting [CII], the following quantities associated with each SPH particle are required: the position ($[x, y, z]$), velocity ($[v_x, v_y, v_z]$), smoothing length (h), gas mass (m_{SPH}), hydrogen density (n_H), gas kinetic temperature (T_k), electron fraction ($x_e = n_e/n_H$), star formation rate (SFR), metallicity (Z) as well as the relative abundances of carbon ([C/H]) and oxygen ([O/H]). The key s.pdf involved in the post-processing are illustrated in Fig. 6.1 and briefly listed below (with details given in subsequent sections):

1. The SPH gas is separated into its neutral and ionized constituents as dictated by the electron fraction provided by the GADGET-3 simulations.

¹Collaborators: Thomas R. Greve, Desika Narayanan, Robert Thompson, Sune Toft and Christian Brinch

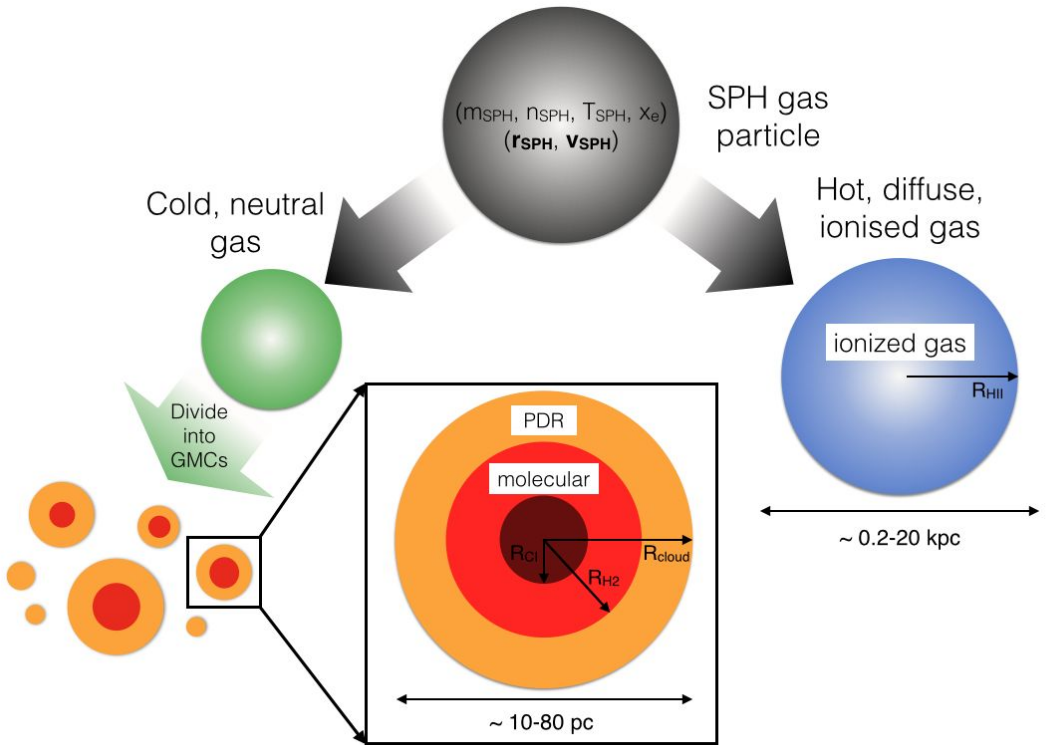


Figure 6.1 Schematic illustrating the sub-grid procedures applied to the SPH simulation in post-processing. Each SPH particle is a hybrid of neutral and ionized gas. The neutral gas associated with each SPH gas particle is divided into GMCs with masses and sizes following the Galactic mass-spectrum and mass-size relation for GMCs. Each GMC has an onion-layer structure, set by the stratification of the impinging FUV-field, which consist of an outer atomic (PDR) layer of HI and CII, and an inner molecular region where carbon is found in its single ionized state, and in neutral form further in (Section 6.4.1). The ionized gas associated with each SPH particle is assumed to reside in spherical clouds with radii and temperatures given by the SPH smoothing length and gas temperature (Section 6.4.2).

2. The neutral gas is divided into giant molecular clouds (GMCs) according to the observed mass function of GMCs in the Milky Way (MW) and nearby quiescent galaxies. The GMCs are modelled as logotropic spheres with their sizes and internal velocity dispersions derived according to pressure-normalized scaling relations.
3. Each GMC is assumed to consist of three spherically symmetric regions: 1) a FUV-shielded molecular core region where all carbon is locked up in CI and CO; 2) an outer molecular region where both CI and CII can exist; and 3) a largely neutral atomic layer of HI, HII and CII. The last region mimics the FUV-stratified PDRs observed at the surfaces of molecular clouds (Hollenbach & Tielens, 1999). The relative extent of these regions within each cloud, and thus the densities at which they occur, ultimately depends on the strength of the impinging FUV-field and CR ionization rate. The latter are set to scale with the local SFR volume density and, by requiring thermal balance with the cooling from line emission (from CII, OI, and H₂), determine the temperatures of the molecular and atomic gas phases.
4. The remaining ionized gas of the SPH simulation is divided into HII clouds of radius

equal to the smoothing lengths, temperature equal to that of the SPH simulation and constant density.

5. The [CII] emission from the molecular, atomic/PDR, and diffuse ionized gas is calculated separately and summed to arrive at the total [CII] emission from the galaxy. In doing so it is assumed that there is no radiative coupling between the clouds in the galaxy.

The SPH simulations used in this project, and the galaxies extracted from them, are described in the following section.

6.3 SPH SIMULATIONS

Our simulations are evolved with an updated version of the public GADGET-3 cosmological SPH code (Springel 2005 and Huang et al. 2015 in prep). It includes cooling processes using the primordial abundances as described in Katz et al. (1996), with additional cooling from metal lines assuming photo-ionization equilibrium from Wiersma et al. (2009). We use the more recent ‘pressure-entropy’ formulation of SPH which resolves mixing issues when compared with standard ‘density-entropy’ SPH algorithms (see Saitoh & Makino, 2013; Hopkins, 2013, for further details). Our code additionally implements the time-step limiter of Saitoh & Makino (2009); Durier & Dalla Vecchia (2012) which improves the accuracy of the time integration scheme in situations where there are sudden changes to a particle’s internal energy. To prevent artificial fragmentation (Schaye & Dalla Vecchia, 2008; Robertson & Kravtsov, 2008), we prohibit gas particles from cooling below their effective Jeans temperature which ensures that we are always resolving at least one Jeans mass within a particle’s smoothing length. This is very similar to adding pressure to the interstellar medium as in Springel & Hernquist (2003); Schaye & Dalla Vecchia (2008), except instead of directly pressurizing the gas we prevent it from cooling and fragmenting below the Jeans scale.

We stochastically form stars within the simulation from molecular gas following a Schmidt (1959) law with an efficiency of 1% per local free-fall time (Krumholz & Tan, 2007; Lada et al., 2010). The molecular content of each gas particle is calculated via the equilibrium analytic model of Krumholz et al. (2008, 2009); McKee & Krumholz (2010). This model allows us to regulate star formation by the local abundance of H₂ rather than the total gas density, which confines star formation to the densest peaks of the interstellar medium. Further implementation details can be found in Thompson et al. (2014). Galactic outflows are implemented using the hybrid energy/momentum-driven wind (ezw) model fully described in Davé et al. (2013); Ford et al. (2015). We also account for metal enrichment from Type II supernovae (SNe), Type Ia SNe, and AGB stars as described in Oppenheimer & Davé (2008).

6.3.1 SPH SIMULATIONS OF $z = 2$ MAIN SEQUENCE GALAXIES

We use the cosmological zoom-in simulations presented in Thompson et al. (2015), and briefly summarized here. Initial conditions were generated using the MUSIC code (Hahn & Abel, 2011) assuming cosmological parameters consistent with constraints from the *Planck* (Planck Collaboration et al., 2013) results, namely $\Omega_m = 0.3$, $\Omega_\Lambda = 0.7$, $H_0 = 70$, $\sigma_8 = 0.8$, $n_s = 0.96$. Six target halos were selected at $z = 2$ from a low-resolution N-body simulation consisting of 256^3 dark-matter particles in a $(16h^{-1}\text{Mpc})^3$ volume with an effective comoving spatial resolution of $.pdfilon = 1.25 h^{-1}$ kpc. Each target halo is populated with higher resolution particles at

$z = 249$, with the size of each high resolution region chosen to be 2.5 times the maximum radius of the original low-resolution halo. The majority of halos in our sample are initialized with a single additional level of refinement ($.pdfilon = 0.625 h^{-1}\text{kpc}$), while the two smallest halos are initialized with two additional levels of refinement ($.pdfilon = 0.3125 h^{-1}\text{kpc}$).

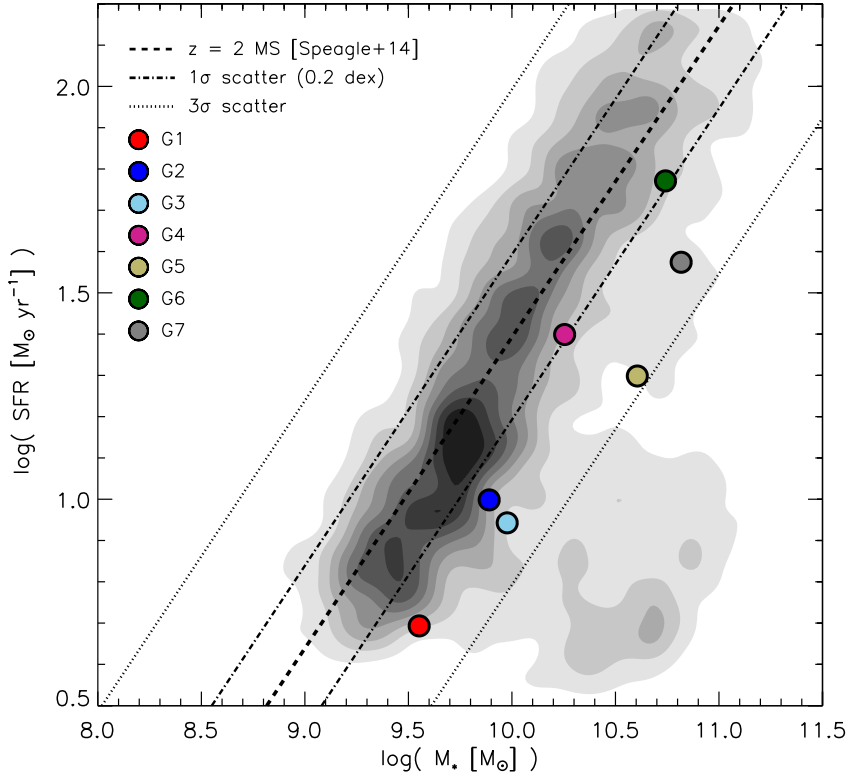


Figure 6.2 The SFR– M_* relation at $z \simeq 2$ as determined by Speagle et al. (2014) (dashed line) with the location of our seven simulated galaxies highlighted (filled circles). Dot-dashed and dotted lines indicate the 1σ and 3σ scatter around the relation of Speagle et al. (2014). For comparison we also show the locus defined by 3754 $1.4 < z < 2.5$ galaxies from the NEWFIRM Medium-Band Survey (grey filled contours), with masses and SFRs calculated using a Kroupa IMF (Whitaker et al., 2011).

The six halos produce seven star-forming galaxies at $z = 2$ that are free from all low-resolution particles within the virial radius of their parent halo. Their stellar masses (M_*) range from 3.6×10^9 to $6.6 \times 10^{10} M_\odot$ and their star formation rates from $5 - 60 M_\odot \text{ yr}^{-1}$ (Table 6.1). We hereafter label the galaxies G1, ..., G7 in order of increasing M_* . Other relevant global properties directly inferred from the SPH simulations, such as total gas mass (M_{gas}), neutral and ionized gas masses (M_{neutral} and M_{ionized} , respectively), average SFR surface density (Σ_{SFR}), and average metallicity (Z'), can also be found in Table 6.1. Fig. 6.2 shows the locations of G1, ..., G7 in the SFR– M_* diagram. The galaxies are consistent with observational determinations of the $z \sim 2$ main sequence (MS) of star-forming galaxies (Whitaker et al., 2011; Speagle et al., 2014).

Table 6.1 Global properties of the seven simulated galaxies used for this work at $z = 2$.

	G1	G2	G3	G4	G5	G6	G7
$M_* [10^{10} M_\odot]$	0.36	0.78	0.95	1.80	4.03	5.52	6.57
$M_{\text{gas}} [10^{10} M_\odot]$	0.42	0.68	1.26	1.43	2.59	2.16	1.75
$M_{\text{neutral}} [10^{10} M_\odot]$	0.09	0.13	0.57	0.20	0.29	0.29	0.39
$M_{\text{ionized}} [10^{10} M_\odot]$	0.33	0.55	0.69	1.23	1.30	1.87	1.36
SFR [$M_\odot \text{ yr}^{-1}$]	4.9	10.0	8.8	25.1	19.9	59.0	37.5
$\Sigma_{\text{SFR}} [M_\odot \text{ yr}^{-1} \text{ kpc}^{-2}]$	0.016	0.032	0.028	0.080	0.063	0.188	0.119
Z'	0.43	0.85	0.64	1.00	1.00	1.67	1.72

All quantities have been calculated at $z = 2$ using a fixed cut-out radius of $R_{\text{cut}} = 10 \text{ kpc}$, which is the radius at which the accumulative stellar mass function of each galaxy flattens. M_{gas} is the total gas mass, and M_{neutral} and M_{ionized} the gas masses in neutral and ionized form, respectively (see Section 6.4). The metallicity ($Z' = Z/Z_\odot$) is the mean of all SPH gas particles within R_{cut} .

6.4 MODELING THE ISM

As illustrated in Fig. 6.1, the first step in modelling the ISM is to split each SPH particle into an ionized and a neutral gas component. This is done using the electron fraction, x_e , associated with each SPH particle, i.e.:

$$m_{\text{neutral}} = (1 - x_e)m_{\text{SPH}} \quad (6.1)$$

$$m_{\text{ionized}} = x_e m_{\text{SPH}}. \quad (6.2)$$

The electron fraction from GADGET-3 gives the density of electrons relative to that of hydrogen, n_e/n_H , and can therefore reach values of ~ 1.16 in the case where helium is also ionized. As a result we re-normalized the distribution of x_e values to a maximal x_e of 1 so as to not exceed the total gas mass in the simulation. Fig. 6.3 shows the distribution of SPH gas particles masses in G4 – chosen for its position near the center of the stellar and gas mass ranges of G1, ..., G7 – along with the mass distributions of the neutral and ionized gas components obtained from eqs. 6.1 and 6.2.

The ionized gas is seen to have a relatively flat distribution spanning the mass range $\sim 10^{4.3} - 10^{5.8} M_\odot$. The neutral gas, however, peaks at two characteristic masses ($\sim 10^{5.5} M_\odot$ and $\sim 10^{5.8} M_\odot$), where the lower mass peak represents gas particles left over from the first generation of stars in the simulation.

6.4.1 GIANT MOLECULAR CLOUDS

Masses, sizes and velocity dispersion

The neutral gas mass, m_{neutral} , associated with a given SPH particle is divided into GMCs by randomly sampling the GMC mass spectrum as observed in the Galactic disk and Local Group galaxies: $\frac{dN}{dm_{\text{GMC}}} \propto m_{\text{GMC}}^{-\beta}$ with $\beta = 1.8$ (Blitz et al., 2007). Similar to Narayanan et al. (2008b,a), a lower and upper cut in mass of $10^4 M_\odot$ and $10^6 M_\odot$, respectively, are enforced in order to ensure the GMC masses stay within the range observed by Blitz et al. (2007). Up to 40 GMCs are created per SPH particle but typically most ($> 90\%$) of the SPH particles are split into four GMCs or less. While m_{neutral} never exceeds the upper GMC mass limit ($10^6 M_\odot$), there are instances where m_{neutral} is below the lower GMC mass limit ($10^4 M_\odot$). In those cases we simply

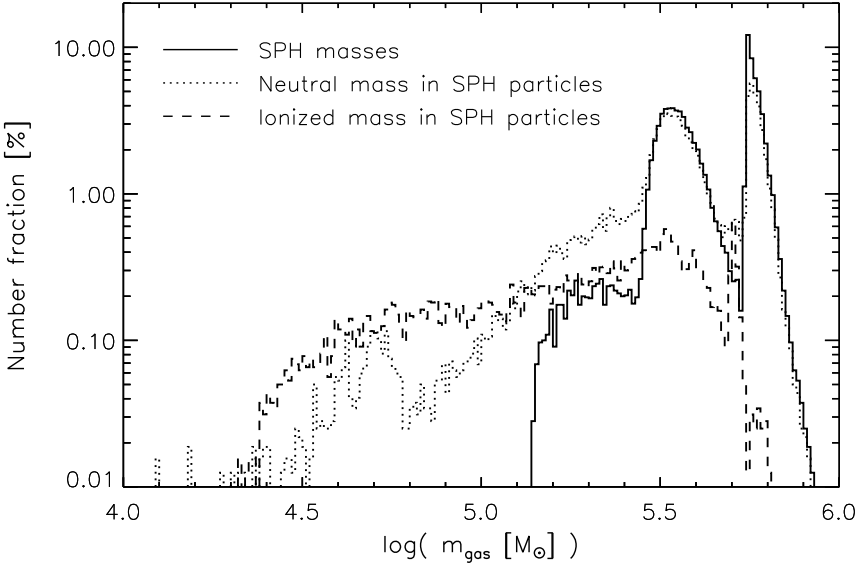


Figure 6.3 The distribution of SPH gas particle masses (solid histogram) in G4. The distribution peaks at two characteristic masses ($\sim 10^{5.5} M_{\odot}$ and $\sim 10^{5.8} M_{\odot}$), where the lower mass peak represents gas particles left over from the first generation of stars in the simulation. Splitting the gas into its neutral and ionized components according to eqs. 6.1 and 6.2 results in the mass distribution given by the dotted and dashed histograms, respectively.

discard the gas, i.e. remove it from any further sub-grid processing. For the highest resolution simulations in our sample (G1 and G2), the discarded neutral gas amounts to $\sim 6\%$ of the total neutral gas mass, and $\lesssim 0.02\%$ in the remaining five galaxies. We shall therefore assume that it does not affect our results significantly.

The GMCs are randomly distributed within $0.2 \times$ the smoothing length of the original SPH particle, but with the radial displacement scaling inversely with GMC mass in order to retain the original gas mass distribution as closely as possible. To preserve the overall gas kinematics as best possible, all GMCs associated with a given SPH particle are given the same velocity as that of the SPH particle.

GMC sizes are obtained from the pressure-normalized scaling relations for virialized molecular clouds which relate cloud radius (R_{cloud}) with mass (m_{GMC}) and external pressure (P_{ext}):

$$\frac{R_{\text{cloud}}}{\text{pc}} = \left(\frac{P_{\text{ext}}/k_{\text{B}}}{10^4 \text{ cm}^{-3} \text{ K}} \right)^{-1/4} \left(\frac{m_{\text{GMC}}}{290 M_{\odot}} \right)^{1/2}. \quad (6.3)$$

We assume $P_{\text{ext}} = P_{\text{tot}}/(1 + \alpha_0 + \beta_0)$ for relative cosmic and magnetic pressure contributions of $\alpha_0 = 0.4$ and $\beta_0 = 0.25$ (Elmegreen, 1989). For the total pressure (P_{tot}) we adopt the external hydrostatic pressure at mid-plane for a rotating disk of gas and stars, i.e.:

$$P_{\text{tot}} \approx \frac{\pi}{2} G \Sigma_{\text{gas}} \left[\Sigma_{\text{gas}} + \left(\frac{\sigma_{\text{gas},\perp}}{\sigma_{*,\perp}} \right) \Sigma_{*} \right], \quad (6.4)$$

where Σ_{gas} and Σ_{*} are the local surface densities of gas and stars, respectively, and $\sigma_{\text{gas},\perp}$

and $\sigma_{*,\perp}$ their local velocity dispersions measured perpendicular to the mid-plane (see e.g., Elmegreen (1989); Swinbank et al. (2011)). For each SPH particle, all of these quantities are calculated directly from the simulation output (using a radius of $R = 1$ kpc from each SPH particle), and it is assumed that the resulting P_{ext} is the external pressure experienced by all of the GMCs generated by the SPH particle. We find that GMCs in our simulated galaxies are subjected to a wide range of external pressures ($P_{\text{ext}}/k_B \sim 10^2 - 10^7 \text{ cm}^{-3} \text{ K}$). For comparison, the range of pressures experienced by clouds in our Galaxy and in Local Group galaxies is $P_{\text{ext}}/k_B \sim 10^3 - 10^7 \text{ cm}^{-3} \text{ K}$ with an average of $P_{\text{ext}}/k_B \sim 10^4 \text{ cm}^{-3} \text{ K}$ in Galactic clouds (Elmegreen, 1989; Blitz et al., 2007). This results in GMC sizes in our simulations ranging from $R_{\text{cloud}} = 1 - 300 \text{ pc}$.

The internal velocity dispersion (σ_v) of the GMCs is inferred from the virial theorem, which provides us with a pressure-normalized $\sigma_v - R_{\text{GMC}}$ relation:

$$\sigma_v = 1.2 \text{ km s}^{-1} \left(\frac{P_{\text{ext}}/k_B}{10^4 \text{ cm}^{-3} \text{ K}} \right)^{1/4} \left(\frac{R_{\text{cloud}}}{\text{pc}} \right)^{1/2}, \quad (6.5)$$

where the normalization of 1.2 km s^{-1} comes from studies of Galactic GMCs (Larson, 1981; Elmegreen, 1989; Swinbank et al., 2011).

GMC density and temperature structure

We assume a truncated logotropic profile for the total hydrogen number density of the GMCs, i.e.:

$$n_{\text{H}}(R) = n_{\text{H,ext}} \left(\frac{R_{\text{cloud}}}{R} \right), \quad (6.6)$$

where $n_{\text{H}}(R > R_{\text{cloud}}) = 0$. For such a density profile it can be shown that the external density, $n_{\text{H,ext}}$, is $2/3$ of the average density:

$$n_{\text{H,ext}} = 2/3 \langle n \rangle = 2/3 \frac{m_{\text{GMC}}}{4/3 \pi m_{\text{H}} R_{\text{cloud}}^3}. \quad (6.7)$$

While the total hydrogen density follows a logotropic profile, the transition from H₂—→HI/HII is assumed to be sharp. Similarly for the transition from CI—→CII. This is illustrated in Fig. 6.4, which shows an example density profile of a GMC from our simulations. From the center of the GMC and out to R_{H_2} , hydrogen is in molecular form. Beyond R_{H_2} , hydrogen is found as HI and HII out to R_{cloud} .

The size of the molecular region, when adopting the logotropic density profile, is related to the total molecular gas mass fraction (f'_{mol}) of each GMC:

$$f'_{\text{mol}} = \frac{m_{\text{mol}}}{m_{\text{GMC}}} = \frac{\int_0^{R_{\text{H}_2}} \rho_{\text{ext}} \frac{R_{\text{GMC}}}{R} 4\pi R^2 dR}{\int_0^{R_{\text{GMC}}} \rho_{\text{ext}} \frac{R_{\text{GMC}}}{R} 4\pi R^2 dR} \quad (6.8)$$

$$= \frac{\int_0^{R_{\text{H}_2}} R dR}{\int_0^{R_{\text{GMC}}} R dR} = \left(\frac{R_{\text{H}_2}}{R_{\text{GMC}}} \right)^2 \quad (6.9)$$

$$\Rightarrow r_{\text{H}_2} = \sqrt{f'_{\text{mol}}}, \quad (6.10)$$

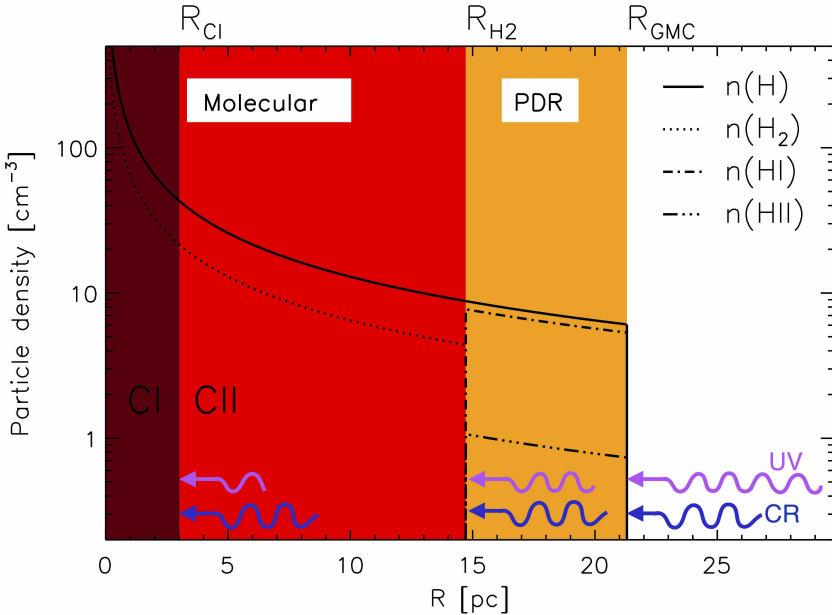


Figure 6.4 Example H number density profile (solid line) for a GMC of mass $m_{\text{GMC}} = 1.3 \times 10^4 M_{\odot}$ and radius $R_{\text{GMC}} = 21$ pc. Also shown are the density profiles of H_2 ($= 0.5n_{\text{H}}$), HI and HII . Note, the transition from molecular to atomic H is assumed to happen instantaneously at R_{H_2} . The total C abundance follows that of H but scaled with the $[\text{C}/\text{H}]$ abundance (as provided by the ‘parent’ SPH particle, see Section 6.2). CII can exist throughout the cloud except for the very inner region ($R < R_{\text{CI}}$; indicated in brown), with the CI to CII transition happening instantaneously at R_{CI} . $[\text{CII}]$ emission from the layer $R_{\text{CI}} \leq R \leq R_{\text{H}_2}$ (indicated in red) is referred to as ‘molecular’ emission, while $[\text{CII}]$ emission from $R_{\text{H}_2} < R \leq R_{\text{GMC}}$ (indicated in orange) is referred to as atomic or ‘PDR’ emission. The relative thickness of these layers is set by the impinging FUV radiation field and cosmic rays (illustrated as purple and blue arrows, respectively), with the former undergoing attenuation further into the cloud.

where r_{H_2} is the fractional radius, $r_{\text{H}_2} = R_{\text{H}_2}/R_{\text{cloud}}$. We find f'_{mol} by assuming $\text{HI} \leftrightarrow \text{H}_2$ equilibrium and using the analytical steady-state approach of Pelupessy et al. (2006) for inferring f'_{mol} for a logotropic cloud subjected to a radially incident FUV radiation field (see also Olsen et al., submitted). In this framework, the value of f'_{mol} (and thereby r_{H_2}) depends on:

- The cloud boundary pressure (P_{ext}), which is calculated as explained in Section 6.4.1.
- The metallicity (Z') of the GMC, which is inherited from its parent SPH particle and assumed constant throughout the cloud.
- The kinetic temperature of the gas at the GMC surface ($T_k(R_{\text{GMC}})$). This quantity is calculated in an iterative process together with f'_{mol} by solving the following thermal balance equation:

$$\Gamma_{\text{PE}} + \Gamma_{\text{CR,HI}} = \Lambda_{\text{CII}} + \Lambda_{\text{OI}}, \quad (6.11)$$

where Γ_{PE} is the heating rate associated with the photoelectric ejection of electrons from dust grains by the FUV field and $\Gamma_{\text{CR,HI}}$ is the heating rate by cosmic rays in atomic gas. The main cooling agents are assumed to be due to $[\text{CII}]$ and $[\text{OI}]$ (63 μm and 145 μm) line emission (i.e., Λ_{CII} and Λ_{OI} , respectively). Γ_{PE} , $\Gamma_{\text{CR,HI}}$, and Λ_{CII} all depend on the electron fraction at R_{GMC} ,

which is determined by the degree of HI ionization by the local FUV radiation field and CR ionization rate (see below for how these quantities are derived). For analytical expressions for the heating rates, we refer to Olsen et al., submitted. For Λ_{OI} we use the expressions given in Röllig et al. (2006). The calculation of Λ_{CII} at the GMC surface is detailed in Section 6.5 and Appendix A.3.

- The strength of the local FUV radiation field (G_0) and the CR ionization rate (ζ_{CR}) impinging on the GMCs. These quantities do not come out from the simulation directly, and instead they are calculated by scaling the Galactic FUV field ($G_{0,\text{MW}}$) and CR ionization rate ($\zeta_{\text{CR,MW}}$) with the local SFR volume density in the simulations, i.e., $G_0 \propto G_{0,\text{MW}} (\text{SFRD}_{\text{local}}/\text{SFRD}_{\text{MW}})$ and $\zeta_{\text{CR}} \propto \zeta_{\text{CR,MW}} (\text{SFRD}_{\text{local}}/\text{SFRD}_{\text{MW}})$, where $\text{SFRD}_{\text{local}}$ is estimated for each SPH particle as the volume averaged SFR within a 2 kpc radius². We have adopted Milky Way values of $G_{0,\text{MW}} = 0.6$ Habing (Seon et al., 2011) and $\zeta_{\text{CR,MW}} = 3 \times 10^{-17} \text{ s}^{-1}$ (Webber, 1998). For SFRD_{MW} we adopt $0.0024 \text{ M}_\odot \text{ yr}^{-1} \text{ kpc}^{-3}$, inferred from the average Galactic SFR ($0.3 \text{ M}_\odot \text{ yr}^{-1}$) within a disk 10 kpc in radius and 0.2 kpc in height (Heiderman et al., 2010; Bovy et al., 2012).
- The electron fraction at the cloud boundary. This fraction is not the previously introduced x_e , which was inherent to the SPH simulations and used to split the SPH gas into a neutral and ionized gas phase. Instead, it is the electron fraction given by the degree of ionization of HI caused by the G_0 and ζ_{CR} impinging on the cloud. This fraction (and thus the HI:HII ratio) is calculated with CLOUDY v13.03 (Ferland et al., 2013) given the hydrogen density and temperature at the cloud boundary and assuming an unattenuated G_0 and ζ_{CR} at R_{GMC} .

The [CII] emitting region in each of our GMCs is defined as the layer between the surface of the cloud and the depth at which the abundances of C and C⁺ are equal. Hence, if the latter occurs at a radius R_{CI} from the cloud center, the thickness of the layer is $R_{\text{cloud}} - R_{\text{CI}}$ (Fig. 6.4). At radii $< R_{\text{CI}}$, all carbon atoms are for simplicity assumed to be in neutral form. In order to determine the fractional radius r_{CI} ($= R_{\text{CI}}/R_{\text{GMC}}$) we follow the work of Röllig et al. (2006) (but see also Pelupessy & Papadopoulos, 2009), who considers the following dominant reaction channels for the formation and destruction of C⁺:



In this case, r_{CI} can be found by solving the following equation:

$$5.13 \times 10^{-10} \text{ s}^{-1} G_0 \int_1^\infty \frac{e^{-\mu \xi_{\text{FUV}} A_V(r_{\text{CI}})}}{\mu^2} d\mu = n_{\text{H}}(r_{\text{CI}}) [a_{\text{C}} X_{\text{C}} + 0.5 k_{\text{C}}], \quad (6.15)$$

where the left-hand side is the C⁺ formation rate due to photo-ionization by the attenuated FUV field at r_{CI} (eq. 6.12), and the right-hand side is the destruction rate of C⁺ due to recombination and radiative association (eqs. 6.13 and 6.14). The constants $a_{\text{C}} = 3 \times 10^{-11} \text{ cm}^{-3} \text{ s}^{-1}$ and

²In contrast to the method described in Chapter 3, the number of parameters defining each GMC is not causing a time-consuming issue in SÍGAME, and we can have a different prescriptions for ζ_{CR} and G_0 , keeping ζ_{CR} more directly tied to local star formation.

$k_C = 8 \times 10^{-16} \text{ cm}^{-3} \text{ s}^{-1}$ are the recombination and radiative association rate coefficients. Note, we have accounted for an isotropic FUV field since $\mu = \cos \theta$, where θ is the angle between the Poynting vector and the normal direction. $A_V(r_{\text{CI}})$ is the visual extinction corresponding to the $R_{\text{cloud}} - R_{\text{CI}}$ layer, and is given by $A_V(r_{\text{CI}}) = 0.724\sigma_{\text{dust}}Z'\langle n_{\text{H}} \rangle R_{\text{cloud}} \ln(r_{\text{CI}}^{-1})$, where $\sigma_{\text{dust}} = 4.9 \times 10^{-22} \text{ cm}^2$ is the FUV dust absorption cross section (Pelupessy & Papadopoulos, 2009; Mezger et al., 1982). ξ_{FUV} accounts for the difference in opacity between visual and FUV light and is set to 3.02. X_C is the carbon abundance relative to H and is calculated by adopting the carbon mass fractions of the parent SPH particle (self-consistently calculated as part of the overall SPH simulation) and assuming it to be constant throughout the GMC.

The temperature of the [CII]-emitting molecular gas (i.e., from the gas layer between R_{CI} and R_{H_2}) is assumed to be constant and equal to the temperature at R_{H_2} . The latter is given by the thermal balance:

$$\Gamma_{\text{PE}} + \Gamma_{\text{CR}, \text{H}_2} = \Lambda_{\text{H}_2} + \Lambda_{\text{CII}} + \Lambda_{\text{OI}}, \quad (6.16)$$

where $\Gamma_{\text{CR}, \text{H}_2}$ is the cosmic ray heating in molecular gas, and Λ_{H_2} is the cooling due to the S(0) and S(1) rotational lines of H_2 (Papadopoulos et al. (2014); see also Olsen et al., submitted). $\Gamma_{\text{CR}, \text{H}_2}$ depends on x_e , which is calculated with CLOUDY for the local CR ionization rate and the attenuated FUV field at r_{H_2} , i.e. $G_0 e^{-\xi_{\text{FUV}} A_V(r_{\text{H}_2})}$. $A_V(r_{\text{H}_2})$ corresponds the extinction through the outer atomic transition layer of each GMC.

The temperature of the atomic/PDR gas (i.e., from the gas between R_{H_2} and R_{cloud}) is assumed to be constant and equal to the temperature at R_{cloud} .

For each GMC we solve in an iterative manner simultaneously for R_{H_2} (eq. 6.10) and R_{CI} (eq. 6.15), as well as for the gas temperature at R_{cloud} and at R_{H_2} (eqs. 6.11 and 6.16, respectively)

The resulting distributions of R_{H_2} and R_{CI} for the GMC population in G4 are shown in Fig. 6.5 (middle panel), along with the distribution of R_{GMC} (obtained from eq. 6.3). In GMCs in general, we expect $R_{\text{CI}} < R_{\text{H}_2}$, due to efficient H_2 selfshielding. However, as Fig. 6.5 shows some of the GMCs in our simulations have very small R_{H_2} (due to them having virtually zero molecular gas fractions), and in those cases R_{CI} can be equal to or even exceed R_{H_2} . The latter implies that the [CII] emission is only coming from the atomic/PDR phase, with no contribution from the molecular gas.

The distributions of the kinetic temperature of the gas at R_{H_2} and R_{cloud} for the GMC population in G4 are also shown in Fig. 6.5 (bottom panel). The temperatures at the cloud surfaces range from $\sim 8 \text{ K}$ to $\sim 10^{5.5} \text{ K}$, and the temperatures at R_{H_2} lies between $\sim 8 - 1800 \text{ K}$.

With R_{H_2} and R_{CI} determined for each GMC we can calculate the gas masses associated with the molecular and atomic/PDR gas phase, respectively. The resulting mass distributions are shown in the top panel of Fig. 6.5, along with the distribution of total GMC masses (m_{GMC}) as determined by the adopted GMC mass spectrum (Section 6.4.1). We see that most of the molecular and atomic/PDR gas masses follow the total GMC mass spectrum. There is, however, a fraction of GMCs with extremely small molecular gas masses (corresponding to $f'_{\text{mol}} \sim 0$). On the other hand, there are some GMCs with small atomic/PDR gas masses, i.e., clouds that are so shielded from FUV radiation that they are almost entirely molecular.

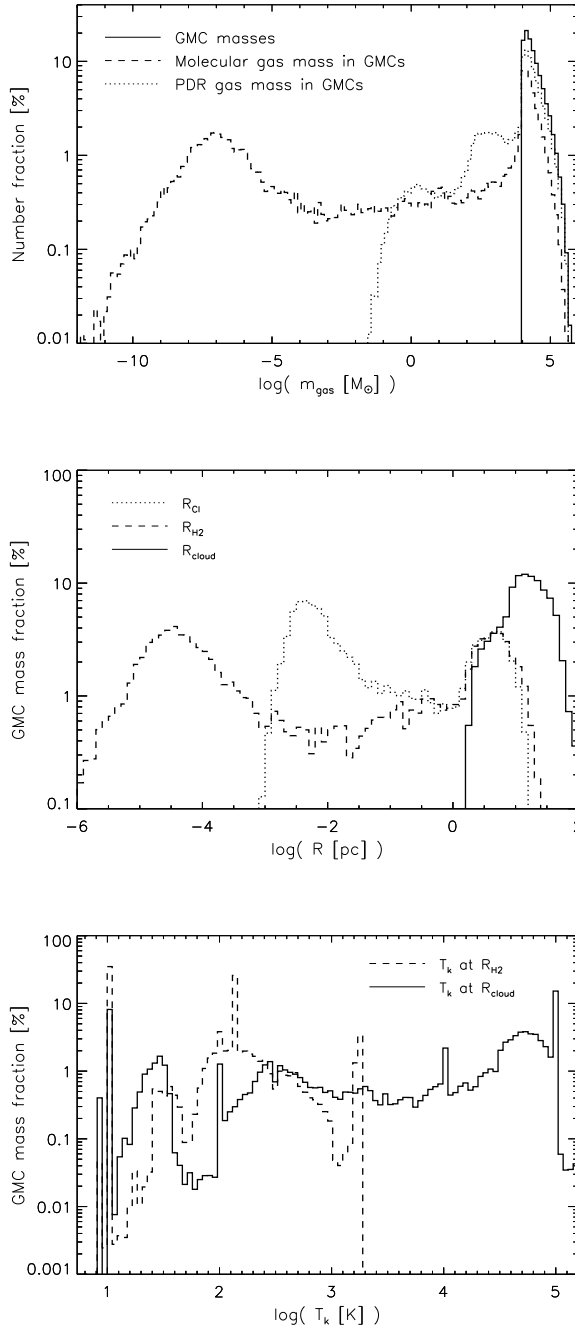


Figure 6.5 Top: The number distribution of GMC masses (solid histogram) together with the number distributions of the molecular (dashed histogram) and PDR (dotted histogram) gas component. **Middle:** GMC-mass-weighted distributions of R_{Cl} (dotted), R_{H_2} (dashed) and R_{cloud} for GMCs in G4. **Bottom:** GMC-mass-weighted distributions of the temperature at R_{H_2} (dashed) and at the cloud surfaces (solid) for GMCs in G4.

6.4.2 THE IONIZED GAS

The ionized gas in our simulations (see eq. 6.2), is assumed to be distributed in spherical clouds of uniform densities and with radii (R_{HII}) equal to the smoothing lengths of the original SPH particles. These ionized regions in our simulations are furthermore assumed to be isothermal with the temperatures equal to that of the SPH gas. Fig. 6.6 shows the size (top) and temperature (bottom) distribution for the ionized clouds in G4. Cloud sizes range from ~ 0.1 kpc to ~ 10 kpc, with more than 60 % of the ionized gas mass residing in clouds of size $\lesssim 1000$ pc. For comparison, the range of observed sizes of HII clouds in nearby galaxies is 10 – 1000 pc (Oey & Clarke, 1997; Hodge et al., 1999). The temperatures range from $\sim 10^2$ K to $\sim 10^6$ K with the bulk of the ionized gas having temperatures $\sim 10^{4-5}$ K.

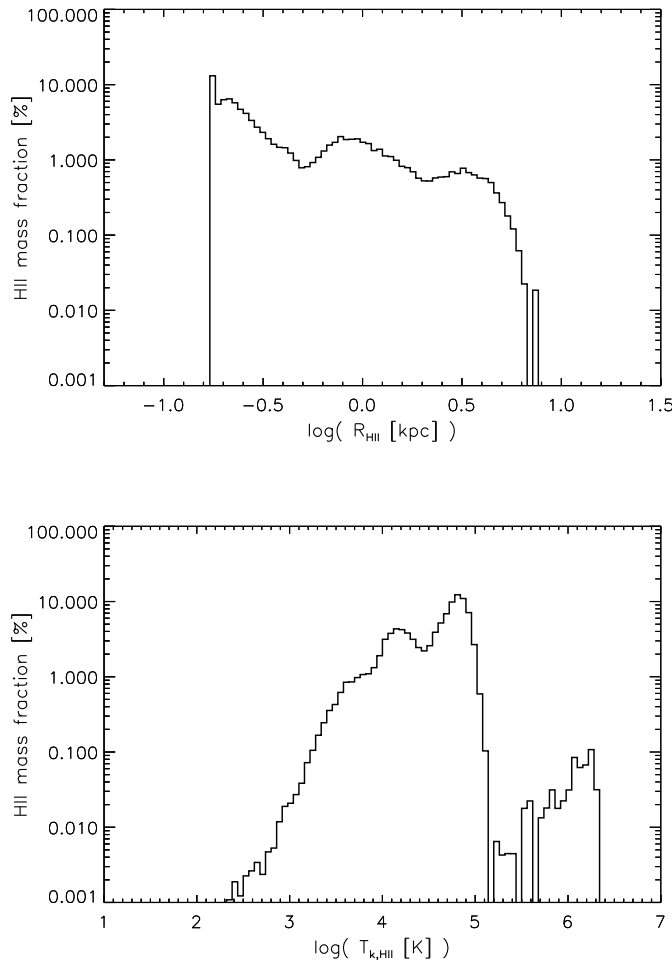


Figure 6.6 Mass-weighted histograms of the size (top) and temperature (bottom) distributions of the ionized clouds in G4.

6.5 THE [CII] LINE EMISSION

The [CII] luminosity of a region of gas is the volume-integral of the effective [CII] cooling rate per volume, i.e.:

$$L_{\text{[CII]}} = \int_{\Delta V} \Lambda_{\text{CII}} dV. \quad (6.17)$$

Since we have adopted spherical symmetry in our sub-grid treatment of the clouds (both neutral and ionized), we have:

$$L_{\text{[CII]}} = 4\pi \int_{R_1}^{R_2} \Lambda_{\text{CII}} R^2 dR, \quad (6.18)$$

where $R_1 = R_{\text{CI}}$ and $R_2 = R_{\text{H}_2}$ for the molecular phase; $R_1 = R_{\text{H}_2}$ and $R_2 = R_{\text{GMC}}$ for the PDR region, and $R_1 = 0$ and $R_2 = R_{\text{HII}}$ for the ionized gas.

The effective [CII] cooling rate is:

$$\Lambda_{\text{CII}} = A_{\text{ul}} \beta f_u n_{\text{CII}} h\nu, \quad (6.19)$$

where A_{ul} ($=2.3 \times 10^{-6} \text{ s}^{-1}$)³ is the Einstein coefficient for spontaneous decay. We ignore the effects of any background radiation field from dust (and the CMB). β is the [CII] photon escape probability for a spherical geometry (i.e., $\beta = (1 - \exp(-\tau))/\tau$, where τ is the [CII] optical depth). f_u is the fraction of singly ionized carbon in the upper ${}^2P_{3/2}$ level and is determined by radiative processes and collisional (de)excitation (see Appendix A.3). The latter can occur via collisions with e^- , HI, or H_2 , depending on the state of the gas. In our simulations the collisional partner is H_2 in the molecular phase, HI and e^- in the PDR regions, and e^- in the ionized gas. Analytical expressions for the corresponding collision rate coefficients as a function of temperature are given in Appendix A.3. n_{CII} is the number density of singly ionized carbon and is given by $n_{\text{CII}} = X_C f_{\text{CII}} n_{\text{H}}$, where f_{CII} is the fraction of carbon atoms in the singly ionized state. For the latter we used tabulated fractions from CLOUDY v13.03 over a wide range in temperature, hydrogen density, FUV field strength, and cosmic ray ionization rate.

We calculate the integral in eq. 6.18 numerically by splitting the $R_2 - R_1$ region up into 100 radial bins. In each bin, n_{H} is set to be constant and – in the case of the molecular and PDR regions – given by the logotropic density profile at the radius of the given bin (Fig. 6.4). For the ionized clouds, n_{H} is constant throughout (Section 6.4.2). For the PDR regions (i.e., from R_{H_2} to R_{GMC}) we assume that the temperature, electron fraction and G_0 are kept fixed to the outer boundary value at R_{GMC} (i.e., no attenuation of the FUV field). This implies that the [CII] luminosity from the PDR gas is an upper limit. Similar for the [CII] emission from the molecular region (i.e., from R_{CI} to R_{H_2}), where we assume that the temperature throughout this region is fixed to its values at R_{H_2} . Also, throughout this region we adopt the attenuated FUV field at R_{H_2} .

³Einstein coefficient for spontaneous emission taken from the LAMDA database: <http://www.strw.leidenuniv.nl/~moldata/>, Schöier et al. (2005)

6.6 RESULTS AND DISCUSSION

Having divided the ISM in our galaxies into molecular, atomic and ionized gas phases, and having devised a methodology for calculating their [CII] emission, we are now in a position to quantify the relative contributions from the aforementioned gas phases to the total [CII] emission, and examine their relationship to the on-going star formation.

6.6.1 RADIAL [CII] LUMINOSITY PROFILES

First, however, to get a sense of the distribution of gas and star formation in our simulated galaxies, we show in Fig. 6.7 surface density maps of the total SPH gas (left column) and star formation rate (middle column) when viewed face-on. The maps reveal spiral galaxy morphologies, albeit with some variety: some (G1, G2 and G3) show perturbed spiral arms due to on-going mergers with satellite galaxies; others (G4, G5, G6 and G7) have seemingly undisturbed, grand-design spiral arms; a central bar-like structure is also seen in some (G2, G4, G5 and G7). Overall, the star formation is seen to be much more centrally concentrated than the SPH gas. This is especially true for G1 and G2, which have very centrally peaked star formation. The radial SFR and [CII] luminosity profiles of G1, ..., G7 – derived by summing up the SFR and the [CII] luminosity within concentric rings (of fixed width: 0.2 kpc) – are also shown in Fig. 6.7. We have inferred the radial [CII] luminosity distribution for the full ISM as well as for the individual gas phases.

The radial SFR profiles of our model galaxies typically peak at $R \sim 0.5$ kpc (in G1 at $R \lesssim 0.5$ kpc) and then tail off with radius. In some cases, local peaks in the star formation activity occur at galactocentric distances $\gtrsim 2$ kpc, corresponding to the locations of either satellite galaxies (G2 and G3) or very dense spiral arms (G5 and G7). In terms of the total [CII] luminosity profiles (grey histograms) tracing the star formation there is a broad agreement in that the former also tends to peak at $R \sim 0.5$ kpc. In fact, for $R \lesssim 1.5$ kpc there is in general a good correspondence between the [CII] emission and the star formation rate. This is due to the fact that the molecular gas dominates the [CII] emission in the central regions and that within this region, the radial [CII] emission profile from this gas phase follows that of the SFR relatively well. At larger galactocentric distances ($R \gtrsim 2$), however, the [CII] emission from the molecular gas not only falls off more quickly than the radial SFR, but local enhancements in the latter are not matched by increased [CII] emission from the molecular gas (e.g. G1, G2, and G3). These SFR enhancements are, however, reflected in the [CII] emission profile of the ionized gas, which is the component that best follows the SFR radial profile, although it never contributes by more than a fraction of the total [CII] emission budget. The PDRs start to dominate the [CII] luminosity already at > 1.5 kpc and remain dominant out to $R \sim 8$ kpc.

Fig. 6.8 displays the fractional [CII] luminosity coming from the different ISM phases, in the top panel for the entire disk ($R < 10$ kpc), in the mid panel only within $R = 1$ kpc and in the bottom panel for the outer disk ($R > 2$ kpc).

In the bottom right panel of Fig. 6.7 we show the Galactic SFR and [CII] luminosity radial profiles from Pineda et al. (2014), who observed the [CII] emission from 1) CO-dark H₂ gas and dense PDRs, 2) cold neutral HI gas, and 3) hot ionized gas in our own Galaxy. In order to facilitate an approximate comparison with our simulations we identify these three Galactic ISM phases with the molecular, atomic, and ionized gas in our simulations. It is important to keep in mind, however, that the ISM in our simulations has a higher pressure, is kinematically more violent, and is more actively forming stars than is the case in our Galaxy.

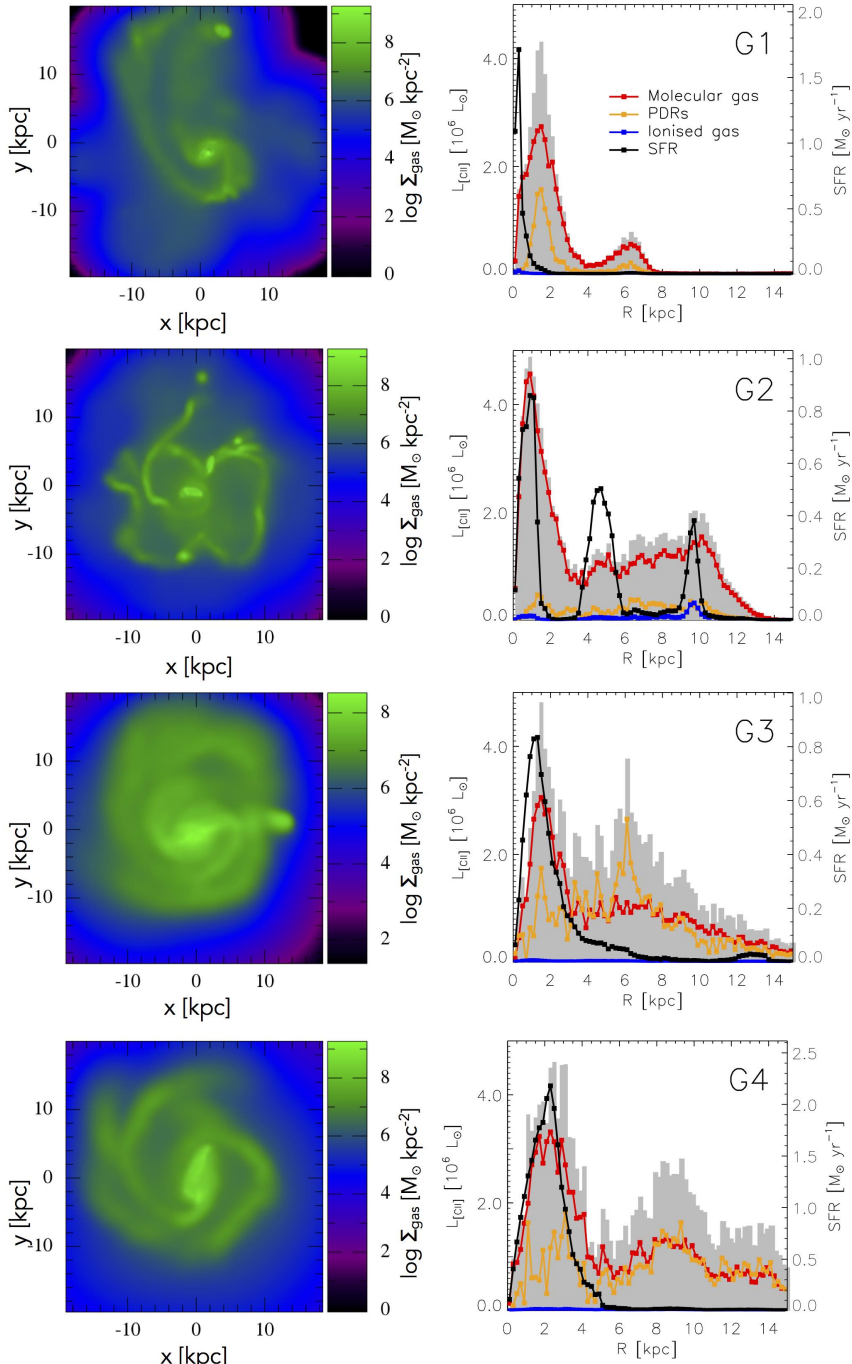


Figure 6.7 Gas and SFR surface density maps (left and middle columns, respectively) of our SPH simulated galaxies viewed face-on (see also Thompson et al. (2015)). The horizontal white bars correspond to a physical scale of 5 kpc. The radial profiles of the total [CII] luminosity (grey histogram) and the contributions from molecular gas (red), PDRs (orange) and ionized gas (blue) are shown in the righthand column. Also shown is the radial SFR profile (black curve) inferred from the 1.4 GHz intensity distribution (Pineda et al., 2014).

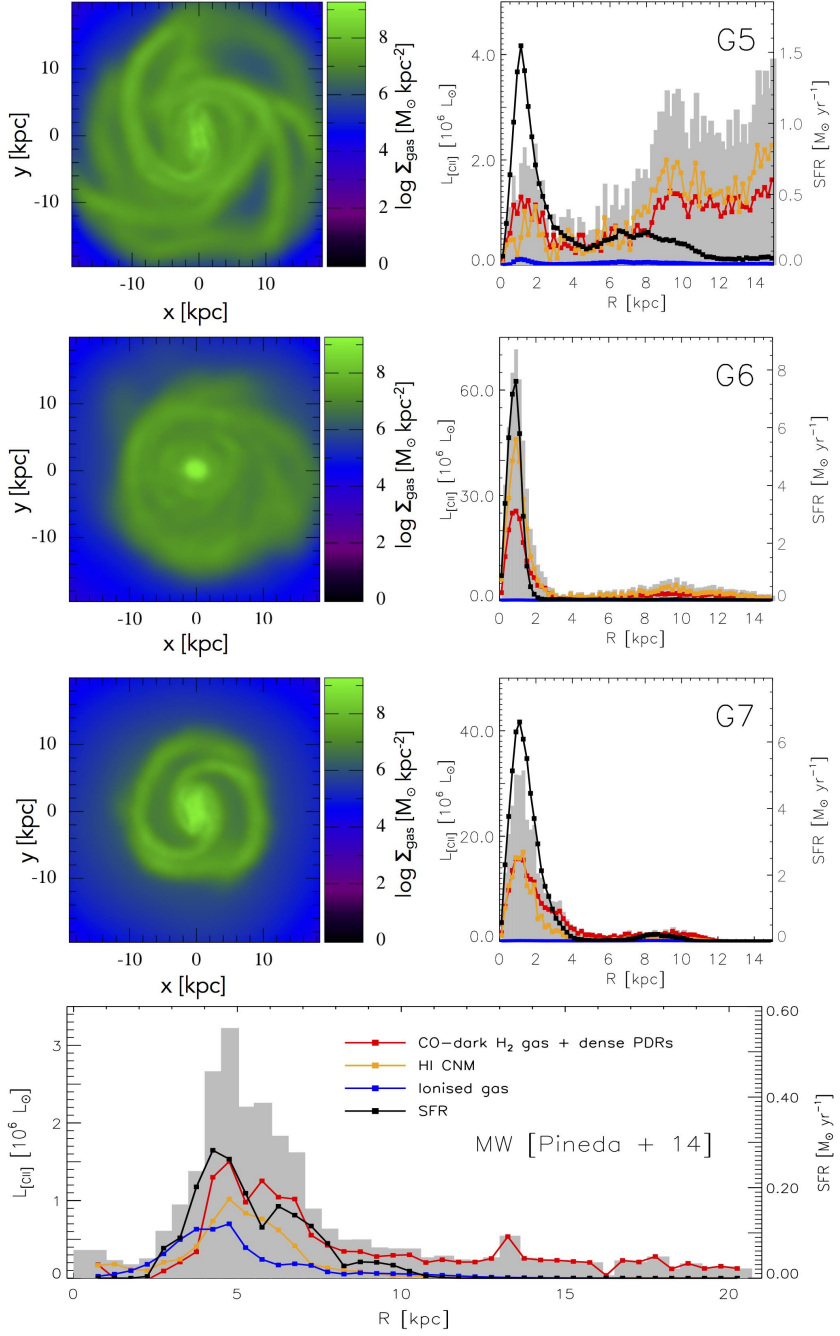


Figure 6.7 Continued. Bottom panel shows, as a reference, the radial L_{CII} profile of the Galaxy (grey histogram) along with the contributions from CO-dark H₂ gas and dense PDRs (red curve), cold H₁ (orange curve), and ionized gas (blue curve) (Pineda et al., 2014).

The SFR and [CII] profiles in our Galaxy peak at larger radii ($R \sim 4 - 5$ kpc) than in our simulated galaxies. This is not surprising given the low content of star formation and gas in

the Galactic bulge, and the fact that the bulk of star formation in our Galaxy takes place in the disk. In contrast, gas is still being funneled towards the centre in our simulations where it is converted into stars. Thus the SFR level in our simulated galaxies is much higher (by $\gtrsim 10\times$) and more centrally concentrated than in our Galaxy, where stars form at a rate of $0.1 \text{ M}_\odot \text{ yr}^{-1}$ out to $R \gtrsim 8 \text{ kpc}$. Remarkably, significant levels of [CII] emission extend out to $R \sim 20 \text{ kpc}$ in our Galaxy, well beyond the point where star formation has ceased. Here, the emission is completely dominated by CO-dark H₂ gas and dense PDR regions. This is similar to the picture seen in our simulated galaxies where the [CII] emission at large radii is dominated by a neutral gas phase – designated PDR gas in our simulations, dubbed CO-dark H₂ + dense PDR gas in Pineda et al. (2014) – that is seemingly uncoupled from star formation. The radial [CII] profile of the ionized gas in the Galaxy roughly follows the SFR profile, as is the case in our simulations.

6.6.2 THE INTEGRATED $L_{[\text{CII}]}$ -SFR RELATION

(Karen: Moved this paragraph down here, from previous section:) In terms of integrated luminosities (i.e. within $R \leq 10 \text{ kpc}$), the molecular gas can constitute from $\sim 32\%$ (G1) to $\sim 91\%$ (G7) of the total [CII] luminosity; for the PDR gas the range is $\sim 8\%$ (G7) to $\sim 68\%$ (G1); the contribution from the ionized gas is $\lesssim 1\%$ (Fig. 6.8). In the Galaxy, however, the this phase seems to be a more important contributor to the overall [CII] budget. Pineda et al. (2014) estimates that 55 % of the total Galactic [CII] luminosity is from molecular gas and dense PDRs, 25 % from cold HI, and 20 % from the ionized gas.

Fig. 6.9 shows the integrated $L_{[\text{CII}]}$ – SFR relations for our model galaxies, first for their entire ISM in the top panel, and in separate panels below for each of the three ISM phases considered in our simulations.

When considering the entire ISM a tight correlation between $L_{[\text{CII}]}$ and SFR emerges, which is well fit in log-log space by a straight line with slope 1.27 ± 0.17 (solid line in the top panel). This relation is largely set by the molecular and PDR gas phases. The molecular gas phase, itself exhibiting a strong correlation between [CII] and SFR with slope 1.72 ± 0.22 , drives the slope of the total correlation. The PDR gas on the other hand, exhibits a weak dependence on [CII] with a slope of 0.43 ± 0.20 but contributes significantly to the overall normalization of the total [CII] – SFR relation, especially at the low SFR end (see Fig. 6.9). The [CII] emission from the ionized gas also shows a weak dependency on SFR (slope 0.44 ± 0.30) compared to the molecular gas but, again, does not contribute significantly to the total [CII] emission, its normalization factor being $\gtrsim 10\times$ below that of both the PDR and molecular gas at the low SFR end of our sample (Fig. 6.9, bottom panel).

In the top panel of Fig. 6.9 we compare the $L_{[\text{CII}]}$ – SFR relation obtained from our simulated galaxies with various samples compiled from the literature of [CII] detected galaxies in the redshift range $z \sim 0 - 6.5$. In terms of the slope of the $L_{[\text{CII}]}$ – SFR relation our model galaxies display a steeper slope (1.27 ± 0.17) than do $z \sim 0$ normal star-forming spiral galaxies with similar levels of SFR ($\sim 0.2 - 100 \text{ M}_\odot \text{ yr}^{-1}$; Malhotra et al. 2001), which have a slope of unity. The latter is obtained from a power-law fit to the [CII] and FIR (42.5 – 122.5 μm) luminosities (in units of L_\odot) of the Malhotra et al. (2001) sample: $L_{[\text{CII}]} = 10^{-2.51} L_{\text{FIR}}$ (Magdis et al., 2014), which we then convert to $L_{[\text{CII}]} = 1.05 \times 10^7 \text{ SFR}$ using $\text{SFR} = L_{\text{FIR}} / 3.4 \times 10^9$. This relationship is shown as the dotted line in Fig. 6.9. While the slope of our model galaxies differ by $> 1\sigma$ from the $z \sim 0$ sample (spirals and (U)LIRGs), their luminosities agree at least on the low SFR

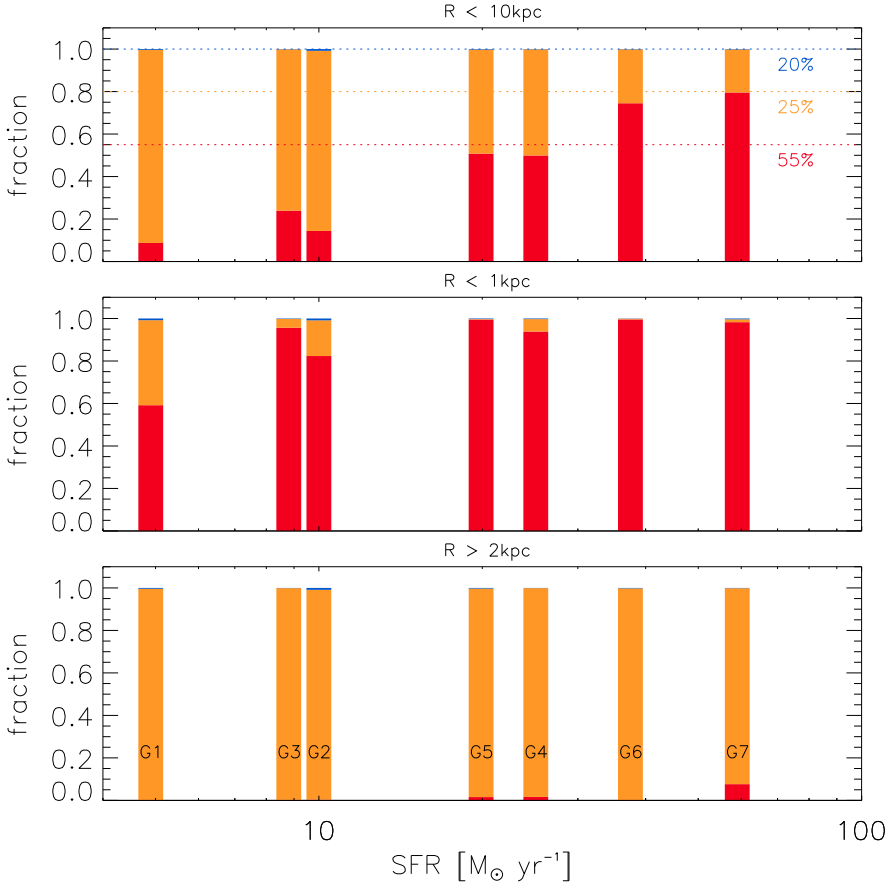


Figure 6.8 Contributions to the total [CII] luminosity from the molecular (red), PDR (yellow), and ionized (blue) gas phases for each of our simulated galaxies, ranked according to their total SFRs. The three panels show the relative contributions within $R < 10$ kpc (top), for $R < 1$ kpc (middle), and for $R > 2$ kpc (bottom). The horizontal dashed lines and the percentages given indicate the relative contributions to the total [CII] luminosity of our own Galaxy from CO-dark H₂ + dense PDR gas (red; 55%), cold atomic gas (yellow; 25%), and ionized gas (blue; 20%) (Pineda et al., 2014).

side, where the two relations cross at $\text{SFR} \sim 10 \text{ M}_\odot \text{ yr}^{-1}$.

A direct comparison with [CII] detected galaxies at high redshifts is complicated by the fact that the latter typically have significantly larger SFRs than our model galaxies. Furthermore, high- z samples are often heterogeneous (e.g., significant AGN contribution, cf. Gullberg et al., 2015). It is clear from Fig. 6.9, however, that the observed high- z galaxies lie significantly below the trend defined by our model galaxies extended to higher SFRs. For example, a power-law fit to the $z > 1$ star-forming galaxies with $\text{SFR} \gtrsim 300 \text{ M}_\odot \text{ yr}^{-1}$ compiled by D14 yields: $L_{[\text{CII}]} = 1.7 \times 10^7 \text{ SFR}^{0.85}$ (D14; shown as the dashed line in Fig. 6.9), i.e. $> 1\sigma$ below our slope (1.27 ± 0.17). However, restricting our findings to the [CII] emission of moderately star-forming galaxies, we find that the global $L_{[\text{CII}]} - \text{SFR}$ relation matches extragalactic observations, but only when the [CII] emission from all ISM phases is included, in concurrence with the conclusions of Pineda et al. (2014).

Finally, we note that the scatter of our simulated galaxies around their best-fit relation is 0.14 dex, which is significantly lower than the observed scatter of typically 0.2 – 0.4 dex (e.g.

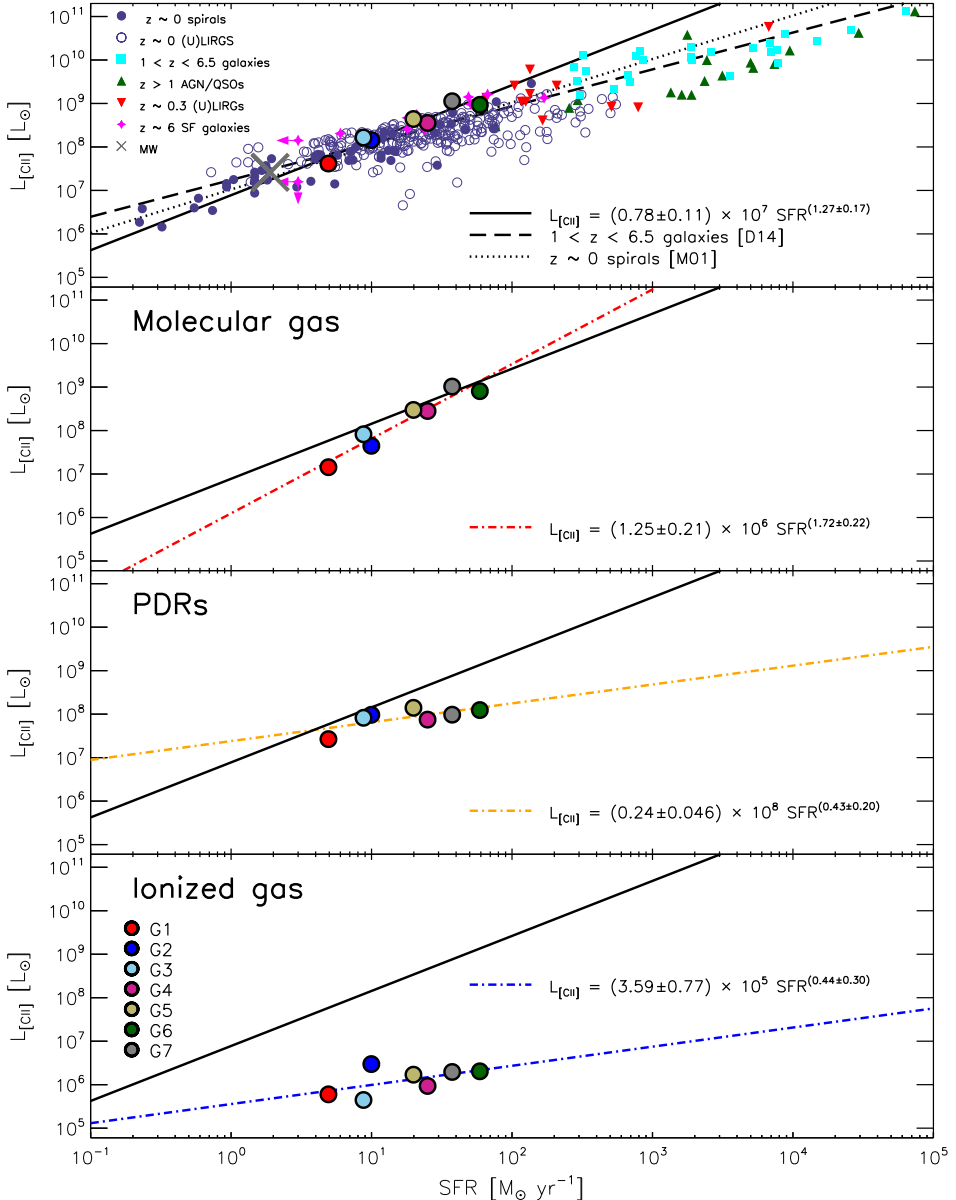


Figure 6.9 $L_{\text{[CII]}}$ vs. SFR for our simulated galaxies (big filled circles). The same color-coding as in Fig. 6.2 is used and listed again for convenience in the bottom panel. From top to bottom panel we show the [CII] luminosity from the full ISM (grey), the molecular gas (red), PDRs (orange), and ionized gas (blue). For comparison, we show individual [CII] observations of 54 $z \sim 0$ spirals (purple filled circles; Malhotra et al., 2001), with the best fit to this sample given by the dotted line (see main text for details). Also shown are 240 $z \sim 0$ (U)LIRGs (purple open circles; Díaz-Santos et al., 2013; Farrah et al., 2013), and 12 $z \sim 0.3$ (U)LIRGs (red triangles; Magdis et al., 2014). The high- z comparison samples include 25 $1 < z < 6$ star-forming galaxies (cyan squares; D14) and the dashed line indicate the best fit to this sample. Also shown are 16 $z \sim 4 - 7$ QSOs (green triangles; Iono et al., 2006; Walter et al., 2009; Wagg et al., 2010; Gallerani et al., 2012; Wang et al., 2013; Venemans et al., 2012; Carilli et al., 2013; Willott et al., 2013), and 10 normal star-forming $z \sim 5 - 6$ galaxies (magenta stars) observed by Capak et al. (2015). The Galaxy is shown for reference with a grey cross (Pineda et al., 2014).

D14). We attribute this to the fact that our simulated galaxies constitute a fairly homogeneous (and small) sample spanning a rather small range in, for example, SFR, $L_{\text{[CII]}}$, and Z' , unlike the observed samples with which we are comparing.

6.6.3 THE RESOLVED $\Sigma_{\text{[CII]}} - \Sigma_{\text{SFR}}$ RELATION

In Fig. 6.10, we show the combined $\Sigma_{\text{[CII]}} - \Sigma_{\text{SFR}}$ relation of all seven simulated galaxies in their face-on configuration, for the entire ISM (top panel) and for each of the separate gas phases (bottom three panels). Surface densities were determined within $1 \text{ kpc} \times 1 \text{ kpc}$ regions. Contours reflect the number of regions at a given $(\Sigma_{\text{SFR}}, \Sigma_{\text{[CII]}})$ -combination and are given as percentages of the peak number of regions.

Given the variations in the local star formation conditions within our model galaxies, we can explore the relationship between [CII] and star formation over a much wider range of star formation intensities than is possible with the integrated quantities. A $\Sigma_{\text{[CII]}} - \Sigma_{\text{SFR}}$ correlation spanning more than five decades in Σ_{SFR} is seen for the entire ISM as well as for the individual ISM phases. Similar to the integrated [CII] vs. SFR relations in the previous section, the molecular and PDR phases dominate the resolved [CII] emission budget at all star formation rate surface densities, and with the molecular relation being steeper and exhibiting a larger degree of scatter. Again, the contribution from the ionized phase, while clearly depending on Σ_{SFR} , is largely negligible at all star formation densities.

We compare the $\Sigma_{\text{[CII]}} - \Sigma_{\text{SFR}}$ relation for our simulated galaxies to that of three resolved surveys of nearby galaxies: 1) the $\sim 50 \text{ pc}$ -scale relation derived from five $3' \times 3'$ fields towards M31 (K15; shown as green points in Fig. 6.10), 2) the kpc-scale relation obtained for 48 local dwarf galaxies covering a wide range in metallicities ($Z/Z_{\odot} = 0.02 - 1$, D14; cyan crosses), and 3) the kpc-scale relations for mostly spiral galaxies (H15; magenta contours). The data from these surveys have been converted to the Chabrier IMF assumed by our simulations by multiplying Σ_{SFR} with a factor 0.94 when a Kroupa IMF was adopted (D14; K15) or 0.92 when a truncated Salpeter IMF was used (H15), following Calzetti et al. (2007) and Speagle et al. (2014). Regarding the observations by H15, we adopt the raw $\Sigma_{\text{[CII]}}$ measurements rather than the IR-color-corrected ones. From Fig. 6.10 it is clear that over the range in Σ_{SFR} ($\sim 0.001 - 1 M_{\odot} \text{ yr}^{-1} \text{ kpc}^{-2}$) spanned by these three surveys, the $\Sigma_{\text{[CII]}} - \Sigma_{\text{SFR}}$ relation defined by our simulations is shallower than the observations, with a slope of 0.60 ± 0.02 compared to slopes in the range $0.67 - 0.76$ found by K15 for the five fields in M31, with an average of 0.77. In addition, the $\Sigma_{\text{[CII]}} - \Sigma_{\text{SFR}}$ relation of our model galaxies overshoots the observations, which could be either an issue with the model or an actual difference between typical ISM locally and at $z = 2$.

Beyond the above Σ_{SFR} -range a comparison with the observations has to rely on extrapolations of the simple power-law fits to the observed $\Sigma_{\text{[CII]}} - \Sigma_{\text{SFR}}$ relations (shown as dashed, dotted, and dash-dotted lines for D14, H15, and K15, respectively. See Fig. 6.10). At low Σ_{SFR} ($\lesssim 0.001 M_{\odot} \text{ yr}^{-1} \text{ kpc}^{-2}$), our simulations predict [CII] emission levels $\gtrsim 10 \times$ higher than the survey-based extrapolations. This excess [CII] emission is driven by the PDR gas in our simulations (second panel in Fig. 6.10) and its very shallow, nearly constant, $\Sigma_{\text{[CII]}} - \Sigma_{\text{SFR}}$ relationship. Interestingly, in at least two of the five fields in M31 studied by K15 (green dots), a similar – albeit much less severe – [CII]-excess relative to the power-law fit (dashed line) is observed at $\Sigma_{\text{SFR}} \lesssim 0.001 M_{\odot} \text{ yr}^{-1} \text{ kpc}^{-2}$ (see also Fig. 7 in K15). K15 argues that the excess is due to a contribution from diffuse, ionized gas (HII), although they cannot discount the possibility that

the larger dispersion is at least partly due to being close to the sensitivity limit of their survey at such low Σ_{CII} . Our simulations, however, clearly show no significant contribution from the diffuse HII gas phase at low Σ_{SFR} .

At high Σ_{SFR} ($\gtrsim 0.1 \text{ M}_\odot \text{ yr}^{-1} \text{ kpc}^{-2}$), our $z = 2$ simulations predict less [CII] emission than do the locally observed relation, due to the dominating PDR gas which flattens out at low Σ_{SFR} and sets the shallow slope of our model galaxies. But, reassuringly, the contours of our models incorporate the few observations so far made at $\Sigma_{\text{SFR}} \gtrsim 0.1 \text{ M}_\odot \text{ yr}^{-1} \text{ kpc}^{-2}$, i.e. the sample from D14 (cyan points in Fig. 6.10) and the $z = 4.76$ galaxy observed last year by (red cross; De Breuck et al. 2014).

The aforementioned studies of local galaxies typically measure both obscured (e.g. from $24 \mu\text{m}$) and un-obscured (from either FUV or H α) SFRs in order to estimate the total Σ_{SFR} and, while intrinsic uncertainties are inherent in the empirical $24 \mu\text{m}/\text{FUV}/\text{H}\alpha \rightarrow \text{SFR}$ calibrations, the Σ_{SFR} values should therefore be directly comparable to those from our simulations. Nonetheless, some caution is called for when comparing our simulations to resolved observations, primarily regarding the determination of Σ_{SFR} on $\lesssim \text{kpc}$ -scales. In particular, as pointed out by D14, the emission from old stellar populations in diffuse regions with no ongoing star formation can lead to overestimates of the SFR when using the above empirical SFR calibrations. Both K15 and H15 account for this by subtracting the expected cirrus emission from old stars in $24 \mu\text{m}$ (using the method presented in Leroy et al. 2012), although on scales $\ll 1 \text{ kpc}$ this correction for $24 \mu\text{m}$ cirrus emission becomes particularly challenging as it was calibrated on $\gtrsim 1 \text{ kpc}$ scales. K15 further points to the problem arising from the possibility of photons leaking between neighboring stellar populations, meaning that average estimates of the SFR on scales $< 50 \text{ pc}$ might not represent the true underlying SFR.

6.6.4 PHYSICAL UNDERPINNINGS OF THE $L_{\text{[CII]}}$ -SFR RELATION

It is well-known that both at low and high redshifts, the star formation rate of galaxies is strongly correlated with their molecular gas content (as traced by CO) (e.g. Kennicutt, 1998; Daddi et al., 2010; Genzel et al., 2010; Narayanan et al., 2012). This SFR – H $_2$ dependency is directly incorporated into the SPH simulations (see Section 6.3), and it is therefore natural to ask whether the integrated [CII] – SFR relation examined in Section 6.6.2 might simply be a case of galaxies with higher star formation rates having larger (molecular) gas masses with higher associated [CII] luminosities. To investigate this, we show in Fig. 6.11 [CII] luminosity vs. gas mass for the full ISM in our simulated galaxies and for their gas phases separately. For the molecular gas we see a strong luminosity–mass scaling (red curve), which would explain the strong $L_{\text{[CII]}}$ –SFR relation for this phase and, at least in part, the $L_{\text{[CII]}}$ –SFR relation for the full ISM. Clearly, the atomic PDR gas and the ionized gas do not exhibit a similar luminosity–mass scaling. Since, on average, significantly more mass resides in each of these two phases than in the molecular phase, this has the effect of weakening the $L_{\text{[CII]}}$ – SFR relation for the full ISM.

The abundances of metals in the ISM is expected to affect the [CII] emission. In their study of low-metallicity dwarf galaxies, D14 compared total (IR+UV) SFRs to SFRs derived using the best-fit $L_{\text{[CII]}}$ – SFR relation to their entire sample. They found an increase in the $\text{SFR}_{\text{IR+UV}}/\text{SFR}_{\text{CII}}$ fraction, corresponding to weaker [CII] emission, towards lower metallicities. In Fig. 6.12 we show $\text{SFR}/L_{\text{[CII]}}$ as a function of $Z_{\text{O/H}}$ ($= 12 + \log [\text{O}/\text{H}]$) for our simulated galaxies as well as for the dwarf galaxy sample of D14. As D14 points out, $Z_{\text{O/H}}$ does not take into account potential deficits of carbon relative to the [O/H] abundance, potentially obscur-

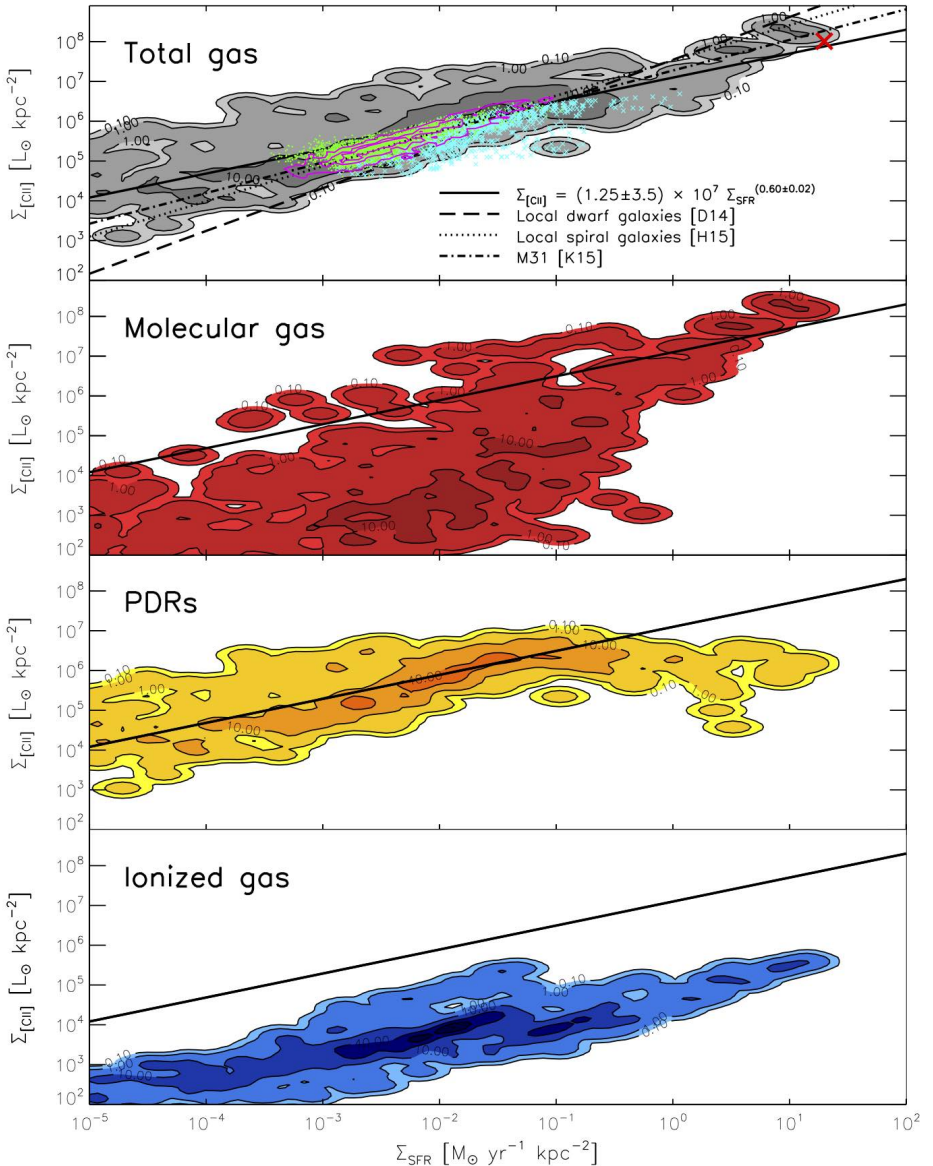


Figure 6.10 $[\text{CII}]$ luminosity surface density ($\Sigma_{\text{[CII]}}$) vs. SFR surface density (Σ_{SFR}) for the full ISM in our simulated galaxies (top panel), and for each of the three ISM phases (bottom three panels). $\Sigma_{\text{[CII]}}$ and Σ_{SFR} are determined over $1 \text{ kpc} \times 1 \text{ kpc}$ regions within all 7 galaxies. The filled colored contours indicate the number of such regions with this combination of Σ_{SFR} and $\Sigma_{\text{[CII]}}$ as a percentage (at 0.1, 1, 10, 40 and 70 %) of the maximum number of regions. The solid line shown in all panels is the best-fit power-law to the total gas $\Sigma_{\text{[CII]}}$ vs. Σ_{SFR} (see legend). For comparison we show observed $\Sigma_{\text{[CII]}}$ vs. Σ_{SFR} for individual 20 pc regions in M 31 (green dots; K15), 1 kpc regions in nearby (mostly spiral) galaxies (magenta contours; H15), and 1 kpc regions in local dwarf galaxies (cyan crosses; D14). The best-fit power-laws to these three datasets are shown as dash-dotted, dotted, and dashed lines, respectively. In the case of M 31 the power-law is fitted to 50 pc regions (see K15). We also show the galaxy-averaged $\Sigma_{\text{[CII]}}$ and Σ_{SFR} of ALESS 73.1 ($z = 4.76$) submillimeter-selected galaxy which was marginally resolved in $[\text{CII}]$ and in the FIR continuum with ALMA, revealing a source size of $R \sim 2 \text{ kpc}$, $L_{\text{[CII]}} = 5.15 \times 10^9 L_{\odot}$, and $\text{SFR} \sim 1000 M_{\odot} \text{ yr}^{-1}$ (De Breuck et al., 2014).

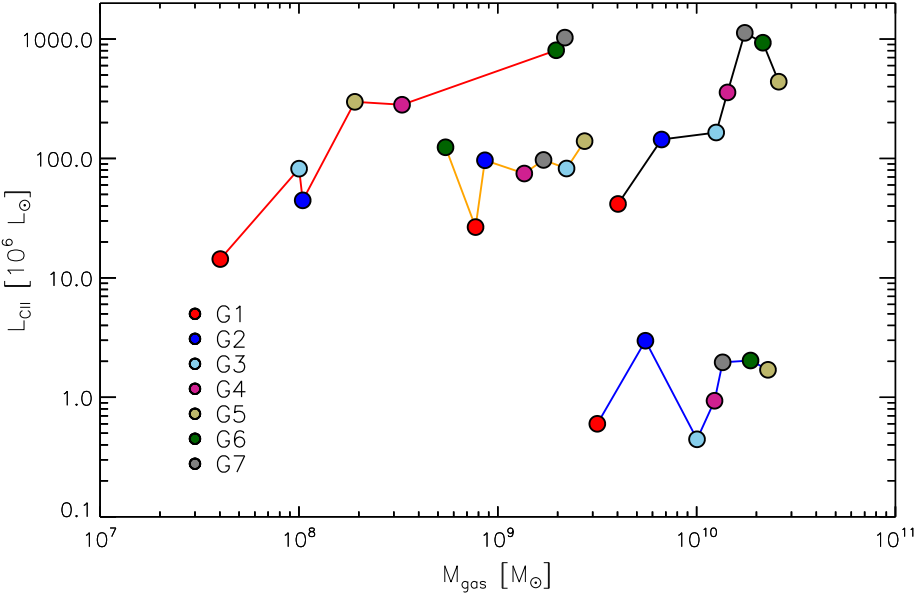


Figure 6.11 [CII] luminosity versus mass for the total ISM (black line), the molecular (red line), PDR (orange line), and HII (blue line) gas phase. The [CII] emission from the molecular gas is seen to increase with the amount of molecular gas available, whereas this is not the case for gas associated with PDRs and HII regions.

ing any potential correlation between [CII] luminosity and actual carbon abundance. In Fig. 6.12 we therefore also plot $SFR/L_{[CII]}$ as a function of $Z_{[C/H]} (= 12 + \log [C/H])$. No trend in $SFR/L_{[CII]}$ is seen for our model galaxies. This is not surprising, since they span a limited range in $Z_{[O/H]}$ ($8.03 - 8.96$) and, as we saw in Section 6.6.2, form a tight (0.1 dex) [CII] – SFR relation.

To better understand how the metallicity and also the ISM pressure affects the [CII] emission, we define a ‘[CII] emission efficiency’ ($\text{.pdf}_{\text{ilon}}_{[CII]}$) of a given gas phase as the [CII] luminosity of the gas phase divided by its mass, and examine how it depends on Z' and P_{ext}/k_B . Specifically, we create a grid of $(Z', P_{\text{ext}}/k_B)$ values, and in each grid point the median $\text{.pdf}_{\text{ilon}}_{[CII]}$ of all clouds in our simulated galaxies is calculated. The resulting $\text{.pdf}_{\text{ilon}}_{[CII]}$ contours as a function of Z' and P_{ext}/k_B are shown in Fig. 6.13 for the molecular (top), PDR (middle), and HII (bottom) phases. For comparison, we also show the median Z' - and P_{ext}/k_B -values for each of our galaxies.

The molecular phase in our simulations is seen to radiate most efficiently in [CII] at relatively high metallicities ($\log Z' \sim 0.5$) and cloud external pressures ($P_{\text{ext}}/k_B \sim 10^6 \text{ cm}^{-3} \text{ K}$). The PDR and ionized phases, however, have their maximal $\text{.pdf}_{\text{ilon}}_{[CII]}$ at $\log Z' \gtrsim 0$ and $P_{\text{ext}} \sim 10^4 \text{ cm}^{-3} \text{ K}$, i.e. at $\sim 100\times$ lower pressures than the molecular phase, and can maintain a significant [CII] efficiency ($\gtrsim 20\%$) even at $P_{\text{ext}}/k_B \sim 10^2 \text{ cm}^{-3} \text{ K}$ provided $\log Z' \gtrsim 0$. This is consistent with our finding in Section 6.6.1, that the molecular phase dominates the [CII] emission in the central, high-pressure regions, while the PDR gas dominates further out in the galaxy where the ISM pressure is less extreme. In all three panels, G6 and G7 lie in regions of high $\text{.pdf}_{\text{ilon}}_{[CII]}$ ($\gtrsim 50\%$ for the molecular and PDR gas). Thus, the reason why these two galaxies have the highest total [CII] luminosities is in part due to the fact that they have

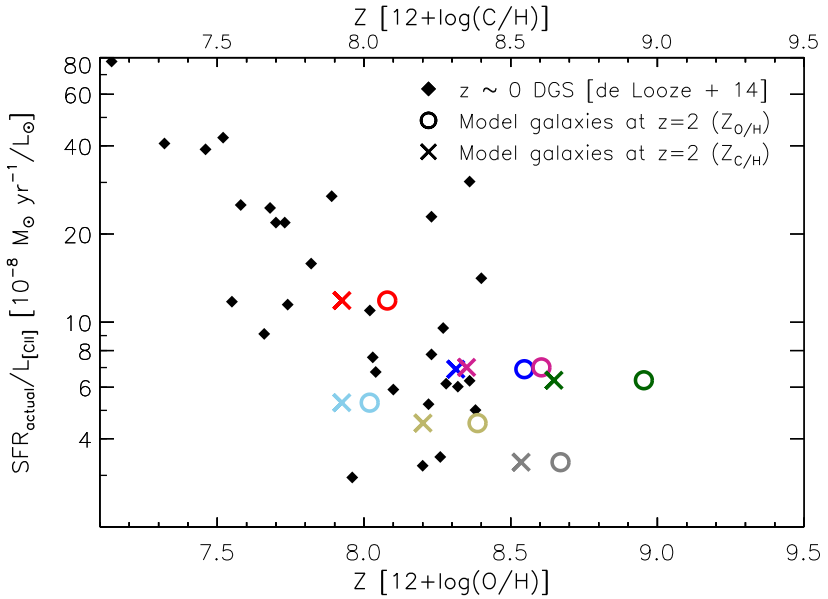


Figure 6.12 SFR/ $L_{\text{[CII]}}$ as a function of metallicity for our model galaxies. The metallicity is parametrized both relative to the oxygen (circles) and the carbon (crosses) abundance. The galaxies are color coded in the usual manner. For comparison, we show SFR/ $L_{\text{[CII]}}$ for the local dwarf galaxy sample of D14, where SFRs are from combined UV and 24 μm measurements.

the highest molecular gas masses (by nearly an order of magnitude, see Fig. 6.11), and in part due to the bulk of their cloud population (GMCs or ionized clouds) having sufficiently high metallicities (on average $\gtrsim 5\times$ higher than G2) and experiencing external pressures ($\sim 100\times$ higher on average than the remaining galaxies) which drives their [CII] efficiencies up.

6.7 COMPARING WITH OTHER [CII] SIMULATIONS

A direct quantitative comparison with other [CII] emission simulation studies in the literature (Nagamine et al., 2006; Vallini et al., 2013, 2015; Popping et al., 2014a; Muñoz & Furlanetto, 2013) is complicated by the fact that there is not always overlap in the masses and/or redshifts of the galaxies simulated by the aforementioned studies and our model galaxies. Furthermore, there are fundamental differences in the simulation approach, with some adopting semi-analytical models (Popping et al., 2014a; Muñoz & Furlanetto, 2013) and others adopting SPH simulations (Nagamine et al., 2006; Vallini et al., 2013, 2015). Also, differences in the numerical resolution of both types of simulations, and in the specifics of the sub-grid physics implemented, can lead to diverging results and make comparisons difficult.

The method presented here for estimating [CII] emission in galaxies combines cosmological galaxy simulations with a sub-grid treatment of a multi-phase ISM that is locally heated by FUV radiation and cosmic rays in a manner that depends on the local star formation rate density within the galaxies. We have applied our method to a high resolution ($\delta m_{\text{SPH}} \simeq 1.7 \times 10^4 M_\odot$) cosmological SPH simulation of $z = 2$ star-forming galaxies (i.e., baryonic mass resolution $\delta m_{\text{SPH}} \simeq 1.7 \times 10^4 M_\odot$ and gravitational softening length $\simeq 0.6 h^{-1} \text{kpc}$, see Section 6.3). In

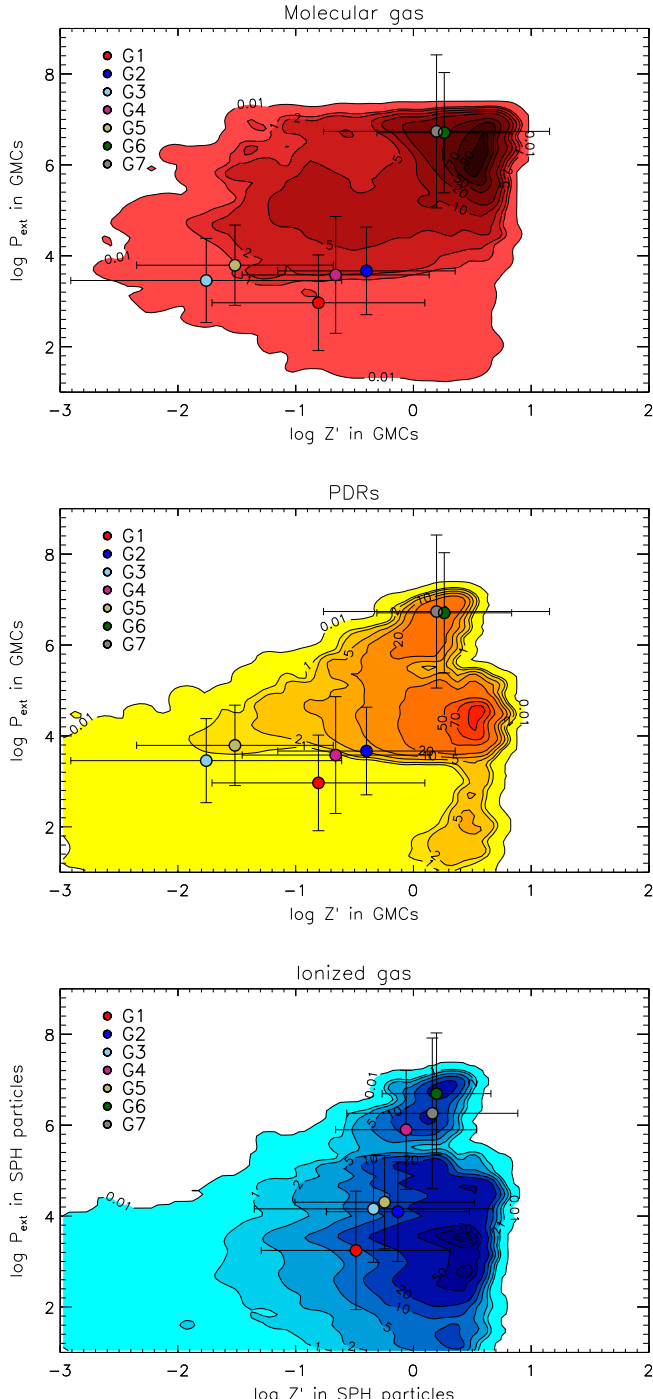


Figure 6.13 Contours of (median) $.pdfilon_{[CII]}$ (i.e. $[CII]$ luminosity per gas mass) as a function of Z' and P_{ext}/k_B for the molecular (top), PDR (middle), and HII (bottom) gas phases in our model galaxies. In each panel the contours indicate 0.01, 1, 2, 5, 10, 20, 50, 70, and 90% percentages of the maximum efficiency. For reference, the maximum (median) $.pdfilon_{[CII]}$ for the molecular, PDR, and ionized gas phases are: 3.7, 6.6, and $0.02 L_\odot/M_\odot$, respectively. Median values of Z' and P_{ext}/k_B and for the GMC and ionized cloud population in each model galaxies are indicated as colored circles (error bars are the 1σ dispersion of the distributions).

our simulations molecular, neutral and ionized ISM phases are considered simultaneously as contributors to the [CII] emission, for the first time in the history of [CII] simulations. Another unique feature of our model is the inclusion of CRs as a route to produce C⁺ deep inside the GMCs where UV photons cannot penetrate (see Section 6.5).

Our simulations probably come closest – both in terms of methodology and galaxies simulated – to those of Nagamine et al. (2006) and Vallini et al. (2015) who both employed cosmological simulations with GADGET-2 (the precursor for GADGET-3 used here) to predict total [CII] luminosities. Nagamine et al. (2006) used their modeling to calculate the [CII] emission from dark matter halos associated with $z \simeq 3$ lyman break galaxies (LBGs) with $M_* \sim 10^{10} M_\odot$ and SFR $\gtrsim 30 M_\odot \text{ yr}^{-1}$ (see also Nagamine et al., 2004). Their simulations employed gas mass resolutions in the range $\delta m_{\text{SPH}} \simeq 3 \times 10^{5-8} M_\odot$ and gravitational softening lengths of typically $> 1 h^{-1} \text{ kpc}$. In their simulations the ISM consist of a cold neutral medium ($T \sim 80 \text{ K}$ and $n \sim 10 \text{ cm}^{-3}$) and a warm neutral medium ($T \sim 8000 \text{ K}$ and $n \sim 0.1 \text{ cm}^{-3}$) in pressure-equilibrium, and the assumption is made that the [CII] emission only originates from the former phase. The thermal balance calculation of the ISM includes heating by grain photo-electric effect, cosmic rays, X-rays, and photo-ionization of CI – all of which are assumed to scale on the local SFR surface density. Their simulations predict $L_{[\text{CII}]} \sim (0.3 - 1) \times 10^8 L_\odot$ for their brightest LBGs (SFR $\gtrsim 30 M_\odot \text{ yr}^{-1}$) which is slightly below the prediction of our integrated [CII] – SFR, namely about $L_{[\text{CII}]} \sim 6 \times 10^8 L_\odot$ (Fig. 6.9). Vallini et al. (2015) improve on their 2013 model, by implementing a density-dependent prescription for the metallicity of the gas, as opposed to a single, fixed value, as well as including the contribution from PDRs (in addition to a previous two-phased CNM+WNM model) and accounting for the effect of the Cosmic Microwave Background (CMB) on the [CII] luminosity. With a cosmological SPH simulation of mass resolution $\delta m_{\text{SPH}} = 1.32 \times 10^5 M_\odot$, Vallini et al. (2015) predict the [CII] emission coming from the ISM of a $z \approx 7$ galaxy. By adopting a range of different SFRs, the authors find that the [CII] emission is dominated by the PDRs, with $< 10\%$ coming from the CNM. This is qualitatively consistent with the results from our simulations at $z = 2$ where the PDR gas dominates the total [CII] emission at least at the low SFR end ($\lesssim 10 M_\odot \text{ yr}^{-1}$). However, our model does not incorporate the CNM to the same extent as that of Vallini et al. (2015), as the PDR gas (expected to contain the CNM) of our model is at relatively high densities with distributions that peak at $\sim 100 - 10,000 \text{ cm}^{-3}$, well above typical CNM densities. It is therefore reassuring that Vallini et al. (2015) find the CNM to be an insignificant contributor, at least at high- z .

The work of Muñoz & Furlanetto (2013) also focuses on $z \gtrsim 6$ galaxies, however with the help of semi-analytical galaxy models adopting different inflow models. In their study, they consider only the PDRs as contributors to the [CII] emission and keep the metallicity fixed to solar ($Z' = 1$), making a comparison to this work difficult. However, contrary to the extrapolation of our model galaxies at $z = 2$ to high- z , Muñoz & Furlanetto (2013) arrive at relatively low [CII] luminosities compared to high- z observations. At the same time, the authors overpredict the CO line emission, which is taken as a hint of lacking amount of singly ionized carbon as opposed to CO or H₂ in the model galaxies, hence demonstrating the force of combining modeling of atomic and molecular emission.

Employing a semi-analytical model of galaxy formation, Popping et al. (2014a) made predictions of the integrated [CII] luminosity from galaxies at $z = 2$ with $M_* \sim 10^8 - 10^{12} M_\odot$ and SFR $\sim 0.1 - 100 M_\odot \text{ yr}^{-1}$ (see also Popping et al., 2014b). The galaxies are assumed to have exponential disk gas density profiles, with randomly placed ‘over-densities’ mimicking GMCs (constituting $\sim 1\%$ of the total volume). The gas is embedded in a background UV ra-

diation field of 1 Habing, with local variations in the radiation field set to scale with the local SFR surface density. A fixed C⁺ abundance (relative to H₂) of 10⁻⁴ is assumed. The excitation of [CII] occurs via collisions with e⁻, H, and H₂, and the line emission is calculated with a 3D radiative transfer code that takes into account the kinematics and optical depth effects of the gas. For galaxies with SFRs similar to our model galaxies ($\sim 5 - 50 \text{ M}_\odot \text{ yr}^{-1}$) their simulations predict ensemble-median [CII] luminosities of $\lesssim (1 - 6) \times 10^7 L_\odot$.⁴ This is lower than the [CII] luminosities predicted by our simulations and also somewhat on the low side of the observed $z \sim 0 L_{\text{[CII]}} - \text{SFR}$ relation (Fig. 6.9). Allowing for the $+2\sigma$ deviation from the median of the Popping et al. (2014a) models results in $L_{\text{[CII]}} \lesssim (2 - 30) \times 10^7 L_\odot$ for $\text{SFR} \sim 5 - 50 \text{ M}_\odot \text{ yr}^{-1}$, which matches the observed $L_{\text{[CII]}} - \text{SFR}$ relation.

6.8 CONCLUSION

SÍGAME is a novel numerical framework, here manipulated to simulate the [CII] emission from galaxies, capable of separately tracing the [CII] emission from the molecular, atomic, and ionized gas in the ISM. The method was applied to SPH simulations of seven star-forming galaxies at $z = 2$ with stellar masses in the range $\sim (0.3 - 5) \times 10^{10} \text{ M}_\odot$ and star formation rates $\sim 5 - 60 \text{ M}_\odot \text{ yr}^{-1}$ in order to make predictions of the [CII] line emission from main-sequence galaxies during the peak of the cosmic star formation history.

A key result of our simulations is that the total [CII] emission budget from our galaxies is dominated by the molecular gas phase ($\gtrsim 70\%$) in the central regions ($R \lesssim 1 \text{ kpc}$) where the bulk of the star formation occurs and is most intense, and by PDR regions further out ($R \gtrsim 1 - 2 \text{ kpc}$) where the molecular [CII] emission has dropped by at least an order of magnitude compared to their central values. The atomic, partly ionized phase of the PDR regions, while rarely able to produce [CII] emission as intense as the molecular gas in the central regions, is nonetheless able to maintain significant levels of [CII] emission from $R \sim 2 \text{ kpc}$ all the way out to $\sim 8 \text{ kpc}$ from the center. The net effect of this is that on global scales the atomic PDR gas can produce between 8 and 67% of the total [CII] luminosity with the molecular gas responsible for the remaining emission. We see a trend in which galaxies with higher star formation rates also have a higher fraction of their total [CII] luminosity coming from the molecular phase. Our simulations consistently show that the ionized gas contribution to the [CII] luminosity is negligible ($\lesssim 1\%$), despite the fact that this ISM phase is dominant in terms of mass (see Fig. 6.11). This shows that the ionized gas is an inefficient [CII] line emitter, as also underlined by its low $\Sigma_{\text{[CII]}}$ values (Fig. 6.10).

The integrated [CII] luminosities of our simulated galaxies are found to be higher and follow a steeper $L_{\text{[CII]}} - \text{SFR}$ relation (slope 1.27 ± 0.17) in better agreement with [CII] observations of $z \sim 5 - 6$ galaxies with similar SFRs (Capak et al., 2015) than the relation observed for local and other high- z galaxies.

We have also examined the relationship between the 1 kpc-averaged surface densities of $L_{\text{[CII]}}$ and SFR across our simulated galaxies. The resulting $\Sigma_{\text{[CII]}} - \Sigma_{\text{SFR}}$ relation spans more than six orders of magnitude in Σ_{SFR} ($\sim 10^{-5} - 10 L_\odot \text{ kpc}^{-2}$), extending beyond the observed ranges at both the low and high end of the relation. Over most of this range we find that the $\Sigma_{\text{[CII]}} - \Sigma_{\text{SFR}}$ relation is well-described by a power-law, i.e. similar to the observed relation from

⁴Since Popping et al. (2014a) plots $L_{\text{[CII]}}$ against L_{IR} and not SFR, we have converted our SFRs to L_{IR} in order to crudely estimate their predicted [CII] luminosities (see their Fig. 11). For the $\text{SFR} \rightarrow L_{\text{IR}}$ conversion we have used (Bell, 2003). Not all the star formation will be obscured and so the IR luminosities, and thereby the [CII] luminosities given here will be upper limits.

local spirals and dwarf galaxies (D14, H15, K15) but with a shallower slope (0.60 ± 0.02) and a higher normalization versus from observations.

The correlation between [CII] and SFR – in the integrated as well as the resolved incarnation – is found to be strongest (i.e. exhibiting the steepest slope) for the molecular gas phase. We argue that this is due to the fact that the [CII] luminosity scales with the amount of molecular gas present in our simulated galaxies, which again is closely related to the amount of star formation going on. For the atomic and ionized gas phases, we do not find a similar scaling relationship between the [CII] luminosity and gas mass.

Our work therefore supports the notion that for normal star-forming galaxies, [CII] is a *bona fide* tracer of molecular gas and star formation. Furthermore, we hypothesize that galaxies in which a large fraction of the ISM is in the molecular phase and actively forming stars will display a steeper [CII] – SFR relationship than galaxies with ISM dominated by atomic/ionized gas. See the following Outlook chapter for future work that will extend the present study.

7

OUTLOOK

7.1 IMPROVEMENTS ON SÍGAME

The aim of SÍGAME is to model line emission from the ISM of galaxies at any redshift. Such a code has to be as true as possible to the observations of gas and dust, on small and large scale. At high- z (and assuming that physical laws do not change in time), this turns into a limitation in how well we can resolve the ISM spatially or spectroscopically, sometimes leading to rather crude assumptions based on what can be observed locally. As a recently developed code, SÍGAME has several such assumptions with room for improvement, of which three are listed below.

7.1.1 DUST TEMPERATURES WITH A RADIATIVE TRANSFER CODE

With SÍGAME we have demonstrated a new method that takes into account local FUV fields and CR intensities in galaxies. However, our method of scaling these fields to the local SFR and total stellar mass, can be made much more realistic with the inclusion of an actual dust radiative transfer (RT) code. One such code, developed recently, is Hyperion¹ (Robitaille, 2011) for which Powderday² can be used as an interface between Hyperion and galaxy formation simulations. And many alternatives exist as evident from the review by Steinacker et al. (2013). Implementing one of these would allow us to self-consistently derive dust temperatures, taking into account anisotropic scattering, absorption and (re-)emission by interstellar dust, all based on the distribution of stars and dust in the galaxy.

7.1.2 MODELING OF ASYMMETRIC GMCs

At present, there exists a gap between simulations of the ISM on galaxy-scales and those on scales relevant for the formation of individual stars. On galaxy-scales, simulations are typically restricted to model star formation using empirical correlations between gas density and star formation rate. However, more detailed simulations are emerging, following dense gas from kpc-scales down to ~ 0.1 pc where star clusters are formed (Butler et al., 2014; Dobbs, 2015). With modifications, SÍGAME could be applied to resolved simulations of single star formation such as those of Vázquez-Semadeni et al. (2010, 2011) and Dale et al. (2013), in order to make a more precise grid in CO line intensities as a function of more global parameters. The move

¹<http://www.hyperion-rt.org/>

²<https://bitbucket.org/desika/powderday>

from spherically symmetric GMC models towards the clumpy, filamentary clouds observed is an important step forward for SÍGAME.

7.1.3 INCLUDING HEATING BY X-RAYS AND TURBULENT DISSIPATION

Particularly towards the Galactic center, observations demand the presence of non-photon driven heating such as cosmic rays and turbulent dissipation (Ao et al., 2014). But also in normal star-forming GMCs, turbulent dissipation has been suggested as a cause for most of the observed excess in CO lines at $J_{\text{upper}} \geq 6$ (Pon et al., 2012, 2014). In AGNs, the circum-nuclear disks can act like an X-ray Dominated Region (XDR), and X-ray heating is therefore important when modeling these central regions (e.g. Aalto et al., 2007; García-Burillo et al., 2010). We have focused our research projects on normal star-forming galaxies, but if SÍGAME is to work more generally on starburst and AGNs, turbulent dissipation and X-ray heating must be included in the model.

7.2 GOING TO HIGHER REDSHIFT

7.2.1 THE EVOLUTION OF X_{CO} WITH REDSHIFT

Gas mass estimates depend crucially on the dust-to-gas mass ratio or the X-factor, X_{CO} . At $z \sim 2$, SÍGAME predicts X_{CO} factors about half that of the MW for massive star-forming galaxies, and applying the same method to simulations at higher redshift, we could investigate how X_{CO} changes with redshift. Such predictions will be important for future observational campaigns trying to pin down the evolution of f_{gas} with redshift. X_{CO} could also readily be applied to observations of any CO line, if we knew the shape of the CO ladder beforehand. Narayanan & Hopkins (2012) developed a parametrization of the CO ladder with Σ_{SFR} that SÍGAME can now improve on by seeing how it changes at $z > 2$ for normal star-forming galaxies.

7.2.2 THE FULL CALIBRATION TO NORMAL GALAXIES AT $z \sim 2$

As evident from the study of CO and [CII] line emission in normal star-forming $z \sim 2$ galaxies, we are in need of more observations, in particular of the full CO SLED, in order to test models, such as SÍGAME, and use them to their fullest. I plan to continue my involvement in the HELLO (*Herschel* Extreme Lensing Line Observations) project which takes advantage of powerful lensing (by e.g. foreground groups of galaxies) in order to detect [CII] line emission from normal galaxies at $z \sim 2$. With the high spectral resolution of *Herschel*, kinematic studies of the line profiles are used to estimate rotation speed and gas velocity dispersion (Rhoads et al., 2014). Follow-up observations of CO lines with JVLA and ALMA make these galaxies excellent calibrators for SÍGAME, which itself will help in the interpretation of these future line observations.

7.2.3 GALAXIES DURING THE EPOCH OF RE-IONIZATION

In the early universe, at redshifts above 7, spectroscopic observations in the FIR might be our only way to characterize the modest MS galaxies responsible for most star formation, that are otherwise proving difficult to capture in rest-frame UV with existing spectrographs. Observing and modeling the gas conditions during the Epoch of Re-ionization (EoR) will enable us to

answer questions such as: *How did galaxies first acquire their gas masses? When did the gas become enriched by the first supernovae? What role did the gas play in setting the SFR?*

Observing with band 7 of ALMA, Capak et al. (2015) found $> 3\sigma$ detections of [CII] in a sample of 9 normal ($\text{SFR} < 3$ to $\sim 170 \text{ M}_\odot \text{ yr}^{-1}$) galaxies at $z \sim 5 - 6$, of which only 4 are detected in dust continuum, underlining the importance of [CII] as a tracer of the ISM at high redshift. However, many attempts with ALMA (and PdBI) pointing at $z \sim 7$ star-forming MS galaxies for hours, have only resulted in upper limits on both [CII] line emission and dust continuum (Ouchi et al., 2013; Maiolino et al., 2015; Ota et al., 2014; Schaerer et al., 2015; González-López et al., 2014). One preferred explanation is low metallicity because the galaxies might not have had enough time to enrich the primordial gas with metallicities to a degree that their line emission is strong enough for detection (Ouchi et al., 2013; Ota et al., 2014; González-López et al., 2014; Schaerer et al., 2015). Another explanation based on recent simulations, is that molecular clouds in these primeval systems are destroyed and dispersed by strong stellar feedback, pushing most of the carbon to higher ionization states (Maiolino et al., 2015; Vallini et al., 2013). A difference in PDR structure or physical states of the ISM between star-forming galaxies at high-redshift and local ones, might also be enough to explain the low luminosity in [CII] and FIR (Ota et al., 2014).

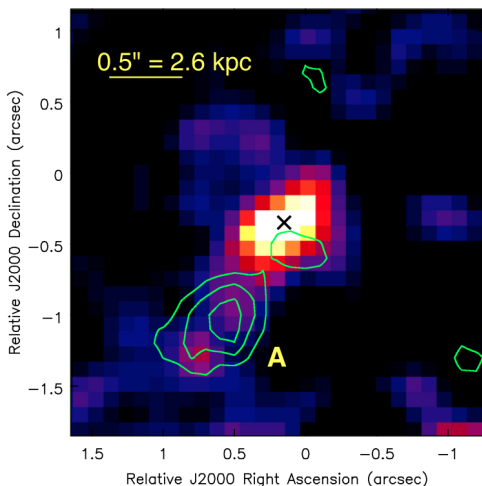


Figure 7.1 Image in rest frame UV stellar continuum and Ly α emission of the $z = 7.109$ galaxy BDF3299. Green contours show the levels of 2, 3 and 4 times the noise per beam in the [CII] map. The detected clump at 4 kpc distance from the galaxy center (black cross) is marked 'A' (Maiolino et al., 2015).

Interestingly, Maiolino et al. (2015) detect a strong (7σ) [CII] signal from a position which is offset from the actual galaxy, BDF3299 at $z = 7.109$, as shown in Fig. 7.1. This is interpreted as an accreting/satellite gas clump of neutral gas about 4 kpc from the galaxy itself. At slightly higher redshift, Watson et al. (2015) managed to detect dust continuum emission from the galaxy A1689-zD1 of $\text{SFR} \sim 10 \text{ M}_\odot \text{ yr}^{-1}$. Such observations nourish the hope that we are but few s.pdf away from using [CII] observations to characterise the gas in normal galaxies and/or the mass assembly from the Circumgalactic Medium (CGM) in the early universe.

With this motivation, I have recently made preliminary attempts at simulating [CII] emission from halos at high redshift, in collaboration with Kristian Finlator, here at the Dark Cosmology Centre. As a simple test, we adopted a NFW profile for the radial halo density profile, and, since little is known about the metal abundance at these redshifts, assumed

three values for the abundance of carbon, going from pessimistic to optimistic: $Z'_C = [10^{-4.5}, 10^{-4}, 10^{-3.5}]$. The resulting rough estimate of [CII] luminosity as a function of halo mass at $z = 6$ is shown in Fig. 7.2 together with a surface brightness map for a halo mass of $5 \times 10^9 \text{ M}_\odot$. With the use of actual cosmological simulations, rather than simple spherically symmetric halo models or constant metallicity and temperature, we can make much more precise predictions for the detectability of the CGM.

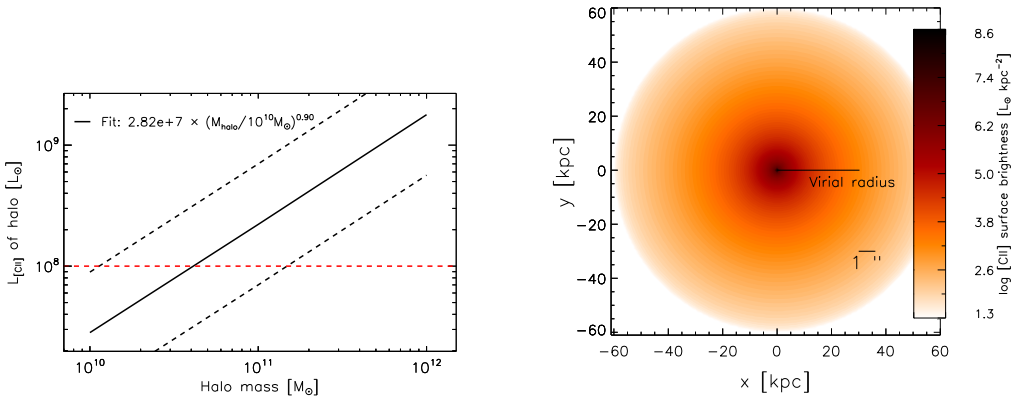


Figure 7.2 *Left*: [CII] luminosity as a function of stellar mass for our fiducial case (solid line) and the optimistic and pessimistic cases (dashed lines). *Right*: Map of [CII] surface brightness from a galaxy of stellar mass $5 \times 10^9 M_\odot$ at $z = 6$ (corresponding to a halo mass of $2.7 \times 10^{11} M_\odot$) within the virial radius, marked on the figure.

7.3 REFERENCES

- Aalto, S., Spaans, M., Wiedner, M. C., & Hüttemeister, S. 2007, *A&A*, 464, 193
 Abel, N. P., Dudley, C., Fischer, J., Satyapal, S., & van Hoof, P. A. M. 2009, *ApJ*, 701, 1147
 Ao, Y., Henkel, C., Menten, K. M., et al. 2014, in IAU Symposium, Vol. 303, IAU Symposium, ed. L. O. Sjouwerman, C. C. Lang, & J. Ott, 89–91
 Bell, E. F. 2003, *ApJ*, 586, 794
 Blitz, L., Fukui, Y., Kawamura, A., et al. 2007, *Protostars and Planets V*, 81
 Boselli, A., Gavazzi, G., Lequeux, J., & Pierini, D. 2002, *A&A*, 385, 454
 Bovy, J., Rix, H.-W., & Hogg, D. W. 2012, *ApJ*, 751, 131
 Brauher, J. R., Dale, D. A., & Helou, G. 2008, *ApJS*, 178, 280
 Butler, M. J., Tan, J. C., & Van Loo, S. 2014, ArXiv e-prints
 Calzetti, D., Kennicutt, R. C., Engelbracht, C. W., et al. 2007, *ApJ*, 666, 870
 Capak, P. L., Carilli, C., Jones, G., et al. 2015, ArXiv e-prints
 Carilli, C. L., Riechers, D., Walter, F., et al. 2013, *ApJ*, 763, 120
 Casey, C. M., Narayanan, D., & Cooray, A. 2014, arXiv/1402.1456
 Crawford, M. K., Genzel, R., Townes, C. H., & Watson, D. M. 1985, *ApJ*, 291, 755
 Croxall, K. V., Smith, J. D., Wolfire, M. G., et al. 2012, *ApJ*, 747, 81
 Daddi, E., Elbaz, D., Walter, F., et al. 2010, *ApJ*, 714, L118
 Dale, J. E., Ngoumou, J., Ercolano, B., & Bonnell, I. A. 2013, *MNRAS*, 436, 3430
 Dartois, E., & Muñoz-Caro, G. M. 2007, *A&A*, 476, 1235
 Davé, R., Katz, N., Oppenheimer, B. D., Kollmeier, J. A., & Weinberg, D. H. 2013, *MNRAS*, 434, 2645
 De Breuck, C., Maiolino, R., Caselli, P., et al. 2011, *A&A*, 530, L8
 De Breuck, C., Williams, R. J., Swinbank, M., et al. 2014, *A&A*, 565, A59
 de Looze, I., Baes, M., Bendo, G. J., Cortese, L., & Fritz, J. 2011, *MNRAS*, 416, 2712
 De Looze, I., Cormier, D., Lebouteiller, V., et al. 2014, ArXiv e-prints
 Díaz-Santos, T., Armus, L., Charmandaris, V., et al. 2013, *ApJ*, 774, 68
 Dobbs, C. L. 2015, *MNRAS*, 447, 3390
 Durier, F., & Dalla Vecchia, C. 2012, *MNRAS*, 419, 465
 Elmegreen, B. G. 1989, *ApJ*, 344, 306

- Esteban, C., García-Rojas, J., Carigi, L., et al. 2014, MNRAS, 443, 624
- Farrah, D., Lebouteiller, V., Spoon, H. W. W., et al. 2013, ApJ, 776, 38
- Ferkinhoff, C., Brisbin, D., Nikola, T., et al. 2011, ApJ, 740, L29
- Ferland, G. J., Porter, R. L., van Hoof, P. A. M., et al. 2013, RxMAA, 49, 137
- Ford, A. B., Werk, J. K., Dave, R., et al. 2015, ArXiv e-prints
- Gallerani, S., Neri, R., Maiolino, R., et al. 2012, A&A, 543, A114
- García-Burillo, S., Usero, A., Fuente, A., et al. 2010, A&A, 519, A2
- Genzel, R., Tacconi, L. J., Gracia-Carpio, J., et al. 2010, MNRAS, 407, 2091
- Goldsmith, P. F., Langer, W. D., Pineda, J. L., & Velusamy, T. 2012, ApJS, 203, 13
- González-López, J., Riechers, D. A., Decarli, R., et al. 2014, ApJ, 784, 99
- Graciá-Carpio, J., Sturm, E., Hailey-Dunsheath, S., et al. 2011, ApJ, 728, L7
- Gullberg, B., De Breuck, C., Vieira, J. D., et al. 2015, MNRAS, 449, 2883
- Hahn, O., & Abel, T. 2011, MNRAS, 415, 2101
- Hailey-Dunsheath, S., Nikola, T., Stacey, G. J., et al. 2010, ApJ, 714, L162
- Heiderman, A., Evans, II, N. J., Allen, L. E., Huard, T., & Heyer, M. 2010, ApJ, 723, 1019
- Herrera-Camus, R., Bolatto, A. D., Wolfire, M. G., et al. 2015, ApJ, 800, 1
- Hodge, P. W., Balsley, J., Wyder, T. K., & Skelton, B. P. 1999, PASP, 111, 685
- Hollenbach, D. J., & Tielens, A. G. G. M. 1999, Reviews of Modern Physics, 71, 173
- Hopkins, P. F. 2013, MNRAS, 428, 2840
- Ibar, E., Lara-López, M. A., Herrera-Camus, R., et al. 2015, ArXiv e-prints
- Iono, D., Yun, M. S., Elvis, M., et al. 2006, ApJ, 645, L97
- James, B. L., Aloisi, A., Heckman, T., Sohn, S. T., & Wolfe, M. A. 2014, ApJ, 795, 109
- Kanekar, N., Wagg, J., Ram Chary, R., & Carilli, C. L. 2013, ApJ, 771, L20
- Kapala, M. J., Sandstrom, K., Groves, B., et al. 2015, ApJ, 798, 24
- Katz, N., Weinberg, D. H., & Hernquist, L. 1996, ApJS, 105, 19
- Kennicutt, Jr., R. C. 1998, ARA&A, 36, 189
- Kramer, C., Abreu-Vicente, J., García-Burillo, S., et al. 2013, A&A, 553, A114
- Krumholz, M. R., McKee, C. F., & Tumlinson, J. 2008, ApJ, 689, 865
- . 2009, ApJ, 693, 216
- Krumholz, M. R., & Tan, J. C. 2007, ApJ, 654, 304
- Kurtz, N. T., Smyers, S. D., Russell, R. W., Harwit, M., & Melnick, G. 1983, ApJ, 264, 538
- Lada, C. J., Lombardi, M., & Alves, J. F. 2010, ApJ, 724, 687
- Larson, R. B. 1981, MNRAS, 194, 809
- Lebouteiller, V., Cormier, D., Madden, S. C., et al. 2012, A&A, 548, A91
- Leech, K. J., Völk, H. J., Heinrichsen, I., et al. 1999, MNRAS, 310, 317
- Leroy, A. K., Bigiel, F., de Blok, W. J. G., et al. 2012, AJ, 144, 3
- Luhman, M. L., Satyapal, S., Fischer, J., et al. 2003, ApJ, 594, 758
- . 1998, ApJ, 504, L11
- Madden, S. C., Genzel, R., Herrmann, F., et al. 1992, in Bulletin of the American Astronomical Society, Vol. 24, American Astronomical Society Meeting Abstracts, 1268
- Magdis, G. E., Rigopoulou, D., Hopwood, R., et al. 2014, ApJ, 796, 63
- Magrini, L., Stanghellini, L., Corbelli, E., Galli, D., & Villaver, E. 2010, A&A, 512, A63
- Maiolino, R., Carniani, S., Fontana, A., et al. 2015, ArXiv e-prints
- Malhotra, S., Helou, G., Stacey, G., et al. 1997, ApJ, 491, L27
- Malhotra, S., Kaufman, M. J., Hollenbach, D., et al. 2001, ApJ, 561, 766
- McKee, C. F., & Krumholz, M. R. 2010, ApJ, 709, 308
- Mezger, P. G., Mathis, J. S., & Panagia, N. 1982, A&A, 105, 372

- Muñoz, J. A., & Furlanetto, S. R. 2013, MNRAS, 435, 2676
- Nagamine, K., Springel, V., Hernquist, L., & Machacek, M. 2004, MNRAS, 350, 385
- Nagamine, K., Wolfe, A. M., & Hernquist, L. 2006, ApJ, 647, 60
- Narayanan, D., Cox, T. J., Shirley, Y., et al. 2008a, ApJ, 684, 996
- Narayanan, D., & Hopkins, P. 2012, ArXiv e-prints
- Narayanan, D., Krumholz, M. R., Ostriker, E. C., & Hernquist, L. 2012, MNRAS, 421, 3127
- Narayanan, D., Cox, T. J., Kelly, B., et al. 2008b, ApJS, 176, 331
- Oey, M. S., & Clarke, C. J. 1997, MNRAS, 289, 570
- Oppenheimer, B. D., & Davé, R. 2008, MNRAS, 387, 577
- Ota, K., Walter, F., Ohta, K., et al. 2014, ApJ, 792, 34
- Ouchi, M., Ellis, R., Ono, Y., et al. 2013, ApJ, 778, 102
- Papadopoulos, P. P., Zhang, Z.-Y., Xilouris, E. M., et al. 2014, ApJ, 788, 153
- Pelupessy, F. I., & Papadopoulos, P. P. 2009, ApJ, 707, 954
- Pelupessy, F. I., Papadopoulos, P. P., & van der Werf, P. 2006, ApJ, 645, 1024
- Pineda, J. L., Langer, W. D., & Goldsmith, P. F. 2014, A&A, 570, A121
- Pineda, J. L., Langer, W. D., Velusamy, T., & Goldsmith, P. F. 2013, A&A, 554, A103
- Planck Collaboration, Ade, P. A. R., Aghanim, N., et al. 2013, ArXiv e-prints
- Pon, A., Johnstone, D., & Kaufman, M. J. 2012, ApJ, 748, 25
- Pon, A., Johnstone, D., Kaufman, M. J., Caselli, P., & Plume, R. 2014, MNRAS, 445, 1508
- Popping, G., Pérez-Beaupuits, J. P., Spaans, M., Trager, S. C., & Somerville, R. S. 2014a, MNRAS, 444, 1301
- Popping, G., Somerville, R. S., & Trager, S. C. 2014b, MNRAS, 442, 2398
- Rhoads, J. E., Malhotra, S., Allam, S., et al. 2014, ApJ, 787, 8
- Robertson, B. E., & Kravtsov, A. V. 2008, ApJ, 680, 1083
- Robitaille, T. P. 2011, A&A, 536, A79
- Röllig, M., Ossenkopf, V., Jeyakumar, S., Stutzki, J., & Sternberg, A. 2006, A&A, 451, 917
- Russell, R. W., Melnick, G., Gull, G. E., & Harwit, M. 1980, ApJ, 240, L99
- Saitoh, T. R., & Makino, J. 2009, ApJ, 697, L99
- . 2013, ApJ, 768, 44
- Sanders, N. E., Caldwell, N., McDowell, J., & Harding, P. 2012, ApJ, 758, 133
- Sargsyan, L., Lebouteiller, V., Weedman, D., et al. 2012, ApJ, 755, 171
- Schaerer, D., Boone, F., Zamojski, M., et al. 2015, A&A, 574, A19
- Schaye, J., & Dalla Vecchia, C. 2008, MNRAS, 383, 1210
- Schmidt, M. 1959, ApJ, 129, 243
- Schöier, F. L., van der Tak, F. F. S., van Dishoeck, E. F., & Black, J. H. 2005, A&A, 432, 369
- Seon, K.-I., Edelstein, J., Korpela, E., et al. 2011, ApJS, 196, 15
- Speagle, J. S., Steinhardt, C. L., Capak, P. L., & Silverman, J. D. 2014, ApJS, 214, 15
- Spergel, D. N., Verde, L., Peiris, H. V., et al. 2003, ApJS, 148, 175
- Springel, V. 2005, MNRAS, 364, 1105
- Springel, V., & Hernquist, L. 2003, MNRAS, 339, 289
- Stacey, G. J., Geis, N., Genzel, R., et al. 1991, ApJ, 373, 423
- Stacey, G. J., Hailey-Dunsheath, S., Ferkinhoff, C., et al. 2010, ApJ, 724, 957
- Stacey, G. J., Smyers, S. D., Kurtz, N. T., & Harwit, M. 1983, ApJ, 268, L99
- Steinacker, J., Baes, M., & Gordon, K. D. 2013, ARA&A, 51, 63
- Swinbank, A. M., Papadopoulos, P. P., Cox, P., et al. 2011, ApJ, 742, 11
- Swinbank, A. M., Karim, A., Smail, I., et al. 2012, MNRAS, 427, 1066
- Thompson, R., Davé, R., Huang, S., & Katz, N. 2015, ArXiv e-prints

- Thompson, R., Nagamine, K., Jaacks, J., & Choi, J.-H. 2014, ApJ, 780, 145
- Tielens, A. G. G. M., & Hollenbach, D. 1985, ApJ, 291, 722
- Vallini, L., Gallerani, S., Ferrara, A., & Baek, S. 2013, MNRAS, 433, 1567
- Vallini, L., Gallerani, S., Ferrara, A., Pallottini, A., & Yue, B. 2015, ArXiv e-prints
- Vázquez-Semadeni, E., Banerjee, R., Gómez, G. C., et al. 2011, MNRAS, 414, 2511
- Vázquez-Semadeni, E., Colín, P., Gómez, G. C., Ballesteros-Paredes, J., & Watson, A. W. 2010, ApJ, 715, 1302
- Venemans, B. P., McMahon, R. G., Walter, F., et al. 2012, ApJ, 751, L25
- Wagg, J., Carilli, C. L., Wilner, D. J., et al. 2010, A&A, 519, L1
- Walter, F., Riechers, D., Cox, P., et al. 2009, Nature, 457, 699
- Wang, R., Wagg, J., Carilli, C. L., et al. 2013, ApJ, 773, 44
- Watson, D., Christensen, L., Knudsen, K. K., et al. 2015, Nature, 519, 327
- Webber, W. R. 1998, ApJ, 506, 329
- Whitaker, K. E., Labb  , I., van Dokkum, P. G., et al. 2011, ApJ, 735, 86
- Wiersma, R. P. C., Schaye, J., Theuns, T., Dalla Vecchia, C., & Tornatore, L. 2009, MNRAS, 399, 574
- Willott, C. J., Omont, A., & Bergeron, J. 2013, ApJ, 770, 13

Part II

The AGN-galaxy co-evolution at $z \sim 2$

8

HOW TO DETECT AN AGN

A general concern when estimating the SFR by fitting the broadband SED of a galaxy with stellar population synthesis models, is the relative dominance of AGN versus star formation. The dominant contributor to the mid-infrared (MIR) light is from UV-light reprocessed by dust, but the UV light can be emitted by either young stars or an AGN. At $z \sim 2$ it is not clear, without the aid of high spatial and spectral resolution, what is causing the observed MIR emission from massive galaxies; is dust in the central regions being heated by AGN activity, is dust across a larger region of the galaxy being heated by star formation, or is a combination of the two scenarios taking place?

X-ray emission, on the other hand, does not suffer from strong dust obscuration. Observing in X-ray can thus lift the apparent degeneracy in interpreting the origin of the MIR light, and thereby help to give the true AGN fraction of a sample of galaxies. A galaxy dominated by AGN activity can be distinguished from a galaxy dominated by star formation by having a harder X-ray spectrum if the AGN is obscured by dust, or by simply having a very high X-ray luminosity, $L_{0.5-8\text{ keV}}$. The most heavily obscured ‘Compton-thick’ AGNs, with column densities $N_{\text{H}} > 10^{24} \text{ cm}^{-2}$, might be missed by X-ray selection, but can instead be identified via an excess of MIR emission over that expected from purely star-forming galaxies (e.g., Daddi et al., 2007; Treister et al., 2009).

The shape of the MIR spectrum can also reveal AGNs, as the intense nuclear emission re-emitted by dust leads to a power-law spectrum in the MIR. For this purpose, color cuts have been devised using the *Spitzer* data (e.g., Stern et al., 2005; Donley et al., 2012). While this technique has the capability of detecting even Compton-thick AGNs, otherwise missed in X-ray, it has a low efficiency for low- to moderate-luminosity AGNs and its robustness has yet to be verified at $z \gtrsim 2$ (Cardamone et al., 2008).

In a galaxy where star formation is dominant, the total hard band X-ray luminosity, $L_{2-10\text{ keV}}$, can be used to estimate the SFR (e.g., Grimm et al., 2003; Ranalli et al., 2003; Lehmer et al., 2010). An AGN will reveal itself if the X-ray SFR inferred this way is much larger than the SFR derived from other tracers such as H α , UV, or MIR luminosity. Also, if star formation dominates the radiation output, the $L_x \rightarrow \text{SFR}$ conversion will give an upper limit on the SFR as has been obtained for sub-mm galaxies (Laird et al., 2010) and for massive, star-forming galaxies at $1.2 < z < 3.2$ (Kurczynski et al., 2012).

At redshifts around 2, high-ionization lines in the rest-frame UV can be used as AGN indicators, but X-ray observations remain a more efficient way of identifying AGNs (Lamareille, 2010).

8.1 DISSECTING THE X-RAY EMISSION FROM AN AGN

I will focus this section on X-ray emission generated by the accretion of matter onto a SMBH, as described in Section 1.3.1, since it is this characteristic that I use for detecting AGN in my study of the presence of AGN at high- z (Part II).

Fig. 8.1 shows the X-ray part of the SED of a type I AGN, together with individual contributions from its components, the nature of which is elaborated on below.

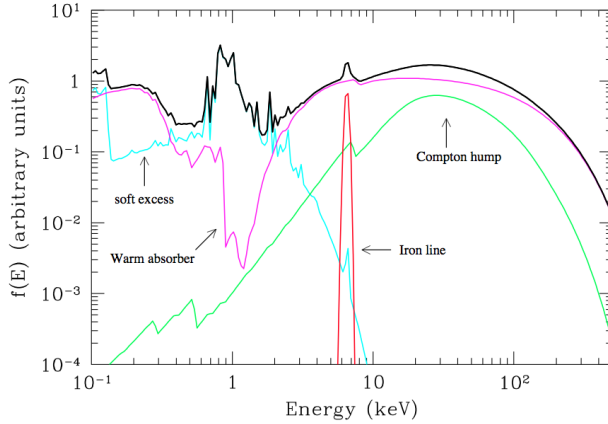


Figure 8.1 The X-ray spectrum (black) of a typical type I AGN, with curves showing the contribution from a primary continuum component (pink) resembling a power law but absorbed at soft energies by warm gas, a cold reflection component (green; Compton hump) and a soft excess (cyan). Also shown is iron K α emission – the most relevant narrow feature (red), arising in the inner parts of the accretion disk. Figure from the review by Risaliti & Elvis (2004).

At high X-ray energies (~ 30 keV), the SED is dominated by reflection component ('Compton hump') consisting of primary emission from the accretion disk being scattered by ionized gas, i.e. electrons. This component will be largest if the reflector is Compton-thick but smaller in the Compton-thin case in which case some of the incident radiation escapes without interaction (Risaliti & Elvis, 2004). An additional hard component is sometimes present, most likely caused by inverse-Compton scattering of the radio-synchrotron photons off of electrons in the relativistic jet itself. At lower energies ($\lesssim 2$ keV) with an almost universal effective temperature of $\sim 0.1 - 0.2$ keV, a 'soft excess' is often observed but less understood. Models suggest that the strongest soft excesses are found in AGNs with low mass accretion rates Done et al. (2012), and typically atomic processes are invoked to explain the soft excess via either ionized reflection with light bending or the remaining part of a high-energy power law subject to ionized absorption (Vasudevan et al., 2014). But also comptonization models have been proposed, in which the soft excess consists of UV/soft-X-ray photons by a population of hot electrons Matt et al. (2014). The joint NuSTAR/XMM program as well as future X-ray missions such as ASTRO-H and ASTROSAT (to be launched this year) are likely to break the degeneracy between these models (see Section 1.5). Finally a warm, ionized absorber exists that reflects the incident continuum without changing its spectral shape.

To first order though, the intrinsic or 'primary' emission from the central engine is a power law extending from 1 to 100 keV, with the slope determined by the different components described. The slope of the power law can be used to determine the amount of obscuration in the AGN, as more obscuration will result in a steeper power law (harder). In order to estimate the column density of obscuring material, one has to take a guess at the spectral slope, Γ , of the

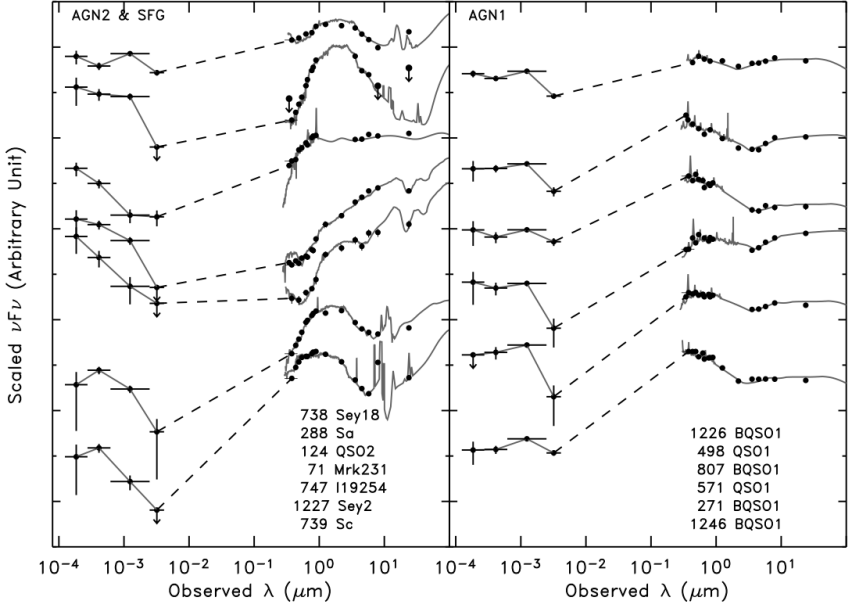


Figure 8.2 X-ray spectra of 13 galaxies from the work of Tajer et al. (2007). *Left:* Top two spectra are consistent with star-forming template SEDs shown, while the following 4 galaxies have type 2 AGN SEDs. *Right:* Type 1 AGN SEDs.

intrinsic emission from the obscured source:

$$dN/dE[\text{photons cm}^{-2} \text{s}^{-1} \text{keV}^{-1}] \propto E^{-\Gamma} \quad (8.1)$$

where dN is the number of photons with energy in the dE energy range. Note that a harder spectrum has *lower* Γ as shown in the left-hand plot of Fig. 8.3. A value of $\Gamma = 1.9$ is usually adopted, based on observations showing that Γ is roughly constant for large samples of low-luminosity Seyfert galaxies and bright QSOs for redshifts up to ~ 5 (e.g. Nandra & Pounds, 1994; Reeves & Turner, 2000; Piconcelli et al., 2005).

Fig. 8.2 shows 13 SEDs from X-ray to FIR ($100 \mu\text{m}$) of type I and type II AGN with best-fit galaxy templates. The X-ray part consists of data from XMM (see Section 1.5) sampled with 4 bands at 0.3-0.5, 0.5-2, 2-4.5, 4.5-10 and 2-10 keV.

The high angular resolution ($\sim 0.5''$) of *Chandra* combined with the high sensitivity in the deep fields CDF-N and CDF-S (see Section 1.4), makes these fields advantageous for searches of AGN at low and high redshift (Bauer et al., 2004; Xue et al., 2011; Treister et al., 2009; Alexander et al., 2011). For those studies, the observed X-ray spectra of *Chandra* are typically divided into a full (0.5 – 8 keV), a soft (0.5 – 2 keV) and a hard (2 – 8 keV) band. A proxy for the powerlaw slope is the ‘hardness ratio’, HR, defined as:

$$\text{HR} = (H - S)/(H + S) \quad (8.2)$$

where H and S are the counts in hard and soft band respectively. Hardness ratio has the advantage, in comparison to Γ , of avoiding any assumptions regarding the shape of the spectrum.

Assuming an intrinsic obscured power law with $\Gamma = 1.9$, HR converts into a column density that increases with the ‘hardness’ of the spectrum as shown in the right-hand plot of Fig. 8.3.

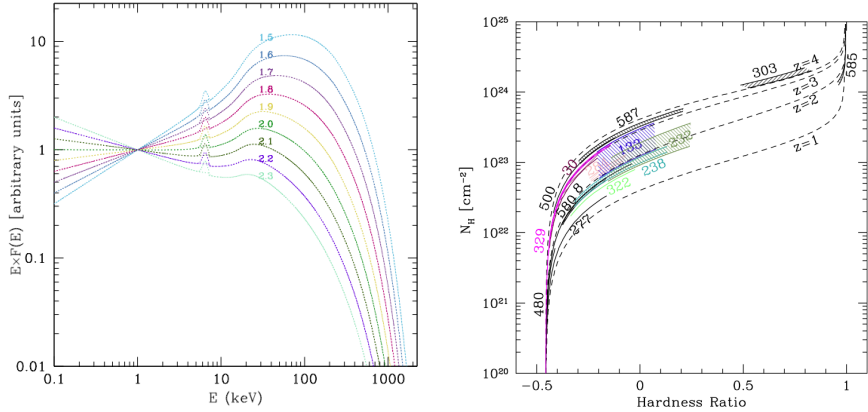


Figure 8.3 Measures of intrinsic power law slope in AGN. *Left:* SED templates for unobscured Seyferts normalized at 1 keV (Gilli et al., 2007). *Right:* Column density of obscuring material as a function of hardness ratio, HR, for 15 $z \lesssim 5$ X-ray detected heavily obscured AGN candidates in the extended CDF-S (Treister et al., 2009).

The criteria for finding an AGN are a high full-band X-ray luminosity ($\gtrsim 2 \times 10^{42}$ ergs/s) of a hard spectrum with $\text{HR} > -0.2$ for sources of lower luminosity. These criteria are meant to rule out galaxies with SEDs consistent with star formation processes only. However, a third possible origin of a bright X-ray component in the area-integrated SED, is a hot gas halo embracing the galaxy (Mulchaey & Jeltema, 2010). Such a component can be ruled out, if the observed X-ray source is predominantly point-like, rather than extended.

8.1.1 THE AGN FRACTION AT $z \gtrsim 2$ FROM OBSERVATIONS IN X-RAY

Several studies of massive $z \sim 2$ galaxies have been made with the aim of uncovering AGN fractions, using the *Chandra* X-ray observatory. Rubin et al. (2004) performed a study of 40 massive ($M_* = (1\text{-}5) \times 10^{11} M_\odot$) red ($J_s - K_s \geq 2.3$) galaxies at $z \gtrsim 2$ by analyzing a 91 ks *Chandra* exposure. Roughly 5% of these were found to host an AGN with intrinsic $L_{2\text{-}10\,\mathrm{keV}} > 1.2 \times 10^{43}$ erg s $^{-1}$. Assuming that the stacked X-ray signal from the remaining X-ray undetected galaxies in X-ray comes from star formation alone, they derived a mean SFR broadly consistent with the typical mean SFRs estimated from SED fits. Alexander et al. (2011) analyzed the 4Ms *Chandra* observations of 222 $z \approx 2$ star-forming BzK galaxies ($M_* \sim 10^{10}\text{-}10^{11} M_\odot$, Daddi et al., 2007) in the Chandra Deep Field-South (CDF-S). 10%(23) showed X-ray emission consistent with AGN dominance, of which 5%(11) were found to contain heavily obscured AGNs, 4%(9) to have luminous, unobscured AGNs, and 3 out of 27 low-luminosity systems showed excess variability over that expected from star formation processes, indicating that at least some low-luminosity (rest-frame $L_{2\text{-}10\,\mathrm{keV}} < 10^{43}$ erg s $^{-1}$) systems may contain AGNs.

9

ON THE PREVALENCE OF AGN AT $z \sim 2$ (PAPER III)

9.1 AIM OF THIS PROJECT

The aim of this project was to determine the AGN fraction in massive $z \sim 2$ galaxies, and reveal any differences between quiescent and star-forming galaxies.

9.2 OUR METHOD AND GALAXY SAMPLE

We addressed the matter by analyzing the X-ray emission from a mass-complete ($M_* > 5 \times 10^{10} M_\odot$) sample of $1.5 \leq z \leq 2.5$ galaxies residing in the CDF-S. The CDF-S, observed for 4 Ms, is currently the deepest X-ray view of the universe and so provides the best opportunity to study high- z galaxies across a relatively large area (464.5 arcmin²).

We selected our galaxies from the FIREWORKS¹ catalog (Wuyts et al., 2008), which covers a field situated within the CDF-S and contains photometry in 17 bands from the *U* band to the MIR. For this study we extracted a mass-complete sample of $M_* > 5 \times 10^{10} M_\odot$ galaxies at $1.5 \leq z \leq 2.5$ in a way similar to that of Franx et al. (2008) and Toft et al. (2009). We used spectroscopic redshifts when available (Vanzella et al., 2008; Xue et al., 2011), and photometric redshifts from the FIREWORKS catalog otherwise. In order to maximize the signal-to-noise (S/N) on results from X-ray stacking (Zheng et al., 2012) and ensure a relatively homogeneous PSF across the *Chandra* field employed, we considered only galaxies that lie within 6' of the average *Chandra* aimpoint.

We adopted galaxy stellar masses from the SED fitting results of Franx et al. (2008) and Toft et al. (2009). In short, the SED fits were carried out with models by Bruzual & Charlot (2003), choosing the best fit from adopting three different star formation histories (a single stellar population with no dust, an exponentially declining star formation history of timescale 300 Myr with dust, and a constant star formation history with dust). In cases where the spectroscopic redshift differed by more than 0.1 from the original FIREWORKS photometric redshift, we redid the SED fits in FAST² using an exponentially declining star formation history with a range of possible timescales from 10 Myr to ~ 1 Gyr. As a quality parameter of the SED modeling, we demanded an upper limit on the reduced χ^2_ν of 10 on the best-fit model. The SED fits pro-

¹<http://www.strw.leidenuniv.nl/fireworks/>

²<http://astro.berkeley.edu/~mariska/FAST.html>

vide SFR estimates, but we used SFRs derived from rest-frame UV+IR luminosities (see Section 9.2.3) as these include obscured star formation and are subject to less assumptions. From the observed photometry, rest-frame fluxes in U , V , J band and at 2800 Å have been derived using InterRest³ (Taylor et al., 2009).

We divided the resulting sample of 123 galaxies into quiescent and star-forming galaxies using the rest-frame U , V and J (falling roughly into the observed J , K and IRAC 4.5 μm bands at $z \sim 2$) colors. Dust-free but quiescent galaxies differ from dust-obscured starburst galaxies in that they obey the following criteria by Williams et al. (2009):

$$U - V > 1.3 \quad (9.1)$$

$$V - J < 1.6 \quad (9.2)$$

$$(U - V) > 0.88 \times (V - J) + 0.49 \quad (9.3)$$

The fraction of quiescent galaxies identified within our sample using this method is $22\% \pm 5\%$ (27/123). This is rather low compared to the 30–50% found by Toft et al. (2009) for the same redshift and mass limit, but under the requirement that the sSFR ($=\text{SFR}/M_*$) from SED fitting is less than 0.03 Gyr^{-1} . If applying this criterion, we would have arrived at a fraction of $42\% \pm 7\%$ (51/123). A possible reason for the discrepancy between the two methods may be that we were using the UVJ criterion in the limits of the redshift range in which it has so far been established. As the redshift approaches 2, the quiescent population moves to bluer $U - V$ colors, possibly crossing the boundaries of Equation (9.3). However, we preferred the UVJ selection technique in contrast to a cut in sSFR, because rest-frame colors are more robustly determined than star formation rates from SED fits.

9.2.1 X-RAY DATA AND STACKING ANALYSIS

The raw X-ray data from the CDF-S survey consist of 54 individual observations taken between 1999 October and 2010 July. We build our analysis on the work of Xue et al. (2011), who combined the observations and reprojected all images. They did so in observed full band (0.5–8 keV), soft band (0.5–2 keV) and hard band (2–8 keV), and the resulting images and exposure maps are publicly available.⁴

We extracted source and background count rates in the X-ray maps for all galaxies using the method of Cowie et al. (2012). Source counts were determined within a circular aperture of fixed radii: $0''.75$ and $1''.25$ at off-axis angles of $\theta \leq 3'$ and $\theta > 3'$ respectively. Background counts were estimated within an annulus $8''$ – $22''$ from the source, excluding nearby X-ray sources from the catalog of Xue et al. (2011).

Each galaxy was classified as ‘X-ray detected’ if detected in at least one band at $\geq 3\sigma$ significance, thereby creating 4 subsamples containing 8 quiescent and detected, 19 quiescent and undetected, 43 star-forming and detected, and 53 star-forming and undetected galaxies.

While the X-ray detected galaxies could be analyzed individually, we stacked the X-ray non-detected galaxies in order to constrain the typical X-ray flux from these. Stacked X-ray images of the 4 subsamples are shown in Figure 9.1 with all galaxies aligned to their K_s band galaxy center positions from FIREWORKS. Representative count rates and associated errors for these stacks were calculated using the optimally weighted mean procedure of Cowie et al.

³<http://www.strw.leidenuniv.nl/~ent/InterRest>

⁴<http://www2.astro.psu.edu/users/niel/cdfs/cdfs-chandra.html>

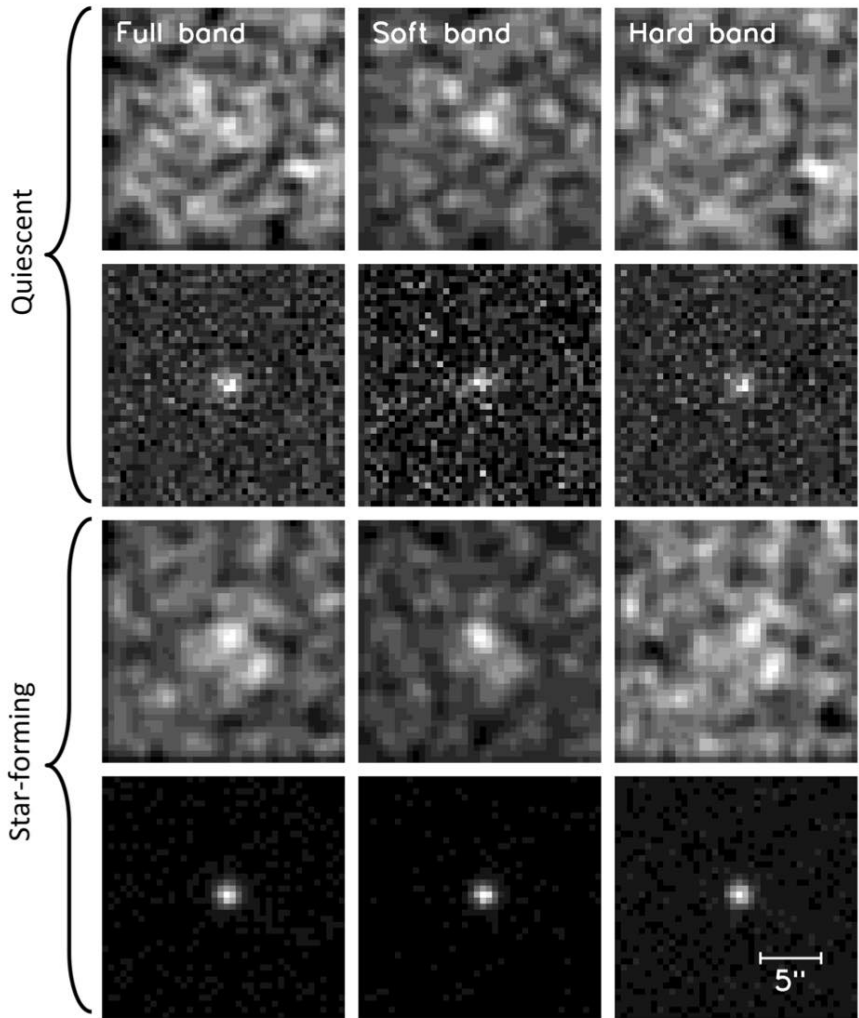


Figure 9.1 Stacked, background-subtracted and exposure-corrected $20'' \times 20''$ images in the three energy bands (columns) for the individually non-detected (top row) and detected (bottom row) quiescent and star-forming galaxies. Images of the non-detections have been smoothed with a Gaussian of width 2 pixels.

(2012) and tabulated in Table 9.1 together with S/N values.

	Count Rate $\pm 1\sigma$ (10^{-6} s^{-1}) in		
	Full Band	Soft Band	Hard Band
Q	0.71 ± 0.96 (0.7)	2.01 ± 0.41 (4.9)	-1.67 ± 0.86 (-1.9)
SF	2.51 ± 0.55 (4.5)	1.08 ± 0.24 (4.5)	1.29 ± 0.49 (2.7)

Table 9.1 Stacking results for Quiescent (Q) and Star-forming (SF) galaxies not detected individually in X-Rays (in Parentheses the corresponding S/N)

The reliability of our chosen method for X-ray stacking and source count extraction was

tested with Monte Carlo (MC) simulations. With 500 MC simulations of 53 (corresponding to the number of star-forming galaxies not detected in X-rays) randomly selected positions having no X-ray detections nearby, we obtained a histogram of stacked S/N values that is well fitted by a normal distribution with a center at -0.02 ± 0.8 , that is, consistent with no detection. Similar results were obtained using a sample size of 19, the number of quiescent non-detections.

$L_{0.5-8\text{ keV}}$ (erg s^{-1})	HR	Classification
$> 3 \times 10^{42}$	< -0.2	Unobscured AGNs ($N_{\text{H}} < 10^{22} \text{ cm}^{-2}$)
$> 3 \times 10^{42}$	> -0.2 and < 0.8	Moderately obscured AGNs ($10^{22} < N_{\text{H}} < 10^{24} \text{ cm}^{-2}$)
$> 3 \times 10^{42}$	> 0.8	Compton-thick AGNs ($N_{\text{H}} > 10^{24} \text{ cm}^{-2}$)
$< 3 \times 10^{42}$	< -0.2	Star-forming galaxy
$< 3 \times 10^{42}$	> -0.2	Low-luminosity obscured AGNs or star-forming galaxy

Table 9.2 Classification scheme used in this work, with limits from Szokoly et al. (2004), Wang et al. (2004), and Treister et al. (2009)

We quantified the hardness of the X-ray spectra using the hardness ratio (see eq. 8.2). Assuming a power-law spectrum, we also derived a photon index, Γ , with the online mission count rate simulator WebPIMMS⁵ using a Galactic H I column density of $8.8 \times 10^{19} \text{ cm}^{-2}$ (Stark et al., 1992) and not including intrinsic absorption. Whenever the S/N in either soft or hard band was below 2, we used the corresponding 2σ upper limit on the count rate to calculate a limit on both HR and Γ , leading to a limit on the luminosity as well. When neither a hard- nor a soft-band flux was detected with an S/N above 2, a typical faint source value of $\Gamma = 1.4$ (Xue et al., 2011) was assumed, corresponding to $\text{HR} \sim -0.3$ for an intrinsic powerlaw spectrum of $\Gamma = 1.9$ (Wang et al., 2004).

We derived the unabsorbed flux from the count rate by again using the WebPIMMS tool, now with the Γ tied to the observed value of either the individually detected galaxy or the stack in question. With this method, a count rate of $\sim 10^{-5} \text{ counts s}^{-1}$ corresponds to a flux of nearly $10^{-16} \text{ erg cm}^{-2} \text{ s}^{-1}$ in full band at a typical value of $\Gamma = 0.8$. Finally, the flux was converted into luminosity in the desired rest-frame bands using XSPEC version 12.0.7 (Arnaud, 1996).

9.2.2 LUMINOUS AGN IDENTIFICATION

In the top panel of Figure 9.2 are shown the rest-frame X-ray full band luminosities, $L_{0.5-8\text{ keV}}$, not corrected for intrinsic absorption, versus observed hardness ratio, HR, for all X-ray detected galaxies as well as stacked non-detections. A typical detection limit on $L_{0.5-8\text{ keV}}$ has been indicated with a dotted line in Figure 9.2, calculated as two times the background noise averaged over all source positions. A few detected galaxies were found below this limit due to these residing at relatively low z and/or in regions of lower-than-average background. Galaxies with $L_{0.5-8\text{ keV}} > 3 \times 10^{42} \text{ erg s}^{-1}$ were selected as luminous AGN, since star-forming galaxies are rarely found at these luminosities (Bauer et al., 2004). In addition, we adopted the HR criteria in Table 9.2 in order to identify obscured and unobscured AGNs.

About 53%(27/51) of the X-ray detected galaxies were identified as luminous AGNs, with 22 moderately to heavily obscured ($-0.2 < \text{HR} < 0.8$) and 5 unobscured ($\text{HR} < -0.2$) AGNs.

⁵<http://heasarc.nasa.gov/Tools/w3pimms.html>

The rest had X-ray emission consistent with either low-luminosity AGNs or star formation. We did not identify any Compton-thick AGNs directly, but three galaxies had lower limits on their hardness ratios just below $\text{HR} = 0.8$, thus potentially consistent with Compton-thick emission (see Table 9.2). In total, we detected a luminous AGN fraction of $22\% \pm 5\%$ (27/123), a fraction which is $23\% \pm 5\%$ (22/96) for the star-forming and $19\% \pm 9\%$ (5/27) for the quiescent galaxies.

Stacking the non-detections resulted in average X-ray source properties that exclude high luminosity AGNs. However, the inferred limits on their HR were consistent with a contribution from low-luminosity AGNs, the importance of which cannot be determined from this plot alone.

9.2.3 X-RAY INFERRED SFR

From the rest-frame hard band luminosity, $L_{2-10\text{ keV}}$ it is possible to derive estimates of the SFR, as the number of high-mass X-ray binaries (HMXBs) is proportional to the SFR (Ranalli et al., 2003). Kurczynski et al. (2012) made a comparison of different SFR indicators, by applying three different $L_x \rightarrow \text{SFR}$ conversions to 510 star-forming BzK galaxies at $1.2 < z < 3.2$, selected as having $L_{2-10\text{ keV}} < 10^{43} \text{ erg s}^{-1}$. While relations by Persic et al. (2004) and Lehmer et al. (2010) overestimated the true SFR (from rest-frame UV and IR light) by a factor of ~ 5 , the relation by Ranalli et al. (2003) provided a good agreement at $1.5 < z < 3.2$. But, as pointed out by Kurczynski et al. (2012), all relations might lead to an overestimation due to contamination by obscured AGNs in the sample of SF galaxies. As we did not know the exact amount of obscured AGN contamination in the stacks, we chose to use the following relation by Ranalli et al. (2003) as a conservative estimate of the SFR:

$$\text{SFR}_{2-10\text{ keV}} = 2.0 \times 10^{-40} L_{2-10\text{ keV}} \quad (9.4)$$

with SFR measured in $M_\odot \text{ yr}^{-1}$ and $L_{2-10\text{ keV}}$ in erg s^{-1} . Another reason for not using the more recent relation by Lehmer et al. (2010) is that this relation was constructed for galaxies with $\text{SFR} > 9 M_\odot \text{ yr}^{-1}$ only, whereas a large part of our sample had very low SFRs as inferred from SED fitting ($< 1 M_\odot \text{ yr}^{-1}$). Following Kurczynski et al. (2012), we used the observed soft band flux to probe the rest-frame hard band luminosity. The uncertainty on the SFR is estimated from the error on the observed soft-band flux together with a systematic error in the relation itself of 0.29 dex, as given by Ranalli et al. (2003).

For comparison, the ‘true’ SFR is inferred from rest-frame UV and IR light, $\text{SFR}_{\text{UV+IR}}$, following the method of Papovich et al. (2006):

$$\text{SFR}_{\text{UV+IR}} = 1.8 \times 10^{-10} (L_{\text{IR}} + 3.3 L_{2800}) / L_\odot \quad (9.5)$$

where L_{IR} is the total infrared luminosity and L_{2800} is the monochromatic luminosity at rest-frame 2800 Å. L_{2800} comes from the rest-frame UV flux, $f_{2800\text{\AA}}$, and in this context, the errors on $f_{2800\text{\AA}}$ are negligible. We derived L_{IR} from the observed 24 μm flux, $f_{24\mu\text{m}}$, using redshift-dependent multiplicative factors, $a(z)$, from the work of Wuyts et al. (2008), Section 8.2 in that paper):

$$L_{\text{IR}}[L_{\odot, 8-1000\mu\text{m}}] = 10^{a(z)} \cdot f_{24\mu\text{m}} \quad (9.6)$$

The errorbars on L_{IR} derive from the errors on $f_{24\mu\text{m}}$ and we further assume an uncertainty

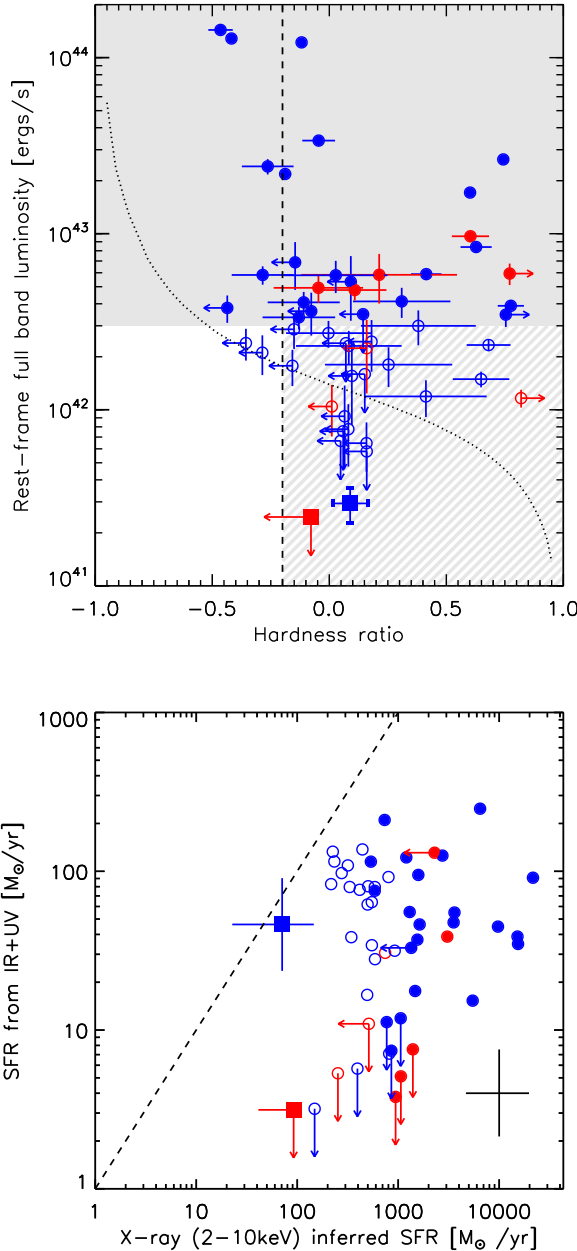


Figure 9.2 Top: $L_{0.5-8 \text{ keV}}$ vs. HR for all galaxies. Red: quiescent galaxies. Blue: star-forming galaxies. Squares: stacks of non-detected samples. Filled circles: luminous AGNs (selected with the X-ray criteria indicated by a shaded area). Open circles: galaxies dominated by low-luminosity AGNs or star formation processes alone (selected with X-ray criteria indicated by a hatched area). Dashed line: separating obscured ($N_H \gtrsim 10^{22} \text{ cm}^{-2}$) from unobscured AGNs. Dotted line: typical detection limit. Errorbars display 2σ errors and limits are indicated with arrows. Bottom: $\text{SFR}_{\text{UV+IR}}$ vs. $\text{SFR}_{2-10\text{keV}}$ (see the text). Dashed line: equality. Typical errors on X-ray detected galaxies are shown in the lower right corner. Symbols are as above.

of 0.3 dex in the relation of Papovich et al. (2006) as found by Bell (2003) when comparing to H α - and radio-derived SFRs. The X-ray undetected quiescent galaxies were not detected with S/N > 3 in 24 μm either (except in one case) leading to a mean flux of $1.2 \pm 1.7 \mu\text{Jy}$, of which we adopted a 2σ upper limit for the remaining analysis.

In the bottom panel of Figure 9.2, $\text{SFR}_{2-10\text{ keV}}$ is compared to $\text{SFR}_{\text{UV+IR}}$ with the dashed line indicating equality. It is no surprise that nearly all of the individual X-ray detections have very high $\text{SFR}_{2-10\text{ keV}}$ as compared to $\text{SFR}_{\text{UV+IR}}$, as we were largely insensitive to individual purely star-forming galaxies, given the detection limits in the top panel of Figure 9.2 and the criteria in Table 9.2.

For the star-forming stack, the X-ray inferred SFR of $71 \pm 51 M_\odot \text{ yr}^{-1}$ is consistent with the IR+UV inferred SFR of $46 \pm 33 M_\odot \text{ yr}^{-1}$, whereas the quiescent stack shows an $\text{SFR}_{2-10\text{ keV}}$ of $92 \pm 65 M_\odot \text{ yr}^{-1}$ ($89 \pm 17 M_\odot \text{ yr}^{-1}$ when bootstrapping this sample 200 times), well exceeding $\text{SFR}_{\text{UV+IR}} \leq 3 M_\odot \text{ yr}^{-1}$.

9.3 AN OVERWHELMINGLY LARGE AGN POPULATION

9.3.1 LUMINOUS AGN FRACTION

In total, 22 X-ray detected galaxies have emission consistent with containing a luminous (rest-frame $L_{0.5-8\text{keV}} > 3 \times 10^{42} \text{ erg s}^{-1}$) and obscured ($10^{22} < N_{\text{H}} < 10^{24} \text{ cm}^{-2}$) AGN, and a further five have emission consistent with a luminous unobscured ($N_{\text{H}} < 10^{22} \text{ cm}^{-2}$) AGN. This leads to a luminous AGN fraction of the full sample of $22\% \pm 5\%$ (27/123) and of the detected galaxies only, $53\% \pm 13\%$ (27/51). The AGN fraction among both quiescent and star-forming galaxies, according to their X-ray spectra, is measured to be around 20% as Table 9.3 shows, meaning that AGNs in massive $z \sim 2$ galaxies, even quiescent ones, are common, as proposed by Kriek et al. (2009) who studied the near-IR spectrum of one quiescent galaxy.

	Quiescent (27)	Star-forming (96)
Luminous AGNs	5	22
Low-luminosity AGNs	2 (det) 12–19 (non-det)	19 (det) 0–21 (non-det)
Luminous AGN fraction	$19\% \pm 9\%$	$23\% \pm 5\%$
Total AGN fraction	70%–100%	43%–65%

Table 9.3 X-Ray derived AGN Numbers and Fractions for Quiescent and Star-forming Galaxies, Divided into Luminous AGNs and Detected and Non-detected Low-luminosity AGNs

This luminous AGN fraction is high when compared to the 5% found by Rubin et al. (2004) (see the introduction), but this is likely a consequence of their 4σ detection limit of $1.2 \times 10^{43} \text{ erg s}^{-1}$ in rest-frame 2–10 keV being about twice as high as our limit of $5.5 \times 10^{42} \text{ erg s}^{-1}$ (at $\Gamma = 1.4$), as calculated from the average background noise in the observed soft band. Adopting the detection limit of Rubin et al. (2004) and requiring an S/N of at least 4, we reduce our fraction of luminous AGN to $8\% \pm 3\%$ (10/123), consistent with the results of Rubin et al. (2004). Alexander et al. (2011), using also the 4 Ms CDF-S data, found a much lower X-ray detection fraction of $21\% \pm 3\%$ as compared to ours ($53\% \pm 7\%$), and a luminous AGN fraction of only $9\% \pm 2\%$ (20/222). We believe that the discrepancies have several reasons, the main ones being: (1) our use of a mass-complete sample, whereas the BzK selection technique used by Alexander et al. (2011) includes galaxies down to $M_* \sim 10^{10} M_\odot$ for which the total AGN fraction,

assuming a fixed Eddington ratio, is expected to be lower above our detection limit,⁶ (2) our updated source count extraction and stacking method leading to higher S/N, and (3) the use of Γ instead of HR in the AGN identification conducted by Alexander et al. (2011). For comparison, Tanaka et al. (2012) recently discovered a group of quiescent galaxies at $z = 1.6$ with only one main-sequence star-forming galaxy. This group differed from local groups in having a remarkably high AGN fraction of $38^{+23}_{-20}\%$, consistent with our result, and which they interpret as possible evidence for AGN activity quenching star formation.

9.3.2 IMPORTANCE OF LOW-LUMINOSITY AGNs

As seen in Figure 9.2, the X-ray-identified luminous AGNs in general show an excess in SFR compared to that inferred from IR+UV emission. Among the galaxies classified as being dominated by either low-luminosity AGN or star formation, about $\sim 90\% (21/24)$ have $SFR_{2-10\text{ keV}}$ more than 1σ above $SFR_{\text{UV+IR}}$.

Surprisingly, the quiescent stack also has a much larger $SFR_{2-10\text{ keV}}$ than $SFR_{\text{IR+UV}}$. Even when removing the marginally undetected galaxies with $2 < \text{S/N} < 3$, the resulting $SFR_{2-10\text{ keV}} = 62 \pm 19 M_{\odot} \text{ yr}^{-1}$ is still more than 3σ above $SFR_{\text{IR+UV}}$. This discrepancy is only further aggravated if instead assuming the $\text{SFR}-L_X$ relation of Lehmer et al. (2010). If caused by obscured star formation, we would have expected an average $24\mu\text{m}$ flux of $90\mu\text{Jy}$ for the individual galaxies, in order to match the lower limit on $SFR_{2-10\text{ keV}}$. This is far above the upper limit of $3.4\mu\text{Jy}$ for the stack, suggesting that the X-ray flux of this stack is instead dominated by low-luminosity AGNs, but that their contribution to the $24\mu\text{m}$ flux remains undetectable in the *Spitzer*-MIPS data.

We derived a lower limit on the low-luminosity AGN contribution for this stack of 19 objects by constructing a mock sample of the same size and with the same redshifts, but containing N low-luminosity AGNs with luminosities $L_{0.5-8\text{ keV}} = 10^{42} \text{ erg s}^{-1}$ just below the detection limit and $19 - N$ galaxies with $L_{0.5-8\text{ keV}} = 10^{41} \text{ erg s}^{-1}$ (all of them with $\Gamma = 1.4$). From random realizations of this mock sample we found that at least $N = 12$ low-luminosity AGNs are required to match the observed rest-frame 2–10 keV luminosity of the stack. Similarly, we found that by removing at least 12 randomly selected galaxies it is possible to match the low SFR predicted by IR+UV emission, though only with a small probability ($\sim 1\%$ of 200 bootstrappings). We therefore adopted 63% ($= 12/19$) as a conservative lower limit on the low-luminosity AGN fraction among quiescent X-ray non-detections, but we note that the data were consistent with all the quiescent galaxies hosting low-luminosity AGNs if the luminosity of these was assumed to be only $L_{0.5-8\text{ keV}} = 7 \times 10^{41} \text{ erg s}^{-1}$.

Interestingly, the quiescent stack was only detected in the soft band, cf. Table 9.1, whereas one might expect a significant contribution to the hard band flux from a low-luminosity AGN population as the one proposed above. The lack of a hard band detection can be explained by the fact that the sensitivity of the CDF-S observations drops about a factor of six from the soft to the hard band (Xue et al., 2011), meaning that the low-luminosity AGN population must be relatively unobscured ($\Gamma > 1$, consistent with the value of 1.4 assumed here), as it would otherwise have been detected in the hard band with an $\text{S/N} > 2$.

The $SFR_{2-10\text{ keV}}$ of the star-forming stack was consistent with its $SFR_{\text{UV+IR}}$, meaning that a strict lower limit to the low-luminosity AGN fraction here, is zero. However, performing the

⁶For a fixed Eddington ratio, and assuming that galaxy bulge mass increases with total stellar mass, the AGN X-ray luminosity is expected to scale with galaxy stellar mass according to the $M_{\text{bh}}-M_{\text{bulge}}$ relation (Häring & Rix, 2004)

test above with the same model parameters, a maximum of 40%(21/53) low-luminosity AGNs is possible, before the X-ray inferred SFR exceeds the upper limit on $\text{SFR}_{\text{UV+IR}}$.

It should be mentioned that the $24\,\mu\text{m}$ flux, especially at these high redshifts, is an uncertain estimator of the total rest-frame infrared luminosity, i.e., the entire dust peak, used in the conversion to SFR. As shown by Bell (2003), one should ideally use the entire 8–1000 μm range, e.g., by taking advantage of Herschel data, which can lead to systematic downward correction factors up to ~ 2.5 for galaxies with $L_{\text{IR}} \approx 10^{11} L_{\odot}$ (similar to the inferred IR luminosities of our sample galaxies detected in $24\,\mu\text{m}$, showing a median of $L_{\text{IR}} = 10^{11.5} L_{\odot}$) as demonstrated by Elbaz et al. (2010). However, using the same conversion from $f_{24\,\mu\text{m}}$ to L_{IR} as the one implemented in this study, Wuyts et al. (2011) showed that the resulting L_{IR} for galaxies out to $z \sim 3$ are consistent with those derived from PACS photometry with a scatter of 0.25 dex. Hence, we do not expect the inclusion of Herschel photometry in the this study to significantly impact any of our results, and we leave any such analysis for future work.

Table 9.3 gives an overview of the derived AGN fractions, both at high and low X-ray luminosity. Adding the numbers of luminous AGN, X-ray-detected low-luminosity AGNs as well as the estimated lower limit on the low-luminosity AGN fraction among non-detections, we arrive at a lower limit on the total AGN fraction of

$$f_{\text{AGN}} \geq \frac{27 + 21 + 0.6 \cdot 19 + 0 \cdot 53}{123} = 0.48 \quad (9.7)$$

for all massive galaxies at $z \sim 2$. While for the star-forming galaxies this fraction lies in the range from 43%–65%, it must be 70%, and potentially 100%, for the quiescent galaxies. Using the upper limits on these numbers, a tentative upper limit on the total AGN fraction is 0.72.

9.3.3 CONTRIBUTION FROM HOT GAS HALOS

We have so far considered star formation and AGN activity as causes of the X-ray emission observed, but a third possibility is an extended hot gas halo as seen around many nearby early-type galaxies in the same mass-range as our sample galaxies (Mulchaey & Jeltema, 2010) and predicted/observed around similar spirals (Toft et al., 2002; Rasmussen et al., 2009; Anderson & Bregman, 2011; Dai et al., 2012). AGN X-ray emission is expected to come from a very small, $R < 1\,\text{pc}$, accretion disk surrounding the central black hole of the host galaxy (Lobanov & Zensus, 2007), whereas very extended star formation in the galaxy or a hot gas halo surrounding it would lead to more extended emission. We investigated the possibilities for these latter cases by comparing radial surface brightness profiles of the 51 individually X-ray detected galaxies out to a radius of $8''$ in both the stacked observed image and a correspondingly stacked PSF image.

The profiles were calculated in full band only, because of the high S/N here as compared to the other bands (cf. Figure 9.1). For each galaxy, we extracted the background subtracted source count per pixel within 10 concentric rings of width $0''.8$ around the galaxy center positions from the FIREWORKS catalog, and each profile was normalized to the mean count rate in all rings. The same procedure was applied to the corresponding PSF images, extracted with the library and tools that come with CIAO,⁷ allowing for extraction at the exact source positions on the detector. We verified the robustness of using PSF models from the CIAO calibration database

⁷<http://cxc.cfa.harvard.edu/ciao4.3/ahelp/mkpsf.html>

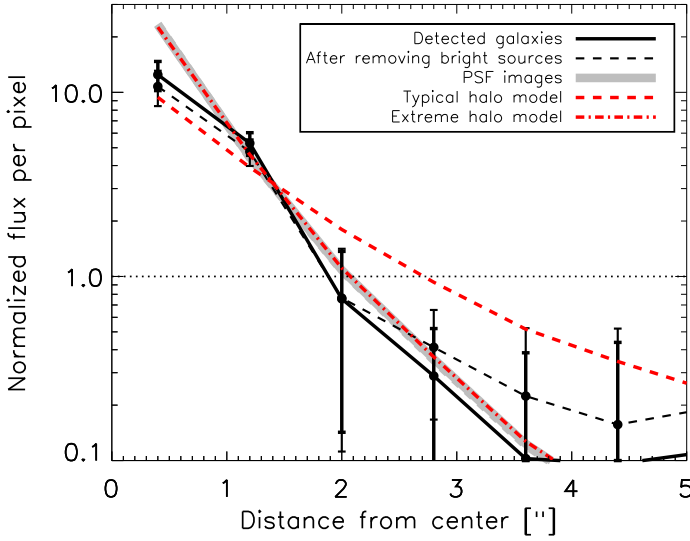


Figure 9.3 Comparison of the radial surface brightness profiles in PSF images vs. observed images in full band for all detected galaxies. Black: stacked observed image centered on K -band positions from FIREWORKS for all detected galaxies (solid line) and if excluding the three X-ray brightest sources (dashed line). Grey line: stacked PSF image. Red: stack of halo model images, with $\beta = 0.5$, $R_c = 2.5$ kpc (dashed) and $\beta = 1$, $R_c = 1$ kpc (dot-dashed).

for this purpose, by repeating the above procedure for 51 known X-ray bright point-like sources from the catalog of Xue et al. (2011), and confirming that the resulting mean profile was fully consistent with that of the corresponding model PSFs.

As can be observed in Figure 9.3, the combined radial profile of our X-ray detected galaxies in the full band is consistent with the PSF of point sources stacked at the same detector locations. A Kolmogorov-Smirnov (K-S) test yields a statistic of 0.2 and allow us to rule out the null hypothesis that the two profiles were drawn from the same parent sample, with a p value of 0.9996%.

Omitting the three sources with $L_{0.5-8\text{ keV}} > 10^{44} \text{ erg s}^{-1}$ (cf. Figure 9.2) leads to a more extended profile (dashed black line in Figure 9.3), but the result still shows a high corresponding K-S probability of 70%. We also compared the profiles while recentering the images on the center of the X-ray emission as derived using WAVDETECT⁸ instead of the K -band center positions listed in the FIREWORKS catalog, in order to test for the impact of any off-set between the X-ray and optical centroids. However, the recentering only resulted in small variations within the errorbars on the original profile. The same conclusions applied to the subsample of X-ray detected star-forming galaxies only, whereas the S/N was too low to perform a similar study on the quiescent, X-ray detected sample alone.

For comparison, we also simulated the stacked profile of extended hot gas halos, using for the surface brightness profile the β -model first introduced by Cavaliere & Fusco-Femiano (1976). With default parameters of $\beta = 0.5$ and core radius $R_c = 2.5$ kpc, both taken from the study of $z \lesssim 0.05$ early-type galaxies by O’Sullivan et al. (2003), the stacked profile of the halos, convolved with the corresponding PSFs, is well outside the errorbars of the measured

⁸WAVDETECT is part of the CIAO software.

profile. Only if assuming an extremely compact case of $\beta = 1$ and $R_c = 1 \text{ kpc}$, does the halo emission become sufficiently compact to mimic that of the PSF profile (see dash-dotted line in Figure 9.3), but the halo model then overpredicts the observed surface brightness on scales smaller than $1''$. In conclusion, a hot gas halo alone, described by a β -model, cannot explain the emission, unless one chooses model parameters that render the profile indistinguishable from a point-like source.

9.3.4 QUENCHING OF STAR FORMATION BY AGNs?

It remains debated whether the presence of AGN is connected with internal galaxy properties associated with secular evolution or, to a higher degree, with external processes (Darg et al., 2010). For example, the cosmic star formation rate density and the number density of AGN share a common growth history with a peak in activity around $z \sim 2\text{--}3$ (Treister & Urry, 2012; Dunlop, 2011), hinting at a co-evolution between SFR and supermassive black hole (SMBH) accretion (Schawinski, 2011). We investigated the correlation, if any, between the presence of AGNs and internal/external processes, treating luminous and low-luminosity AGNs separately. As typical internal properties governing secular evolution we focused on stellar mass, M_* , and SFR (Peng et al., 2010), while major mergers were taken as a likely case of external processes and as a phenomenon often associated with luminous AGNs (Treister et al., 2012).

Starting with our X-ray identified luminous AGNs, we found that the fraction of these does not correlate with star formation in our sample (cf. Table 9.3). In addition, the distribution of luminous AGNs and that of the rest with regards to their $\text{SFR}_{\text{IR+UV}}$ are similar, with a K-S test yielding a statistic of 0.21 with a probability of 59%. Similarly, Harrison et al. (2012) found no correlation between AGN luminosity and quenching of star formation, albeit at a higher luminosity ($L_{2\text{--}8\text{ keV}} > 10^{44} \text{ erg s}^{-1}$) than probed here. Dividing the sample according to M_* instead, by constructing two bins around the median mass of $1.1 \times 10^{11} M_\odot$, we arrived at similar luminous AGN fractions above and below this mass limit, namely $21\% \pm 7\%$ (13/61) and $23\% \pm 7\%$ (14/62), respectively. We thus find no clear evidence for the luminous AGN fraction of our sample to correlate with internal properties, suggesting that an external factor is of larger importance.

An alternative is that luminous AGNs are primarily triggered by non-secular processes such as major mergers. Treister et al. (2012) found that major mergers are the only processes capable of triggering luminous ($L_{\text{bol}} \gtrsim 10^{45} \text{ erg s}^{-1}$) AGN at $0 < z < 3$. Our luminous AGN fraction is consistent with the major merger fraction of massive ($M_* > 10^{11} M_\odot$) galaxies at $1.7 < z < 3$ found by Man et al. (2012) to be $15\% \pm 8\%$ (compared to a luminous AGN fraction of $11 \pm 3\%$ (13/123) when excluding galaxies with $M_* < 10^{11} M_\odot$). This is consistent with the idea that our luminous AGNs are triggered by major mergers, but a more direct test of this scenario would be to search for major mergers using the imaging data available in CDF-S. Indeed, Newman et al. (2012) used *HST* CANDELS imaging in the GOODS-South field residing within CDF-S (along with the UKIRT Ultra Deep Survey) to arrive at roughly equal pair fractions when comparing massive ($M_* > 10^{10.7} M_\odot$) quiescent to massive star-forming galaxies at $0.4 < z < 2$. Again, this is in agreement with our result that the luminous AGN fraction does not vary between quiescent and star-forming galaxies. A detailed morphological study of our X-ray identified luminous AGN using the *HST*/WFC3 data to search for evidence of merging is an interesting extension to the work presented here, which we leave for a future study.

Turning toward our low-luminosity AGNs, we *do* see X-ray evidence for an enhanced pop-

ulation among the quiescent galaxies when compared to their star-forming equivalents. The mean masses of our non-detected samples of quiescent and star-forming galaxies are similar (14.6 ± 1.6 and $12.7 \pm 1.0 \times 10^{10} M_{\odot}$ respectively), suggesting that the relevant factor here is SFR. At $0.01 < z < 0.07$, Schawinski et al. (2009) found that massive ($M_* \gtrsim 10^{10} M_{\odot}$) host galaxies of low-luminosity AGNs all lie in the green valley, that is, at some intermediate state after star formation quenching has taken place and before the SED is truly dominated by old stellar populations. The observation that these host galaxies had been quiescent for ~ 100 Myr, ruled out the possibility that one short-lived, luminous AGN suppressed star formation and, at the same time, made it unlikely that the same AGN quenching star formation was still active, given current AGN lifetime estimates of $\sim 10^7$ – 10^8 yr (Di Matteo et al., 2005). Rather, the authors favored a scenario in which a low-luminosity AGN already shut down star formation, followed by a rise in luminosity, making the AGN detectable. At $z \sim 2$, SED fits of massive ($M_* > 10^{11} M_{\odot}$) quiescent galaxies show that the quenching typically took place ~ 1 Gyr before the time of observation (Toft et al., 2012; Krogager, J.-K. et al., in preparation), demanding an even longer delay or an episodic AGN activity as frequently applied in models (Croton et al., 2006). Episodic AGN activity could explain why we see evidence for a higher low-luminosity AGN fraction among quiescent as compared to star-forming galaxies, but it would also require the low-luminosity AGN phase in quiescent galaxies to last at least as long as the dormant phase. Future modeling and observations will show whether this is in fact possible.

We conclude that our data are consistent with a scenario in which luminous AGNs in massive galaxies at $z \sim 2$ are connected with major mergers or other non-secular processes, while the presence of low-luminosity AGNs in the majority of quiescent galaxies suggests that these AGNs present an important mechanism for quenching star formation and keeping it at a low level. Ultimately what happens at $z \sim 2$ has to agree with the subsequent evolution that changes size and morphology of quiescent galaxies (Barro et al., 2013).

9.4 CONCLUSIONS

Our main conclusions are on the following two topics:

1. *Luminous AGN fraction*

We find a luminous AGN fraction of $22\% \pm 5\%$ among massive ($M_* > 5 \times 10^{10} M_{\odot}$) galaxies at redshifts $1.5 \leq z \leq 2.5$, using their X-ray properties extracted from the 4 Ms Chandra Deep Field South observations. Among the X-ray detected galaxies, $53\% \pm 13\%$ harbor high-luminosity AGNs, while stacking the galaxies not detected in X-ray, leads to mean detections consistent with low-luminosity AGNs or pure star formation processes. The luminous AGN fraction among quiescent and star-forming galaxies is similar ($19\% \pm 9\%$ and $23\% \pm 5\%$, respectively) and does not depend on galaxy M_* .

We confirmed that extended X-ray emission from a hot gaseous halo is not a viable explanation for the observed X-ray emission of the X-ray detected galaxies.

2. *Limits on total AGN fraction*

We convert the rest-frame hard band X-ray luminosity into an upper limit on the star formation rate, $SFR_{2-10\text{ keV}}$ and compare to that derived from the rest-frame IR+UV emission, $SFR_{\text{IR+UV}}$. All luminous AGNs show an excess in $SFR_{2-10\text{ keV}}$ as expected, and so does a large fraction ($\sim 90\%$) of the remaining detected galaxies. While the star-forming galaxies not detected in X-ray have a mean X-ray inferred SFR of $71 \pm 51 M_{\odot} \text{ yr}^{-1}$, consis-

tent with their $\text{SFR}_{\text{IR+UV}}$, the stack of quiescent galaxies shows an excess in $\text{SFR}_{2-10\,\text{keV}}$ of a factor > 10 above the upper limit on $\text{SFR}_{\text{IR+UV}}$. For these galaxies, we find that a minimum fraction of $\sim 60\%$ must contain low-luminosity ($L_{0.5-8\,\text{keV}} \approx 10^{42}\,\text{erg s}^{-1}$) AGNs if the SFR estimates from X-ray are to be explained, and that low-luminosity AGNs might be present in all of them. On the other hand, for the star-forming stack, we derive a low-luminosity AGN fraction of 0–40%.

Gathering all low- and high-luminosity AGNs, we derive a lower limit to the total AGN fraction of 48%, with a tentative upper limit of 72%.

Our study was the first to present observational evidence that, at $z \sim 2$, the majority of quiescent galaxies host a low- to a high-luminosity AGN, while the AGN fraction is significantly lower in star-forming galaxies. These findings are consistent with an evolutionary scenario in which low-luminosity AGN quench star formation via the energetic output from SMBH accretion, which, if believed to continue in an episodic fashion as often invoked by models, would need to have ‘dormant’ phases at least as long as ‘active’ phases.

We find that the high-luminosity AGNs are likely related to non-secular processes such as major mergers. In the future, examining the X-ray properties of galaxies in a larger sample, cross-correlated with signs of major mergers, may shed further light on the co-evolution of AGNs and host galaxy.

10

OUTLOOK

Since we published these results in 2013, many additional observational studies have been carried out with the aim of shedding light on AGN-galaxy co-evolution at $z \sim 2$. A short summary is provided here together with future directions in this field.

10.1 THE AGN-MORPHOLOGY CONNECTION

First of all, we found no clear evidence for a correlation between the presence of a luminous AGN and the internal properties of massive galaxies at $z \sim 2$. This was interpreted as an argument for the need of external factors triggering the luminous AGN phase rather than events associated with secular evolution. However, we only considered stellar mass and SFR, whereas more recent observations have established a clear correlation between the presence (and strength) of AGN and the morphology of its host galaxy.

In this regard, Barro et al. (2013) analysed the morphologies and SFRs of $M_* > 10^{10} M_\odot$ galaxies at $z = 1.4 - 3$ in the GOODS-S and CANDELS UDS fields, for comparison with AGN activity as a function of redshift. Barro et al. (2013) found a population of compact star-forming galaxies (cSFGs; defined as having $\log(M_*/r_e^{1.5})$ below $10.3 M_\odot \text{ kpc}^{-1.5}$) at $z = 2.6 - 3.0$ that disappears before the compact quiescent galaxies (CQGs) of similar structural properties appear at lower redshifts. At the same time, the AGN fraction among cSFGs is higher at $z > 2$ than at lower redshifts and X-ray luminous ($L_{2-8 \text{ keV}} > 10^{43} \text{ erg s}^{-1}$) AGNs are found $\sim 30\%$ more frequently in cSFGs than in non-compact ones at $z > 2$. This was interpreted as a sign that at least some cSFGs evolve directly into the CQGs observed at $z \sim 2$ via the evolutionary path described in Section 2.1.5, whereas non-compact quiescent galaxies, formed later on, are the result of normal SFGs that are quenched by other mechanisms which partially preserve the structural properties.

Deriving the total IR luminosity directly from the $24 \mu\text{m}$ flux only, is a rough approximation that could possibly affect our results and those of Barro et al. (2013), as the possible contribution from an AGN to the FIR luminosity can lead to overestimates of the SFR. Mancini et al. (2015) did a more careful estimate of L_{IR} with (*Spitzer+Herschel*) photometry from $24 \mu\text{m}$ to $250 \mu\text{m}$ of $56 M_* \geq 10^{11} M_\odot$ galaxies at $1.4 \leq z \leq 2$ in the GOODS-S field, for a better estimate of $\text{SFR}_{\text{IR+UV}}$. Defining AGN as those with excess X-ray and/or radio (VLA 1.4 GHz) luminosity with respect to the expected $\text{SFR}_{\text{IR+UV}}$ or SFR_{SED} , and classifying galaxies as star-forming/quiescent based on sSFR as well as UVJ color, the authors found relatively high AGN fractions of $\sim 40 \pm 10\%$ and $\sim 22 \pm 7\%$ for star-forming and quiescent galaxies, respectively

(though fractions very close to ours when adopting the same criteria). In agreement with Barro et al. (2013), Mancini et al. (2015) also found that the presence of an AGN correlates with compactness as probed by a steep radial surface brightness profile in rest-frame optical. Over a wider redshift range, $1.4 < z < 3$ but with a similar method, Rangel et al. (2014) concluded that compact galaxies, both quiescent and star-forming, display higher intrinsic $2 - 8 \text{ keV}$ luminosities and levels of obscuration than in extended galaxies.

These studies show that of out massive galaxies at $z \sim 2$, compact ones contain the most powerful AGN, and that when studying quiescent/star-forming galaxy samples across redshift, observations seem to promote a picture in which cSFGs evolve directly into CQGs via a relatively obscured AGN phase, albeit of high (absorption-corrected) X-ray luminosity.

10.2 DIRECT OBSERVATIONS OF AGN FEEDBACK

Direct evidence for the radiative and quasar mode of AGN feedback is now existing for a few, mostly nearby, objects (see review by Fabian, 2012). For example, in a study of the UV absorption line profiles of $226 \text{ M}_* \geq 10^{11} \text{ M}_\odot$ galaxies at $1 < z < 3$, Cimatti et al. (2013) found possible gas outflow velocities of up to $\sim 500 \text{ km s}^{-1}$, but only in galaxies classified as luminous AGNs (with $L_{2-8 \text{ keV}} > 10^{42.3} \text{ ergs s}^{-1}$). This indicates that the gas here is moving faster than the escape velocity of active galaxies, resulting in the ejection of part of the ISM possible decrease in SFR. With the X-ray satellite NuStar, sensitive to high energy X-rays of $3 - 79 \text{ keV}$, it is also possible to see such outflows in X-ray absorption and emission lines as demonstrated by Nardini et al. (2015). Likewise but at high redshift, Nesvadba et al. (2011) observed evidence for outflows of turbulent gas traced by narrow-line emission in the rest-frame UV and optical of two quasars at $z \sim 3.4$ and ~ 3.9 . In addition to observations in UV, AGN feedback has been confirmed with radio and sub-mm observations, in particular in the form of strong molecular outflows (e.g. Feruglio et al., 2010; Cicone et al., 2014; Tombesi et al., 2015). Comparing the mass outflow (or inflow) rates of ionized or molecular gas to the accretion rate to the AGN, hints at the effect that these might have on the global SFR, as summarized by e.g. Bergmann (2012) and Storchi-Bergmann (2014). However, *more observations of both jets and outflows, observationally confirmed in at least some AGNs at redshifts out to almost $z \sim 4$, are needed in order to settle how they affect the ISM of their host galaxies as a whole.*

10.3 FUTURE DIRECTIONS: DISCERNING VARIABILITY WITH TIME

In particular the arrival of new observing facilities, will open up this field towards high redshift by studying both individual cases and global properties of large samples.

Seeing the strong connection between compactness and AGN activity at high- z , as revealed over recent years, this field will benefit tremendously from the arrival of JWST, that will enable rest-frame optical imaging out to $z \sim 10$ with 3 times better angular resolution than HST at $1.6 \mu\text{m}$ (Beichman et al., 2012). That means being able to see whether AGNs are associated with compact galaxies all the way out to Epoch of Re-ionization (EoR). With the high NIR spectral resolution of JWST, the absence of poly-aromatic hydrocarbon (PAH) emission at $\sim 6 - 11 \mu\text{m}$ can also be used to select possible AGN candidates without the need of X-ray observations (Windhorst et al., 2009; Hanami et al., 2011). The combined forces of JVLA, JWST and ALMA will also allow detections of molecular outflows at high- z by measuring gas

kinematics as traced by molecular and fine structure lines (Fabian, 2012).

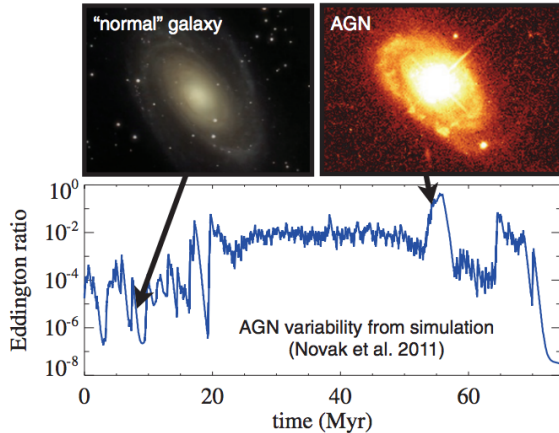


Figure 10.1 Illustration of AGN variability from Hickox et al. (2014) who took the Eddington ratio, a measure of BHAR, as a function of time from a hydrodynamic simulation presented by Novak et al. (2011) (bottom). Depending on the time of observation, the same galaxy can happen to be in an inactive state or a bright AGN state.

A potentially very important factor, but not completely revealed in any of the above studies, is time variation. As mentioned in Section 9.3.4, major mergers at $0 < z < 3$ have been associated with the most luminous AGNs (Treister et al., 2012), whereas moderate-luminosity ($L_{0.5-8\text{ keV}} \sim 10^{42-44} \text{ ergs s}^{-1}$) AGNs at $z \sim 2$ are not associated with disturbed morphologies, indicative of recent mergers, any more than non-active galaxies are (Kocevski et al., 2012). This said, the apparent lack of merger signatures in AGNs cannot rule out a connection between AGNs and mergers. First of all, if mergers in the initial phase generally produce obscured AGNs, then these will be harder to detect in X-rays, unless one has access to the hard X-rays that penetrate the obscuring gas better than the soft ones. One would then expect moderate AGNs to be primarily observed in post-starburst galaxies, in agreement with our stacking of un-detected X-ray sources, that revealed a *higher* signal from quiescent galaxies than from SFGs. Another exception would be if there exists a time delay between the merger and the actual onset of the luminous AGN phase. With JWST and upcoming X-ray observatories (see Section 1.5), we can start to piece together the redshift distribution of AGNs and mergers/pairs to look for a possible delay. A second time-related issue, possibly blurring the observable relationship between AGNs and their hosts, is variability of the AGN luminosity as shown in Fig. 10.1. Models show, that when reasonable variability for the AGN luminosity is assumed, the weak correlations between SFR and L_{AGN} can be reproduced, even if there is a tight underlying correlation between SFR and BHAR (Novak et al., 2012; Hickox et al., 2014).

In conclusion, new observatories can explore the presence of AGNs at $z > 2$, with particular focus on compactness, jets and in/outflows that are crucial for the overall SFR of the host galaxy. We also need to understand the time domain of AGNs in more detail, and as Fig. 10.1 illustrates, such observations of AGN variability will be aided by a wealth of emerging simulations attempting to model the AGN-host co-evolution (e.g. Vogelsberger et al., 2013; Gabor & Bournaud, 2014; DeGraf et al., 2014).

10.4 REFERENCES

- Alexander, D. M., Bauer, F. E., Brandt, W. N., et al. 2011, *ApJ*, 738, 44
- Anderson, M. E., & Bregman, J. N. 2011, *ApJ*, 737, 22
- Arnaud, K. A. 1996, in *Astronomical Society of the Pacific Conference Series*, Vol. 101, *Astro-nomical Data Analysis Software and Systems V*, ed. G. H. Jacoby & J. Barnes, 17
- Barro, G., Faber, S. M., Pérez-González, P. G., et al. 2013, *ApJ*, 765, 104
- Bauer, F. E., Alexander, D. M., Brandt, W. N., et al. 2004, *AJ*, 128, 2048
- Beichman, C. A., Rieke, M., Eisenstein, D., et al. 2012, in *Society of Photo-Optical Instrumentation Engineers (SPIE) Conference Series*, Vol. 8442, *Society of Photo-Optical Instrumentation Engineers (SPIE) Conference Series*, 2
- Bell, E. F. 2003, *ApJ*, 586, 794
- Bergmann, T. S. 2012, in *Astronomical Society of the Pacific Conference Series*, Vol. 460, *AGN Winds in Charleston*, ed. G. Chartas, F. Hamann, & K. M. Leighly, 133
- Bruzual, G., & Charlot, S. 2003, *MNRAS*, 344, 1000
- Cardamone, C. N., Urry, C. M., Damen, M., et al. 2008, *ApJ*, 680, 130
- Cavaliere, A., & Fusco-Femiano, R. 1976, *A&A*, 49, 137
- Cicone, C., Maiolino, R., Sturm, E., et al. 2014, *A&A*, 562, A21
- Cimatti, A., Brusa, M., Talia, M., et al. 2013, *ApJ*, 779, L13
- Cowie, L. L., Barger, A. J., & Hasinger, G. 2012, *ApJ*, 748, 50
- Croton, D. J., Springel, V., White, S. D. M., et al. 2006, *MNRAS*, 365, 11
- Daddi, E., Dickinson, M., Morrison, G., et al. 2007, *ApJ*, 670, 156
- Dai, X., Anderson, M. E., Bregman, J. N., & Miller, J. M. 2012, *ApJ*, 755, 107
- Darg, D. W., Kaviraj, S., Lintott, C. J., et al. 2010, *MNRAS*, 401, 1552
- DeGraf, C., Dekel, A., Gabor, J., & Bournaud, F. 2014, ArXiv e-prints
- Di Matteo, T., Springel, V., & Hernquist, L. 2005, *Nature*, 433, 604
- Done, C., Davis, S. W., Jin, C., Blaes, O., & Ward, M. 2012, *MNRAS*, 420, 1848
- Donley, J. L., Koekemoer, A. M., Brusa, M., et al. 2012, *ApJ*, 748, 142
- Dunlop, J. S. 2011, *Science*, 333, 178
- Elbaz, D., Hwang, H. S., Magnelli, B., et al. 2010, *A&A*, 518, L29
- Fabian, A. C. 2012, *ARA&A*, 50, 455
- Feruglio, C., Maiolino, R., Piconcelli, E., et al. 2010, *A&A*, 518, L155
- Franx, M., van Dokkum, P. G., Schreiber, N. M. F., et al. 2008, *ApJ*, 688, 770
- Gabor, J. M., & Bournaud, F. 2014, *MNRAS*, 441, 1615
- Gilli, R., Comastri, A., & Hasinger, G. 2007, *A&A*, 463, 79
- Grimm, H.-J., Gilfanov, M., & Sunyaev, R. 2003, *MNRAS*, 339, 793
- Hanami, H., Ishigaki, T., & Ishigaki. 2011, in *IAU Symposium*, Vol. 277, *IAU Symposium*, ed. C. Carignan, F. Combes, & K. C. Freeman, 182–185
- Häring, N., & Rix, H.-W. 2004, *ApJ*, 604, L89
- Harrison, C. M., Alexander, D. M., Mullaney, J. R., et al. 2012, in press (ArXiv:1209.3016)
- Hickox, R. C., Mullaney, J. R., Alexander, D. M., et al. 2014, *ApJ*, 782, 9
- Kocevski, D. D., Faber, S. M., Mozena, M., et al. 2012, *ApJ*, 744, 148
- Kriek, M., van Dokkum, P. G., Franx, M., Illingworth, G. D., & Magee, D. K. 2009, *ApJ*, 705, L71
- Kurczynski, P., Gawiser, E., Huynh, M., et al. 2012, *ApJ*, 750, 117
- Laird, E. S., Nandra, K., Pope, A., & Scott, D. 2010, *MNRAS*, 401, 2763
- Lamareille, F. 2010, *A&A*, 509, A53
- Lehmer, B. D., Alexander, D. M., Bauer, F. E., et al. 2010, *ApJ*, 724, 559
- Lobanov, A., & Zensus, J. A. 2007, *Active Galactic Nuclei at the Crossroads of Astrophysics*

- (Springer-Verlag), 147–162
- Man, A. W. S., Toft, S., Zirm, A. W., Wuyts, S., & van der Wel, A. 2012, ApJ, 744, 85
- Mancini, C., Renzini, A., Daddi, E., et al. 2015, ArXiv e-prints
- Matt, G., Marinucci, A., Guainazzi, M., et al. 2014, MNRAS, 439, 3016
- Mulchaey, J. S., & Jeltema, T. E. 2010, ApJ, 715, L1
- Nandra, K., & Pounds, K. A. 1994, MNRAS, 268, 405
- Nardini, E., Reeves, J. N., Gofford, J., et al. 2015, Science, 347, 860
- Nesvadba, N. P. H., Polletta, M., Lehnert, M. D., et al. 2011, MNRAS, 415, 2359
- Newman, A. B., Ellis, R. S., Bundy, K., & Treu, T. 2012, ApJ, 746, 162
- Novak, G. S., Ostriker, J. P., & Ciotti, L. 2011, ApJ, 737, 26
- . 2012, MNRAS, 427, 2734
- O’Sullivan, E., Ponman, T. J., & Collins, R. S. 2003, MNRAS, 340, 1375
- Papovich, C., Moustakas, L. A., Dickinson, M., et al. 2006, ApJ, 640, 92
- Peng, Y.-j., Lilly, S. J., Kovač, K., et al. 2010, ApJ, 721, 193
- Persic, M., Rephaeli, Y., Braito, V., et al. 2004, A&A, 419, 849
- Piconcelli, E., Jimenez-Bailón, E., Guainazzi, M., et al. 2005, A&A, 432, 15
- Ranalli, P., Comastri, A., & Setti, G. 2003, A&A, 399, 39
- Rangel, C., Nandra, K., Barro, G., et al. 2014, MNRAS, 440, 3630
- Rasmussen, J., Sommer-Larsen, J., Pedersen, K., et al. 2009, ApJ, 697, 79
- Reeves, J. N., & Turner, M. J. L. 2000, MNRAS, 316, 234
- Risaliti, G., & Elvis, M. 2004, in Astrophysics and Space Science Library, Vol. 308, Supermassive Black Holes in the Distant Universe, ed. A. J. Barger, 187
- Rubin, K. H. R., van Dokkum, P. G., Coppi, P., et al. 2004, ApJ, 613, L5
- Schawinski, K. 2011, in New Horizons in Astronomy, Proceedings of the Frank N. Bash Symposium 2011, held October 9–11, 2011. Austin, Texas, USA. Edited by S. Salviander, J. Green, and A. Pawlik. Published online at <http://pos.sissa.it/cgi-bin/reader/conf.cgi?confid=149>
- Schawinski, K., Virani, S., Simmons, B., et al. 2009, ApJ, 692, L19
- Stark, A. A., Gammie, C. F., Wilson, R. W., et al. 1992, ApJS, 79, 77
- Stern, D., Eisenhardt, P., Gorjian, V., et al. 2005, ApJ, 631, 163
- Storchi-Bergmann, T. 2014, ArXiv e-prints
- Szokoly, G. P., Bergeron, J., Hasinger, G., et al. 2004, ApJS, 155, 271
- Tajer, M., Polletta, M., Chiappetti, L., et al. 2007, A&A, 467, 73
- Tanaka, M., Finoguenov, A., Mirkazemi, M., et al. 2012, PASJ, in press (ArXiv:1210.0302)
- Taylor, E. N., Franx, M., van Dokkum, P. G., et al. 2009, ApJS, 183, 295
- Toft, S., Franx, M., van Dokkum, P., et al. 2009, ApJ, 705, 255
- Toft, S., Gallazzi, A., Zirm, A., et al. 2012, ApJ, 754, 3
- Toft, S., Rasmussen, J., Sommer-Larsen, J., & Pedersen, K. 2002, MNRAS, 335, 799
- Tombesi, F., Melendez, M., Veilleux, S., et al. 2015, ArXiv e-prints
- Treister, E., Schawinski, K., Urry, C. M., & Simmons, B. D. 2012, ApJ, 758, L39
- Treister, E., & Urry, C. M. 2012, Advances in Astronomy, Seeking for the Leading Actor on the Cosmic Stage: Galaxies versus Supermassive Black Holes, 35
- Treister, E., Cardamone, C. N., Schawinski, K., et al. 2009, ApJ, 706, 535
- Vanzella, E., Cristiani, S., Dickinson, M., et al. 2008, A&A, 478, 83
- Vasudevan, R. V., Mushotzky, R. F., Reynolds, C. S., et al. 2014, ApJ, 785, 30
- Vogelsberger, M., Genel, S., Sijacki, D., et al. 2013, MNRAS, 436, 3031
- Wang, J. X., Malhotra, S., Rhoads, J. E., & Norman, C. A. 2004, ApJ, 612, L109

- Williams, R. J., Quadri, R. F., Franx, M., van Dokkum, P., & Labb  , I. 2009, ApJ, 691, 1879
- Windhorst, R. A., Mather, J., Clampin, M., et al. 2009, in Astronomy, Vol. 2010, astro2010: The Astronomy and Astrophysics Decadal Survey, 317
- Wuyts, S., Labb  , I., Schreiber, N. M. F., et al. 2008, ApJ, 682, 985
- Wuyts, S., F  rster Schreiber, N. M., van der Wel, A., et al. 2011, ApJ, 742, 96
- Xue, Y. Q., Luo, B., Brandt, W. N., et al. 2011, ApJS, 195, 10
- Zheng, Z.-Y., Malhotra, S., Wang, J.-X., et al. 2012, ApJ, 746, 28

SUMMARY

Piecing together the puzzle of galaxy evolution precise knowledge about *the shape of the pieces to the puzzle*, i.e. the physical conditions of the galaxies, not just of the stellar component, but of the interstellar medium (ISM) and black hole as well. This thesis focuses on deriving the actual shape of those puzzle pieces, with particular focus on characterising the ISM as well as the gas accretion onto the central black hole, in order to better understand their effects on the SFR and general evolution of massive galaxies. With this aim in mind, the following three studies were carried out:

Amount and distribution of molecular gas in the ISM

A combination of density and temperature is the main agent shaping the CO spectral line energy distribution (SLED), and observations thereof can consequently be used to probe the conditions of the star-forming, molecular gas in the ISM. However, detailed modeling is needed in order to interpret observations. For that purpose, a new method is constructed and presented here; SImulator of GALaxy Millimeter/submillimeter Emission (SÍGAME). The method is combined with the radiative transfer code LIME in order to simulate CO line emission, and by applying SÍGAME to three galaxies from cosmological simulations, the following conclusions are drawn for simulated massive galaxies at $z \sim 2$:

- The CO SLED resembles the low-excitation one of the Milky Way (MW), in that it peaks at CO(3 – 2), but also with significant line intensity at higher transitions, not seen in the MW.
- Global α_{CO} factors range from 1.4 to $1.6 \text{ M}_{\odot} \text{ pc}^{-2} (\text{K km s}^{-1})^{-1}$ or about a third of the typically assumed MW values.
- Total CO(3 – 2) luminosities are within the range of observations of corresponding $z \sim 1 - 2.5$ star-forming galaxies.
- Radial profiles of line ratios within each galaxy reveal more excited gas towards the center, in agreement with observations of nearby galaxies, and suggesting ULIRG-like environments in the central ($R < 5 \text{ kpc}$) regions.
- The α_{CO} factor displays a decrease towards the center of each model galaxy, however, slightly lower than what is observed in local spiral galaxies.

Tracing SFR on local and global scales

SÍGAME is expanded and adapted in order to model [CII] – the fine-structure line of singly ionized carbon (C^+), thereby being the first code to simulate the [CII] emission reliably on kpc-scales in normal star-forming galaxies. [CII] is typically the strongest cooling line in neutral ISM, and correlates strongly with SFR on global and local scales, but its origin is so far unclear. These are the major findings from applying SÍGAME to seven $z = 2$ star-forming galaxies from another simulation:

- SÍGAME predicts a $L_{[CII]}$ -SFR relation of normal $z \sim 2$ galaxies which is steeper than that observed for corresponding galaxies at $z < 0.5$.
- The [CII] emission that originates in PDRs tends to dominate the total [CII] luminosity at low SFR, but at higher SFR, the molecular component takes over, while the HII regions contribute with negligible amounts.
- On resolved (1 kpc) scales, an expression is provided for the $\Sigma_{[CII]}-\Sigma_{\text{SFR}}$ relation.
- The low scatter around the modelled $L_{[CII]}$ -SFR relation in molecular gas owes to a tight correlation between molecular gas amount and SFR, whereas the larger scatter in PDRs and ionized gas is caused by a combination of SFR density and metallicity of the gas.
- No metallicity dependency is found in the scatter around the $L_{[CII]}$ -SFR relation, but $\text{SFR}/L_{[CII]}$ does increase towards the center of each galaxy together with metallicity, as also observed in local spiral galaxies.

Importance of AGNs in massive galaxies at $z \sim 2$

The deep *Chandra* X-ray survey CDF-S is analysed, and AGNs of high and low X-ray luminosity are extracted via AGN classification methods, and stacking techniques of non-detections, in X-ray. The galaxies investigated come from a mass-complete (at $M_* > 5 \times 10^{10} M_\odot$) sample at $1.5 \leq z \leq 2.5$ with stellar masses from fits of stellar population synthesis models to their spectral energy distribution. By statistical analysis, the following results are obtained:

- Among both star-forming and quiescent galaxies, a similar fraction of $22 \pm 5\%$ is found to have rest-frame X-ray luminosities ($L_{0.5-8\text{keV}} > 3 \times 10^{42} \text{ erg s}^{-1}$) consistent with hosting luminous AGNs.
- An excess in X-ray-inferred SFR compared to that from infrared and ultraviolet emission for the stacked non-detections, converts into even higher fractions of low- or high-luminosity AGNs among these. This fraction is higher (70 – 100 %) among quiescent galaxies than among star-forming ones (43 – 65 %).
- Hot gas halos are rejected as potential sources for the strong X-ray emission in the detected galaxies, based on the very limited spatial extent of their X-ray emission.
- The fraction of luminous AGNs does not depend on SFR nor stellar mass, suggesting that external effects are triggering the AGNs.

SAMMENFATNING

Det er et sandt puslespil at stykke galakse-udviklingen sammen ud fra observationer ved forskellige rødforskydninger. For at løse puslespillet er det først of fremmest afgørende at kende formen af brikkerne, dvs. den fysiske tilstand af galakserne – ikke bare af deres stellare del men også af deres interstellare medium (ISM) og centrale sorte hul. Med dette mål for øje, består denne afhandling af følgende tre projekter:

Mængde og fordeling af molekulær gas i ISM af galakser

Den spektrale linie energi fordeling (SLED; Spectral Line Energy Distribution) for CO molekylet er bestemt af hovedsagelig tæthed og temperatur af den gas hvor linien udsendes fra, og observationer af CO SLEDs kan derfor bruges til at bestemme tilstanden af den stjernedannende, molekulære gas i ISM af galakser. For at kunne oversætte observationer af SLED'en til sådanne gas tilstande, er detaljeret modellering nødvendig. Til det formål bliver en ny metode skabt og præsenteret her; SImulator of GALaxy Millimeter/submillimeter Emission (SÍGAME). Denne metode kombineres med en kode for strålingstransport af millimeter of infrarød stråling (LIME) for at kunne simulere CO linie emission, og ved at anvende SÍGAME på tre galakser fra kosmologiske simulationer, bliver de følgende konklusioner draget for massive galakser ved $z \sim 2$:

- CO SLED'en minder om den lavt eksiterede SLED i Mælkevejen, i og med at den har maksimum i CO(3 – 2), men de har også signifikant linie intensitet ved højere overgange, hvilket ikke ses i Mælkevejen.
- Globale α_{CO} faktorer ligger på omkring 50 % af Mælkevejens, nemlig fra $2.26 \text{ M}_{\odot} \text{ pc}^{-2} (\text{K km s}^{-1})^{-1}$.
- De totale CO(3 – 2) luminositeter er alle omkring $1 - 2\sigma$ under middel af observationer af sammenlignelige $z \sim 1 - 2.5$ stjernedannende galakser, højst sandsynlig pga. relativt lave molekulære gas masser i vores model galakser.
- Radielle profiler af CO linie forhold viser at hver model galakse indeholder mere eksiteret gas i de centrale dele sammenlignet med længere ude i disken. Dette er i overensstemmelse med observationer af lokale galakser og antyder at de centrale ($R < 5 \text{ kpc}$) områder minder om de forhold man finder i ULIRGs (Ultra-Luminøse Infrarøde Galakser).
- α_{CO} faktoren aftager mod centrum i galakserne som også observeret, dog med et mindre relativt fald ift. til det man typisk observerer i lokale spiral-galakser.

Afdækning af SFR på små og store skalaer

SÍGAME udvides og adapteres til at modellere [CII]- fin-struktur linien fra enkelt-ioniseret carbon (C^+), og er dermed den første kode til troværdigt at simulere [CII] emission på kpc-skala i normale stjernedannende galakser. [CII] er typisk den linie der kraftigst køler neutral ISM, og den skalerer med SFR på globale såvel som på lokale skalaer. Men dens fysiske oprindelse i gassen er stadig uklar. Disse er de første konklusioner, som SÍGAME indtil nu har ført til på det område:

- SÍGAME forudsiger at relationen mellem $L_{[CII]}$ og SFR for kan for normale galakser følger er mere stejl end den for tilsvarende galakser ved $z < 0.5$.
- [CII] emission udspringer hovedsageligt fra PDRs (Photon Dominated Regions) for lave SFR værdier, men molekulær gas overtager ved højere SFR. HII gas bidrager derimod med neglicibel [CII] intensitet.
- På opløste (1 kpc) skalaer, opstilles et udtryk for $\Sigma_{[CII]}$ som funktion af Σ_{SFR} .
- Den lave spredning i $L_{[CII]}$ -SFR relationen for molekulær gas skyldes en tæt sammenhæng mellem molekulær gas masse of total SFR. I PDRs og ioniseret gas skyldes den større spredning derimod en kombination af SFR tæthed of metallicitet i gassen.
- Der ses ikke nogen metallicitets-afhængighed for spredningen omkring $L_{[CII]}$ -SFR relationen, men $SFR/L_{[CII]}$ raten stiger imod centrum af galakserne sammen med metalliciteten, hvilket også er blevet observeret i lokale spiral-galakser.

En vigtig rolle af AGNs i massive galakser ved $s \sim 2$

Aktive galaksekerner (AGNs; Active Galactic Nuclei) af høj og lav X-ray luminositet afdækkes i feltet CDF-S, der er blevet studeret i røntgen med lang eksponering (4 Ms) af *Chandra* rum-observatoriet. Gruppen af galakser som undersøges dækker fuldstændigt stellar masser over $5 \times 10^{10} M_\odot$ ved $1.5 \leq z \leq 2.5$. Ved brug af AGN klassificerings-teknikker (og opsummerings-metoder for de galakser der ikke detekteres individuelt i røntgen), opnåes de følgende resultater:

- En brøkdel på $22 \pm 5\%$ blandt stjerne-dannende såvel som blandt passive galakser, har X-ray lystyrker svarende til lysstærke AGNs.
- En endnu større brøkdel blandt de ikke-detekterede galakser, viser tegn på at indeholde AGNs af lav til høj luminositet, med højere brøkdel (70 – 100 %) blandt passive galakser sammenlignet med de stjerne-dannende (43 – 65 %).
- Grundet den rumligt koncentrerede X-ray emission fra de undersøgte galakser, kan en ekstremt varm gas halo udelukkes som årsag til X-ray emissionen i de detekterede galakser.
- Brøkdelen af lysstærke AGNs afhænger ikke af SFR eller stellar masse, hvilket tyder på at eksterne faktorer spiller ind på antændelsen af deres AGNs.

ACKNOWLEDGMENTS

My passion for astronomy was sparked during long, cold nights in the observatory of my high school, AGS, in Sønderborg. I am thankful for having benefitted from an educational system that incorporates astronomy, and more particularly from the incredible enthusiasm of my first astronomy teacher, Mogens Winther, and those classmates that made it fun to stay up at night. Since then, so many inspirational people have opened up the sky for me, both in Aarhus, where I finished my bachelors in physics, and later on in Copenhagen. These past 4 years, that journey has been eased and guided by two amazing people, my supervisors Thomas and Sune. In your own very separate ways, you have taught me how to believe in myself as a researcher.

From the moment I hand in my thesis, I will miss life at Dark. Dark Cosmology Centre is nothing less of a paradise for any astronomer; daily provisions of coffee and fruit and a non-tiring staff of administration and support. Thank you for patiently answering all of my stupid questions and fixing my mistakes (even on weekends). And to the rest of my ‘darklings’; thank you for all those great moments; excursions, movie nights, alleviating lunch breaks, parties and laughters at the coffee machine.

I would not have gotten very far, in astronomy or anything else, without my friends. First thanks to my ‘old’ friends in Copenhagen that I occasionally forget how lucky I am to have; Tomatito, Lotte (x2), Helene. Thanks to my dear friends spread across the world – your warmth, generosity and wisdom still reaches and amazes me; Marty, Cat, Urs and papa-J, Sam, Chang, Rosa, Scott (the dad and the pilot), Fan-Fan, Hannah, Carol, Lila, Henry, Charlotte, Britta and Kaare to name a few, but certainly not all! I will also not forget to thank my flamenco girls; Rut, Rebecka, Elisabeth and all those crazy, lovely people I meet doing capoeira or aerial acrobatics, in Denmark and accross the world.

Towards the end of my PhD, I was blessed by meeting my own ‘curandero’. From the other side of the ocean, you support me in everything I do and make me laugh on my most solemn days. I will never know how many bruises and dangers you saved me from.

Finally, I can’t wait to thank my family (yes, that includes you guys, tía mía and Erk who I always wish to see more). You’ve there with love and encouragement (and sund fornuft), even when Als seems light years away. In particular, thank you mamita for taking those field trips to Copenhagen and reminding me of how to go shopping.

Tak, gracias, obrigada, thank you!

Karen

Appendices

A

APPENDIX TO CHAPTER 4

A.1 THERMAL BALANCE OF THE ATOMIC GAS PHASE

As explained in §4.3.2, we cool the initial hot SPH gas down by considering the following heating and cooling mechanisms and equating their energy rates: $\Gamma_{\text{CR,HI}} = \Lambda_{\text{ions+atoms}} + \Lambda_{\text{rec}} + \Lambda_{\text{f-f}}$.

$\Gamma_{\text{CR,HI}}$ is the heating rate of the atomic gas due to cosmic ray ionizations (Draine, 2011):

$$\begin{aligned} \Gamma_{\text{CR,HI}} &= 1.03 \times 10^{-27} n_{\text{HI}} \left(\frac{\zeta_{\text{CR,HI}}}{10^{-16}} \right) \\ &\quad \times \left[1 + 4.06 \left(\frac{x_e}{x_e + 0.07} \right)^{1/2} \right] \text{ erg cm}^{-3} \text{ s}^{-1}, \end{aligned} \quad (\text{A.1})$$

where $\zeta_{\text{CR,HI}}$ is the primary CR ionization rate of HI atoms (determined locally in our simulations according to eq. 4.12), and x_e is the hydrogen ionization fraction calculated with a procedure kindly provided by I. Pelupessy; see also Pelupessy (2005). The term containing x_e in eq. A.1 above accounts for the fact that in gas of high ionization, the electron created by the primary CR ionization has a high probability of transferring its kinetic energy into heat via long-range Coulomb scattering off free electrons. In the case of low ionization, this term becomes insignificant as a higher fraction of its energy will go to secondary ionizations or excitation of bound states in stead of heating.

$\Lambda_{\text{ions+atoms}}$ is the total cooling rate due line emission from H, He, C, N, O, Ne, Mg, Si, S, Ca, and Fe, calculated using the publically available code of Wiersma et al. (2009) which takes T_k , n_H and the abundances of the above elements as input. Wiersma et al. (2009) compute the cooling rates with the photoionization package `CLOUDY` under the assumption of CIE. They also adopt a value for the meta-galactic UV and X-ray field equal to that expected at $z \sim 2$ (Haardt & Madau, 2001). At $z \sim 2$, the emission rate of HI ionizing radiation is higher by a factor of about ~ 30 than at $z = 0$ (Puchwein et al., 2014), and thus plays an important role in metal line cooling calculations.

Λ_{rec} is the cooling rate due to hydrogen recombination emission (Draine, 2011):

$$\Lambda_{\text{rec}} = \alpha_B n_e n_{\text{H}^+} \langle E_{rr} \rangle \text{ ergs cm}^{-3} \text{ s}^{-1}, \quad (\text{A.2})$$

where α_B is the radiative recombination rate for hydrogen in the case of optically thick gas in

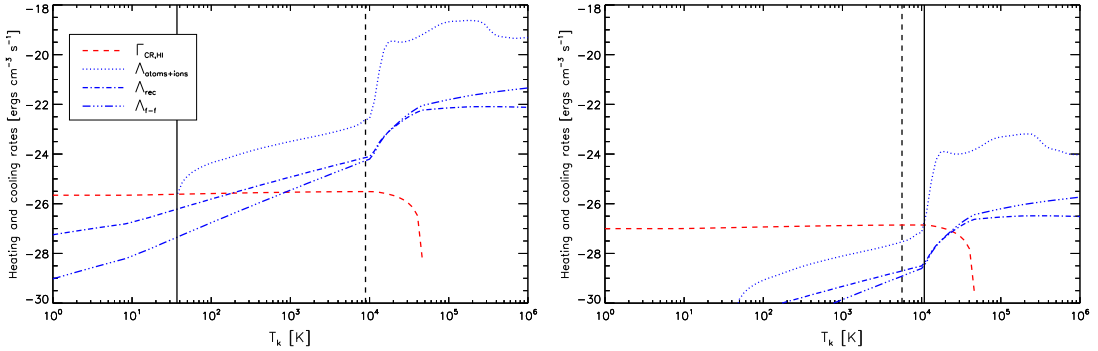


Figure A.1 Heating and cooling rates as functions of temperature for two SPH gas particles with $[n_{\text{H}} = 14.62 \text{ cm}^{-3}, \zeta_{\text{CR}} = 4.02 \times 10^{-16} \text{ s}^{-1}, x_e (T_{k,\text{SPH}} = 8892 \text{ K}) = 0.006]$ (left) and $[n_{\text{H}} = 0.09 \text{ cm}^{-3}, \zeta_{\text{CR}} = 3.92 \times 10^{-16} \text{ s}^{-1}, x_e (T_{k,\text{SPH}} = 5649 \text{ K}) = 0.001]$ (right). The left-hand side plot illustrates the case of an SPH particle of high gas density and metallicity leading to relatively high metal line cooling as compared to the heating from cosmic rays of moderate intensity. This results in a low temperature for the WCNM of $T_k = 37 \text{ K}$. The right-hand side plot shows a case of lower density and metallicity causing less cooling by metal lines, hence a higher equilibrium temperature for a similar cosmic ray field strength. Vertical black solid lines mark the resulting temperature of the neutral gas phase in each SPH particle, found where the difference between heating and cooling rate is smallest, when starting at the original SPH gas temperature, indicated with vertical black dashed lines.

which ionizing photons emitted during recombination are immediately reabsorbed. We adopt the approximation for α_B given by Draine (2011):

$$\alpha_B = 2.54 \times 10^{-13} T_4^{(-0.8163 - 0.0208 \ln T_4)} \text{ cm}^3 \text{ s}^{-1}, \quad (\text{A.3})$$

where T_4 is defined as $T_k/10^4 \text{ K}$. The density of ionised hydrogen, n_{H^+} , is set equal to the electron density, n_e , from eq. A.1 and E_{rr} is the corresponding mean kinetic energy of the recombining electrons:

$$\langle E_{rr} \rangle = [0.684 - 0.0416 \ln T_4] k_B T_k \text{ ergs}. \quad (\text{A.4})$$

Λ_{f-f} is the cooling rate due to free-free emission from electrons in a pure H plasma (i.e., free electrons scattering off H^+), and is given by (Draine, 2011):

$$\Lambda_{f-f} = 0.54 T_4^{0.37} k_B T_k n_e n_{\text{H}^+} \alpha_B \text{ ergs cm}^{-3} \text{ s}^{-1}, \quad (\text{A.5})$$

where the recombination rate, α_B , is calculated in the same way as for Λ_{rec} .

Figure A.1 shows the above heating and cooling rates pertaining to two example SPH particles with similar initial temperatures ($\sim 10^4 \text{ K}$). Because of different ambient conditions (i.e., n_{H_1} , x_e , Z' , and ζ_{CR}) the equilibrium temperature solutions for the two gas particles end up being significantly different.

A.2 THERMAL BALANCE OF THE MOLECULAR GAS PHASE

As described in Section 4.3.4 SÍGAME assumes the molecular gas resides exclusively in giant molecular clouds that have Plummer radial density profiles (i.e., given by eq. 4.11). Throughout the clouds the gas temperature is solved for according to the heating and cooling equilibrium requirement $\Gamma_{\text{PE}} + \Gamma_{\text{CR},\text{H}_2} = \Lambda_{\text{H}_2} + \Lambda_{\text{CO}} + \Lambda_{\text{CII}} + \Lambda_{\text{OI}} + \Lambda_{\text{gas-dust}}$ (eq. 4.14).

Γ_{PE} is the heating rate of the gas due to photo-electric ejection of electrons from dust grains by FUV photons, and is given by (Bakes & Tielens, 1994):

$$\Gamma_{\text{PE}} = 10^{-24} \cdot \text{pdfilon} G_{0,\text{att}} n_{\text{H}} \text{ ergs cm}^{-3} \text{ s}^{-1}, \quad (\text{A.6})$$

where $G_{0,\text{att}}$ is the local attenuated FUV field in Habing units, derived following eq. 4.13, and pdfilon is the heating efficiency:

$$\begin{aligned} \text{pdfilon} = & \frac{4.87 \times 10^{-2}}{1 + 4 \times 10^{-3} (G_{0,\text{att}} T^{0.5} / n_e)^{0.73}} \\ & + \frac{3.65 \times 10^{-2}}{1 + 4 \times 10^{-3} (G_{0,\text{att}} T^{0.5} / n_e)^{0.73}}, \end{aligned} \quad (\text{A.7})$$

where n_e is the electron density, calculated as $x_e n_{\text{H}}$, with x_e again calculated using the procedure of I. Pelupessy.

$\Gamma_{\text{CR,H}_2}$ is the heating rate by cosmic rays traveling through molecular gas (Stahler & Palla, 2005):

$$\Gamma_{\text{CR,H}_2} = 1.068 \times 10^{-24} \left(\frac{\zeta_{\text{CR,H}_2}}{10^{-16}} \right) \left(\frac{n_{\text{H}_2}}{10^3 \text{ cm}^{-3}} \right) \text{ ergs cm}^{-3} \text{ s}^{-1} \quad (\text{A.8})$$

where $\zeta_{\text{CR,H}_2}$ is the local CR primary ionization rate of H_2 molecules, which is approximately $1.6 \times$ higher than that of HI atoms (Stahler & Palla, 2005).

Λ_{H_2} is the H_2 line cooling rate, and we use the parameterization made by Papadopoulos et al. (2014) that includes the two lowest H_2 rotational lines (S(0) and S(1), the only lines excited for $T_k \lesssim 1000 \text{ K}$):

$$\begin{aligned} \Lambda_{\text{H}_2} = & 2.06 \times 10^{-24} \frac{n_{\text{H}_2}}{1 + r_{\text{op}}} \left[1 + \frac{1}{5} e^{510 \text{ K} / T_k} \left(1 + \frac{n_0}{n_{\text{H}_2}} \right) \right]^{-1} \\ & \times (1 + R_{10}) \text{ ergs cm}^{-3} \text{ s}^{-1}, \end{aligned} \quad (\text{A.9})$$

where R_{10} is defined as:

$$R_{10} = 26.8 r_{\text{op}} \left[\frac{1 + (1/5) e^{510 \text{ K} / T_k} \left(1 + \frac{n_0}{n_{\text{H}_2}} \right)}{1 + (3/7) e^{845 \text{ K} / T_k} \left(1 + \frac{n_1}{n_{\text{H}_2}} \right)} \right], \quad (\text{A.10})$$

and $n_0 \sim 54 \text{ cm}^{-3}$ and $n_1 \sim 10^3 \text{ cm}^{-3}$ are the critical densities of the S(0):2-0 and S(1):3-1 rotational lines. r_{op} is the ortho- H_2 /para- H_2 ratio (set to 3 which is the equilibrium value).

For the cooling rates due to the [C II]158 μm and [O I]63 μm +146 μm fine-structure lines we adopt the parameterizations by Röllig et al. (2006). The C II cooling rate (Λ_{CII}) is:

$$\begin{aligned} \Lambda_{\text{CII}} = & 2.02 \times 10^{-24} n Z' \\ & \times \left[1 + \frac{1}{2} e^{92 \text{ K} / T_k} (1 + 1300 / n_{\text{H}}) \right]^{-1} \text{ ergs cm}^{-3} \text{ s}^{-1}, \end{aligned} \quad (\text{A.11})$$

where a carbon to hydrogen abundance ratio that scales with metallicity according to $\chi_{[\text{C}]} = 1.4 \times 10^{-4} Z'$ is assumed. For the parameterization of the O I cooling rate ($\Lambda_{\text{OI}} = \Lambda_{63 \mu\text{m}} + \Lambda_{146 \mu\text{m}}$) we refer to eqs. A.5 and A.6 in Röllig et al. (2006) and simply note that we adopt (in accordance

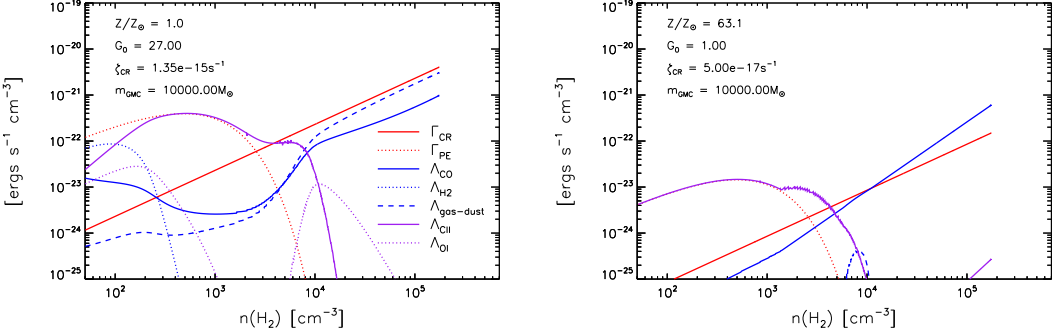


Figure A.2 Equilibrium heating (red curves) and cooling (blue+purple curves) rates as functions of H_2 density for two different GMC models with [$m_{\text{GMC}} = 10^4 \text{ M}_{\odot}$, $Z' = 1$, $G_0 = 27$, $P_{\text{ext}} = 10^4 \text{ K cm}^{-3}$] (left) and [$m_{\text{GMC}} = 10^4 \text{ M}_{\odot}$, $Z' = 63$, $G_0 = 1$, $P_{\text{ext}} = 10^4 \text{ K cm}^{-3}$] (right). In the case of high FUV and cosmic ray fields (left), heating and cooling in the outer region ($n_{\text{H}_2} \lesssim 1500 \text{ cm}^{-3}$) are dominated by photoelectric heating (red dotted) and [[CII]] line cooling (purple solid), while in the inner region ($n_{\text{H}_2} \gtrsim 10000 \text{ cm}^{-3}$), cosmic ray heating (red solid) and gas-dust interactions (blue dashed) are the important mechanisms in determining the temperature. In the case of high metallicity (right), photoelectric heating and [[CII]] line cooling are also dominating in the outer region, but cooling in the inner region is mainly controlled by CO line emission.

with Röllig et al. (2006)) an oxygen to hydrogen abundance ratio of $\chi_{[\text{O}]} = 3 \times 10^{-4} Z'$.

Λ_{CO} is the cooling rate due to CO rotational transitions. We use the parameterization provided by Papadopoulos & Thi (2013):

$$\Lambda_{\text{CO}} = 4.4 \times 10^{-24} \left(\frac{n_{\text{H}_2}}{10^4} \right)^{3/2} \left(\frac{T_{\text{k}}}{10 \text{ K}} \right)^2 \left(\frac{\chi_{\text{CO}}}{\chi_{[\text{C}]}} \right) \text{ ergs cm}^{-3} \text{ s}^{-1}, \quad (\text{A.12})$$

where $\chi_{\text{CO}}/\chi_{[\text{C}]}$ is the relative CO to neutral carbon abundance ratio, the value of which we determine by interpolation, assuming that $\chi_{\text{CO}}/\chi_{[\text{C}]} = (0.97, 0.98, 0.99, 1.0)$ for $n_{\text{H}_2} = 5 \times 10^3, 10^4, 10^5, 10^6 \text{ cm}^{-3}$, respectively (Papadopoulos & Thi, 2013).

$\Lambda_{\text{gas-dust}}$ is the cooling rate due to gas-dust interactions and is given by (Papadopoulos et al., 2011):

$$\Lambda_{\text{gas-dust}} = 3.47 \times 10^{-33} n_{\text{H}}^2 \sqrt{T_{\text{k}}} (T_{\text{k}} - T_{\text{dust}}) \text{ ergs cm}^{-3} \text{ s}^{-1}, \quad (\text{A.13})$$

where the dust temperature (T_{dust}) is calculated using eq. 4.15 (Section 4.3.4).

A.3 GMC MODELS

Each SPH particle is divided into several GMCs as described in §4.3.4, and we derive the molecular gas density and temperature within each from three basic parameters which are SFR density, GMC mass, m_{GMC} , and metallicity, Z'/Z_{\odot} . Derived from these basic parameters are the far-UV and cosmic ray field strengths, the H_2 gas mass fraction of each SPH particles, as well as the GMC properties used to derive the CO excitation and emission; H_2 density and temperature. Histograms of the basic parameters are shown in Figure A.3, while properties derived thereof can be found in Figure A.4.

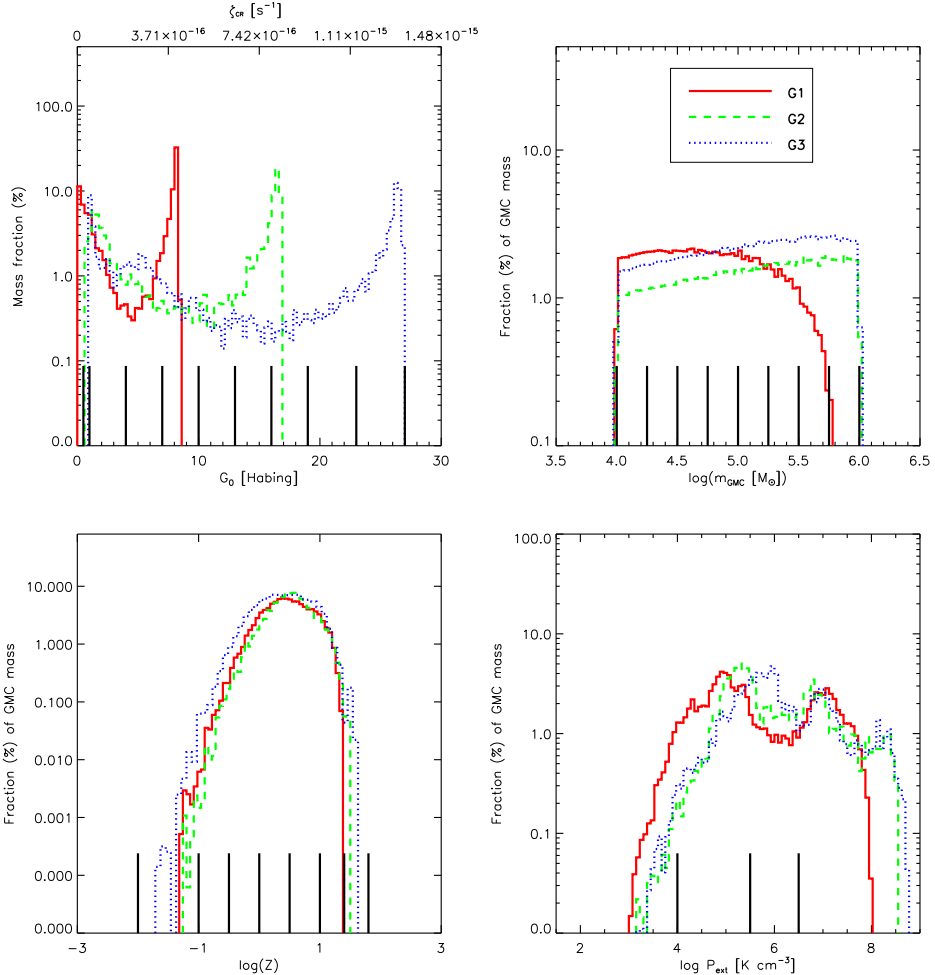


Figure A.3 Mass-weighted histograms of the basic parameters of the GMCs in G1 (red solid), G2 (green dashed), and G3 (blue dotted). From top left and clockwise: the local far-UV field (G_0) (and CR ionization rate since $\zeta_{\text{CR}} \propto G_0$), GMC mass (m_{GMC}), metallicity (Z') and external pressure (P_{ext}). Black vertical lines indicate the G_0 , m_{GMC} , Z' , P_{ext} -values for which $T_k - n_{\text{H}_2}$ curves were calculated (see Figure A.4) – a total of 630 GMCs which make up our grid GMC models. Each GMC in the galaxies is assigned the $T_k - n_{\text{H}_2}$ curve of the GMC model at the closest grid point.

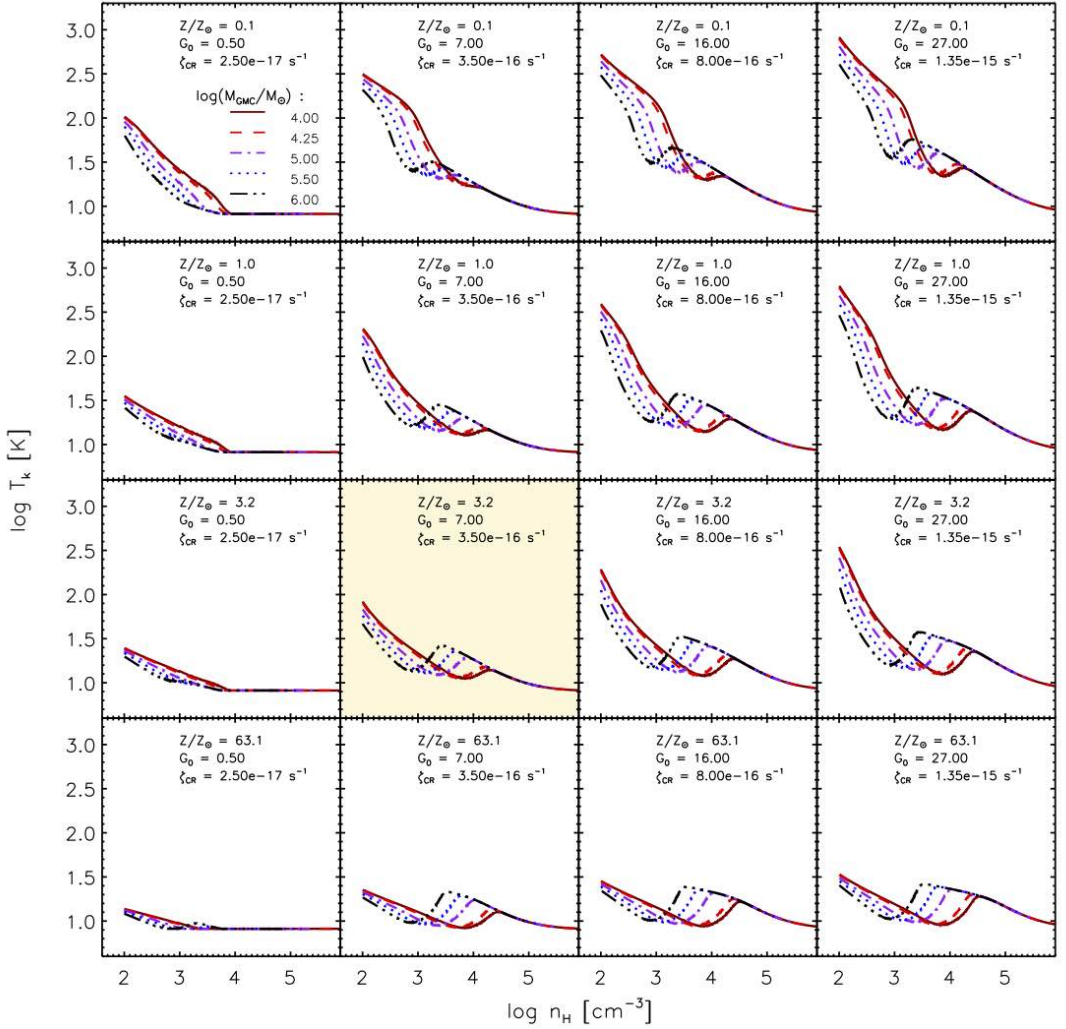


Figure A.4 Kinetic temperature versus H_2 density curves for 80 out of the 630 grid model GMCs that span the full (G_0, M_{GMC}, Z') parameter space set by and marked on top of the distributions in Figure A.3 (see also Section 4.3.4) for a pressure of $P_{\text{ext}} = 10^4 \text{ K cm}^{-3}$. The grid model most often assigned to GMCs in G1 is indicated by the red dashed curve in the highlighted panel and corresponds to $G_0 = 7.0$ ($\zeta_{\text{CR}} = 3.5 \times 10^{-16} \text{ s}^{-1}$), $\log m_{\text{GMC}}/\text{M}_\odot = 4.25$, and $Z' = 3.2$. In general, higher metallicity (from top to bottom) leads to more cooling via emission lines of ions, atoms and molecules, and hence lower temperatures. On the other hand, higher UV and CR fields (from left to right) cause more heating and therefore higher T_k . The decreasing trend of T_k with higher values of n_{H_2} is mainly caused by the gradual attenuation of the UV field as one moves into the cloud. The ‘bump’ at $n_{\text{H}_2} \sim 10^3 - 10^4 \text{ cm}^{-3}$ corresponds to the transition from CII line cooling to the less efficient CO line cooling at higher densities. At densities above $n_{\text{H}_2} = 10^4 \text{ cm}^{-3}$, gas-dust interactions set in and eventually cools the gas down to the CMB temperature in all GMC cores. In areas with very high SFRD this will not happen in reality, but our moderately star-forming galaxies rarely reach such high SFRD values.

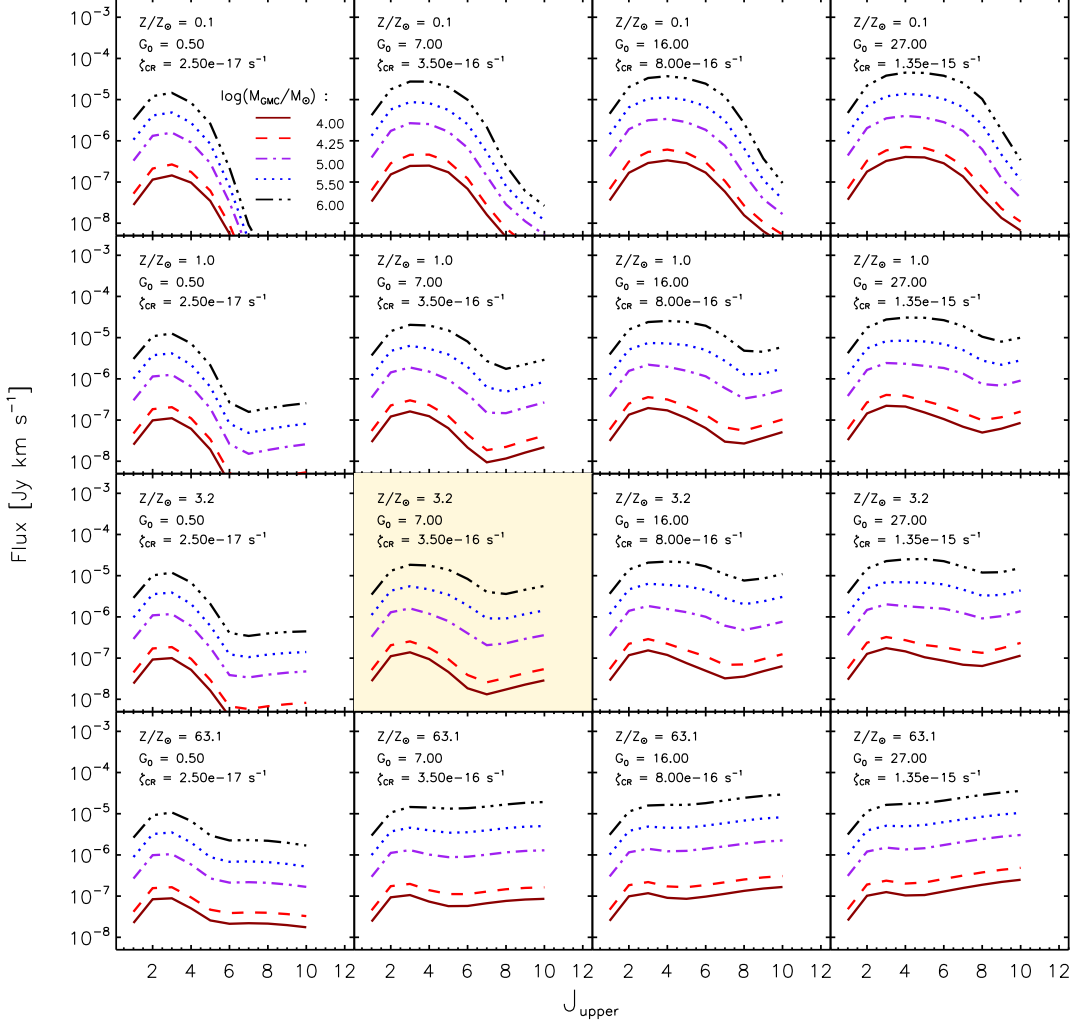


Figure A.5 CO SLEDs obtained with `LIME` for the 80 model GMCs whose $T_k - n_{H_2}$ curves are shown in Figure A.4. The CO SLED used most often in G1 is shown as the red dashed curve in the highlighted panel. These CO SLEDs were made for a fixed external pressure of $P_{\text{ext}}/k_B = 10^4 \text{ cm}^{-3} \text{ K}$ and a default Plummer density profile.

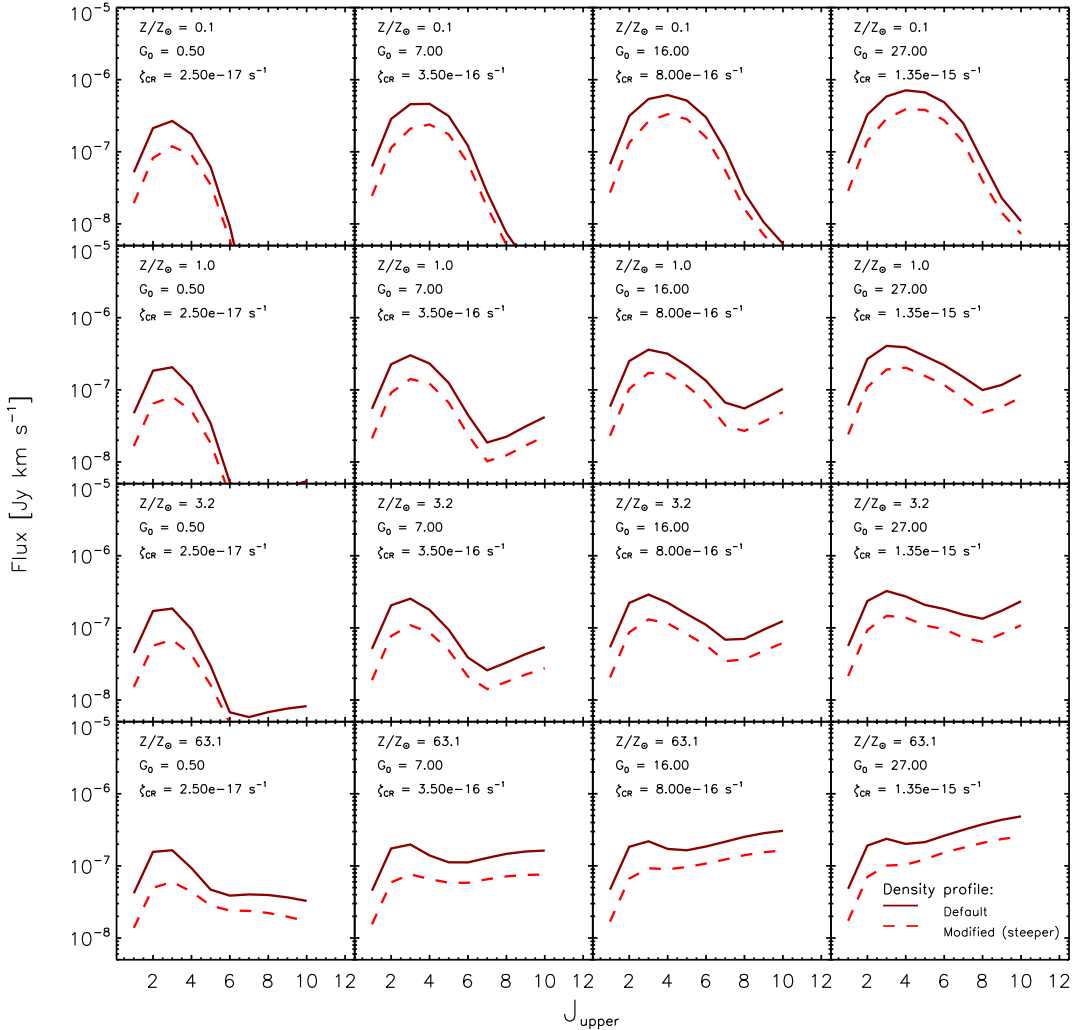


Figure A.6 CO SLEDs obtained with LIME for the same $[G_0, Z']$ values as shown in the panels of Figure A.5 for Plummer density profiles with power-law index $-5/2$ (solid curve) and $-7/2$ (dashed curve). In all panels, the external pressure has been fixed to $P_{\text{ext}}/k_B = 10^4 \text{ cm}^{-3} \text{ K}$ and the GMC mass to $m_{\text{GMC}} = 10^{4.25} M_\odot$.

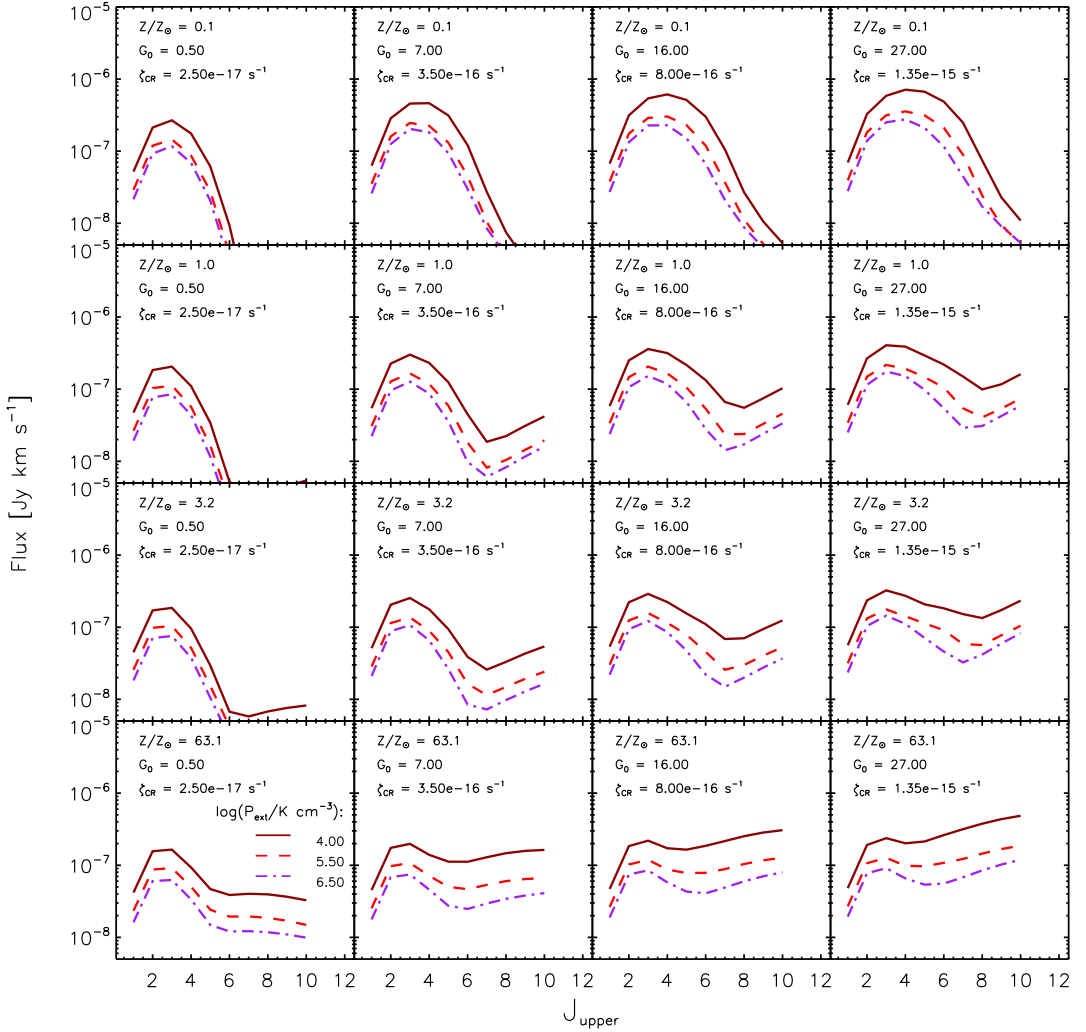


Figure A.7 CO SLEDs obtained with LIME for the same $[G_0, Z']$ values as shown in the panels of Figure A.5 for $P_{\text{ext}}/k_{\text{B}} = 10^4 \text{ cm}^{-3} \text{ K}$ (solid curves), $10^{5.5} \text{ cm}^{-3} \text{ K}$ (dashed curves), and $10^{6.5} \text{ cm}^{-3} \text{ K}$ (dot-dashed curves). In all panels, the GMC mass is fixed to $10^{4.25} M_{\odot}$. Higher pressure environments are seen to lead to a decrease in luminosity for all transitions.

B

APPENDIX TO CHAPTER 6

B.1 DENSITY OF SINGLY IONIZED CARBON

The strength of the [CII] emission from any gas phase depends on the fraction of total carbon atoms that are singly ionized, f_{CII} . For calculating f_{CII} , we chose to employ the microphysics code CLOUDY v13.03, that simultaneously solves the equations for statistical and thermal equilibrium for a wide range of optional elements. We set up CLOUDY to work on a small parcel of gas with a single temperature and a constant density across its volume. The incident radiation field on the gas parcel is set to the local interstellar radiation field, as provided by CLOUDY, but scaled by a factor (in practice, our G_0). In addition, a cosmic ray ionization rate can be specified in units of s^{-1} .

As a test to judge whether we are using CLOUDY correctly, the fraction of CIV, f_{CIV} , as a function of density and temperature was compared to the work of Oppenheimer & Schaye (2013) by reproducing their CIV fractions at $z = 1$ for a Haardt & Madau (2001) background radiation field. This comparison is shown in Fig. B.1 with plots of the CIV abundance (rela-

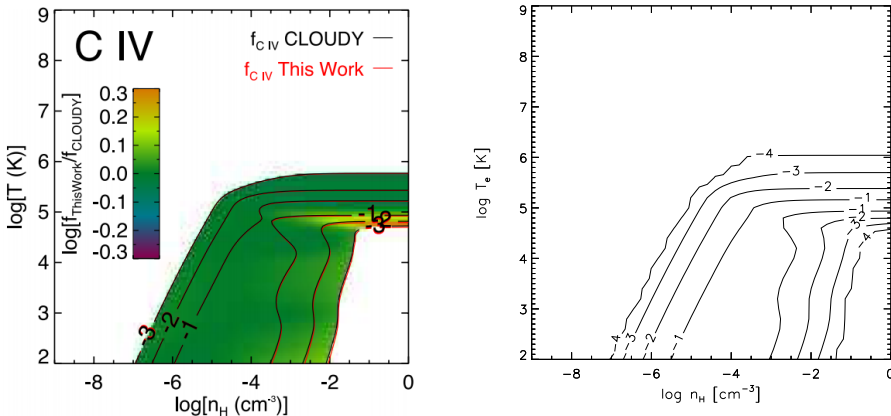


Figure B.1 A comparison of f_{CIV} as calculated by Oppenheimer & Schaye (2013) using CLOUDY v10.00 (left) and by SIGAME using CLOUDY v13.03 (right). In both cases a Haardt & Madau 2005 background radiation field (embedded in CLOUDY) at $z = 1$ was used together with solar abundances. A good agreement is seen, in particular with decreasing f_{CIV} towards high densities and low temperatures, where carbon exists in lower ionizational states such as CII, see Fig. B.2 below.

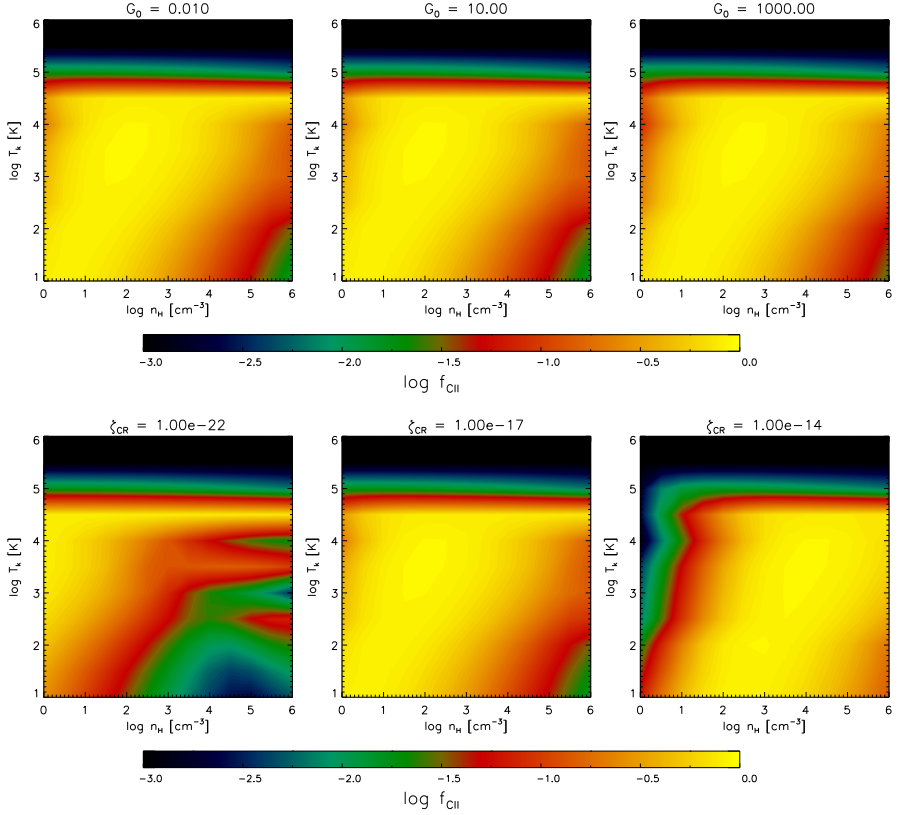


Figure B.2 Maps of f_{CII} as function of gas temperature and hydrogen density made with `CLOUDY v13.03` as part of the grid used in `SÍGAME` to derive x_e and f_{CII} in the ISM. *Top row:* For three values of G_0 (and ζ_{CR} fixed at 10^{-17} s^{-1}). *Bottom row:* For three values of ζ_{CR} (with G_0 fixed to 1 Habing). Note how f_{CII} drops at $T_k \gtrsim 10^5 \text{ K}$ in all cases, and depends on ζ_{CR} while being largely insensitive to changes in G_0 .

tive to the total number of carbon atoms) as a function of hydrogen density and kinetic gas temperature. A good agreement with the figure of Oppenheimer & Schaye (2013) is achieved when using the build-in Haardt & Madau 2005 background of `CLOUDY` ('HM05' command in `CLOUDY`, including galaxies and quasars but not the CMB) at $z = 1$ together with default solar abundances.

In order to keep the computing time of `SÍGAME` low, we set up a grid in $[n_{\text{H}}, T_{\text{k}}, \zeta_{\text{CR}}, G_0]$ and calculated f_{CII} with `CLOUDY` for each grid point. Though metallicity and element abundances (of C, O, Si and Fe) are followed in our simulated galaxies, we chose the default solar composition that comes with `CLOUDY` for the sake of having fewer parameters in the grid. Visualizations of this grid are shown in Fig. B.2 for three values of G_0 (and ζ_{CR} fixed at 10^{-17} s^{-1} , close to the adopted $\zeta_{\text{CR,MW}} = 10^{-17} \text{ s}^{-1}$) in the top row and three values of ζ_{CR} (with G_0 fixed to 1 Habing, close to $G_{0,\text{MW}} = 0.6$ Habing) in the bottom row. As can be seen, f_{CII} does not seem to depend at all on G_0 , but much more on the intensity of cosmic rays.

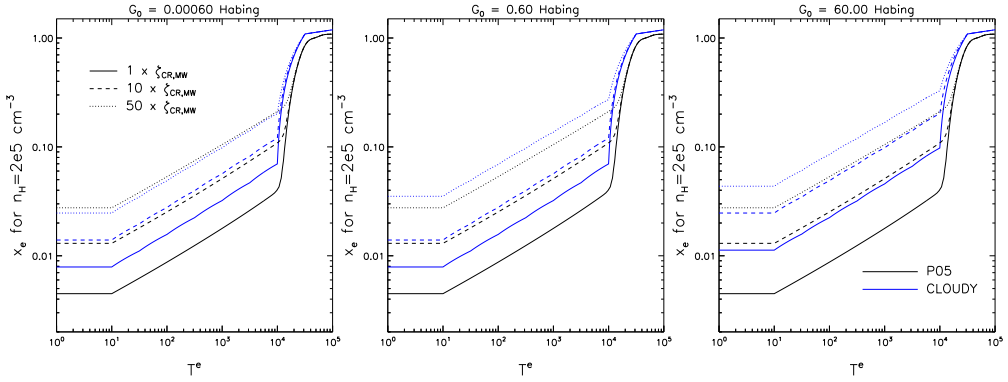


Figure B.3 A comparison of `CLOUDY` and the method described in Pelupessy (2005) for deriving x_e as a function of electron temperature, T^e , at a density of $n_H = 2 \times 10^5 \text{ cm}^{-3}$. The two methods agree about the shape of increasing x_e with T^e , including the sharp rise at $T_k \sim 10^4 \text{ K}$ due to Balmer lines. The P05 method does not include ionization by the FUV radiation field, meaning that it takes the same shape in each panel. Note that x_e rises above 1 due to the inclusion of other elements than hydrogen, that can contribute to the electron number.

B.2 ELECTRON FRACTION

In order to be consistent with the calculation of f_{CII} , we also decided to calculate the electron fraction, x_e , with `CLOUDY` v13.03 rather than the method of Pelupessy (2005) (P05) used in the previous project (Chapter 4). Fig. B.3 shows how `CLOUDY` and the P05 method compare as a function of electron temperature at a density of $n_H = 2 \times 10^5 \text{ cm}^{-3}$, for different combinations of interstellar radiation field (G_0) and cosmic ray ionization rate (ζ_{CR}). The P05 method is aimed for application in the interior of GMCs and therefore only considers ionization by cosmic rays that are expected to dominate the ionization of hydrogen, whereas `CLOUDY` takes G_0 and ζ_{CR} as separate variables.

Furthermore, P05 method does not depend on density, whereas the calculation with `CLOUDY` does. Fig. B.4 gives the same comparison as the previous figure, but for a lower density of $n_H = 100 \text{ cm}^{-3}$, where `CLOUDY` derives much larger electron fractions than the P05 model. This is expected, since at low densities, the gas is less shielded from the incident radiation field. We therefore consider the inclusion of the `CLOUDY`, with its sensitivity towards G_0 and n_H , an improvement of SÍGAME with respect to the electron fraction.

B.3 HEATING AND COOLING RATES OF MOLECULAR AND ATOMIC GAS INSIDE GMCs

Table B.1 provides a summary of the various heating and cooling mechanisms adopted in the molecular and atomic gas regions of our GMC models, along with the physical quantities on which they depend. The most important references are also given, and see also Appendix A.1 and A.2 for a more detailed description.

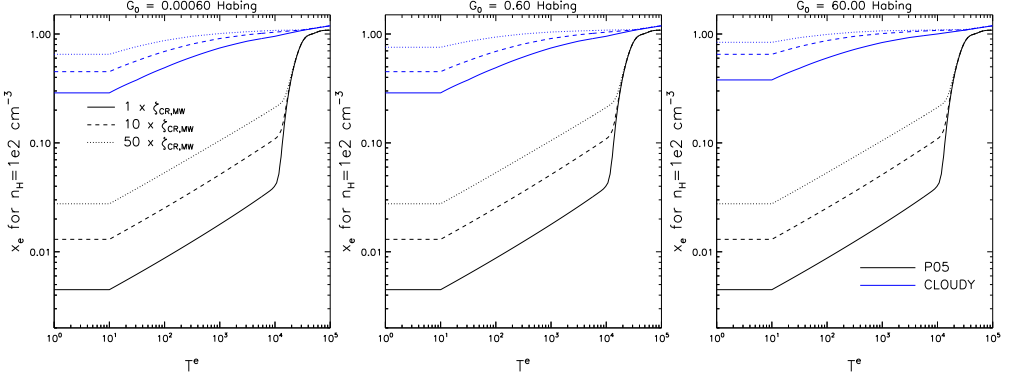


Figure B.4 Same as Fig. B.3, but for a density of $n_{\text{H}} = 100 \text{ cm}^{-3}$.

Cooling and heating rates in GMC models

Process		Parameters	Reference
Γ_{PE}	Photo-electric heating	$G_0, T_{\text{k}}, n_{\text{e}}, n_{\text{H}}$	Bakes & Tie-lens (1994)
$\Gamma_{\text{CR,HI}}$	Cosmic ray heating in atomic gas	$\zeta_{\text{CR}}, n_{\text{HI}}, x_{\text{e}}$	Draine (2011)
$\Gamma_{\text{CR,H}_2}$	Cosmic ray heating in molecular gas	$\zeta_{\text{CR}}, n_{\text{H}_2}$	Stahler & Palla (2005)
Λ_{H_2}	H ₂ line cooling	$n_{\text{H}_2}, T_{\text{k}}$	Papadopoulos et al. (2014)
Λ_{OI}	OI line cooling	$n_{\text{H}}, T_{\text{k}}$	Röllig et al. (2006)
Λ_{CII}	[CII] line cooling in ionized gas	$G_0, T_{\text{k}}, n_{\text{H}}, X_{\text{C}}, \sigma_v$	Goldsmith et al. (2012)

Table B.1

B.4 THE [CII] COOLING RATE IN GAS OF DIFFERENT CONDITIONS

For a two-level system such as [CII] embedded in a radiation field with energy density U at the transition frequency, the general rate equation governing the population levels can be written as:

$$\frac{n_u}{n_l} = \frac{B_{lu}U + C_{lu}}{A_{ul} + B_{ul}U + C_{ul}} = \frac{gB_{ul}U + gKC_{ul}}{A_{ul} + B_{ul}U + C_{ul}}, \quad (\text{B.1})$$

where A_{ul} ($= 2.3 \times 10^{-6} \text{ s}^{-1}$) is the spontaneous emission rate, and B_{ul} and B_{lu} are the stimulated emission and absorption rate coefficients, respectively (Goldsmith et al., 2012). Here we have invoked detailed balance, i.e. $B_{lu}U = gB_{ul}U$ and $C_{lu} = gKC_{ul}$, where g ($= g_u/g_l$) is the ratio of the statistical weights and $K = e^{-h\nu/k_{\text{B}}T_{\text{k}}} = e^{-91.25 \text{ K}/T_{\text{k}}}$. We can then write the fraction

of C⁺ in the upper level, f_u , as:

$$\begin{aligned} f_u &= \frac{n_u}{n_l + n_u} = \frac{1}{\frac{n_l}{n_u} + 1} \\ &= \frac{gB_{ul}U + gKC_{ul}}{A_{ul} + (1+g)B_{ul}U + C_{ul} + gKC_{ul}} \\ &= \frac{gK + gB_{ul}U/C_{ul}}{1 + gK + A_{ul}/C_{ul} + (1+g)B_{ul}U/C_{ul}}. \end{aligned} \quad (\text{B.2})$$

In general, $U = (1-\beta)U(T_{\text{ex}}) + \beta U(T_{\text{bg}})$, where $U(T_{\text{bg}})$ is the energy density from a background field (e.g. CMB or radiation from dust), and β is the escape probability fraction at the [CII] frequency (see also Goldsmith et al., 2012). We shall ignore any background, however, in which case we can write the stimulated downward rate as:

$$B_{ul}U = \frac{(1-\beta)A_{ul}}{e^{-91.25 \text{ K}/T_{\text{ex}}} - 1}, \quad (\text{B.3})$$

and the excitation temperature as:

$$e^{-91.25 \text{ K}/T^{\text{ex}}} = K \left(1 + \frac{\beta A_{ul}}{C_{ul}} \right), \quad (\text{B.4})$$

see Goldsmith et al. (2012). For the escape probability we assume a spherical geometry with a radial velocity gradient proportional to radius, such that $\beta = (1 - \exp(-\tau))/\tau$. In calculating the integral in eq. 6.18 we split the integral up into 100 radial bins of thickness ΔR (see Section 6.5), and we approximate the optical depth in each such bin with that of a homogeneous static slab of gas of thickness ΔR (Draine, 2011):

$$\tau = \frac{g_u}{g_l} \frac{A_{ul}c^3}{4(2\pi)^{3/2}\nu^3\sigma_v} n_l \Delta R \left(1 - \frac{n_u g_l}{n_l g_u} \right), \quad (\text{B.5})$$

where σ_v is the gas velocity dispersion, which is calculated according to eq. 6.5 for the PDR and molecular gas regions in the GMCs, and is set to the local velocity dispersion in the SPH simulation in the case of the ionized clouds. We use eqs. B.2, B.3, B.4, and B.5 to iteratively solve for consistent values of f_u and β in each ΔR bin. This is done by first assuming optically thin emission ($\beta = 1$) in order to get an initial estimate of f_u (eq. B.2), which is subsequently used to calculate τ and β (eq. B.5) and from that T_{ex} and $B_{ul}U$ (eqs. B.4 and B.3), etc. Once consistent values for f_u and τ have been reached, we calculate the total cooling rate according to eq. 6.19. This cooling rate is used to determine the thermal balance at various points within the GMCs as well as the [CII] emission from the ionized clouds as described in Section 6.5. We emphasize that our methods assumes that the [CII] emission from the different ΔR bins within a cloud is radiatively de-coupled, and that the total [CII] emission from a cloud is therefore the sum of the emission from each bin.

As explained in Section 6.5 [CII] is collisionally (de)excited by H₂ in the molecular phase, by e⁻ and HI in the PDR region, and by e⁻ in the ionized gas. For a single collision partner the collision rates are equal to the density (n) of the collision partner times the rate coefficients, i.e. $C_{ul} = nR_{ul}$ and $C_{lu} = nR_{lu}$. In case of two collision partners we have $C_{ul} = n_1 R_{ul,1} + n_2 R_{ul,2}$ and $C_{lu} = n_1 R_{lu,1} + n_2 R_{lu,2}$. Fig. B.5 shows the [CII] dexcitation rate coefficients that we

have adopted in our work for collisions with e^- H I, and H₂ as a function of temperature. For collisions with electrons, we adopt the following expression for the deexcitation rate coefficient as a function of electron temperature (T_e):

$$R_{ul}(e^-) = 8.7 \times 10^{-8} (T_e/2000\text{ K})^{-0.37} \text{ cm}^3 \text{ s}^{-1}, \quad (\text{B.6})$$

which is applicable for temperatures from $\simeq 100\text{ K}$ to $20,000\text{ K}$ (Goldsmith et al., 2012). At temperatures $> 20,000\text{ K}$ we set $R_{ul}(e^-) \sim T_e^{-0.85}$ (Wilson & Bell, 2002; Langer & Pineda, 2015). For the PDR gas, the electron density is calculated using CLOUDY and the electron temperature is set to the kinetic temperature of the gas (calculated according to eq. 6.16). For the ionized gas we assume $n_e = n_{\text{HII}}$, i.e., $x_e = 1$, and the electron temperature gas is set to the SPH gas kinetic temperature (see Section 6.4.2). For the deexcitation rate coefficient for collisions with H I we use the analytical expression provided by Barinovs et al. (2005) and shown as the dotted curve in Fig. B.5:

$$R_{ul}(\text{H I}) = 7.938 \times 10^{11} \exp(-91.2/T_k) \left(16 + 0.344\sqrt{T_k} - 47.7/T_k \right) \text{ cm}^3 \text{ s}^{-1}. \quad (\text{B.7})$$

While Barinovs et al. (2005) cites an application range for the above expression of $15\text{ K} < T_k < 2000\text{ K}$, a comparison with $R_{ul}(\text{H I})$ -values found by Keenan et al. (1986) over the temperature range $10\text{ K} < T_k < 100,000\text{ K}$ shows that eq. B.7 provides an excellent match over this larger temperature range (Fig. B.5). For collisions with H₂ we follow Goldsmith et al. (2012) and assume that the collision rate coefficients are approximately half those for collisions with H over the relevant temperature range for the molecular gas, i.e. $R_{ul}(\text{H}_2) = 0.5 \times R_{ul}(\text{H})$.

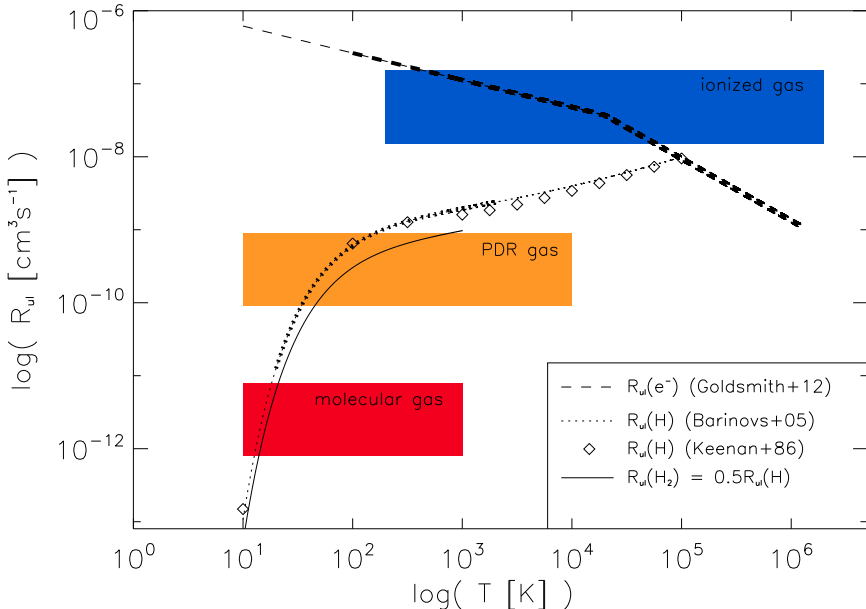


Figure B.5 [CII] deexcitation coefficients (R_{ul}) as a function of temperature for collisions with e^- (dashed line), H I (dotted line), and H₂ (solid line and diamonds). The curves are thicker over the temperature ranges where they are formally applicable. The blue, orange, and red rectangles indicate the temperature range encountered in the ionized, atomic, and molecular phase in our simulated galaxies, respectively (see sections 6.4.1 and 6.4.2).

B.5 SPH PROPERTIES RELEVANT FOR THE [CII] EMISSION

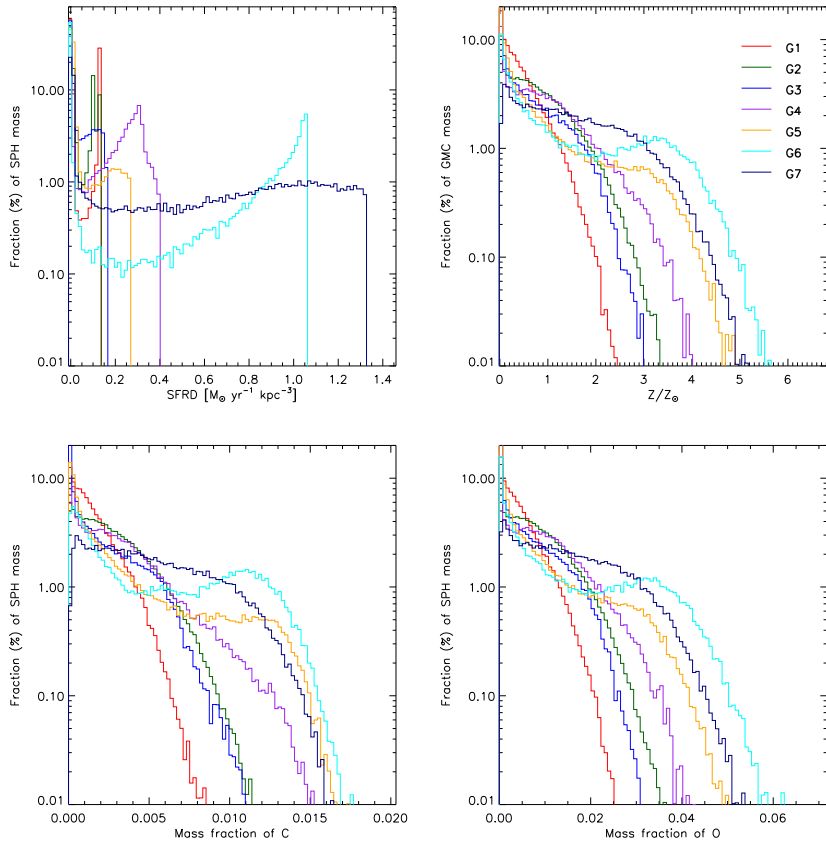


Figure B.6 Mass-weighted (by SPH mass) histograms of SPH gas properties in the simulations of our set of seven model galaxies at $z = 2$.

B.6 REFERENCES

- Bakes, E. L. O., & Tielens, A. G. G. M. 1994, *ApJ*, 427, 822
Barinovs, Ģ., van Hemert, M. C., Krems, R., & Dalgarno, A. 2005, *ApJ*, 620, 537
Draine, B. T. 2011, *Physics of the Interstellar and Intergalactic Medium* (Princeton University Press)
Goldsmith, P. F., Langer, W. D., Pineda, J. L., & Velusamy, T. 2012, *ApJS*, 203, 13
Haardt, F., & Madau, P. 2001, in *Clusters of Galaxies and the High Redshift Universe Observed in X-rays*, ed. D. M. Neumann & J. T. V. Tran
Keenan, F. P., Lennon, D. J., Johnson, C. T., & Kingston, A. E. 1986, *MNRAS*, 220, 571
Langer, W. D., & Pineda, J. L. 2015, ArXiv e-prints
Oppenheimer, B. D., & Schaye, J. 2013, *MNRAS*, 434, 1043
Papadopoulos, P. P., & Thi, W.-F. 2013, in *Advances in Solid State Physics*, Vol. 34, *Cosmic Rays in Star-Forming Environments*, ed. D. F. Torres & O. Reimer, 41
Papadopoulos, P. P., Thi, W.-F., Miniati, F., & Viti, S. 2011, *MNRAS*, 414, 1705
Papadopoulos, P. P., Zhang, Z.-Y., Xilouris, E. M., et al. 2014, *ApJ*, 788, 153
Pelupessy, F. I. 2005, PhD thesis, Leiden Observatory, Leiden University, P.O. Box 9513, 2300 RA Leiden, The Netherlands
Puchwein, E., Bolton, J. S., Haehnelt, M. G., Madau, P., & Becker, G. D. 2014, ArXiv e-prints
Röllig, M., Ossenkopf, V., Jeyakumar, S., Stutzki, J., & Sternberg, A. 2006, *A&A*, 451, 917
Stahler, S. W., & Palla, F. 2005, *The Formation of Stars* (Wiley)
Wiersma, R. P. C., Schaye, J., & Smith, B. D. 2009, *MNRAS*, 393, 99
Wilson, N. J., & Bell, K. L. 2002, *MNRAS*, 337, 1027